



Magnetic moment measurements in stable Sn isotopes using the transient field technique after Coulomb Excitation in inverse kinematics

MEMORIA PRESENTADA PARA LA OBTENCIÓN DEL TÍTULO DE
DOCTOR

Jennifer Deborah Walker

Universidad Autónoma de Madrid
Instituto de Estructura de la Materia, CSIC

Director
Andrea Jungclaus

Instituto de Estructura de la Materia, CSIC

Departamento de Física Teórica
Universidad Autónoma de Madrid
March 2011

Contents

1	Motivation	1
2	The Transient Field Technique after Coulomb Excitation in Inverse Kinematics	13
2.1	Perturbed Angular Correlations	13
2.2	The Transient Magnetic Field	17
2.3	Coulomb Excitation in Inverse Kinematics	21
2.4	The Alpha Transfer Reaction	25
3	The Experiments U234/U236	27
3.1	The Setup	27
3.2	Calibrations	39
3.3	Data Preparation: The Example of $^{114}\text{Sn}/^{118}\text{Te}$	43
3.4	The Example of $^{122}\text{Sn}/^{126}\text{Te}$	62
4	Data Analysis	75
4.1	Determination of the logarithmic slopes	75
4.1.1	Angular Correlation Fits	75
	Angular Correlations with Velocity Corrections	75
	Determining the Lifetimes from the lineshapes	80
	Angular Correlations	82
	Combining the total number of detected events for the $3^- \rightarrow 2^+$ and $4^+ \rightarrow 2^+$ transitions in cases with large yields	88
4.1.2	Comparison between experimental and calculated angular correlations	90

Using MuSTanG to obtain the angular correlation for directly populated states	90
Comparing the results	94
4.1.3 The Angular Correlation of the directly populated $2^+ \rightarrow 0^+$ transition	98
4.1.4 Other methods to determine the slopes	101
4.2 Determination of the precession angles	105
4.2.1 Obtaining the precession experimentally	105
4.2.2 Precession Results	106
5 The feeding corrections	115
5.1 Introduction	115
5.2 The structure of the computer program	119
5.3 Stopping power	121
5.4 Kinematics	123
5.5 Coulomb excitation cross sections	127
5.6 Calculated Precessions	134
6 g-factor results including feeding corrections	139
6.1 Results	144
7 Discussion	151
8 Resumen en Castellano	159
8.1 Motivación	159
8.2 La técnica de los campos magnéticos transitorios en combinación con la excitación coulombiana en cinemática inversa	161
8.2.1 Correlaciones Angulares perturbadas	161
8.2.2 Campos Magnéticos Transitorios	162
8.2.3 Excitación Coloumbiana en cinemática inversa	163
8.3 Montaje Experimental	164
8.3.1 Preparación de los datos	165
8.4 Análisis de los datos	165

8.5	Correcciones por poblaciones desde estados de alto espín	166
8.6	Los resultados	168
8.7	Resumen y conclusiones	169
A	Summary of literature information concerning level schemes, lifetimes, moments and transition strengths for $^{112,114,116,122,124}\text{Sn}$	171
B	Result Details	175
C	Error Propagation	181
C.1	Error Treatment of Data	181
C.2	Error propagation in the Centre of Mass velocity transformations . .	182
C.2.1	Error in β	182
C.2.2	Error in θ	184
C.2.3	Error in $W_{cm}(\theta)$	184
D	$\beta \pm \Delta\beta$ obtained for all isotopes	187
E	Acknowledgements	193
	Bibliography	195
	List of Figures	205
	List of Tables	210

Chapter 1

Motivation

A key topic of research in experimental and theoretical nuclear physics is the study of the structure of nuclei far from β stability, with a particular focus on the changes to the proton-neutron interaction, the evolution of shell closures and modifications of collective properties. An important question is whether the shell closures which characterize the valley of stability are preserved or disappear in nuclei with large differences in the number of neutrons and protons, up to the limit of nuclear existence. Most of these changes can be understood in terms of the monopole drift of the single-particle states, particularly towards the increasingly neutron-rich nuclei. On the proton-rich side, the Coulomb interaction plays a major role in determining the nuclear properties and in particular whether nuclei are bound or unbound. In the vicinity of the $N=Z$ line however the occupation of identical orbits and the large overlap between protons and neutrons gives rise to additional complexity. Near the $N=Z$ line proton-neutron pairing, core-polarization and isospin symmetry conservation are the object of many experimental studies. Doubly-magic ^{100}Sn is the heaviest proton-bound $N=Z$ nucleus and lies on the edge of the proton dripline. These features make this nucleus and its neighbours an ideal test ground to the various origins of structural modifications in exotic nuclei.

A unique feature of the Sn isotopes, is that between the shell closures of $N = 50$ and $N = 82$, lies the longest experimentally accessible chain of semi-magic ($Z = 50$) nuclei, and are particularly interesting for testing the validity of nuclear structure models. The Sn chain of isotopes produced so far in the lab runs from ^{100}Sn , on the proton dripline with $N=Z$, to the ^{138}Sn isotope with 14 neutrons more than the heaviest stable Sn isotope at ^{124}Sn . There is significant focus on the study

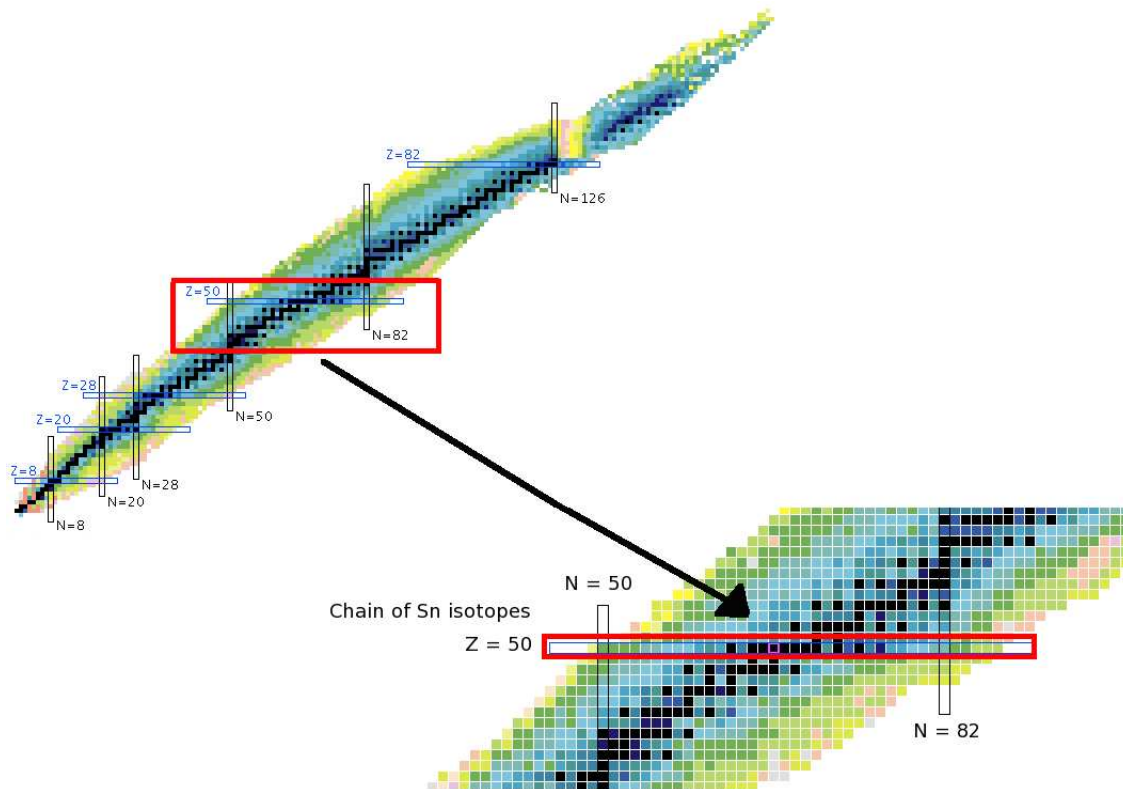


Figure 1.1: The location of the Sn chain in the chart of nuclides.

of excitations of the $Z=50$ core and neutron valence space of a full major shell. The region surrounding the Sn chain is a good study ground for understanding the nuclear structure of nuclei located far away from the valley of stability; from observed quantities such as the excitation energies and the transition strengths, the Sn isotopes have been considered a good example for the approximate validity of the generalized seniority scheme [1],[2]. A good method for investigating core excitation, and a sensitive probe into the structure of these nuclei are the $BE2(E2;0^+_{g.s} \rightarrow 2^+_1)$ values.

Due to the $Z=50$ proton shell being closed, the development of collectivity from the $N=50$ and $N=82$ neutron shell closures towards mid-shell is driven by the neutrons filling successively the $d_{5/2}$, $g_{7/2}$, $d_{3/2}$, $s_{1/2}$ and $h_{11/2}$ orbitals. In the nuclear shell model, a smooth and symmetric increase of collectivity is expected from ^{100}Sn and ^{132}Sn towards the mid-shell nucleus ^{116}Sn , as evidenced by the reduced transition strength $B(E2;0^+ \rightarrow 2^+)$ between the ground state and the first excited 2^+ state.

In recent years experiments have been conducted at REX-ISOLDE[3][4], MSU[5], GSI[6][7], Oak Ridge[9], University of Kentucky[11], and the Inter-University Accelerator Centre (IUAC) in New Delhi[8], to measure the $B(E2;0^+ \rightarrow 2^+)$ transition strength in the neutron deficient, and neutron-rich Sn isotopes using Coulomb excitation of relativistic, intermediate and low energy radioactive ion beams. The result of these studies is the observation of unexpectedly large transition strengths in the light Sn isotopes in which the lower half of the $N=50-82$ major shell is filled. Fig. (1.2) summarizes the known experimental $B(E2;0^+ \rightarrow 2^+)$ values in comparison to shell model calculations which assume a ^{100}Sn core and a neutron effective charge of $1e$.

For isotopes lighter than ^{112}Sn , the transitions strengths were measured using radioactive beams, which explains the larger uncertainties. The deviation from the parabolic shell model prediction is also confirmed in the measurements of the stable isotopes. One can see that for the recent stable isotope measurements the errors are reduced, which makes the stable isotopes good tool to study deviations from the seniority scheme. The measurements of ^{114}Sn by P. Doornenbal [7] and ^{112}Sn by R. Kumar [8] were both stable-beam experiments which were normalized to the previously measured ^{116}Sn .

The asymmetric behaviour of the $B(E2;0^+ \rightarrow 2^+)$ values with respect to the $N=66$ neutron midshell at $A=116$ is striking and is not only in disagreement with the already shown large-scale SM calculation but also with all other available predictions [5, 6].

One possible explanation of this trend of enhanced transition probabilities for the 2^+ states in the light Sn isotopes, is the increasing importance of small admixtures of proton excitations across the $Z=50$ shell gap as the neutron number decreases[6][4]. Shell model calculations which include such proton core excitations of up to four protons show that they indeed result in an increase in the transition strengths. However, due to the seniority truncation used, they still retain the parabolic and symmetric shape (see figure (1.4a) in blue) [6]. These calculations used unscreened values of $e_\pi=1.5e$ and $e_\nu=0.5e$ for the effective proton and neutron charges.

The most sensitive probe into the single particle structure of nuclei, and hence the best possible way to detect small admixtures of proton excitations across the $Z=50$ shell gap in the even Sn isotopes is by the measurement of the magnetic

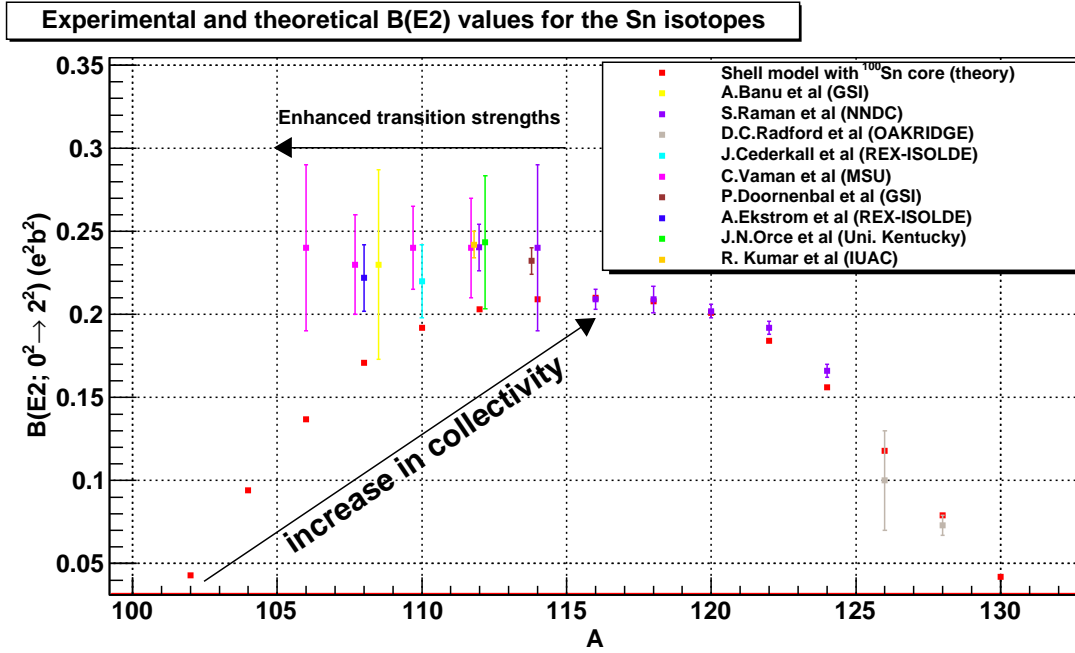


Figure 1.2: The experimentally measured $B(E2; 0^+ \rightarrow 2^+)$ transition strengths for the chain of Sn isotopes compared to a shell model calculation.

moments of their first excited 2^+ states.

The classical definition of a magnetic dipole moment is the vector cross product of the current I with the area A around which the charge circulates. The magnetic moment provides sensitive information regarding the nature of the nucleons which form the current, and the single particle orbitals they occupy. The magnetic moment can be expressed as:

$$\vec{\mu} = g\mu_N\vec{I} \quad (1.1)$$

with I being the spin of the state, μ_N the nuclear magneton and the dimensionless quantity g the gyromagnetic ratio (or g-factor).

The angular momentum of a nucleon in the nucleus includes both a spin and an orbit contribution, and the resulting magnetic moment therefore contains two terms:

$$\vec{\mu} = \mu_N(g_l\vec{l} + g_s\vec{s}) \quad (1.2)$$

where the quantities g_l and g_s , respectively, are the orbit and the spin g-factors. For the proton, the spin and orbit g factors are $g_s^\pi = +5.587$ and $g_l^\pi = 1$ and

for the neutron $g'_s = -3.826$ and $g'_l = 0$. The values of the measured magnetic moments for the neutron and the proton are $\mu(\nu) = -1.91304272(45)$ and $\mu(\pi) = +2.792847337(29)$ [12], respectively.

This large difference between the proton and neutron magnetic moment in both sign and magnitude is the main attribute which permits one to deduce information about the composition of the wavefunction of a nuclear state by measuring its magnetic moment. This is also true for most of those cases in which nuclear states consist of a superposition of different configurations.

If one would assume that the magnetic moments of odd nuclei arise solely from the spin and orbital magnetic moment from the odd unpaired nucleon, the g-factor of a state characterized by the quantum number j and l is:

$$g_{Schmidt} = g_l \pm \frac{g_s - g_l}{2l + 1} \quad (1.3)$$

for $j \pm 1/2$, and it is called the Schmidt value or the Schmidt limit. The magnetic moments found experimentally for almost pure single-particle states are in general smaller than the Schmidt values. This is due to the nucleon being embedded in the nuclear medium, where polarization plays a significant role and the nucleons no longer act “free” [13]. When calculating the g-factors of single particle states one usually uses the “effective” g-factors from experimentally determined values instead of the free-particle g_l and g_s . In general, the difference between the two is roughly: $g_s^{eff}(\pi, \nu) \approx 0.75 \cdot g_s(\pi, \nu)$ and $g_l^{eff} \approx 1.1$ or -0.1 , for protons and neutrons respectively.

In the case of the Sn isotopes, an increase in proton admixtures across the Z=50 shell gap for the 2^+ state would lead to an increase in the measured g-factors because all the relevant proton orbitals above the Z=50 shell gap and the occupied $g_{9/2}$ orbital, have large and positive effective g-factors.

Figure (1.3) shows the effects of proton excitations compared to neutron excitations in the ^{114}Sn nuclei across various shell gaps for the case of the shell model, emphasizing the single particle sensitive information which the magnetic moments provide.

π Orbital	g_{eff}	ν Orbital	g_{eff}
$\pi g_{9/2}$	+1.22	$\nu d_{5/2}$	-0.43
$\pi d_{5/2}$	+1.38	$\nu g_{7/2}$	+0.18
$\pi g_{7/2}$	+0.73	$\nu s_{1/2}$	-1.8
		$\nu d_{3/2}$	+0.46
		$\nu h_{11/2}$	-0.25
π Configuration	g_{eff}	ν Configuration	g_{eff}
$\pi g_{9/2} d_{5/2}$	+1.09	$\nu d_{5/2} g_{7/2}$	+0.23
$\pi g_{9/2} g_{7/2}$	+1.34	$\nu d_{5/2}^{-1} s_{1/2}$	-0.20
		$\nu d_{3/2} s_{1/2}$	-0.11
		$\nu g_{7/2}^{-1} d_{3/2}$	+0.04

Table 1.1: The effective g-factors for the single particle and 2^+ configurations.

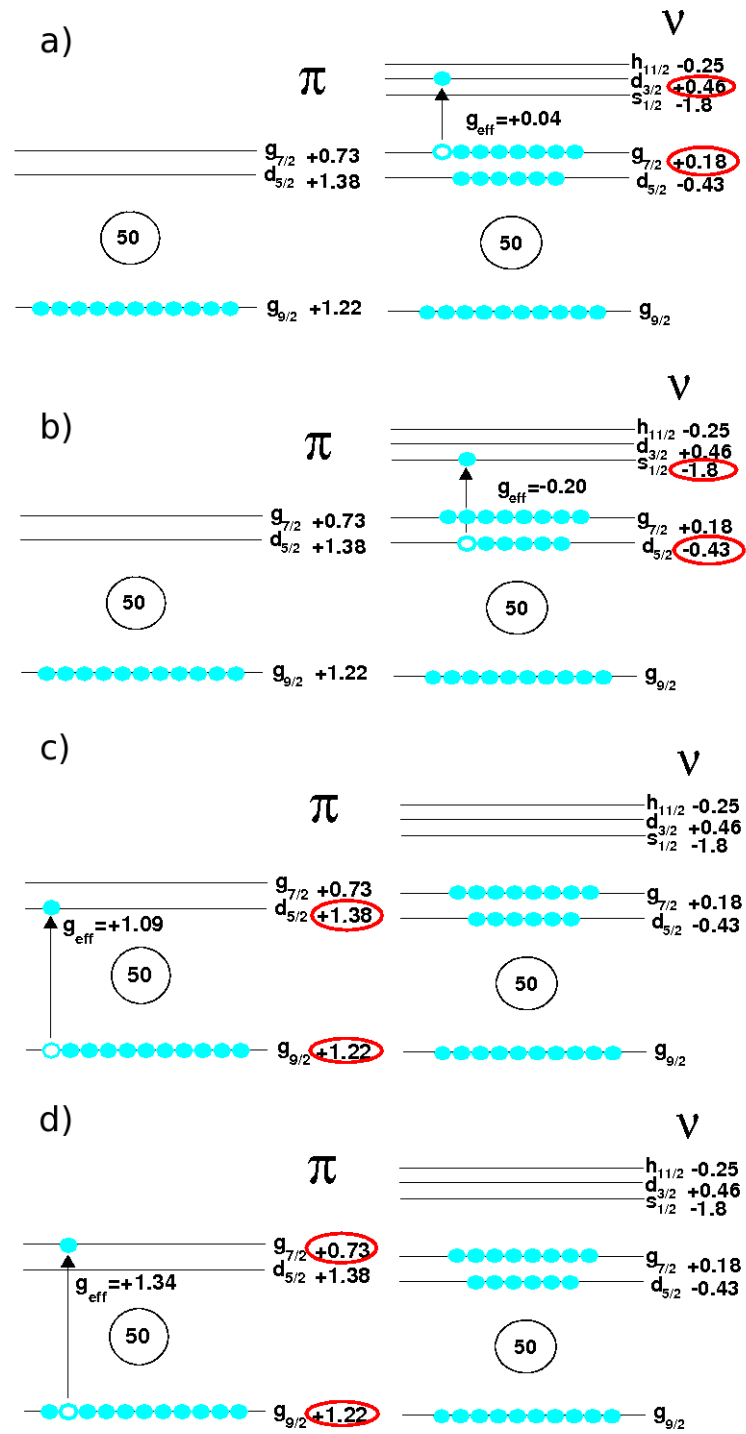


Figure 1.3: The effective g-factors in ^{114}Sn at various excitations across the neutron and proton shell gaps, where a) is the configuration of $\nu g_{7/2}^{-1} d_{3/2}$ b) has the configuration $\nu d_{5/2}^{-1} s_{1/2}$ c) $\pi g_{9/2} d_{5/2}$ d) $\pi g_{9/2} d_{7/2}$

The $B(E2;0^+ \rightarrow 2^+)$ values obtained from current shell model calculations with a core of ^{100}Sn agree with the experimentally measured data for the chain of Sn nuclei between $A=130$ down to the neutron mid-shell at $A=116$; it is after this mid-shell point where the lighter isotopes cease to follow the shell model's $B(E2;0^+ \rightarrow 2^+)$ calculations. This is shown in figure (1.4a) in red, and all the experimental values are shown in black. The corresponding g-factors for this model are shown in red in figure (1.4b). An experimental measurement of the g-factors would aid in understanding the anomalous $B(E2;0^+ \rightarrow 2^+)$ results, because the sign and magnitude of the measured g-factor is so sensitive to the single particle configuration. One can see in figure (1.4a) that the $B(E2;0^+ \rightarrow 2^+)$ values calculated for the shell model with a core of ^{90}Zr core, marked in blue, where there are proton excitations across the $Z=50$ shell gap.

Figure (1.4) also exhibits additional calculations made in the framework of the Quasi Random Phase Approximation (QRPA) model[17][18], and the Relativistic Quasi Particle Phase Approximation (RQRPA) of mean field theory[15][16]. The $B(E2;0^+ \rightarrow 2^+)$ values and g-factor calculations for these models are given in pink (QRPA) and green (RQRPA). The QRPA model satisfies the experimental data for the $B(E2;0^+ \rightarrow 2^+)$ values of isotopes ranging from $A=130-116$, but it decreases parabolically after the neutron mid-shell at $A=116$ towards ^{100}Sn , so the lighter isotopes no longer agree with the observed enhancement of the $B(E2;0^+ \rightarrow 2^+)$ transition strengths; and the RQRPA model agrees with the data in the range of $A=106-110$ but beyond $A=110$ this model ceases to agree with the measured $B(E2;0^+ \rightarrow 2^+)$ values of heavier isotopes. One can see in figure (1.4a) that there is no agreement between the various models and the data, so from the $B(E2;0^+ \rightarrow 2^+)$ values alone the full picture of the nuclear structure of the even-even Sn isotope chain cannot be deduced.

But one can see in figure (1.4b) that the g-factors differ for each model, and a measurement of the magnetic moment could be a very useful way to understand the $B(E2;0^+ \rightarrow 2^+)$ rates and the structure of Sn isotopes. The RQRPA model has a very positive g-factor with a gradual decrease as A increases, originally from the spin contribution of the neutrons as neutron number, N , increases, but one can still observe that there must be a significant proton contribution in this wavefunction. Whereas the QRPA model gives g-factors which are distinctly negative in sign until $A=128$; this could be attributed to single particle configurations of the excited 2^+ state where the excited neutron configurations are dominated by the orbitals of

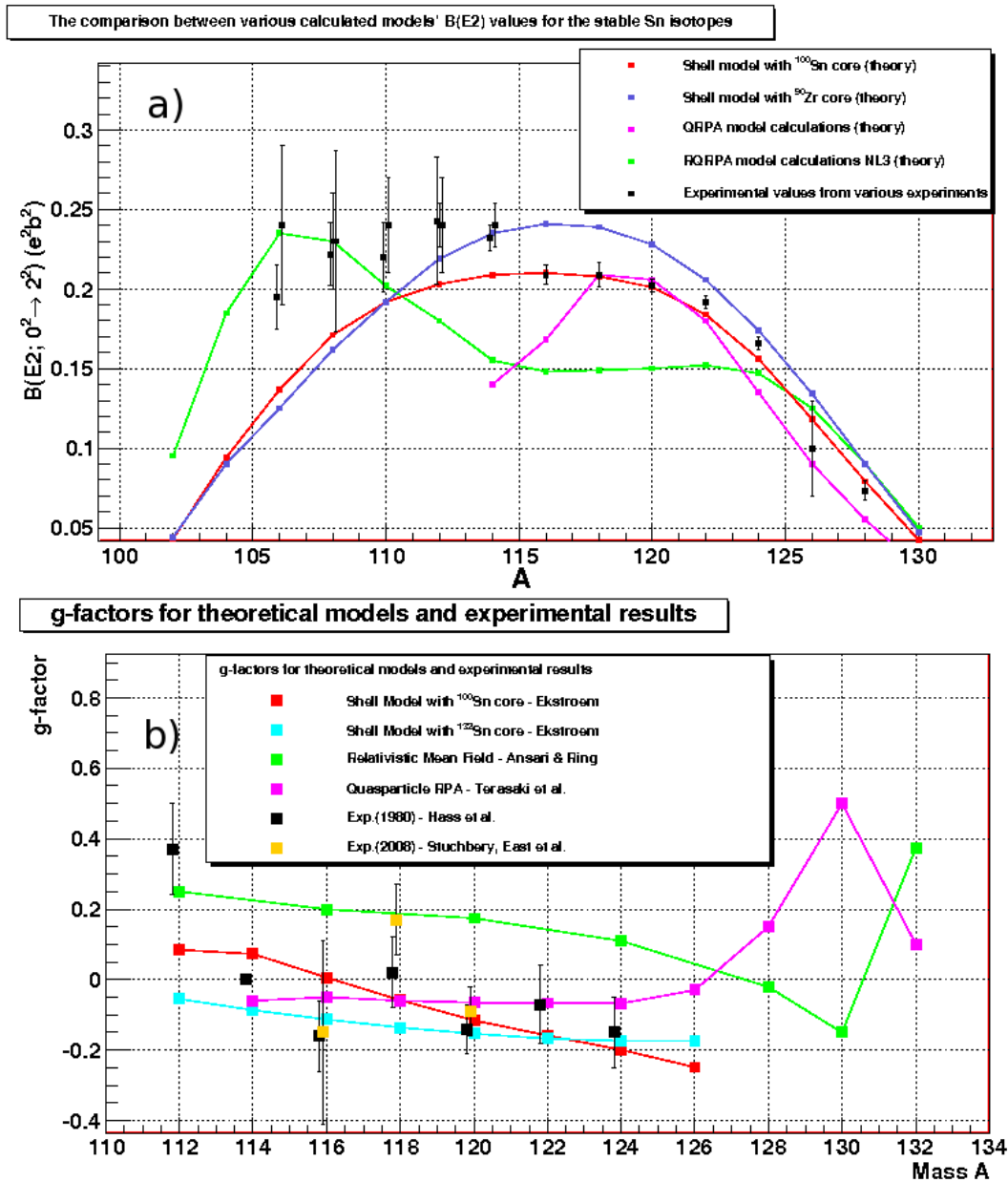


Figure 1.4: a) The $B(E2; 0^+ \rightarrow 2^+)$ values from calculations of different nuclear models compared to the experimental data. b) The g -factors from calculations of different nuclear models when compared to previous data.

$1h_{11/2}, 2d_{5/2}, 3s_{1/2}$ which are all have negative g -factors. Once $N=78$ is reached, the $2d_{3/2}$ shell with a positive effective g -factor begins to dominate the configuration until $N=82$ is reached. Then the $2f_{7/2}$ orbit, which again has a negative g -factor,

becomes increasingly important.

The magnetic moments of even-even Sn isotopes have been experimentally studied, first by M. Hass et al. in 1980 [19], and then later in 2008 by M.C. East and A.E. Stuchbery et al [20].

M. Hass et al. measured the magnetic moments of the 2^+ states of all stable even Sn isotopes using transient magnetic fields and Coulomb excitations employing ^{35}Cl beams [19]. The measured g-factors go from negative values for the heavier isotopes to a positive value for the lightest measured isotope: ^{112}Sn . The results for this experiment are shown in black in figure (1.5), and exhibit large uncertainties. While ^{118}Sn shows a value which is small and positive, yet the neighboring isotopes of ^{116}Sn and ^{120}Sn have negative g-factors. M.C. East and A.E. Stuchbery et al. [20] remeasured these isotopes of $^{116,118,120}\text{Sn}$, since the previous work was limited by the calibration of the transient-field strength relative to the Cd isotopes, which had an uncertainty of about 30%.

The experiment performed in 2008 used the ANU 14UD Pelletron accelerator, with a multilayer target with a thick iron foil and with layers of Sn and Pd evaporated onto it. The Sn and Pd nuclei were Coulomb excited via standard kinematics, using a beam of ^{58}Ni of energy 190MeV. By measuring the Sn and Pd simultaneously, the sources of systematic errors in the calibration can be virtually eliminated, especially since Pd isotopes provide a more reliable measurement of the absolute magnitude of g-factors than the Cd isotopes used in the 1980 experiment. The results from this experiment are marked in figure (1.5) in yellow, and agree well with the data from 1980.

In order to understand the experimental g-factors, one has to consider the relevant configurations in the single particle model. For the heavy isotopes $^{120-124}\text{Sn}$, it is expected that the valence orbitals $h_{11/2}$, $d_{3/2}$ and $s_{1/2}$ will have the lowest energy and therefore contribute to the wavefunction of the 2^+ state. These neutron orbitals have effective g-factors of -0.25, +0.46 and -1.8, respectively. The measured g-factors in $^{120-124}\text{Sn}$ are negative indicating a dominance of the $(h_{11/2}^2)$ and $(d_{3/2}s_{1/2})$ (effective g-factor=-0.11) neutron configurations in the 2^+ state wavefunctions. For the case of ^{116}Sn the 2^+ state $(d_{3/2}s_{1/2})$, with an effective g-factor of g=-0.11, appears to dominate the configuration. In $^{112,114}\text{Sn}$, beyond neutron midshell, one expects that the $g_{7/2}$ neutron orbital decreases in energy. The effective g-factor of this configuration is positive and it can be assumed to be responsible for the positive

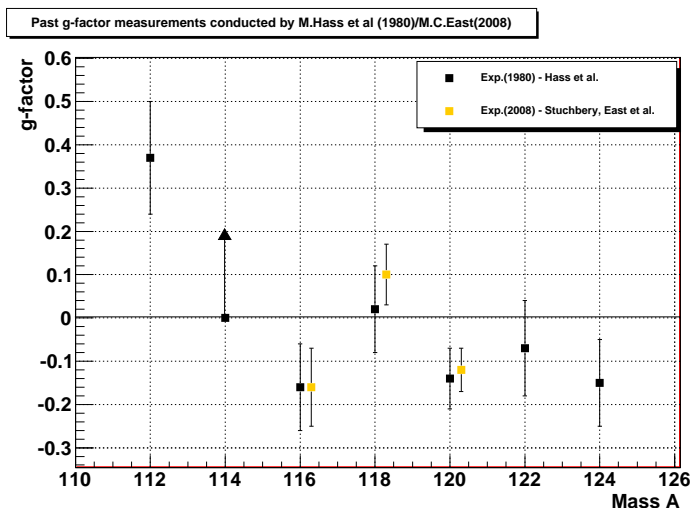


Figure 1.5: The measured g-factors from the experiment conducted by M.Hass et al. (For ^{114}Sn , due to the low-purity target (30%), the experimental $\Delta\phi$ implies only $g(^{114}\text{Sn}, 2^+) \gtrsim 0$ and hence an upper limit is shown here, for more information see reference) [19] and M.C. East and A.E. Stuchbery[20].

measured value of ^{112}Sn , $g=+0.37(13)$. However, considering the effective g-factors (+0.18, -0.17 and +0.23) of the neutron configurations which contribute to the wavefunction of the 2^+ state in ^{112}Sn ($(g_{7/2})^2, (s_{1/2}d_{5/2})$ and $(d_{5/2}g_{7/2})$), the measured value seems to indicate a need for a proton component in the wavefunction.

The above interpretation of the experimental results is of course hampered by their large uncertainties. A more precise determination of the 2^+ g-factors could certainly contribute to a better understanding of the observed anomalous behavior in the transition strengths in the light Sn isotopes with $N \leq 64$. We therefore decided to re-measure $g(2^+)$ in $^{112,114,116,122,124}\text{Sn}$ at the UNILAC accelerator at GSI using an improved experimental technique, namely the transient field in combination with Coulomb excitation in inverse kinematics, and an optimized detection setup for both particle and gamma-ray detection.

The previous results by M. Hass et al and M. East et al. are in agreement with each other, which establishes the reliability of the previous work. In general, one can see these results are in general in agreement with the QRPA model (see figure (1.4b)). The re-measurement of the lighter isotopes in addition to the heavier ones with improved precision would shed insight into the structure of this isotopic

Isotope	g-factor (1980)	g-factor (2008)	adopted g-factor
^{112}Sn	+0.37(13)	-	-
^{114}Sn	$g \gtrsim 0^*$	-	-
^{116}Sn	-0.16(10)	-0.15(26)	-0.16(9)
^{118}Sn	+0.02(10)	0.17(10)	+0.10(7)
^{120}Sn	-0.14(7)	-0.09(7)	-0.12(5)
^{122}Sn	-0.07(11)	-	-
^{124}Sn	-0.15(10)	-	-

Table 1.2: The g-factors of the previously conducted experiments. *Result obtained from a low purity target.

chain. Coulomb excitation in inverse kinematics permits more effective detection of particles in coincidence due to the forward focussing of the target ions, higher velocity through the ferromagnetic layer and hence larger transient magnetic fields - significant improvements can be expected from these new techniques when compared to the previous data published in 1980.

In addition to the g-factor measurement described in this thesis, another analysis was also conducted on this data in order to perform lifetime measurements of the 2^+ states of the Sn isotopes, using the Doppler Shift Attenuation method, and hence a re-measurement of the $B(E2;0^+ \rightarrow 2^+)$ values. The adopted $B(E2;0^+ \rightarrow 2^+)$ values of the $^{112-124}\text{Sn}$ are mostly based on $B(E2)$ measurements from the 1970s, and since information on these isotopes are scarce, the $B(E2)$ values were remeasured via these lifetimes as an independent proof for the observed disagreement in the shell model between ^{114}Sn and ^{116}Sn . These measured lifetimes are discussed in the Discussion chapter. More details on these lifetime measurement can be found in ref. [21].

Chapter 2

The Transient Field Technique after Coulomb Excitation in Inverse Kinematics

2.1 Perturbed Angular Correlations

When a nucleus with a magnetic moment μ experiences a magnetic field B , a torque is induced which causes the nucleus to precess. The frequency of this precession can be described by the Larmor Frequency ω_L [13]:

$$\omega_L = g \frac{\mu_N}{\hbar} B \quad (2.1)$$

where μ_N is the nuclear magneton, g is the g -factor.

For an excited state with a lifetime τ , the torque of the precession will cause the angular distribution of the γ -rays emitted in its decay to rotate by an angle Φ :

$$\Phi = \omega_L \tau = g \tau \frac{\mu_N}{\hbar} B \quad (2.2)$$

for a constant magnetic field B .

If the lifetime of the state is known, the g -factor can be calculated via the measurement of the 2Φ shift in the measured angular correlation measured for both field directions “up” and “down”. The magnitude of this shift is proportional to the strength of the magnetic field B and the lifetime of the state of interest τ . The shorter the lifetime, the larger the magnetic field has to be to observe a significant

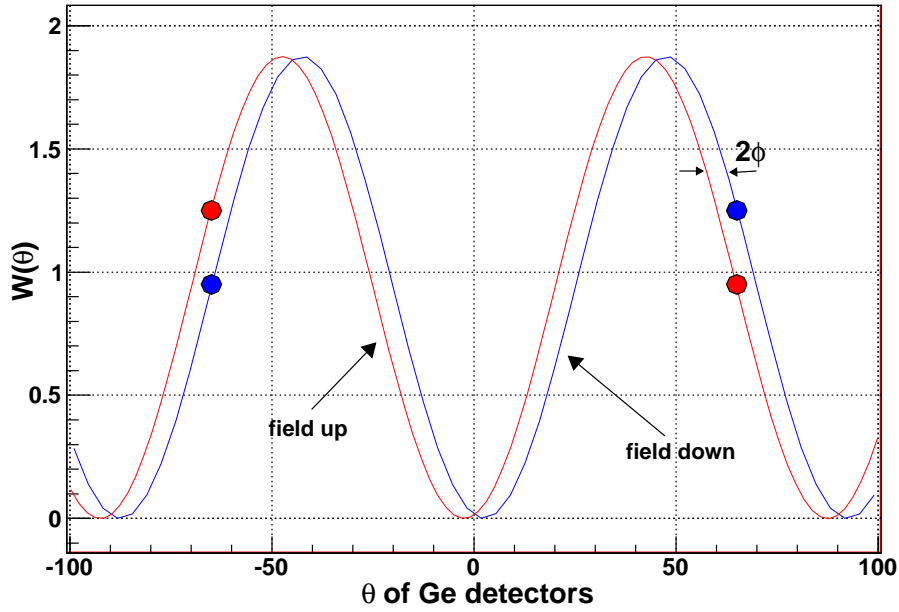


Figure 2.1: The shift 2ϕ for angular correlations measured with two field directions up and down. The points marked in red and blue denote the intensity shift between the up and down field directions for angles $\pm 65^\circ$.

precession. For excited states with lifetimes of a few picoseconds, magnetic fields in the range of kilo Tesla (kT) are needed to introduce measurable precessions of the order of a few mrad. Such field strengths cannot be provided neither by external magnets nor by using static hyperfine fields. To produce magnetic fields large enough to observe the precession of very short lived excited states, transient magnetic fields have to be employed (see section 2.2).

For a magnetic field perpendicular to the beam (quantization) axis, the time-dependent perturbed angular correlation is given by:

$$W(\theta, t, B) = \sum_k A_k P_k(\cos(\theta \pm \omega_L t)) \quad (2.3)$$

where $P_k(\cos(\theta \pm \omega_L t))$ are the Legendre polynomials, and the number of expansion terms, k , is given by the multipolarity L with $k_{max} = 2^L$, i.e. for an E2 transition $k_{max} = 4$.

For short lifetimes only, time-integral precessions can be measured with the so-called *Perturbed Angular Correlation* technique. For γ -rays detected in coincidence with the recoil target ions produced in the target, the generalized form of the

angular correlation is given by [12]:

$$W(\theta_\gamma) = 1 + \sum_k A_k^{exp} P_k(\cos(\theta_\gamma)) \quad (2.4)$$

where $A_k^{exp} = G_k Q_k A_k^{th}$. The parameters A_k^{th} are the theoretical correlation coefficients which apply for angular correlations at maximum alignment. The parameters Q_k and G_k are attenuation coefficients, where Q_k corresponds to the attenuation experienced due to the finite angular acceptance of finite size γ -ray detectors. This attenuation factor is determined by taking into account the solid angle of the detector and its efficiency for the detected incident γ -rays. G_k is the attenuation due to the acceptance angle of the particle detector [12]. The theoretical coefficients A_k^{th} can be calculated via [23]:

$$A_k^{th} = \frac{2L(L+1)}{2L(L+1) - k(k+1)} F_k(I_f I_i L L) = b_k F_k(I_f I_i L L) \quad (2.5)$$

where L is the multipole order of the γ transition and $F_k(I_f I_i L L)$ are tabulated coefficients (see for example Ref. [23]). For a cascade of two transitions ($I \rightarrow M \rightarrow F$), the theoretical parameters are given as:

$$A_k^{th} = b_k F_k(M I L L) F_k(M F L' L') \quad (2.6)$$

where L is the multipolarity of the transition between the states I and M ; L' is the multipolarity of the transition between the states F and M . The theoretical parameters of angular correlations at full alignment for the transitions of interest in the present work are given in table (2.1).

Transition	A_2^{th}	A_4^{th}
$2^+ \rightarrow 0^+$	0.714	-1.714
$4^+ \rightarrow 2^+$	0.510	-0.367
$3^- \rightarrow 2^+$	-0.400	0.000

Table 2.1: Theoretical parameters A_k for different relevant transitions.

Due to parity conservation, only even values of k are allowed for an E2 transition. So the form of the angular correlation for an E2 transition is given by:

$$W(\theta_\gamma) = C[1 + A_2^{exp} P_2(\cos(\theta_\gamma)) + A_4^{exp} P_4(\cos(\theta_\gamma))] \quad (2.7)$$

where C is related to the intensity of the γ transition.

If the angular correlation parameters are measured experimentally, the logarithmic slope, $S(\theta)$ can also be derived. This is a useful quantity given by:

$$S(\theta_\gamma) = \frac{1}{W(\theta_\gamma)} \frac{dW(\theta_\gamma)}{d\theta_\gamma} \quad (2.8)$$

The precession, Φ , is measured by taking the intensity ratios for the magnetic field polarities of up and down for a pair of detectors placed in a horizontal plane perpendicular to the field direction and at symmetric angles, $\pm\theta$, relative to the beamline. The first step for obtaining the measured precession is by taking the double ratios, ρ , defined as [13].

$$\rho = \sqrt{\frac{N(+\theta \uparrow)N(-\theta \downarrow)}{N(+\theta \downarrow)N(-\theta \uparrow)}} \quad (2.9)$$

where $N(+\theta \uparrow)$ is the number of counts measured in the detector at $+\theta$ for field direction up, and $N(-\theta \downarrow)$ is the number of counts measured in detector at $-\theta$ for field direction down, etc. This double ratio is independent of detector efficiencies and the measuring time for the two field directions. The effect, ϵ , is obtained directly from ρ as shown in equation (2.11) and when using the logarithmic slope, $S(\theta)$ the small precessions can hence be obtained by equation (8.6).

$$\epsilon = \frac{\rho - 1}{\rho + 1} \quad (2.10)$$

$$\Phi = \frac{\epsilon}{S(\theta_\gamma)} \quad (2.11)$$

After the precession, Φ , has been measured, the g-factor of the state may be extracted by equation (2.12) [12]:

$$\Phi = -g \frac{\mu_N}{\hbar} \int_{t_{in}}^{t_{out}} B_{TF}(v_{ion}(t)) e^{-t/\tau} dt \quad (2.12)$$

The method for obtaining the precession of a nuclear state as given above only applies for cases when the state is directly populated and does not experience feeding from higher states. If feeding from higher states does occur, then a feeding correction needs to be applied. This is discussed in more detail in chapter 5.

2.2 The Transient Magnetic Field

Transient fields occur when an ion traverses a ferromagnetic material at a velocity v . The nucleus experiences a strong internal hyperfine field with magnitudes of kT to MT depending on the charge of the ion, Z , and the ion velocity. Transient fields arise from a spin exchange with the magnetized electrons of the ferromagnet, which causes a polarization of the spins of the unpaired electrons of the s shells of the moving ion. In the case of a simple model, one can assume this to be a spin exchange between the 1s state of an H-like ion with the polarized electrons of the ferromagnet. The orientation of the transient field is aligned parallel to the external magnetizing field exerted on the ferromagnet.

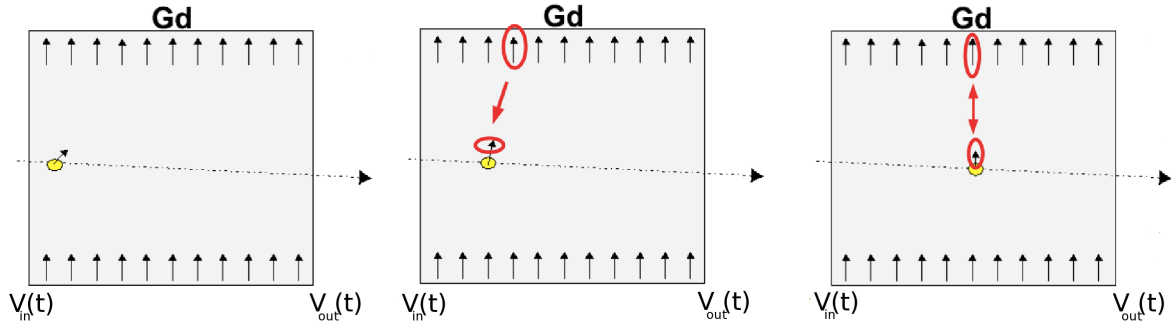


Figure 2.2: The spin exchange between the ferromagnet and the unpaired electrons of the s-shell of the ion, inducing the transient field.

The Fermi contact field is associated with the mechanism which causes the polarization of the s-electrons: an electron from the ferromagnet can be either be captured by a vacant shell or a singly occupied s-shell in the probe ion, which causes the alignment of spins in the s-shell electron to follow the direction of the ferromagnetic polarization. The atomic nature of the Fermi contact field causes the strength of the field to increase with $(\frac{Z}{n})^3$, where Z is the atomic number and n is the principle quantum number of the state in question. There is also an increase in the strength of the transient field as the velocity of the ion increases until it reaches a maximum at the Bohr velocity, $v_0 = \frac{e^2}{h}$; for velocities beyond the Bohr velocity decrease the strength of the transient field.

For the case of a single electron in the s-shell, the largest transient field attainable is given by the relation [12]:

$$B_{TF} = p_{1s}(v, Z, host)q_{1s}(v, Z)B_{1s}(Z) \quad (2.13)$$

where q_{1s} is the fraction of ions with a half-filled 1s orbital, p_{1s} is the degree of polarization and B_{1s} is the hyperfine field produced by an unpaired 1s electron in the nucleus. The hyperfine field can be expressed as [12]:

$$B_{1s} = 16.7 \cdot R(Z) \cdot Z^3 [T] \quad (2.14)$$

where $R(Z)$ is a relativistic correction approximated by:

$$R(Z) \approx 1 + (Z/84)^{5/2} \quad (2.15)$$

The general form of the transient field for more complex cases is given by:

$$B_{TF} = \sum_n p_{ns}(v_{ion}, Z, host)q_{ns}(v_{ion}, Z)B_{ns}(Z) \quad (2.16)$$

Except for the simple case of H-like ions, the strength of the transient field unfortunately cannot be calculated from first principles. To measure g-factors using transient magnetic fields, one has to rely on empirical parameterizations obtained from cases in which the magnetic moment could be measured in parallel using other techniques. The field strength depends on the atomic number Z of the probe ion, the ion velocity in terms of the Bohr velocity $\frac{v}{v_0}$, and the polarization of the ferromagnetic host in terms of the strength parameters a, a', a'' . There are three empirical parameterizations proposed by different groups and which have been widely used in the past:

$$B^{LIN} = a \cdot Z \cdot \frac{v}{v_0} \quad (2.17)$$

$$B^{RUT} = a' \cdot Z^{1.1} \cdot \frac{v^{0.45}}{v_0} \cdot M \quad (2.18)$$

$$B^{CR} = a'' \cdot Z \frac{v}{v_0} \cdot e^{-\beta v/v_0} \quad (2.19)$$

These are the linear [27], the Rutgers [28] and the Chalk-River [29] parameterizations, respectively. The main difference between the various parameterizations is the velocity dependence component. The Rutgers parametrization also includes an explicit magnetization term, M , which is obtained from a magnetometer measurement of the target as a function of temperature. The specific values of a, a', a'' coefficients

[12] and β (v/c) refer to calibration nuclei in different mass regions, where B^{RUT} and B^{CR} are applicable to medium-mass to heavy ions with moderate velocities. For g-factor measurements, B^{LIN} and B^{RUT} are the most commonly used parameterizations. In the present work, the linear parameterization will be employed using the established parameters $a = 17$ T and $a = 12$ T for Gd and Fe hosts, respectively.

An important factor to consider when using heavy ion beams to induce a nuclear reaction, as is the case of Coulomb excitation in inverse kinematics, is the effect which the beam will have on the magnetization of the target and consequently the attenuation of the transient field strength [12]. The attenuation of the transient field is not due to the probe ion but depends on the beam energy and intensity. The attenuation, G_{beam} , is defined as the ratio of the measured transient field B_{TF} to the parameterization value B^{LIN} :

$$G_{beam} = \frac{B^{TF}}{B^{LIN}} \quad (2.20)$$

The key parameter in the attenuation is the energy loss of the beam ions ($\frac{dE}{dX}$) in the ferromagnetic layer, where heavier ions lead to increased attenuations. The magnitude of the attenuation is also sensitive to the velocity of the probe ions, and the higher the velocity the larger the attenuation, this suggests a dependency on the screening of probe ions by the host electrons where the electron-polarized ions are shielded against perturbations caused by the beam ions. Effects of ion velocity and stopping power on the attenuation are shown in figure (2.3). The screening efficiency depends on the velocity of the ion and is largest when the velocity is either close to or below the Fermi velocity of the host electrons. A detailed discussion of the ion beam induced attenuation of the transient field strength can be found in Ref. [12].

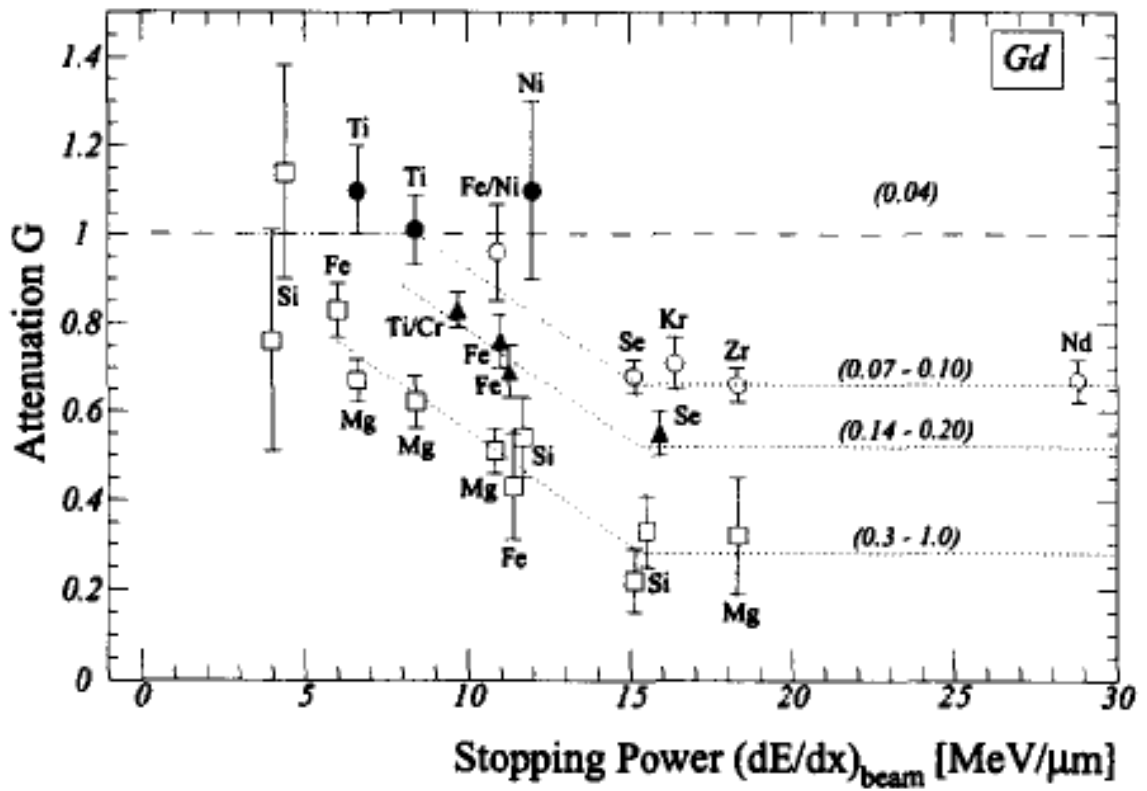


Figure 2.3: Transient field attenuations for different probe ions in Gd hosts vs. the stopping power of the beam ions, where the different regions are divided into sections based on a function of $Z \frac{v}{v_0}$ [12].

2.3 Coulomb Excitation in Inverse Kinematics

The excitation of low-lying collective states is induced by an electric quadrupole field via an electromagnetic interaction between a projectile and a target nucleus. Coulomb excitation occurs when the energy of the projectile is below the Coulomb barrier, so nuclear excitations can occur via a long range electromagnetic interaction between the projectile and target nuclei.

$$E_{CB} = \frac{A_P + A_T}{A_T} \frac{Z_P Z_T e^2}{4\pi\epsilon_0 R} [MeV] \quad (2.21)$$

Equation (2.21) [22] defines the energy of the Coulomb barrier between the projectile P and the target ion T where e is the elementary charge, R is the interaction radius and Z_P and Z_T are the atomic number of the projectile and the target nuclei, where A_P and A_T are the masses of the projectile and target respectively. The interaction radius R is greater or equal to the Coulomb radius which is given in equations (2.22,2.23)[22], where R_i is either the beam or target radius.

$$R_C = R_B + R_T + (3.0 \pm 0.5) fm \quad (2.22)$$

$$R_i = (1.12^3 \sqrt{A_i} - \frac{0.94}{\sqrt[3]{A_i}}) fm \quad (2.23)$$

Nucleus	R_C	E_{CB}
^{112}Sn	10.36(± 0.5) fm	431 MeV
^{114}Sn	10.39(± 0.5) fm	436 MeV
^{116}Sn	10.42(± 0.5) fm	442 MeV
^{122}Sn	10.52(± 0.5) fm	456 MeV
^{124}Sn	10.55(± 0.5) fm	464 MeV

Table 2.2: The Coulomb radii R_C and Coulomb barrier heights for $^{112,114,116,122,124}\text{Sn}$ beams on a ^{12}C target.

Coulomb excitation has many advantages to be used as the mechanism for excitation, firstly its large cross-sections which helps to maximize statistics in the measured data. The differential cross-section for the excitation of a state via an electric multipole transition $E\lambda$ can be expressed as:

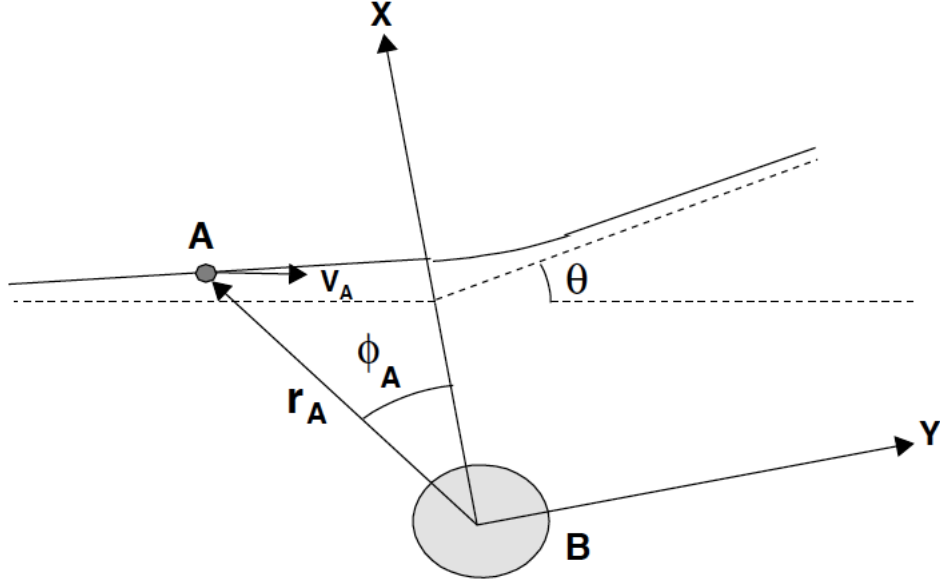


Figure 2.4: Trajectory of the projectile in orbit in the Coulomb field of the target nucleus in the classical picture.

$$d\sigma_{E\lambda} = \left(\frac{Z_P e}{\hbar v}\right)^2 a^{-2\lambda+2} B(E\lambda) df_{E\lambda}(\theta, \zeta) \quad (2.24)$$

$$a = \frac{Z_P Z_T e^2}{m_0 v^2} \quad (2.25)$$

where Z_P is the atomic number of the projectile, a is the distance of closest approach given in equation (2.25) and the function $df_{E\lambda}(\theta, \zeta)$ is a tabulated function in which θ is the scattering angle of the projectile and ζ is the adiabacity parameter. The scattering angle, θ , is in the centre of mass reference frame and m_0 is the reduced mass of the projectile and target nuclei. The integration of equation (2.24) over all scattering directions gives the total excitation cross-section of order $E\lambda$, where $B(E\lambda)$ is the reduced matrix element which is the probability to excite the nucleus to a particular state.

The γ decay of states populated by Coulomb excitation can give information about the spin of the nuclear state from the angular correlations of the emitted γ -rays. Populating the states via Coulomb excitation also introduces a large spin

alignment, which means that a large anisotropy is observed in the measured angular correlations leading to large logarithmic slopes with high sensitivity to the observation of the precession. In Coulomb excitation the probe ions are focussed in the direction of the beam axis: the angular momentum vector $L = r \times p$ is perpendicular to the beam direction. The spin alignment for the probe nuclei is $m(l) = 0$ with the spin projection on the quantization axis (beam axis) [13].

Coulomb excitation in inverse kinematics occurs when a heavy projectile undergoes excitation after interaction with a light target. Instead of detecting the recoiling target ions at backward angles, they are projected forward in the beam direction (see figure (2.6)).

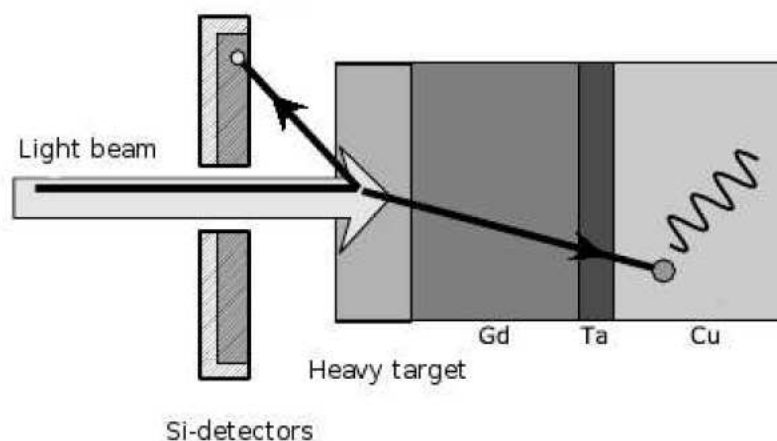


Figure 2.5: A schematic of the standard kinematics in Coulomb excitation where the heavy target ion is excited and the light beam ion is backscattered [22].

As the projectile is excited, both the excited probe ion and the recoiling target ion move in the direction of the beam at high velocity. The target ion has a small charge and mass so it traverses the thick multilayer target and reaches the particle detector placed in forward direction. The heavy projectile ion is stopped in the target backing and the primary beam is stopped in a foil placed between the target and the particle detector. This kinematic focussing of the projectile and target ions in the forward direction has the advantage of improving the number of detected recoil particles at 0° , so there is an improved efficiency in detecting

coincident γ -rays.

Another advantage of using inverse kinematics is that the excited projectile will traverse the ferromagnetic layer of the target at higher velocities. This will cause the ion to experience stronger transient fields since the strength of the transient field depends on the velocity of the ion as discussed in the last section.

Being able to Coulomb excite the projectile also means that the same multi-layer excitation target can be used to measure g -factors in different isotopes. Using different beams on the same target not only allows one to use the beamtime in a very efficient way, but also reduces the systematic uncertainties and leads to very precise relative g -factor values, which in many cases are even more important than the measurement of the absolute g -factor with high precision.

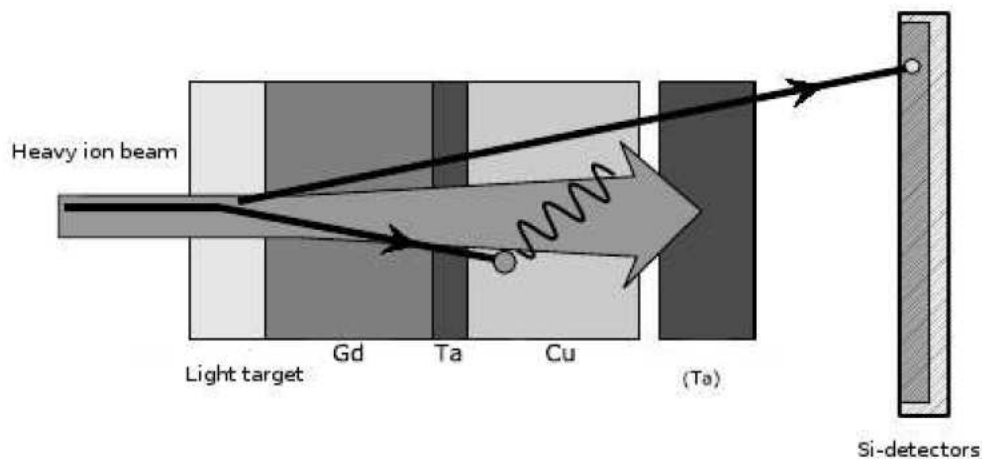
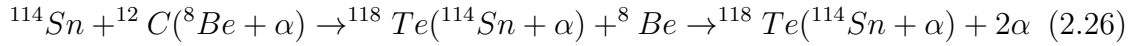


Figure 2.6: A schematic of the inverse kinematics in Coulomb excitation where the heavy beam ion is excited and the light target ion is scattered in the forward direction [22].

2.4 The Alpha Transfer Reaction

For projectile energies slightly below and around the energy of the Coulomb barrier, α -transfer reactions can occur simultaneously with Coulomb excitation. The projectile (in our case a Sn isotope) interacts with the target nucleus (^{12}C), which can be thought of as being a composite bound state of the core ^8Be and an α -particle [31]. During the interaction the α -particle is transferred from the target to the projectile ion leading to a residual nucleus (in this case Te) which can be thought of as a bound state of the projectile (Sn) and an α particle. After the α -transfer, the ^8Be then decays into 2α particles which are detected in the particle detector. For instance, for a ^{114}Sn beam impinging on a ^{12}C target, the reaction could be described by equation:



The α -transfer reaction can also be used for the measurement of magnetic moments. This method has the same advantages of inverse kinematics in that there is also a focussing of the resulting ions in the beam direction, so the particle detector also detects the α particle products which can be used tag the γ -rays of interest by particle coincidences.

The use of α -transfer with a ^{12}C target is an excellent technique to select the state of interest. The first 2^+ state is predominantly populated and the feeding from higher states is significantly reduced.

The spin alignment for ions produced in α -transfer is reduced. The orientation of the angular momentum vector is not fixed in a specific direction as in Coulomb excitation. The angular correlations for nuclei produced in α -transfer will therefore have reduced anisotropies.

Chapter 3

The Experiments U234/U236

3.1 The Setup

The measurement of the g-factors of the 2^+ states for the $^{112,114,116,122,124}\text{Sn}$ isotopes was performed using the transient field technique in combination with projectile Coulomb excitation in inverse kinematics. In the first experiment in 2007 (U234) pure beams of $^{112,114,116}\text{Sn}$ at 4 MeV/u were provided by the UNILAC linear accelerator at GSI and impinged on a multilayer target.

Coulomb excitation of the Sn ions occurred in the first layer of 0.68 mg/cm^2 ^{nat}C . The excited Sn ions then traversed a 10.8 mg/cm^2 thick Gd layer where they experienced a transient field. The gadolinium layer is ferromagnetic, and was magnetized by an external magnetic field which switched polarity between field up and down. The target was cooled via a dewar filled with liquid nitrogen. Gadolinium is ferromagnetic when it is cooled below the Curie temperature of $T_c=293 \text{ K}$, so cooling the target with liquid nitrogen ensures the ferromagnetic layer retains full magnetization during the experiment [33].

As the Sn ions traversed the Gd layer, they experienced a precession. The ions were finally stopped in 4.86 mg/cm^2 Cu layer where they de-excited in a hyperfine interaction-free environment. A thick stopper foil of 24.39 mg/cm^2 Ta was placed after the target before the Si detectors in order to prevent the beam from hitting the Si detectors.

The follow up experiment to U234 - experiment U236 performed in 2009 - utilized the same set up to measure the heavier stable Sn isotopes of $^{122,124}\text{Sn}$ at the UNILAC accelerator in GSI. The differences between the two runs are listed

here, otherwise the set up was the same as described previously. In run U236 the beam energy used was 3.8 MeV/u, with beams of stable ^{122}Sn and ^{124}Sn which impinged on a multilayer target containing an excitation layer, a ferromagnetic layer and a stopper, as before. For the run measuring ^{124}Sn , the target consisted of 0.647 mg/cm² natural carbon, 10.1 mg/cm² gadolinium, 1.0 mg/cm² tantalum and 7.24 mg/cm² copper backing, plus a 5 μm tantalum beam stop. However, halfway through this run modified line shapes were observed.

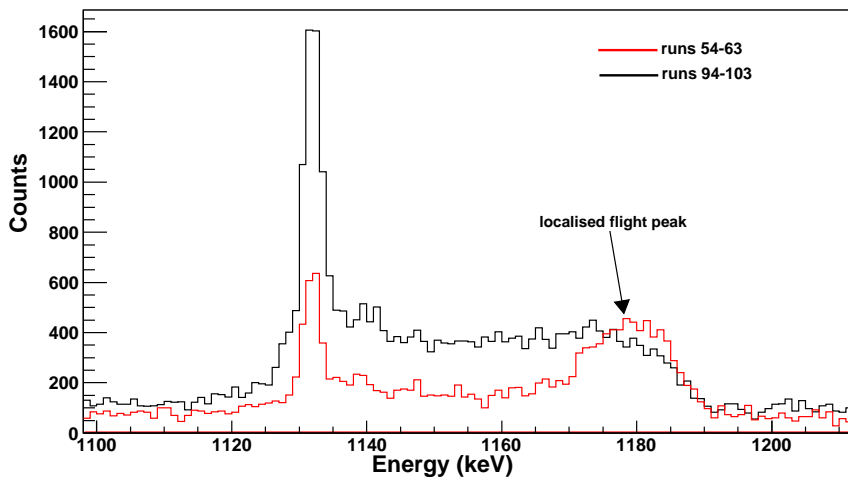


Figure 3.1: The difference seen in the peak between runs.

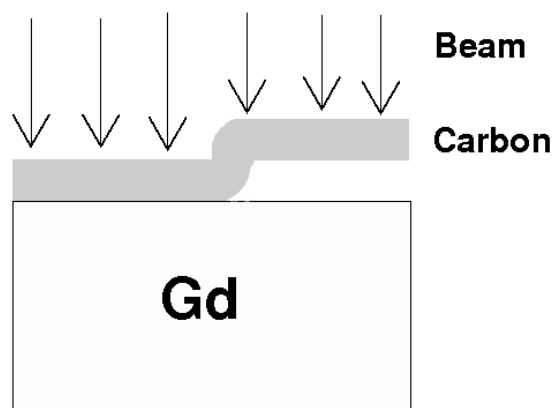


Figure 3.2: A possible explanation as to why the line shape shows a separate flight peak.

The most probable explanation regarding the abnormal line shapes in this run is that a section of the carbon target became detached from the gadolinium, as shown in figure (3.2), and the carbon ions were excited in the detached segment before decaying in vacuum before re-entering the target in the Gd layer. The recoil target ions were still detected in the Si detectors making it impossible to exclude these effects, but for the events after run 90, when the line shape resumed closer to the standard form, one can assume that this detached part of the target “broke” off, leaving a semi intact carbon target attached to the Gd layer, and when gated on the carbon ions, only the valid Sn events are taken into consideration.

For the next run of ^{122}Sn the target was changed because of the broken target in the ^{124}Sn run. The target used for measuring ^{122}Sn consisted of 0.66 mg/cm² layer of natural carbon, 10.9 mg/cm² of Gd, 1.0 mg/cm² Ta and 5.23 mg/cm² Cu stopper, the beam stop used was 20 μm of Ta.

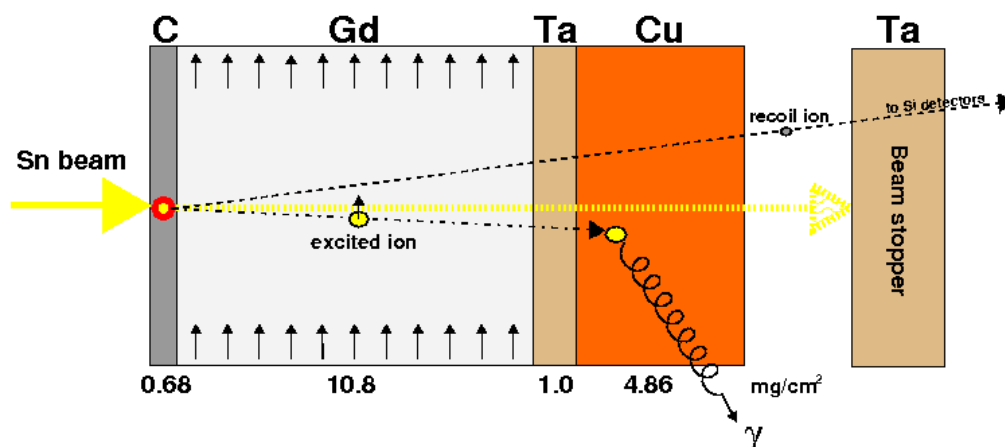


Figure 3.3: Sketch of the multilayer target used in the experiment U234.

About 3 cm behind the multilayer target an array of silicon pin diodes was positioned in order to track the recoil target ions. When a Sn ion of the primary beam undergoes Coulomb excitation, a carbon target ion recoils in forward direction. This ion traversed the multilayer target and was detected by the silicon detector array. The particle detectors consisted of four 1cm x 1cm silicon diodes located symmetrically above and below the beam axis. The particle detectors covered an

angular range of $1.9\text{-}20.1^\circ$ for the inner Si detectors and $23.4\text{-}37.5^\circ$ for the outer detectors. This linear geometry has the advantage of selecting the reactions with the largest spin alignment, leading to large anisotropies of the γ -ray angular correlations and consequently to a higher sensitivity to small precessions.

The γ -rays from the de-excitation of the Sn ions were detected by four EUROBALL cluster detectors [34] in positions at $\pm 65^\circ$ and $\pm 115^\circ$ with respect to the beam axis. The distance from the Ge detectors to the target is 22(1) cm. A single Ge detector at 0° is also included in the set up.

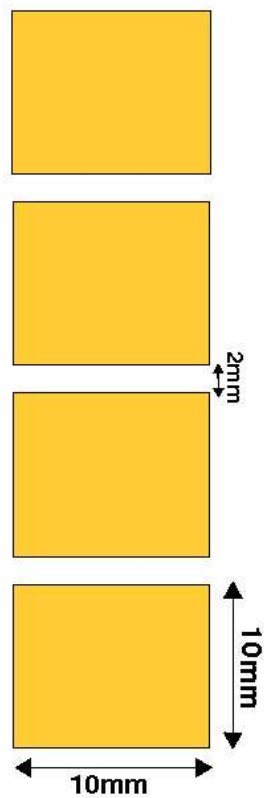
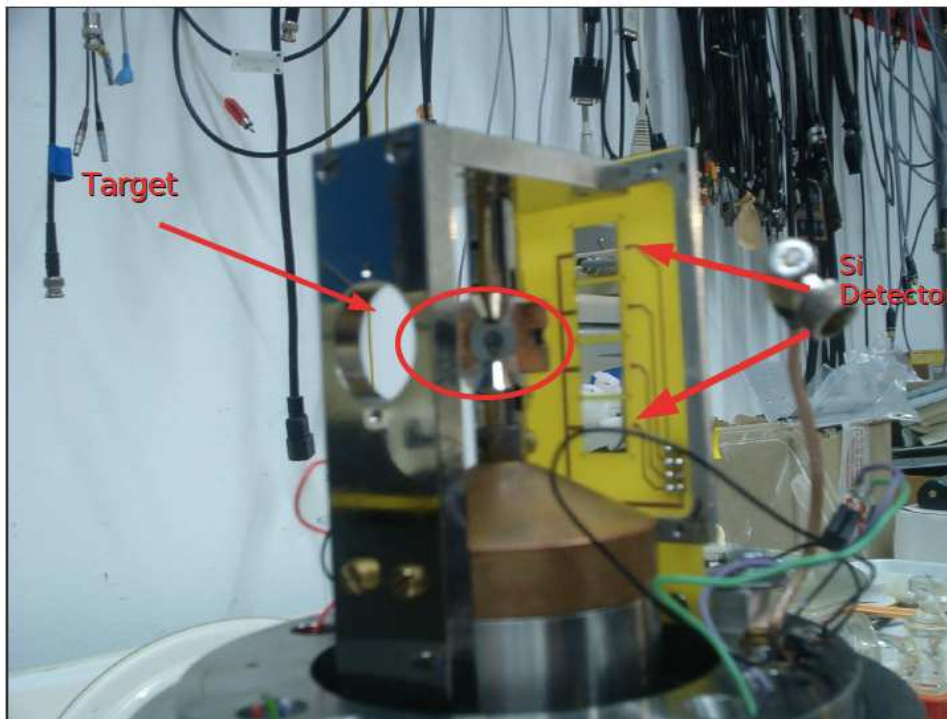


Figure 3.4: Top) Photo of our target chamber. Bottom) A schematic diagram of the particle detector positioned behind the target.

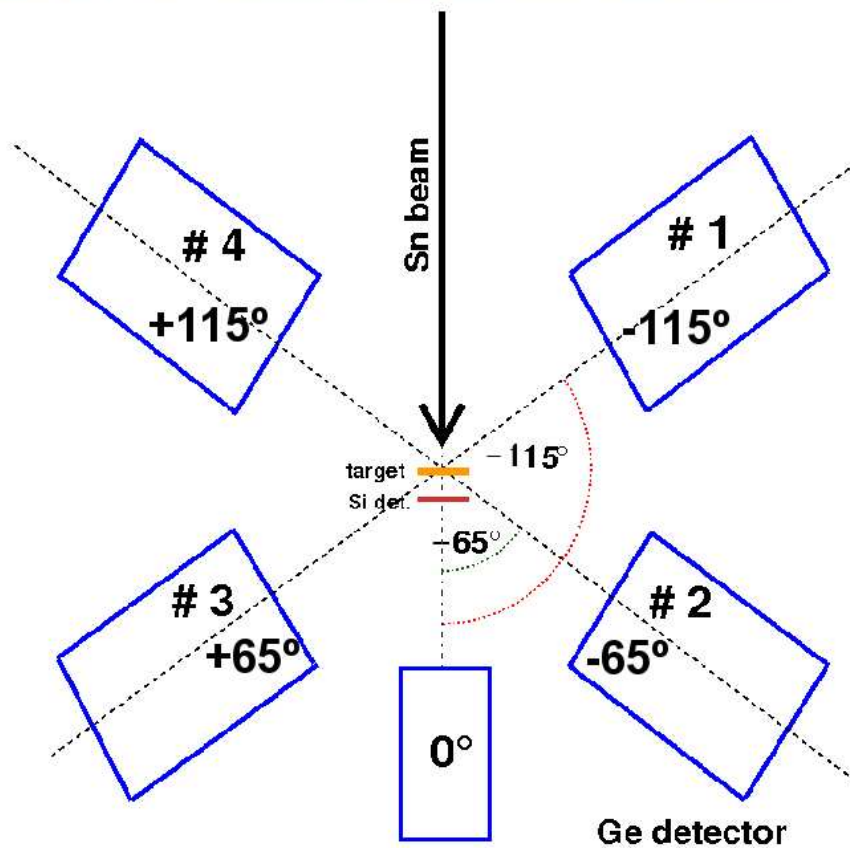
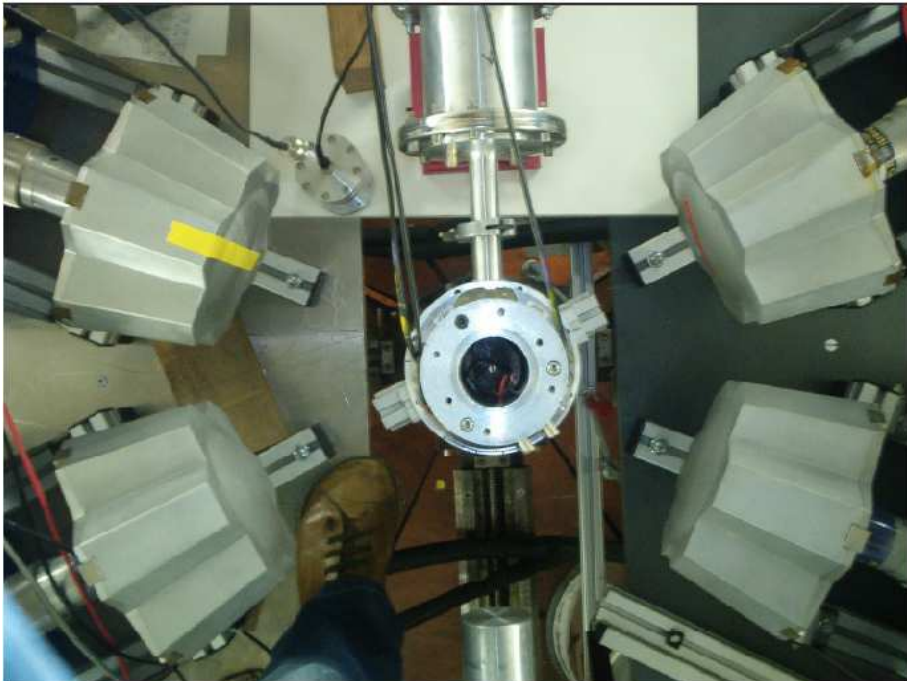


Figure 3.5: Top) Photo of our target chamber. Bottom) The schematic diagram of the Ge detectors with respect to the target and the beam axis.

The EUROBALL cluster detectors each contain 7 individual crystals. Figure (3.6) shows the configuration and labeling of the crystals with respect to the detector setup. Tables (3.1) and (3.2) show the corresponding angles for each crystal of each cluster.

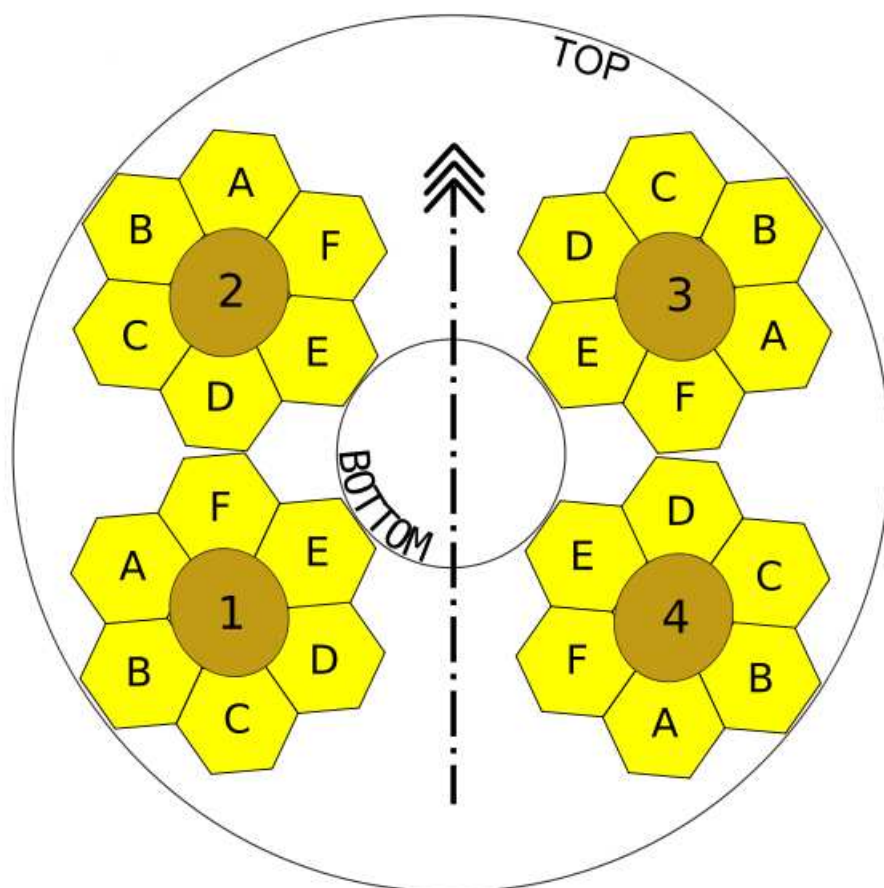


Figure 3.6: Detail of the cluster detectors and the crystals for U234.

To obtain the detector angles θ' (relative to the beam axis in a horizontal plane) and ϕ' (angle out of the horizontal plane), the relative angles between the crystals were calculated using the geometry of the cluster detectors as shown in figures (3.7) and (3.8). The total angles can be calculated by adding to the (θ', ϕ') at the core of the cluster which is either $(\pm 65^\circ, 0^\circ)$ or $(\pm 115^\circ, 0^\circ)$.

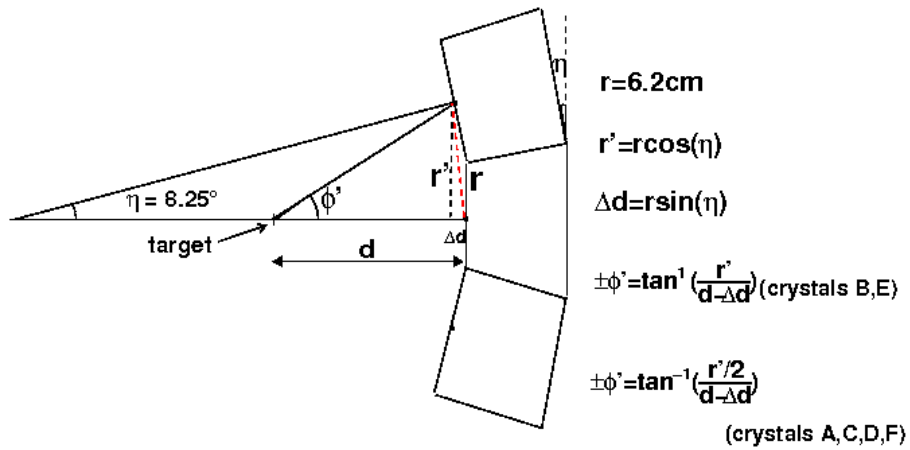


Figure 3.7: Obtaining the relative ϕ between the crystals

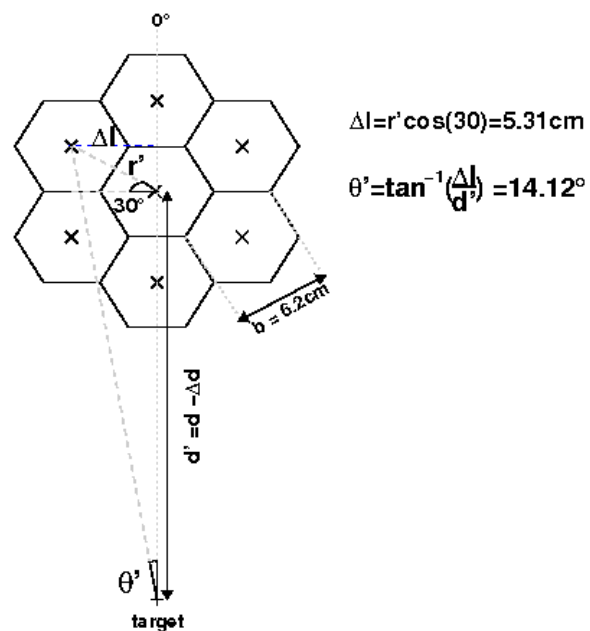


Figure 3.8: Obtaining the relative angle θ between the crystals

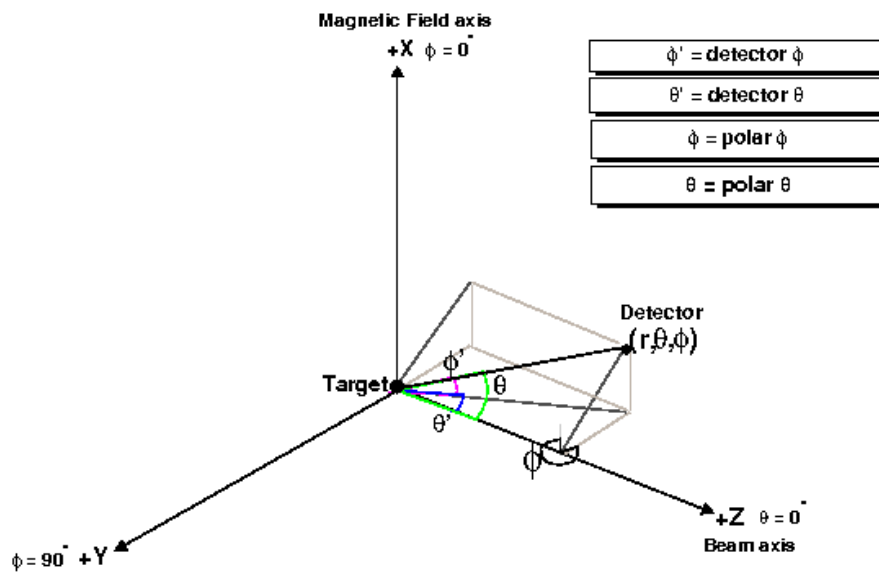


Figure 3.9: The coordinate system showing the detector angles and the polar angles relative to the beam axis [35]

The position of the Ge crystals can also be expressed in terms of the polar angles (θ, ϕ) and the transformation between the two angle reference frames is given by:

$$\cos(\theta) = \cos(\theta') \cos(\phi') \quad (3.1)$$

$$\theta' < 0 : \phi = \pi + \tan^{-1} \left(\frac{\tan(\phi')}{\sin(\theta')} \right) \quad (3.2)$$

$$\theta' > 0, \phi' < 0 : \phi = 2\pi + \tan^{-1} \left(\frac{\tan(\phi')}{\sin(\theta')} \right) \quad (3.3)$$

$$\theta' > 0, \phi' > 0 : \phi = \tan^{-1} \left(\frac{\tan(\phi')}{\sin(\theta')} \right) \quad (3.4)$$

Table 3.1: The crystals and their angles and polar angles: θ', ϕ' are the angles of the detectors, θ, ϕ are the polar angles and d is the distance from the crystal to the target for runs U234.

Cluster	Crystal	$\theta'(^{\circ})$	$\phi'(^{\circ})$	d(cm)	$\theta(^{\circ})$	$\phi(^{\circ})$
1	A	-100.88	+8.27	22.43	-100.77	171.58
1	B	-115.00	+16.20	22.43	-113.94	162.23
1	C	-129.12	+8.27	22.43	-128.64	169.39
1	D	-129.12	-8.27	22.43	-128.64	190.61
1	E	-115.00	-16.20	22.43	-113.94	197.78
1	F	-100.88	-8.27	22.43	-100.77	188.42
1	G	-115.00	0.00	22.00	-115.0	0.00
2	A	-50.88	+8.27	22.43	-51.36	169.39
2	B	-65.00	+16.20	22.43	-66.06	162.23
2	C	-79.12	+8.27	22.43	-79.23	171.58
2	D	-79.12	-8.27	22.43	-79.23	188.42
2	E	-65.00	-16.20	22.43	-66.06	197.77
2	F	-50.88	-8.27	22.43	-51.36	190.61
2	G	-65.00	0.00	22.00	-65.00	0.00
3	A	+79.12	+8.27	22.43	+79.23	8.42
3	B	+65.00	+16.20	22.43	+66.06	17.77
3	C	+50.88	+8.27	22.43	+51.36	10.61
3	D	+50.88	-8.27	22.43	+51.36	349.39
3	E	+65.00	-16.20	22.43	+66.06	342.23
3	F	+79.12	-8.27	22.43	+79.23	351.58
3	G	+65.00	0.00	22.00	+65.00	0.00
4	A	+129.12	+8.27	22.43	+128.64	10.61
4	B	+115.00	+16.20	22.43	+113.94	17.77
4	C	+100.88	+8.27	22.43	+100.77	8.42
4	D	+100.88	-8.27	22.43	+100.77	351.58
4	E	+115.00	-16.20	22.43	+113.94	342.23
4	F	+129.12	-8.27	22.43	+128.64	349.39
4	G	+115.00	0.00	22.00	+115.00	0.00

Table 3.2: The crystals and their angles and polar angles: θ', ϕ' are the angles of the detectors, θ, ϕ are the polar angles and d is the distance from the crystal to the target for runs U236.

Cluster	Crystal	$\theta'(^{\circ})$	$\phi'(^{\circ})$	d(cm)	$\theta(^{\circ})$	$\phi(^{\circ})$
1	A	-99.95	+8.83	21.10	-99.83	171.04
1	B	-115.00	+17.25	21.10	-113.80	161.09
1	C	-130.05	+8.83	21.10	-129.48	168.53
1	D	-130.05	-8.83	21.10	-129.48	191.47
1	E	-115.00	-17.25	21.10	-113.80	198.91
1	F	-99.95	-8.83	21.10	-99.83	188.96
1	G	-115.00	0.00	20.60	-115.00	0.00
2	A	-49.73	+8.96	20.81	-50.32	168.33
2	B	-65.00	+17.50	20.81	-66.23	160.82
2	C	-80.27	+8.96	20.81	-80.39	170.91
2	D	-80.27	-8.96	20.81	-80.39	189.09
2	E	-65.00	-17.50	20.81	-66.23	199.18
2	F	-49.73	-8.96	20.81	-50.32	191.67
2	G	+65.00	0.00	20.30	-65.00	0.00
3	A	+79.91	+8.74	21.29	+80.03	8.87
3	B	+65.00	+17.09	21.29	+66.17	18.74
3	C	+50.09	+8.74	21.29	+50.64	11.33
3	D	+50.09	-8.74	21.29	+50.64	348.67
3	E	+65.00	-17.09	21.29	+66.17	341.26
3	F	+79.91	-8.74	21.29	+80.03	351.13
3	G	+65.00	0.00	20.80	+65.00	0.00
4	A	+130.12	+8.87	21.00	+129.55	11.53
4	B	+115.00	+17.33	21.00	+113.79	19.00
4	C	+99.88	+8.87	21.00	+99.76	9.00
4	D	+99.88	-8.87	21.00	+99.76	351.00
4	E	+115.00	-17.33	21.00	+113.79	341.00
4	F	+130.12	-8.87	21.00	+129.55	348.47
4	G	+115.00	0.00	20.50	+115.00	0.00

3.2 Calibrations

For the energy and efficiency calibrations of the Ge detectors, a ^{152}Eu source was placed in the centre of the target chamber.

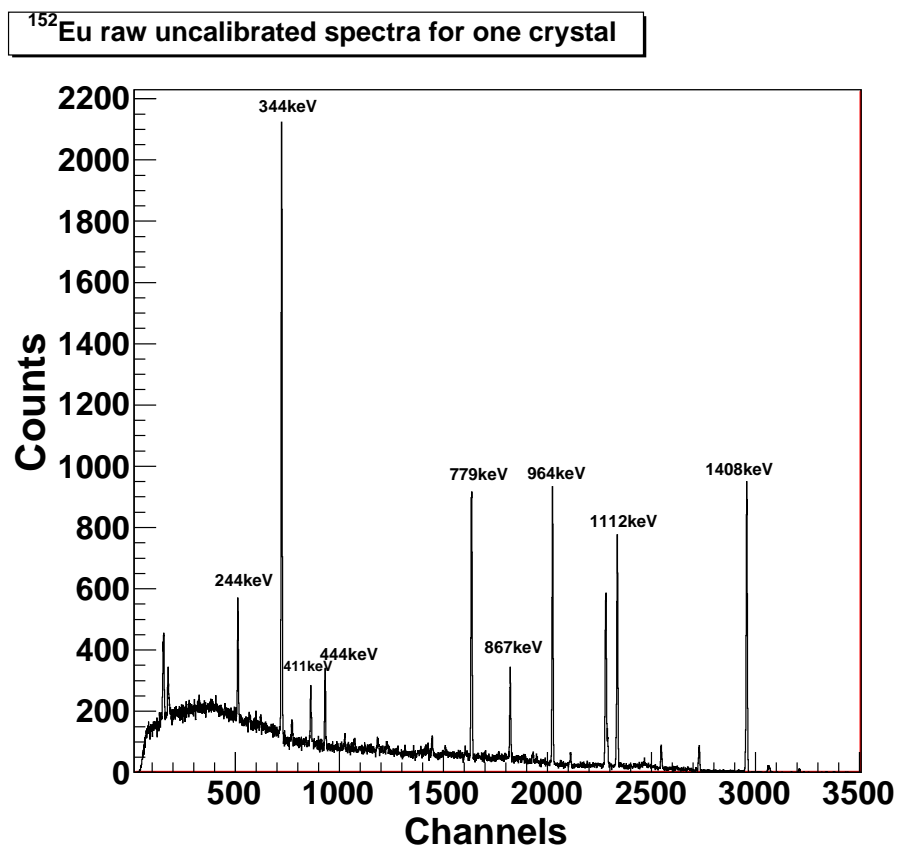


Figure 3.11: An uncalibrated raw gamma spectrum of ^{152}Eu for one crystal.

The centroids of the identified lines in the raw spectra were determined and a linear correlation with the known energies of ^{152}Eu calculated.

An efficiency calibration had to be performed for all individual Ge crystals in order to allow the measurement of angular correlations. The angular correlation is given by the efficiency corrected number of counts in the line of interest in the detectors positioned at different polar angles θ with respect to the beam axis.

The efficiency calibration can be done simultaneously with the energy calibration as this also uses a ^{152}Eu source. For the efficiency calibration the number

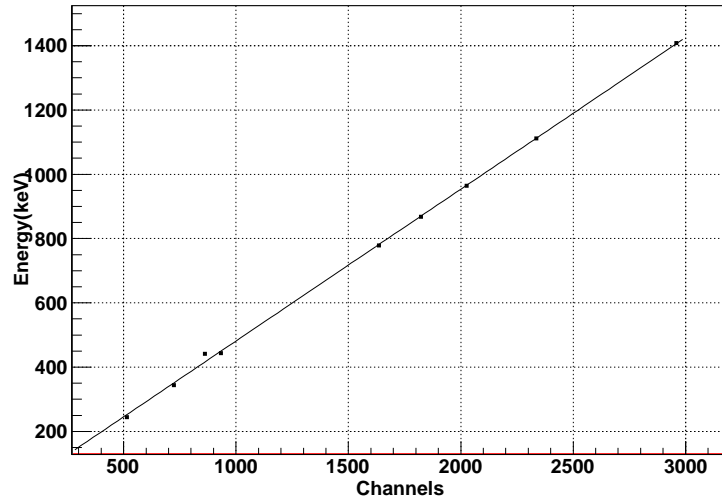


Figure 3.12: The energy of known γ transitions in ^{152}Eu in keV vs the channel number for one Ge crystal.

Energy/keV	Relative Intensity
244.7	36.6(1.1)
344.3	127.2(1.3)
411.1	10.71(0.11)
444.0	15.0(0.15)
778.9	62.6(0.6)
867.4	20.54(0.21)
964.0	70.4(0.7)
1112.1	65.0(0.7)
1408	100.0(1.0)

Table 3.3: The relative intensities of the γ -transitions in the calibration source, ^{152}Eu [36].

of counts observed for each ^{152}Eu transition is obtained from fitting the peaks in the spectrum (3.11). They are then normalized to the known relative intensities of ^{152}Eu given in table (3.3).

After this normalization an efficiency curve can be constructed. The fit of the efficiency curve can be done using the function [37]:

$$f(x) = 0.1 \exp \left[\left[(A + Bx + Cx^2)^{-G} + (D + Ey + Fy^2)^{-G} \right]^{-\frac{1}{G}} \right] \quad (3.5)$$

where $x = \log \frac{E_\gamma}{E1}$ and $y = \log \frac{E_\gamma}{E2}$, with E_γ being the energy of the γ -ray in keV, $E1$ and $E2$ are 100keV and 1MeV respectively.

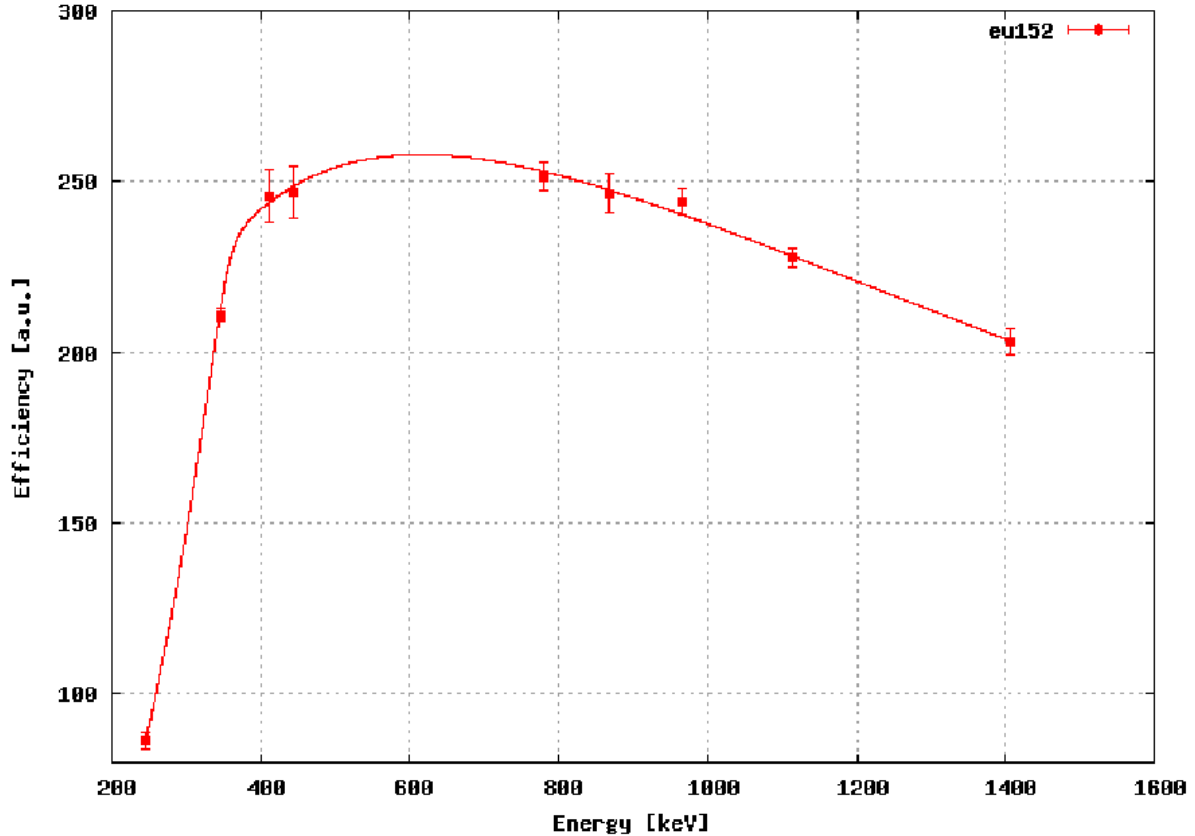


Figure 3.13: The efficiency calibration for one of the Ge crystals.

Using the parameters obtained from the efficiency curve, the relative efficiency of a detector for the energy of interest can be obtained, and then normalized with respect to the other detectors. Figure (3.13) shows a reduced efficiency for γ energies below 400keV. The reason for that is that lead absorbers were set up in front of the Ge detectors to reduce the intensity of low energy gammas seen from the Coulomb excitation of the Gd layer of the target. A significant amount of the primary beam will pass through the carbon layer and cause the Coulomb excitation of gadolinium. The Gd layer of the target is very thick compared to the carbon target, hence there will be a high rate of events from the Coulomb excitation of Gd compared to the excitation of Sn in the target. The Gd target consists of many different

stable isotopes which all have low excitation energies, so putting lead absorbers in front of the Ge detectors helps to reduce the contamination from Gd.

3.3 Data Preparation: The Example of $^{114}\text{Sn}/^{118}\text{Te}$

In the experiment U234, data was taken using beams of ^{112}Sn (36.5 hours), ^{114}Sn (45 hours) and ^{116}Sn (38.5 hours). Here the data preparation will be discussed in detail for the ^{114}Sn run. The isotopes $^{112,116}\text{Sn}$ from run U234 were analyzed in the same way.

The raw detector signals from the detectors are processed by a series of electronics modules, namely ADC's (CAEN ADC V785 [38]), TDC's (CAEN TDC V775 [39]) and DGF's (Digital Gamma Finder - XIA DGF-4C Camac module [40]). This raw data consists of energy and time for the germanium and silicon detectors and the field direction of the magnet. The corresponding modules and data information are given in the tables (3.4) and (3.5).

Module Type	Channel number	Raw Data Information
CAEN ADC V785 (32 ch)	0	Magnet Field up
	1	Magnet Field down
	2	Energy of Si 1
	3	Energy of Si 2
	4	Energy of Si 3
CAEN TDC V775 (32 ch)	5	Energy of Si 4
	0	Time of Si 1
	1	Time of Si 2
	3	Time of Si 3
CAEN TDC V775	4	Time of Si 4
	0-6	Time of Ge cluster 1
	8-14	Time of Ge cluster 2
	16-22	Time of Ge cluster 3
	24-30	Time of Ge cluster 4
	31	Time of Ge at zero degrees

Table 3.4: The raw data information and the corresponding electronic modules.

Module Type	Channel number	Raw Data Information
DGF1	0	Cluster 1 Crystal A
	1	Cluster 1 Crystal B
	2	Cluster 1 Crystal C
	3	Cluster 1 Crystal D
DGF2	0	Cluster 1 Crystal E
	1	Cluster 1 Crystal F
	2	Cluster 1 Crystal G
	3	Ge zero degrees
DGF3	0	Cluster 2 Crystal A
	1	Cluster 2 Crystal B
	2	Cluster 2 Crystal C
	3	Cluster 2 Crystal D
DGF4	0	Cluster 2 Crystal E
	1	Cluster 2 Crystal F
	2	Cluster 2 Crystal G
	3	Empty channel
DGF5	0	Cluster 3 Crystal A
	1	Cluster 3 Crystal B
	2	Cluster 3 Crystal C
	3	Cluster 3 Crystal D
DGF5	0	Cluster 3 Crystal E
	1	Cluster 3 Crystal F
	2	Cluster 3 Crystal G
	3	Empty channel
DGF6	0	Cluster 4 Crystal A
	1	Cluster 4 Crystal B
	2	Cluster 4 Crystal C
	3	Cluster 4 Crystal D
DGF7	0	Cluster 4 Crystal E
	1	Cluster 4 Crystal F
	2	Cluster 4 Crystal G
	3	Empty channel

Table 3.5: The DGF module configuration for experiment U234.

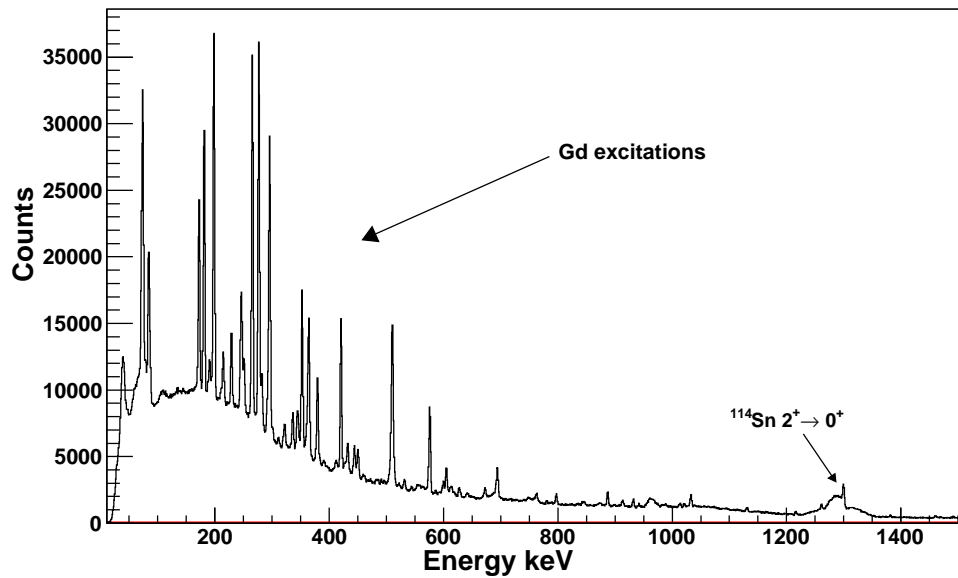


Figure 3.14: The gamma spectrum of ID 1 (Cluster 1 Crystal A) with calibrated energy.

The spectrum shown in figure (3.14) is the result after the energy calibration for one crystal. The line corresponding to the $2^+ \rightarrow 0^+$ transition in ^{114}Sn can be clearly seen. However, there is a very low peak to background ratio in the raw spectra. Most of the contaminants in the spectra come from the de-excitation of the Coulomb excited gadolinium isotopes from the ferromagnetic target layer.

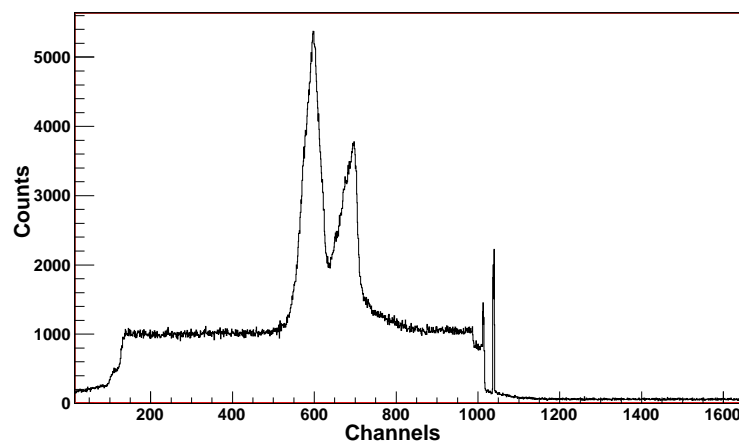


Figure 3.15: The time spectrum of the Ge detector ID 1 (Cluster 1 Crystal A).

Figure (3.15) shows the time spectrum obtained from the TDC module for

one of the germanium crystals. It shows the time difference between the detected γ -ray and the trigger. This and all other TDC spectra show a two peak structure. This can be understood remembering that the p- γ coincidence is triggered by four individual silicon detectors. Each of these four Si has a different time zero (see Fig(3.16)) so the final Ge TDC spectra show structures with more than one peak.

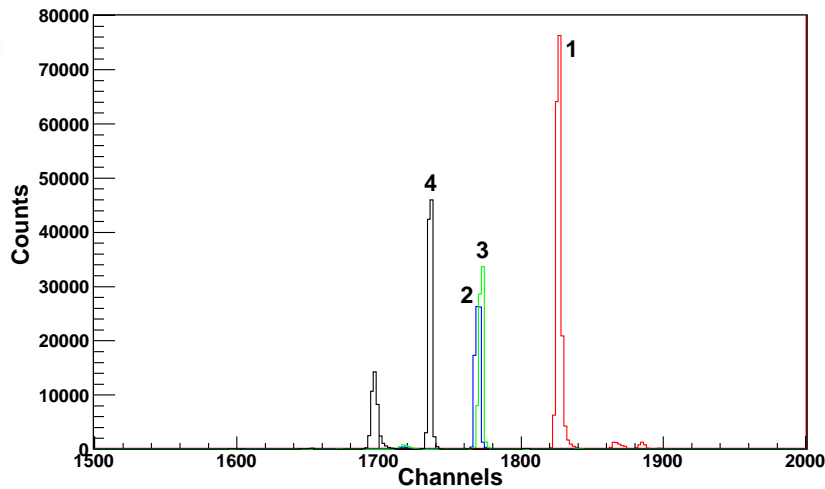


Figure 3.16: The time spectra of the four Si detectors.

When the Ge TDC's are gated by the individual Si TDC's a single peak structure is seen as shown in figure (3.17a). The sum of all four TDC spectra gives the double peak structure seen in the raw Ge TDC spectra. This confirms that each TDC in the Ge triggers on different Si times. This can be corrected by making an event by event subtraction of the Ge TDC from the Si TDC. The difference between the Ge time spectra in coincidence with the inner Si detectors with respect to the outer Si detectors is shown in figure (3.17). A possible explanation for the difference between the inner and outer Si detectors is that the time of flight for the recoil to reach the inner and outer Si detectors is different, since the outer detectors detect recoil ions with lower energies which travel a longer flight path. Hence a different prompt time window for the p- γ trigger will be applied for the inner and outer Si detectors separately.

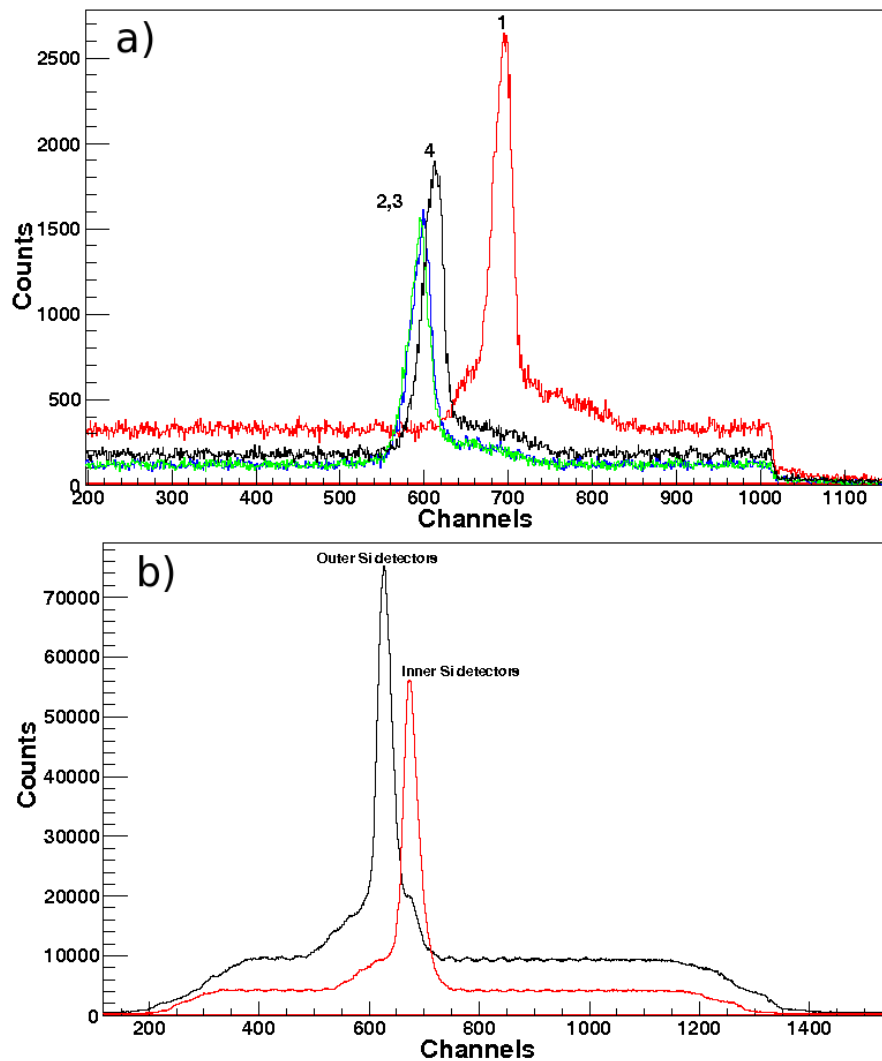


Figure 3.17: a) The time spectra from the Ge detectors when gated on the four different Si TDC's separately. b) The time spectra when the Ge time is subtracted from the time of the triggering Si. (The time is inverted in this spectra as Si TDC - Ge TDC is applied)

For the measurement of the angular correlation and the double ratios it is crucial that the events in the peak for the $2^+ \rightarrow 0^+$ transition in ^{114}Sn come from the Coulomb excitation in the carbon target and not from random events. To ensure that events used in the analysis are valid, conditions and gates are applied to the gamma spectra. The prompt peak of the TDC contains the information of events which occur in the time window when there is a $p\text{-}\gamma$ coincidence. Whether it is Coulomb excitation or α -transfer one is interested in, making a gate on the prompt

peak of the TDC gives the events which are valid when this p- γ condition is fulfilled. Figure (3.18) shows the gate applied for the case of the inner Si detectors. The tail on the left hand side of the peak comes from low energy γ -rays and X-rays which occur in the beam pulse and fusion reactions. These events have poor timing properties due to the poor charge collection times in the detector.

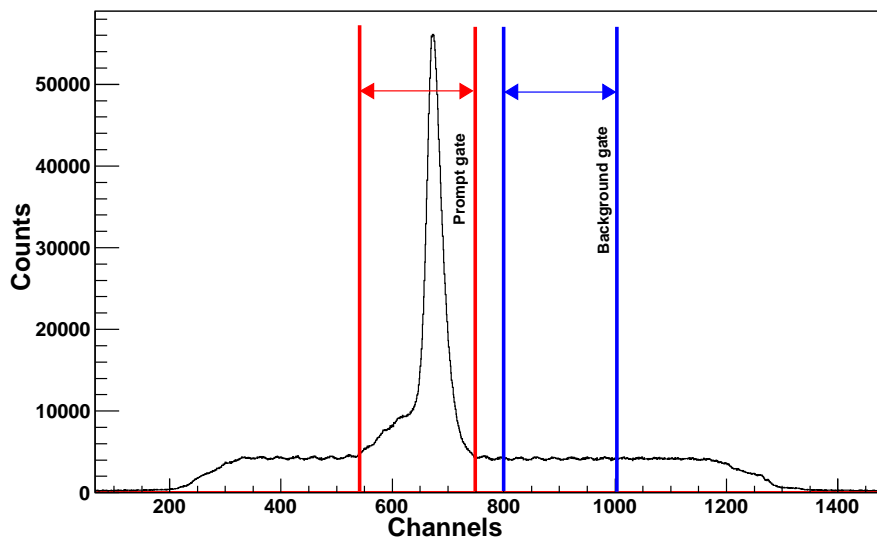


Figure 3.18: Example of the gates applied to the time spectra.

When the prompt gate is used the γ -lines from Coulomb excitation and α -transfer have an enhanced intensity relative to the Gd lines from the background. There is still a contribution from Gd seen in the prompt gated spectra. However when comparing the gamma spectra obtained from the background gate one can see the intensity of the Gd lines is approximately the same as in the prompt gated spectra, but there is a noticeable reduction in the intensity of the lines from ^{114}Sn and ^{118}Te . If the condition is implemented where the background gate is subtracted from the events in the prompt gate, the spectra can be cleaned from the Gd contamination and the γ -spectra only contains the lines from the valid events of ^{114}Sn and ^{118}Te .

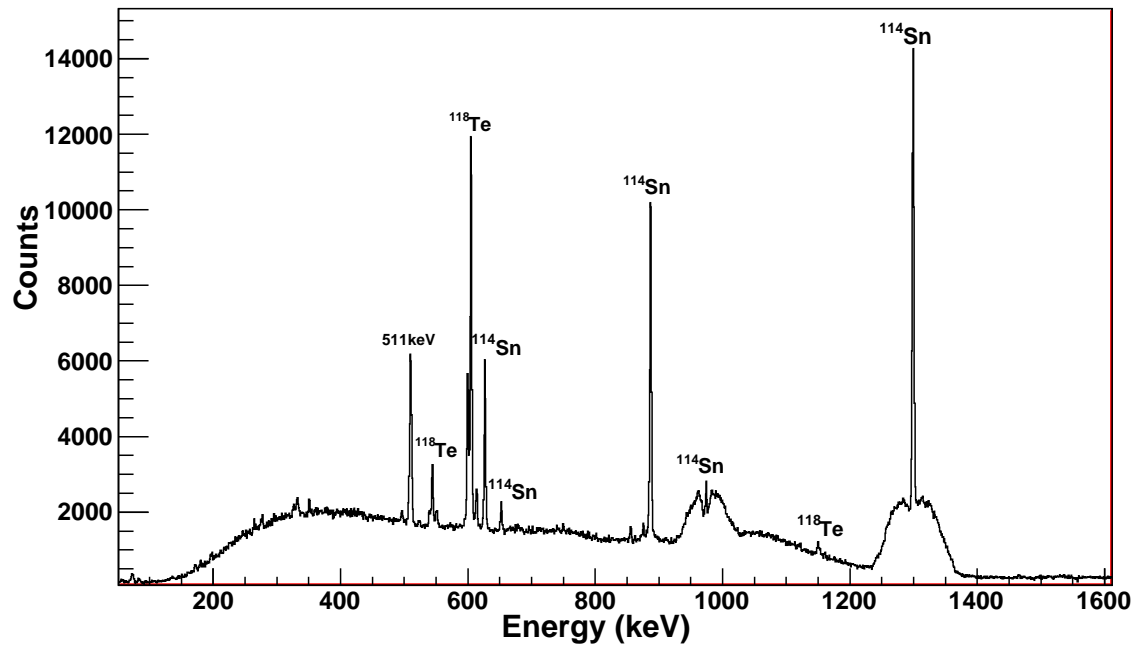


Figure 3.19: Gamma spectrum with the TDC prompt gate implemented and background subtraction for the inner Si detectors for all Ge crystals.

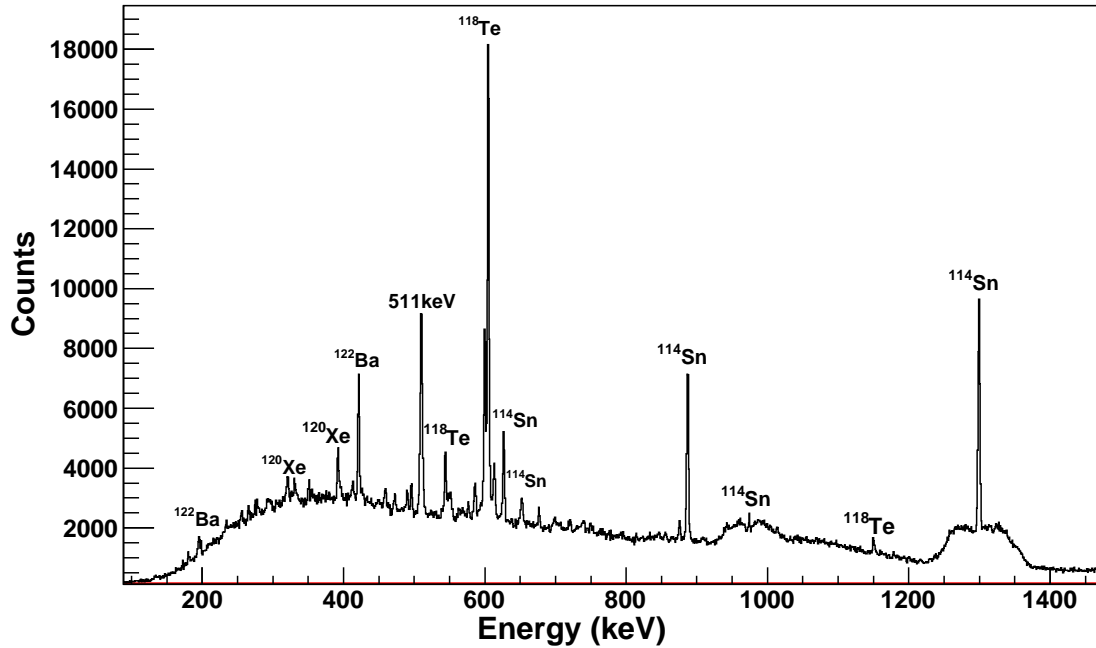


Figure 3.20: Gamma spectrum with the TDC prompt gate implemented and background subtraction for the outer Si detectors for all Ge crystals.

Figure (3.21) shows the energy spectra of recoil particles detected in the silicon detectors. The two reactions of interest, Coulomb excitation and α -transfer, correspond to carbon and α particles being detected respectively. Figure (3.21) show a clear distinction carbon and α particles. Gating on the carbon peak yields the γ -events corresponding to ^{114}Sn , and gating on the α peak results in events of ^{118}Te . Gating on the prompt times for both the Ge and the Si detectors removes the random particle events and noise from the detector.

There is a noticeable difference between the energy spectra of the outer and inner Si detectors. Due to the different angular range, the behavior of the particles for each detector geometry will be different. The energy and the cross-section of the recoiling target ion depends on the scattering angle. When an Sn projectile undergoes Coulomb excitation it interacts with the target ion and the products are scattered as sketched in figure (3.22).

Conservation of energy and momentum dictates how the particles behave with respect to their scattered angles as shown in equations (3.6),(3.7),(3.8) where T is the kinetic energy and P_x is the momentum for each particle.

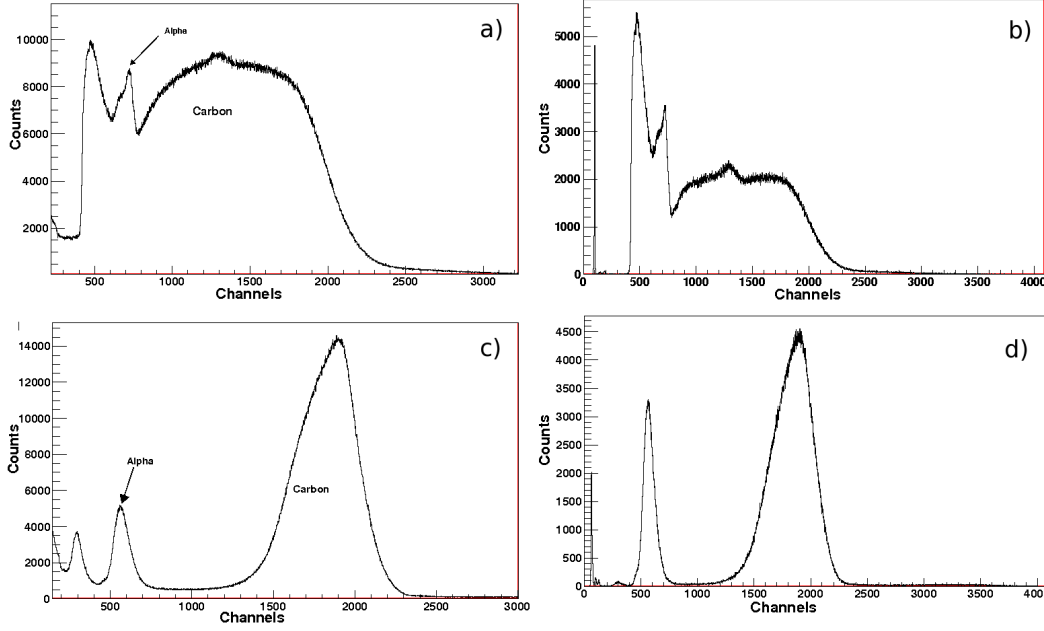


Figure 3.21: The particle energy spectrum for one of the outer silicon detectors a) raw spectrum for ADC2 and b) spectrum gated on the prompt peaks in both Ge and Si TDC's. The particle energy spectrum for one of the inner silicon detectors c) raw spectrum for ADC3 and b) spectrum gated on the prompt peaks in both Ge and Si TDC's.

$$Q = T_{final} - T_{initial} = -E_{excitation} \quad (3.6)$$

$$P_{Sn} = P_C \cos(\theta) + P_{Sn*} \cos(\zeta) \quad (3.7)$$

$$0 = P_C \sin(\theta) - P_{Sn*} \sin(\zeta) \quad (3.8)$$

Coulomb excitation is an inelastic collision, so the Q value is equal to minus the excitation energy of the ion. Usually the scattering of the excited Sn ion is not observed, so the unknown parameters from Sn^* can be eliminated. From equations (3.6), (3.7) and (3.8) the relationship between θ and the kinetic energy of the recoil ion is given by equation (3.9)[41], where θ is measured in the centre of mass frame and T is the kinetic energy of the Sn beam at the point of the target where excitation occurs, m_X are the masses of the reactants and products.

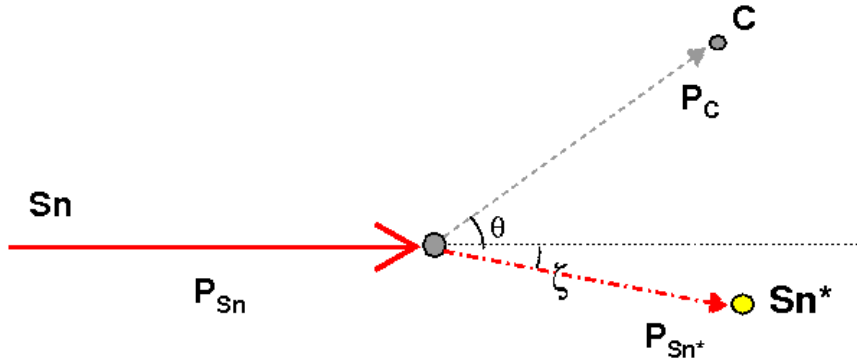


Figure 3.22: The Sn beam interacts with the target to produce the excited Sn ion and an ejected target ion, both scattered in angles ζ and θ , respectively.

$$T_C^{1/2} = \frac{(m_C m_{Sn} T)^{1/2} \cos(\theta) \pm [m_{Sn} m_C T \cos^2(\theta) + (m_{Sn^*} + m_C)(m_{Sn^*} Q + (m_{Sn^*} - m_{Sn} T))]^{1/2}}{m_{Sn^*} + m_C} \quad (3.9)$$

The maximum recoil energy occurs when $\theta=0^\circ$. Using the simulator TRANSI¹, the relationship between the angle of the recoil and its energy can be estimated for this experiment. The difference between the energies of the ions detected in the outer and inner Si detectors is shown in the graph in figure (3.23). TRANSI calculates the Coulomb excitations in different depths of the target for different angle steps of the detected recoil ion. Here the simulation calculates for 10 separate target depths and 10 angle steps.

For the inner Si detector the energies are higher and gradually decrease as the angle increases. The recoil particle energy begins to decrease at a steeper rate as the recoil angle increases for values greater than $\approx 20^\circ$. For the same range of angles, the outer detector experiences a wider range of recoil ion energies when compared to the inner detector. The energy spectrum for the case of the inner detector is expected

¹TRANSI is a fortran program by J.Cub and G.Jakob which simulates a transient field measurement. It takes into account factors such as the excitation in different points in the target, the kinematics at different recoil angles, the excitation cross-section, the slowing down in the target etc.

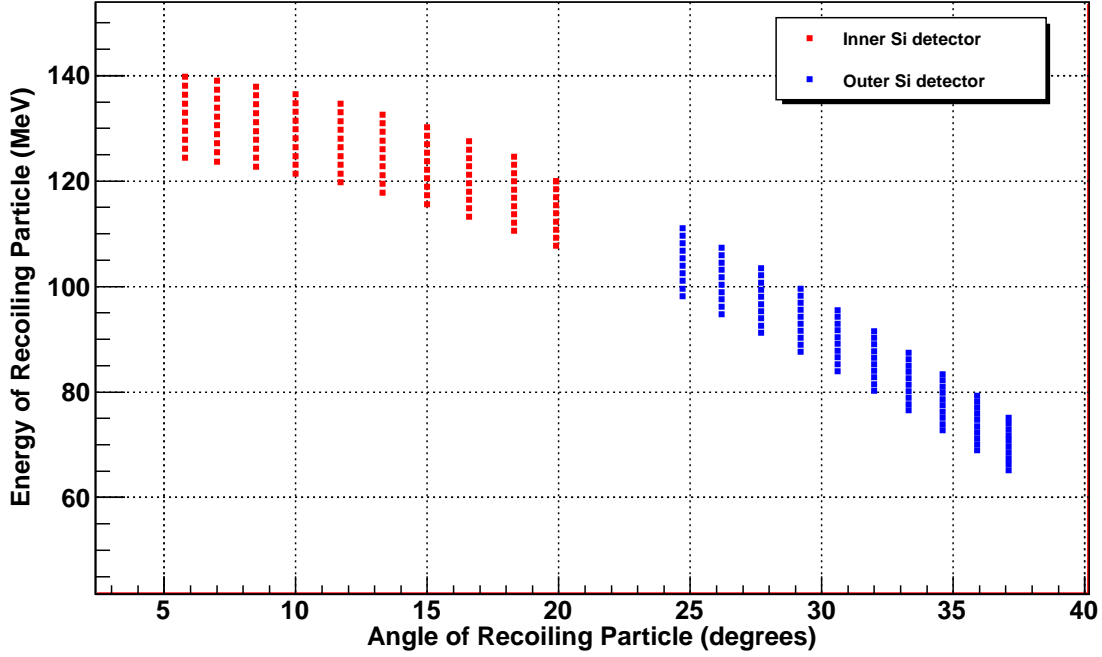


Figure 3.23: The energy of the recoiling target ion vs the recoil angle shown for both inner and outer Si detectors.

to show a concentrated distribution around the energies of 110-140 MeV, whereas for the outer detector a broad peak with lower intensity ranging from 65-115 MeV is expected.

The reaction cross section also depends on the angle of the recoiling particle. The differential cross section for Coulomb excitation is given by [30]:

$$d\sigma = Pd\sigma_R \quad (3.10)$$

where P is the probability that the nucleus is excited in the collision and $d\sigma_R$ is the differential cross-section for Rutherford scattering defined as:

$$d\sigma_R = \frac{1}{4}a^2 \sin^{-4}(\theta/2) d\Omega \quad (3.11)$$

$$a = \frac{Z_1 Z_2 e^2}{m_0 v^2} \quad (3.12)$$

The above equation would give a trend of decreasing cross-section as the recoil angle increases, but the case for inverse kinematics is shown in figure (3.24) calculated from the program TRANSI, which suggests otherwise. The cross-section

increases as the angle θ increases, the solid angle for the inner detector is larger than for the outer ($d\Omega_{in} \approx 0.25$ str, $d\Omega_{out} \approx 0.18$ str). Even with the inner detector having a larger solid angle, the overall cross-section is expected to be larger in the outer detector.

Because of the higher cross-sections, the outer detectors see more events, and with a broader energy spread, as one can see in figure (3.23). For the inner detector, the expected spectra would show a narrow, intense distribution as observed in the figure (3.21d). The outer detectors contain slightly more events due to an increase in the cross-section and the observed counts are spread out over a larger energy leading to a broad distribution, as shown in figure (3.21b). The α particles and carbon ions are separated by their different stopping power in the depletion layer of the detector. However, the above applies to a case when all four detectors run identically, but the number of events in each Si detector is also dependent on the quality of the detector itself. One can see in figure (3.21) that there is a variation, even between geometrically identical detectors. However the shape of the detected carbon ion is consistent with the above - a broad peak for the outer detectors which overlaps at low energies with the α -particles, and the narrow high energy peak of the inner detector completely separate from the α -peak.

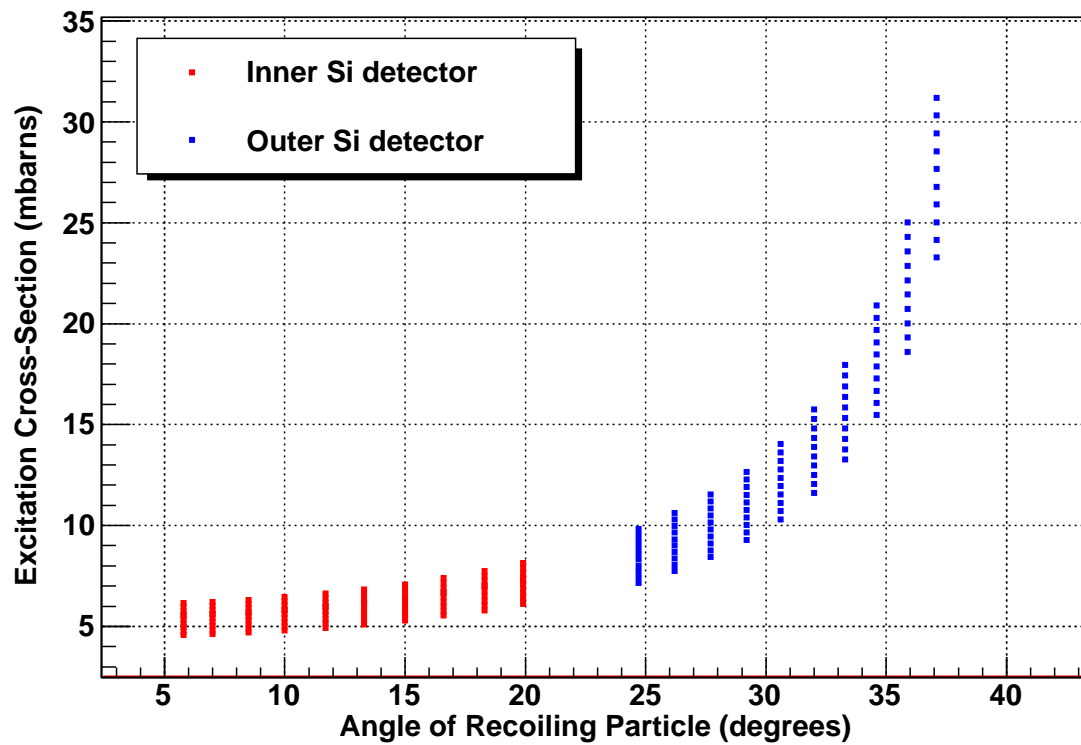


Figure 3.24: The total reaction cross-section vs the recoil angle of the target ions shown for both inner and outer Si detectors.

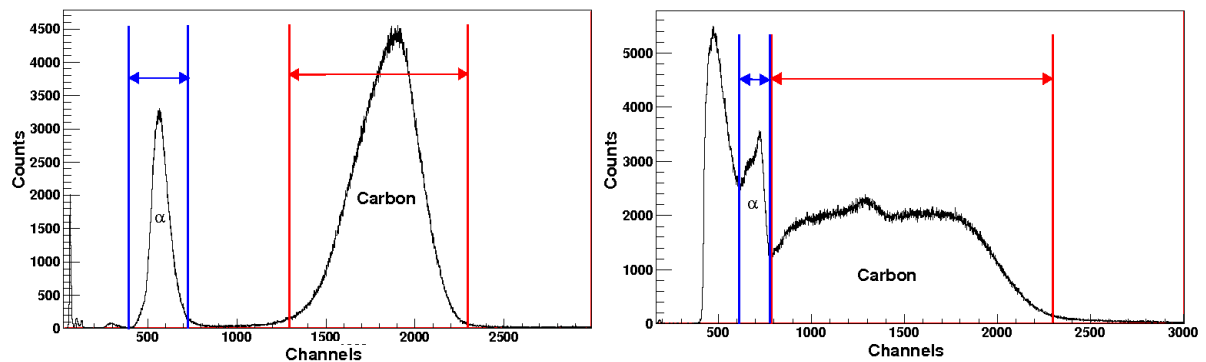


Figure 3.25: Particle energy gates applied in the cases of the outer (left) and inner (right) Si detectors.

Applying the particle and time gates in combination with background subtraction, yields a clean γ -spectrum containing only valid events from reactions in the carbon target and for ^{114}Sn and ^{118}Te . For the inner Si detectors the spectra

which are free from contaminants are shown in figures (3.37) and (3.28).

When the outer Si detectors are used for particle and time gating there is a cross contamination between ^{114}Sn and ^{118}Te even when the particle gate condition is implemented. The contamination between ^{114}Sn and ^{118}Te is due to a significant contribution from pile up, as well as overlapping energies in the particle spectra. Another thing which can be seen in figures (3.29) and (3.30) is that the ^{118}Te and ^{114}Sn spectra include contamination from the fusion reaction products ^{122}Ba and ^{120}Xe . The γ energy of 420 keV which corresponds to the $4^+ \rightarrow 2^+$ transition in ^{122}Ba is seen very strongly in the first particle energy peak. The $2^+ \rightarrow 0^+$ transition in ^{122}Ba at 196keV is also seen in the spectrum but its intensity is very small due to the shielding, which reduces the intensity of low energy γ -rays. For the inner detectors these fusion products are only seen if the particle gates include very low energies below the α peak.

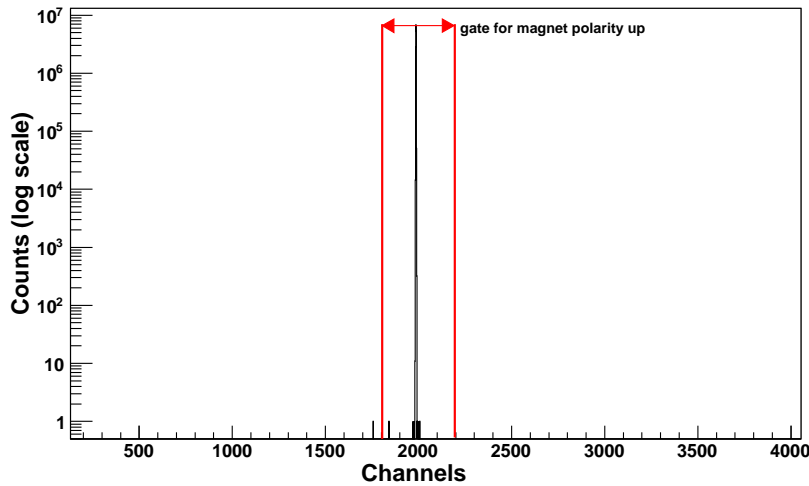


Figure 3.26: Spectrum and applied gate for ADC channel 1 - external magnetic field direction up, the spectra for magnet field down is identical.

For measuring the double ratios, a gate in field directions up or down needs to be assigned, and is an additional condition required when building the γ spectra for ^{114}Sn . Two ADC channels read in the signals from a level adapter which is directly connected to the magnet polarity switcher. These ADC spectra represent the events when the direction of the magnetic field is either up or down. Figure (3.26) shows an example of one of the ADC channels with the gate applied to it. Using this gate as an additional condition to the already cleaned spectra, one can

measure the events for each field direction separately.

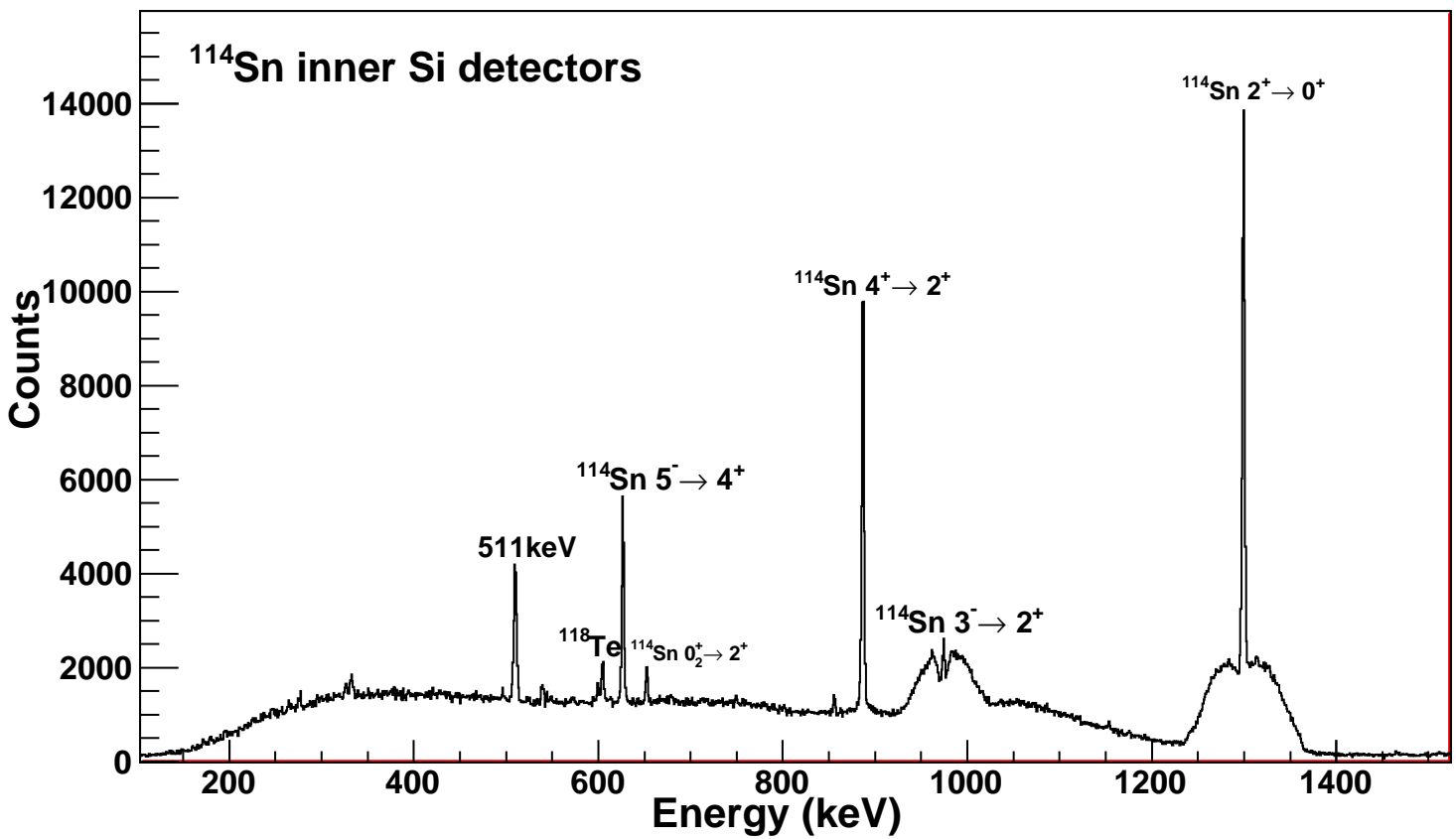


Figure 3.27: ¹¹⁴Sn spectrum obtained with a particle gate in the inner Si detectors.

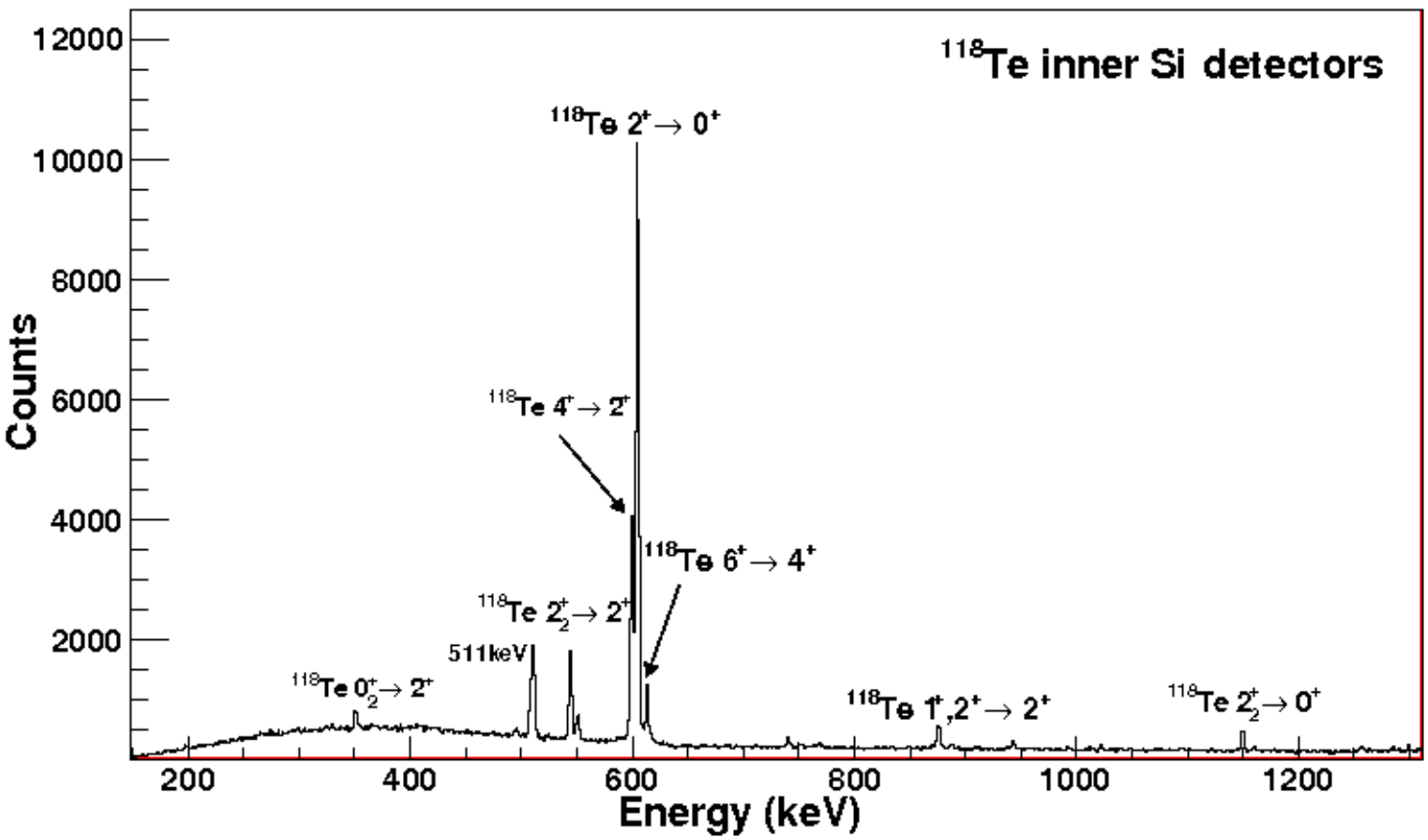


Figure 3.28: ^{118}Te spectrum obtained with a particle gate in the inner Si detectors.

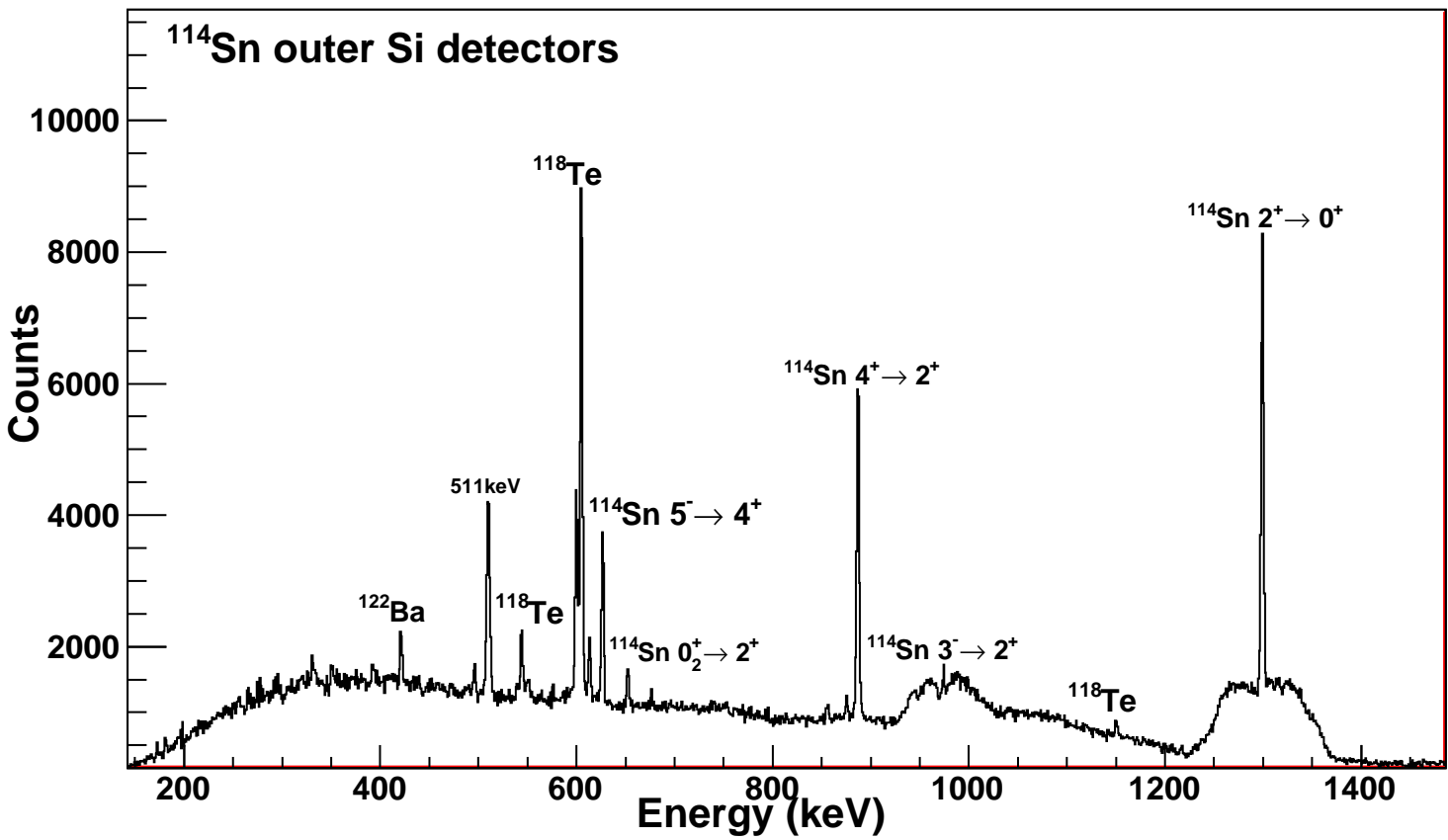


Figure 3.29: ^{114}Sn spectrum obtained with a particle gate in the outer Si detectors.

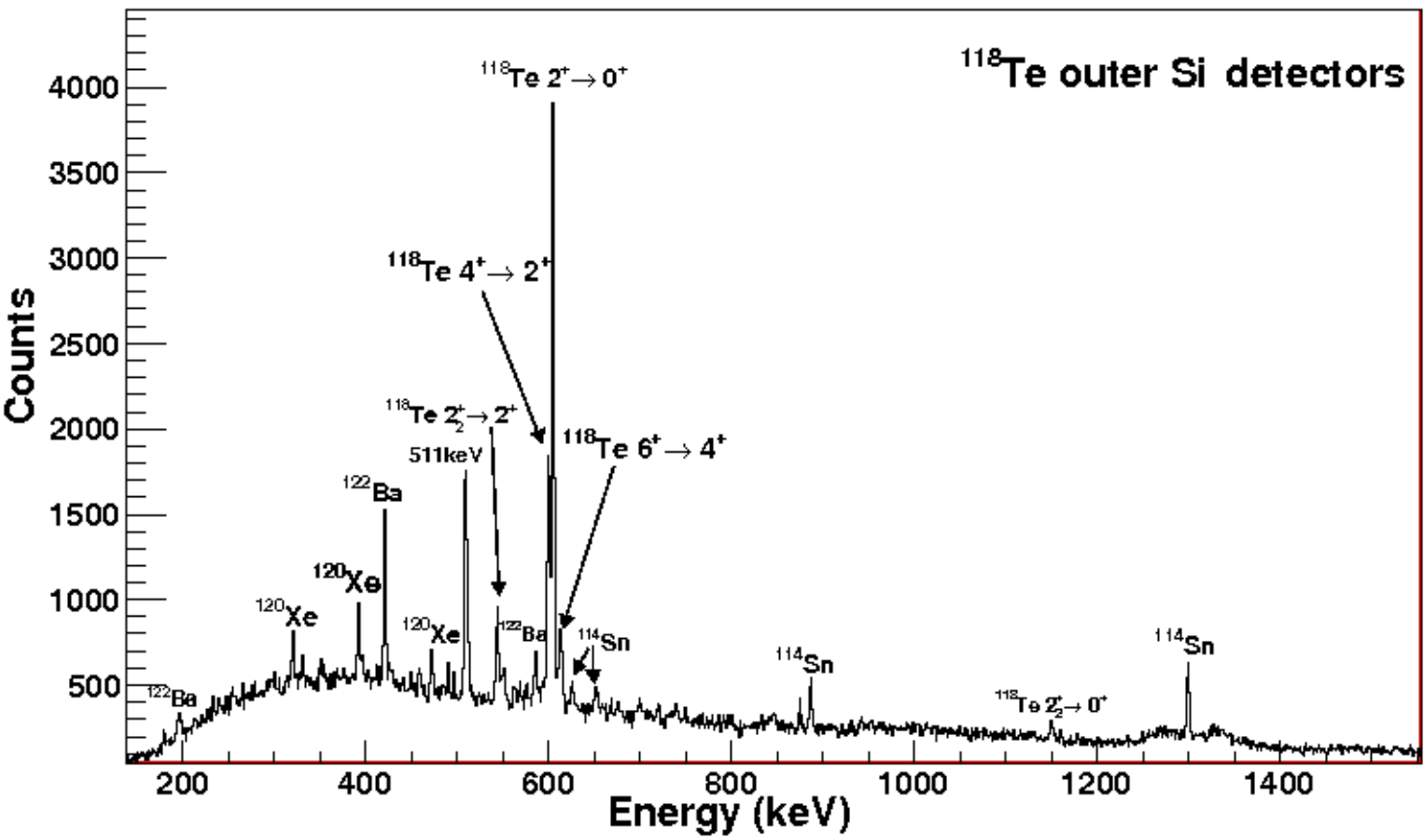


Figure 3.30: ^{118}Te spectrum obtained with a particle gate in the outer Si detectors.

3.4 The Example of $^{122}\text{Sn}/^{126}\text{Te}$

As seen in the Data Preparation section for experiment U234, a set of gating conditions were used to clean up the spectra. For the runs of experiment U236 the same gating conditions were applied as for runs U234: a gate on the TDC for the prompt with background subtraction to eliminate random events, gates on the particle spectra to clean up between Sn and Te events and gates on the magnet polarity - which is the same as for U234 so not discussed. The raw TDC spectra show a double structure due to the effects of the Si TDCs on the Ge TDCs, the effect of gating on each Si TDC one can see that the Ge TDC spectra show a single peak at various locations.

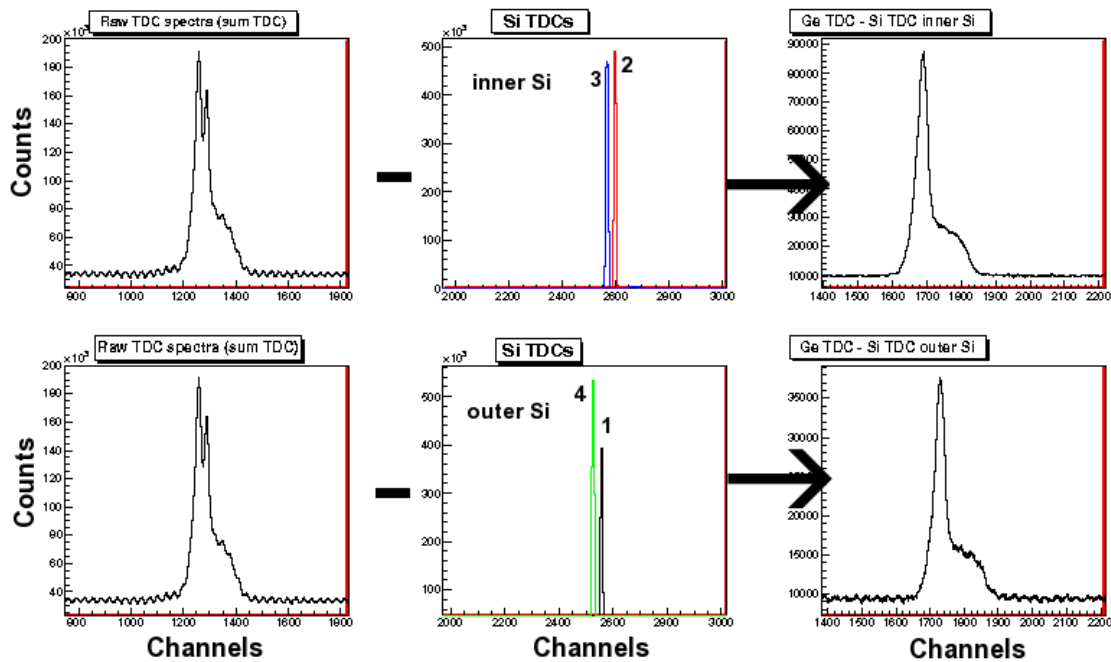


Figure 3.31: The Ge TDC subtracted by Si TDC (+3000 ch). The top set of figures show the subtraction from of the Ge TDCs by the Si TDCs of the inner Si detectors, and the bottom is the same for the outer Si TDCs. The colors red, blue, green and black correspond to the Si TDCs for each Si detector individually.

With the time spectra organized to account for both the Ge and Si time, these gates are applied to obtain a clean ^{122}Sn spectra for inner and outer Si detectors individually. The spectra shown in (3.32) and (3.33) are for all the Ge detectors

summed to show the cleaned spectra. For the analysis the individual Ge detectors were taken with these gates as well as using the ADC gates from the magnet switcher for up and down.

Module Type	Channel number	Raw Data Information
DGF1	0	Cluster 1 Crystal A
	1	Cluster 1 Crystal B
	2	Cluster 1 Crystal C
	3	Cluster 1 Crystal D
DGF2	0	Cluster 1 Crystal E
	1	Cluster 1 Crystal F
	2	Cluster 1 Crystal G
	3	zero degree
DGF3	0	Cluster 2 Crystal A
	1	Cluster 2 Crystal B
	2	Cluster 2 Crystal C
	3	Cluster 2 Crystal D
DGF4	0	Cluster 2 Crystal E
	1	Cluster 2 Crystal G
	2	Cluster 2 Crystal F
	3	Empty channel
DGF5	0	Cluster 3 Crystal A
	1	Cluster 3 Crystal B
	2	Cluster 3 Crystal C
	3	Cluster 3 Crystal D
DGF5	0	Cluster 3 Crystal E
	1	Cluster 3 Crystal F
	2	Cluster 3 Crystal G
	3	Empty channel
DGF6	0	Cluster 4 Crystal A
	1	Cluster 4 Crystal B
	2	Cluster 4 Crystal C
	3	Cluster 4 Crystal D
DGF7	0	Cluster 4 Crystal E
	1	Cluster 4 Crystal F
	2	Cluster 4 Crystal G
	3	Empty channel

Table 3.6: The DGF module configuration for experiment U236, the DGFs for Cluster 2 G and F are in reverse order to the set up in U234.

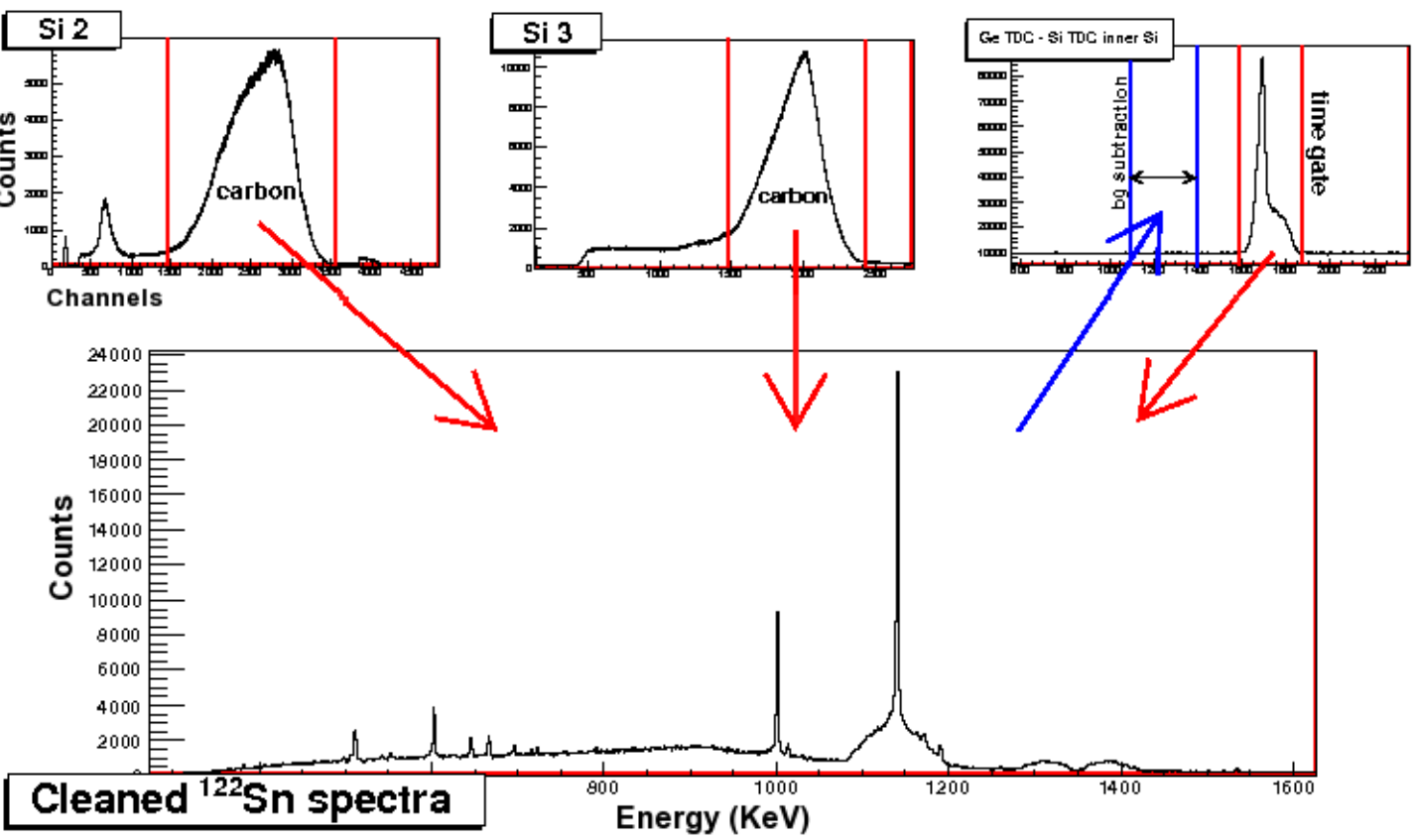


Figure 3.32: The gates used to clean the ^{122}Sn spectra for the inner Si detectors, the red arrows denote the gates used to increment the spectra, and the blue to decrement (background subtraction).

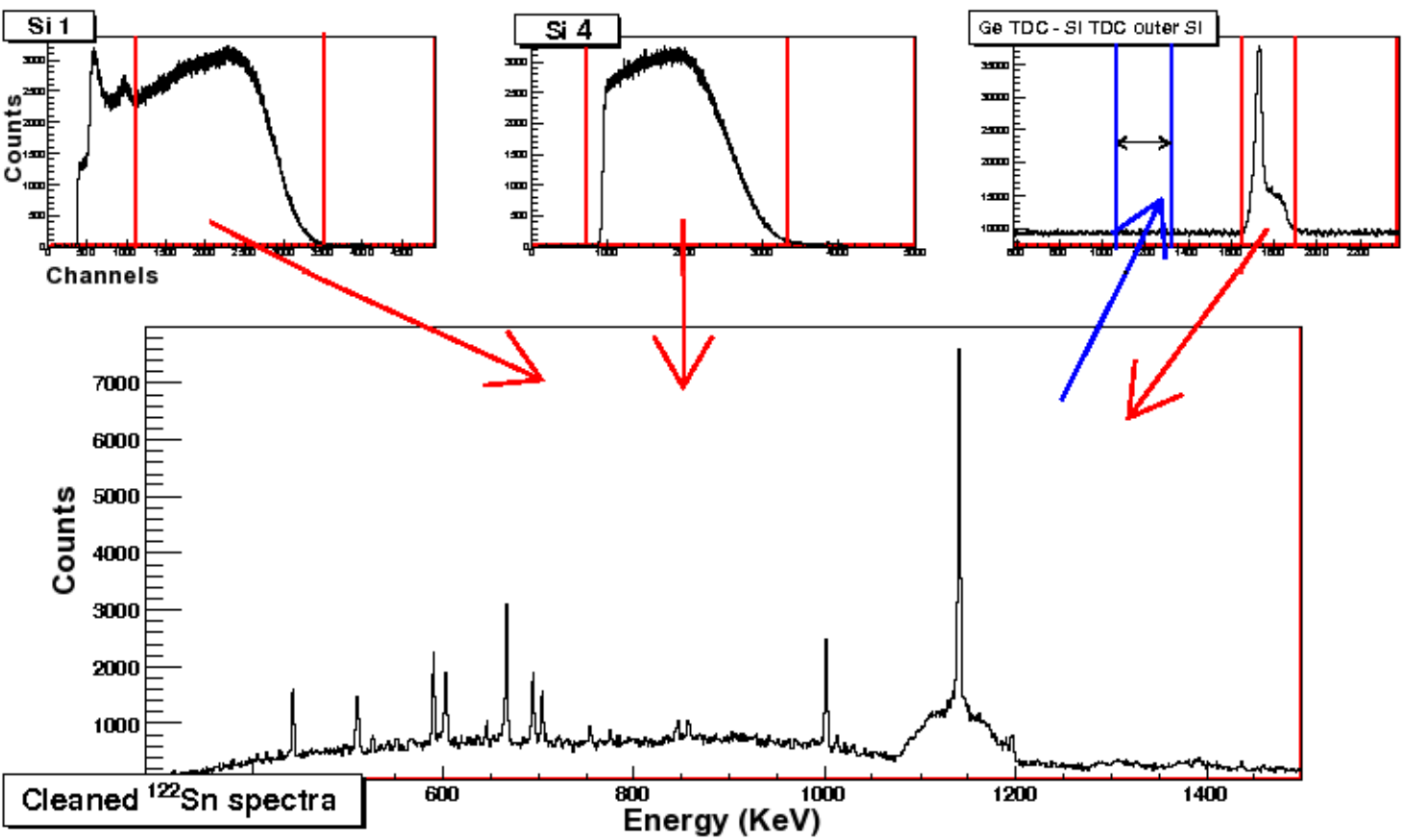


Figure 3.33: The gates used to clean the ^{122}Sn spectra for the outer Si detectors, the red arrows denote the gates used to increment the spectra, and the blue to decrement (background subtraction).

The experimental setup for U236 ran with the same settings, but with different thresholds and settings on the Si detectors. The gating conditions were applied in the similar manner to that of U234, and the example for ^{126}Te are shown in figure (3.36).

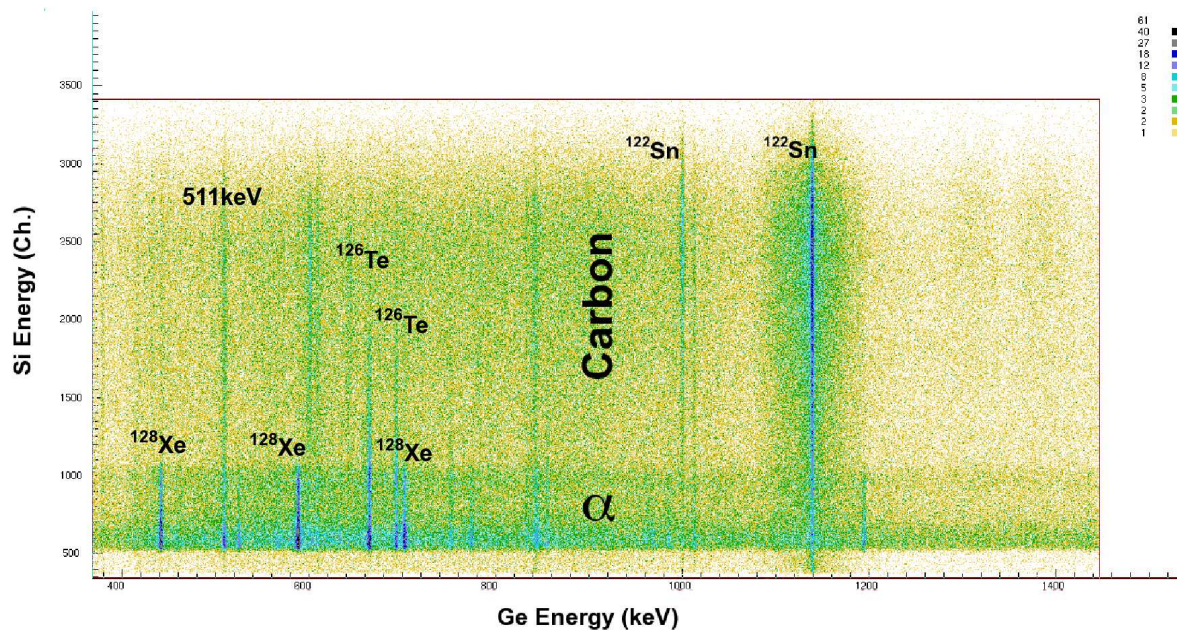


Figure 3.34: The two dimensional matrix between the γ -ray energy detected in the Ge detectors and the energy of the charged particle detected in one of the outer Si detectors for ^{122}Sn .

One can see in figure (3.34) that in addition to Coulomb excitation of the projectile and α -transfer, there are other competing reactions where there is an emission of charged particles which are also observed. Figure (3.34) shows lines from ^{128}Xe which come in coincidence with the α -particle, it is most probable that ^{128}Xe is populated by fusion-evaporation where: $^{122}\text{Sn} + ^{12}\text{C} \rightarrow ^{134}\text{Ba}^* \rightarrow ^{128}\text{Xe} + \alpha 2n$, where an evaporated α particle is detected in the Si detector. In the clean spectra for the outer Si detectors, there are products from incomplete fusion reactions such as ^{124}Te , which is also populated as an $\alpha 2n$ channel.

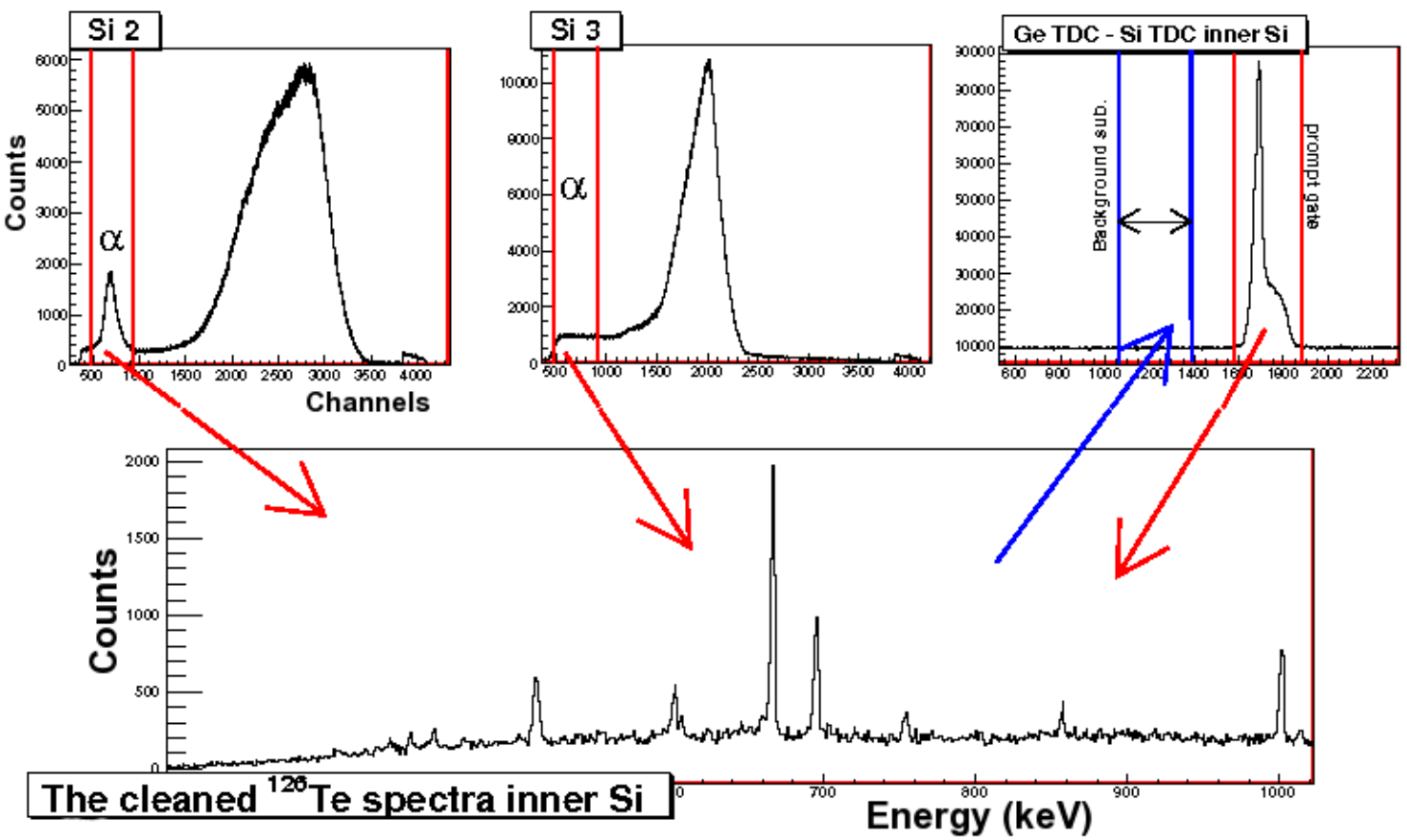


Figure 3.35: The gates used to clean the ^{126}Te spectra for the inner Si detectors, the red arrows denote the gates used to increment the spectra, and the blue to decrement (background subtraction).

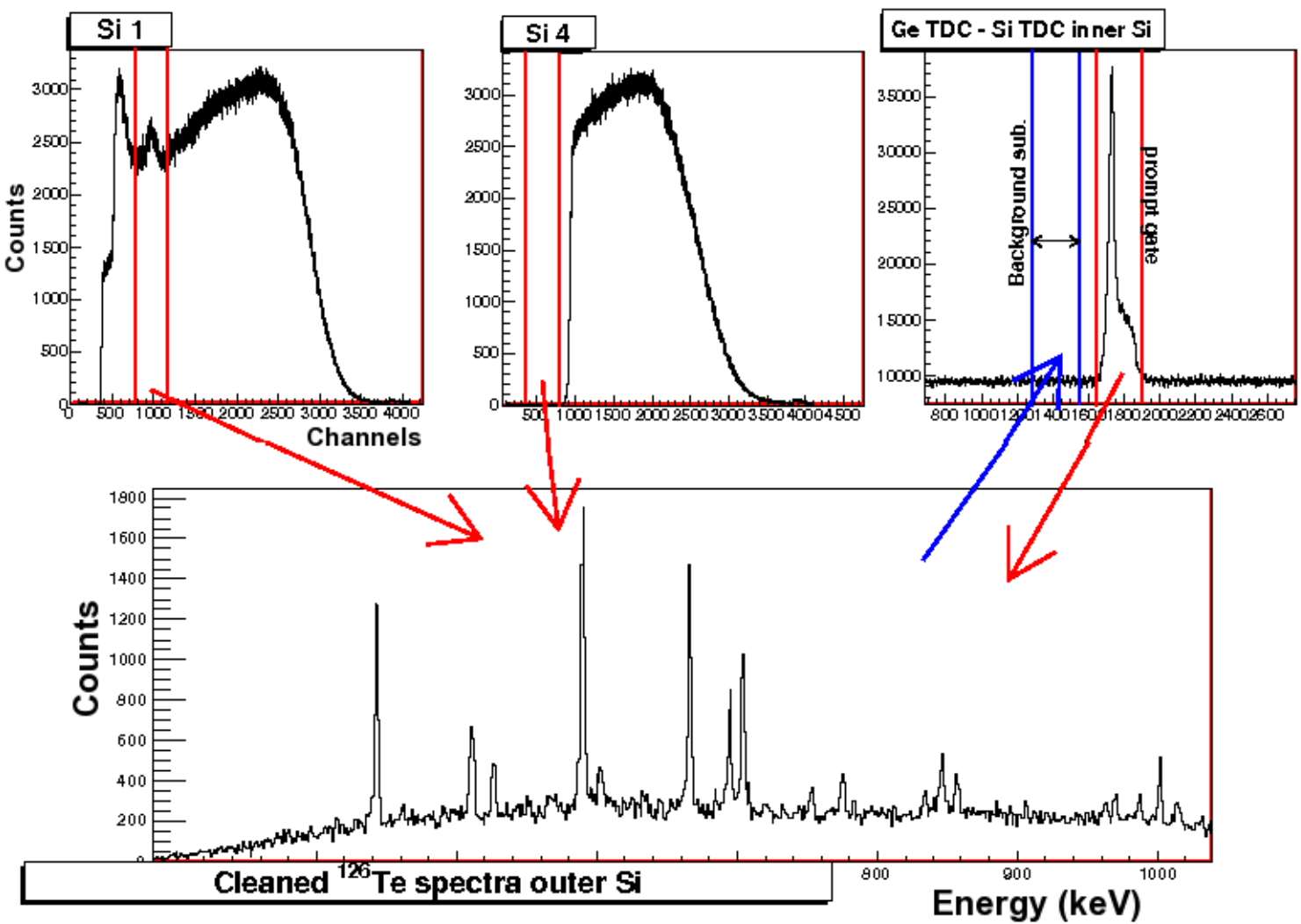


Figure 3.36: The gates used to clean the ^{126}Te spectra for the inner Si detectors, the red arrows denote the gates used to increment the spectra, and the blue to decrement (background subtraction).

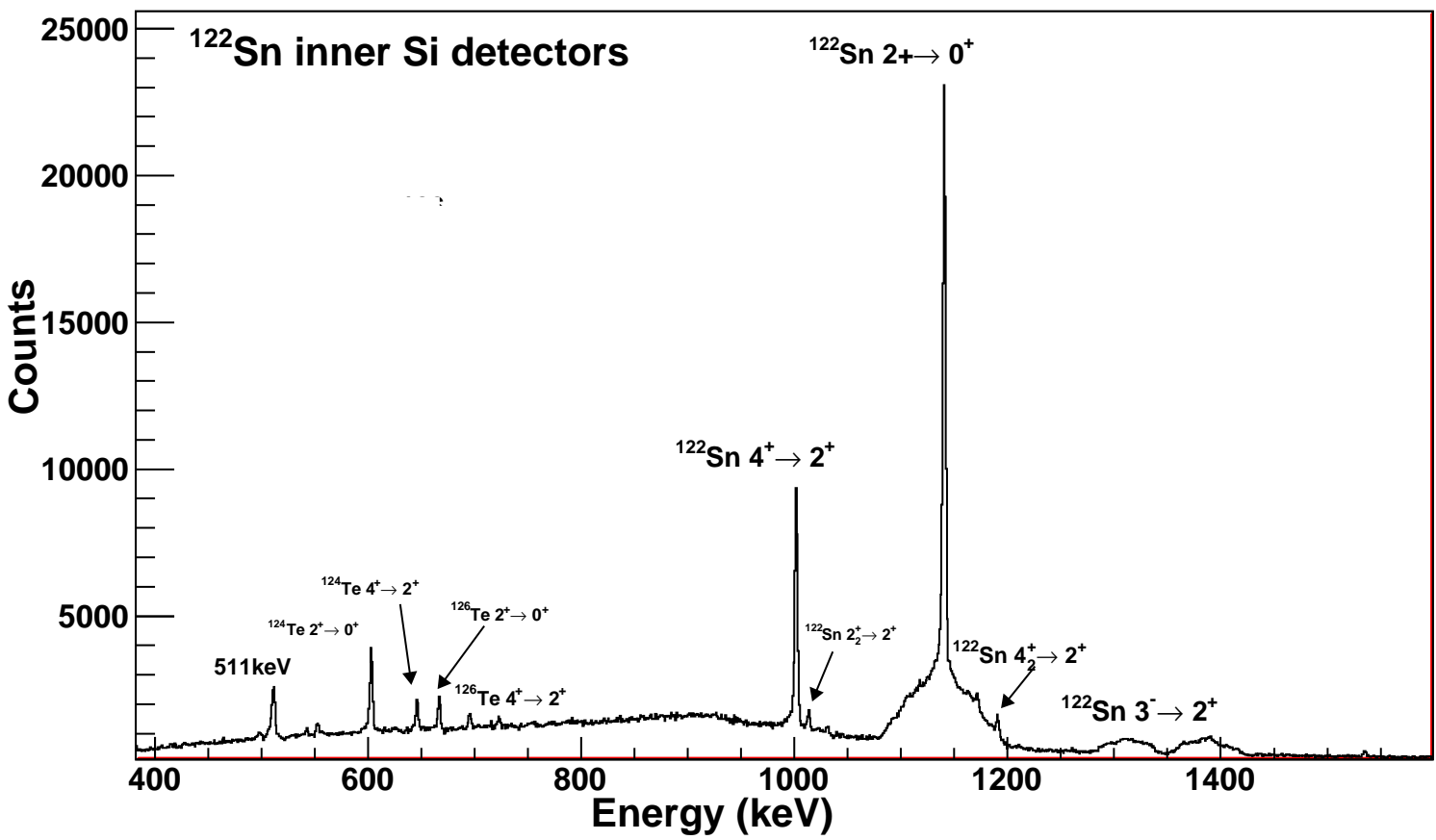


Figure 3.37: ¹²²Sn spectrum obtained with a particle gate in the inner Si detectors.

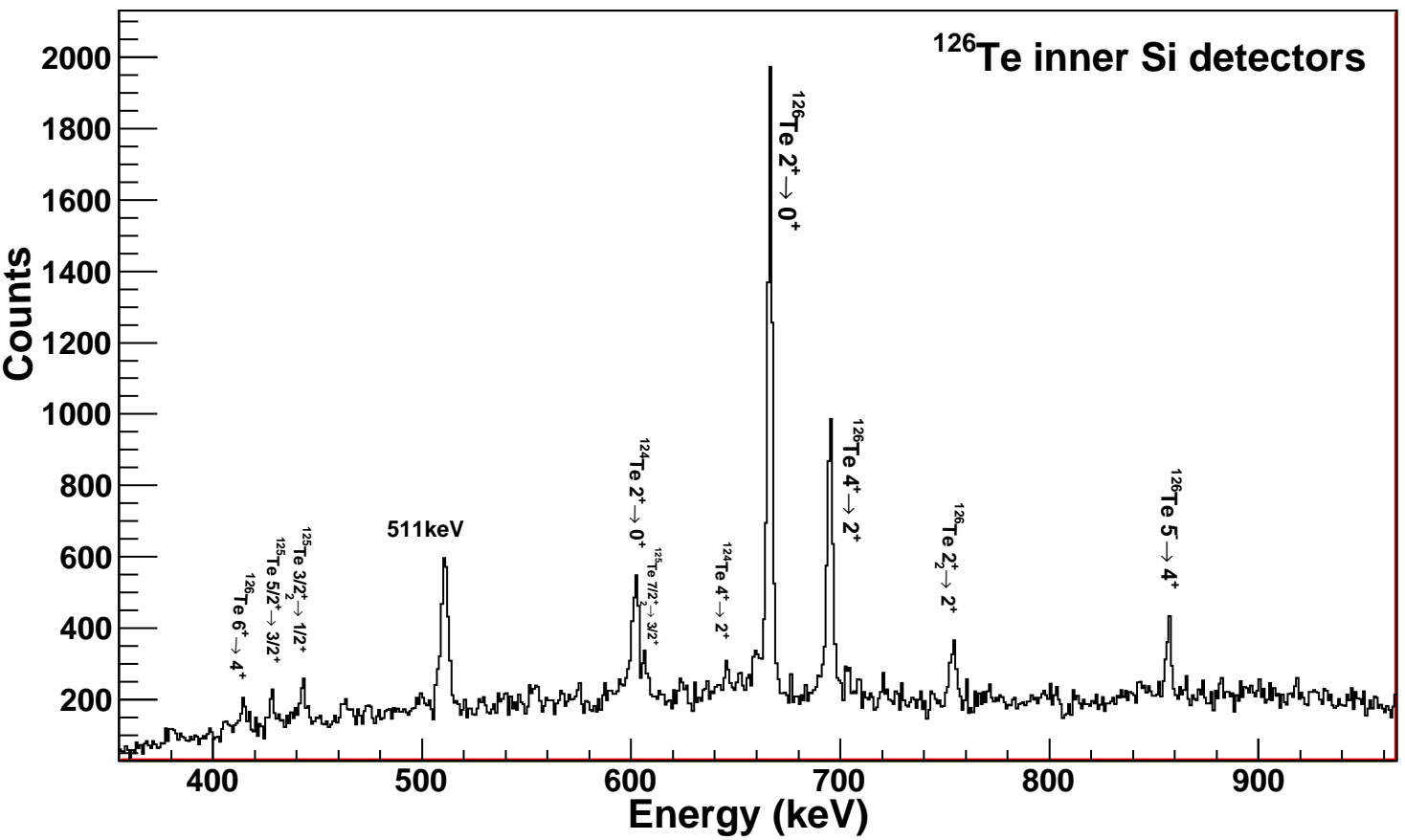


Figure 3.38: ^{126}Te spectrum obtained with a particle gate in the inner Si detectors.

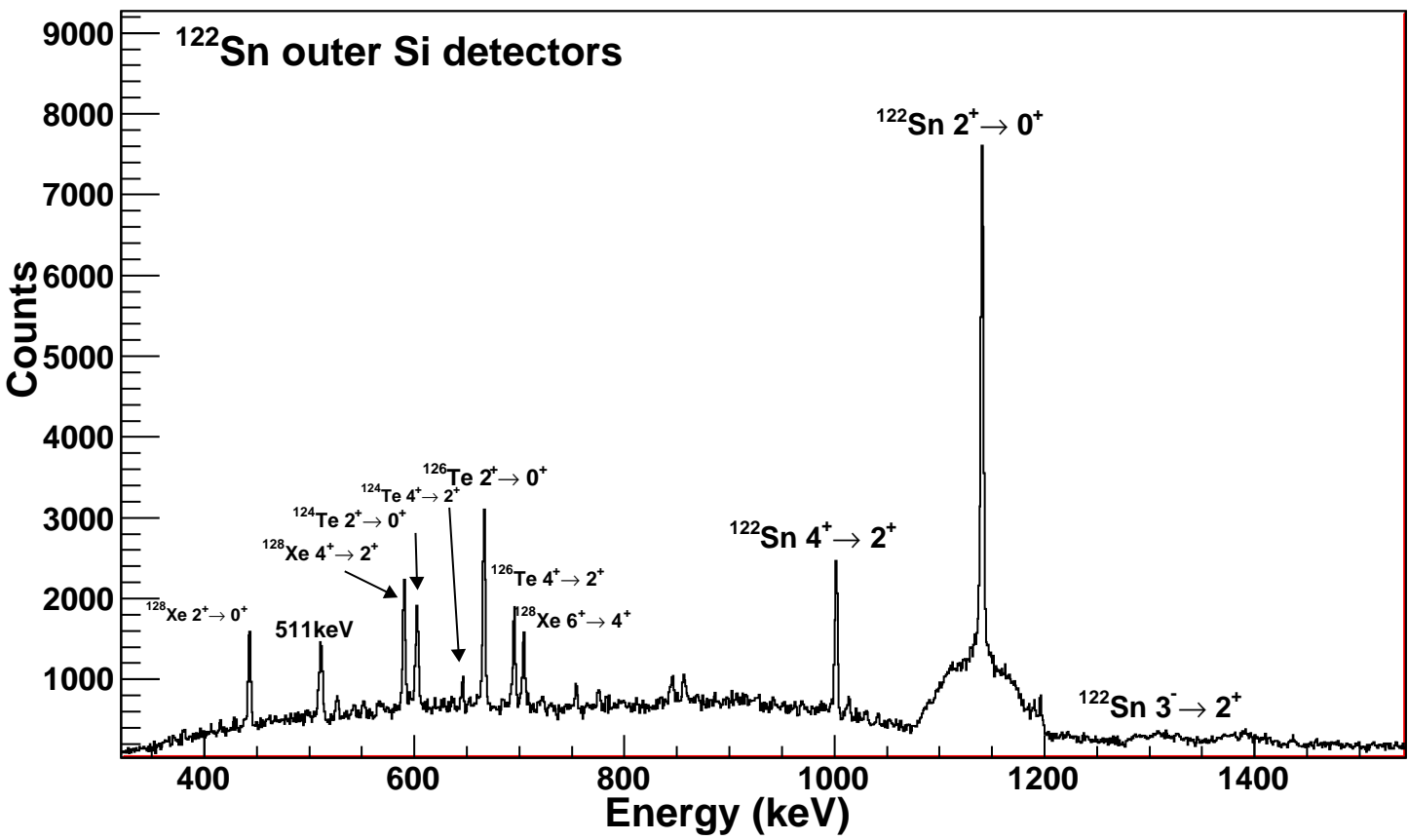


Figure 3.39: ^{122}Sn spectrum obtained with a particle gate in the outer Si detectors.

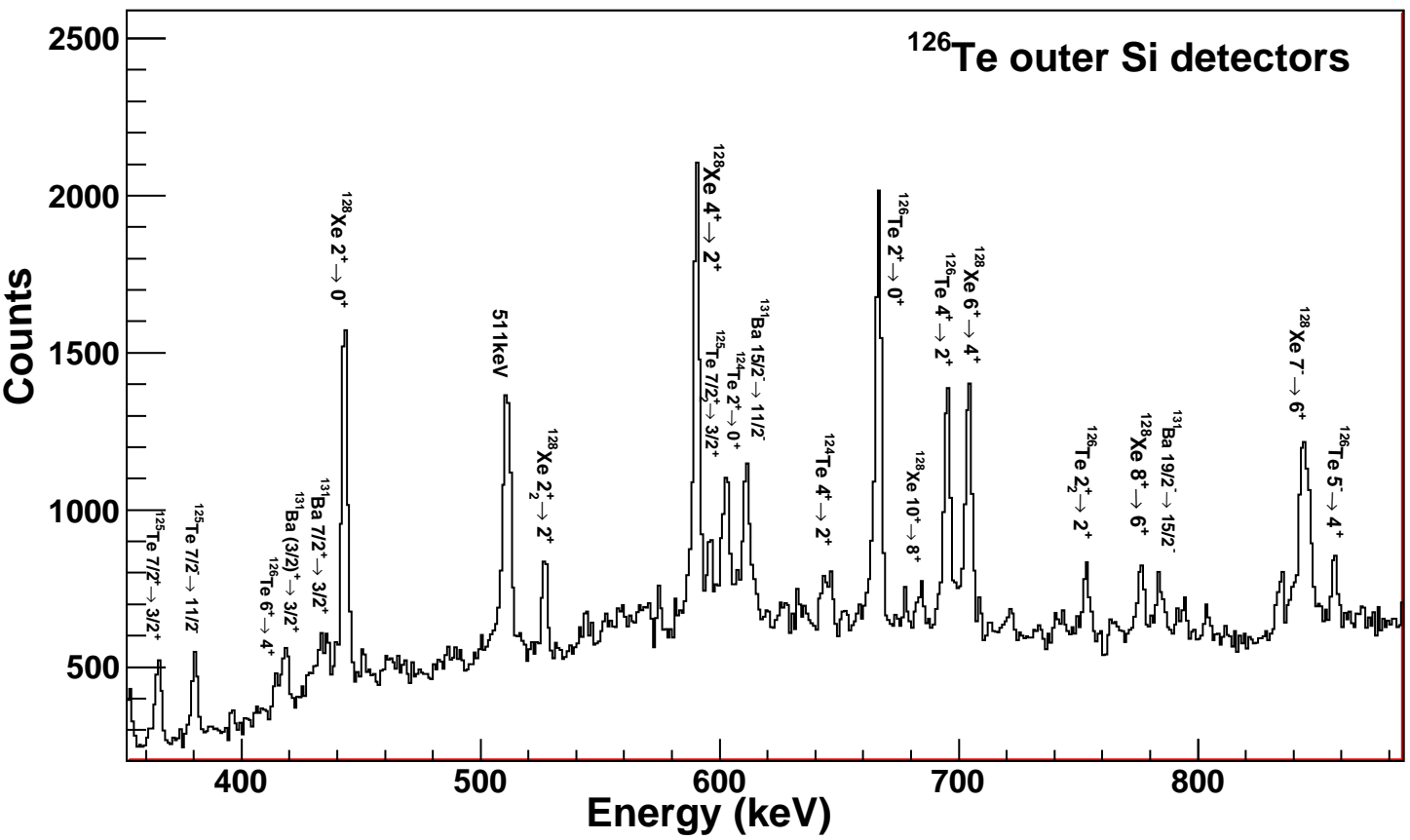


Figure 3.40: ^{126}Te spectrum obtained with a particle gate in the outer Si detectors.

Chapter 4

Data Analysis

4.1 Determination of the logarithmic slopes

4.1.1 Angular Correlation Fits

Angular Correlations with Velocity Corrections

The short-lived states of semi-magic even Sn nuclei partly decay in flight through the ferromagnet before being stopped in the copper backing. The γ -peak from the $2^+ \rightarrow 0^+$ transition consists of a stopped and an in-flight component. When γ -decay occurs while stopped in the Cu backing, its energy remains unchanged, whereas for decays which occur in-flight, the energy undergoes a Doppler shift, and this shifted component requires a transformation to the centre of mass frame.

The energy of the Doppler shifted peak is related to the velocity of the ion and the detected γ -ray angle by the formula:

$$E'_\gamma(\theta, t) = E_\gamma^0 \frac{\sqrt{1 - \beta^2(t)}}{1 - \beta(t)\cos(\theta)} \quad (4.1)$$

where E_γ^0 is the energy of the emitted γ , $\beta = v/c$, v the velocity of the ion at the point of decay of the excited state, θ the angle of the detector in which the observed γ is detected and $E'_\gamma(\theta, t)$ is the shifted γ energy of the decay in-flight. The velocity of the decaying ion can be obtained from the flight peak centroid and FWHM and then used in the transformation to the centre of mass frame.

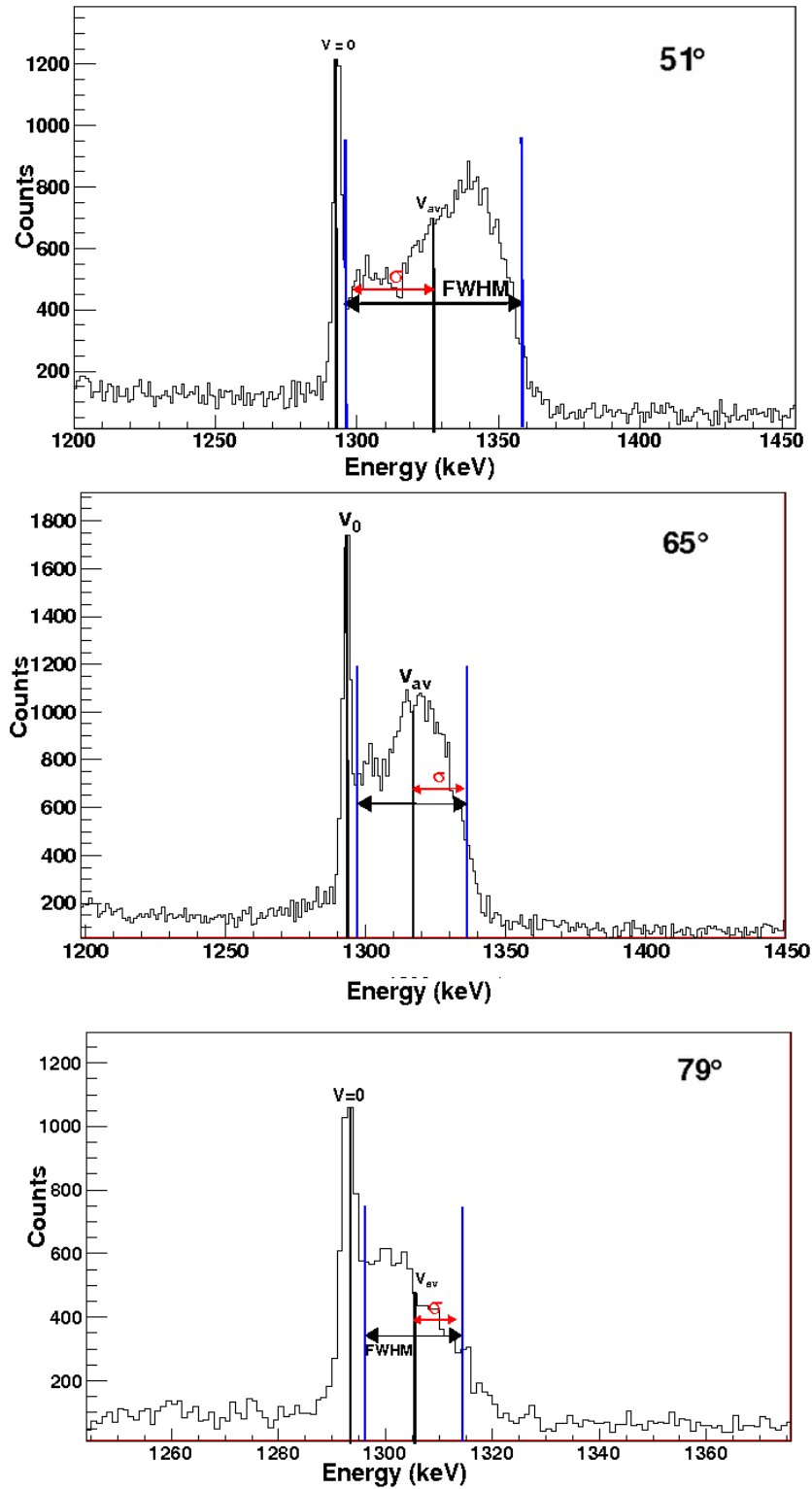


Figure 4.1: The lineshape of the $2^+ \rightarrow 0^+$ transition in ^{116}Sn observed in the inner angles, with the FWHM and σ for the flight peak.

For the cases of the $2^+ \rightarrow 0^+$ and $3^- \rightarrow 2^+$ transitions, the lifetimes of the initial states are short, in the ps range. Most of the excited nuclei will therefore decay before coming to rest in the Cu backing. The classical angular correlation formulas are valid in the rest frame of the recoiling nucleus but not in the laboratory frame. In order to correct for the Lorentz boost, the angles of observation (Ge detector angles) have to be transformed from the laboratory to the rest frame using:

$$\cos(\theta)_{CM} = \frac{\cos(\theta)_{lab} - \beta}{1 - \beta \cos(\theta)_{lab}} \quad (4.2)$$

where β is the velocity (v/c) of the ion traversing the target. β is obtained from the centroid of the flight peak and its error, σ , from the FWHM.

For the $2^+ \rightarrow 0^+$ transition, the stopped component of the peak is emitted at rest hence, one determines the intensities of the stopped and flight components separately, using the intensities of the respective stopped and flight peaks as weights to find the weighted mean angle for the total peak:

$$\theta_{weighed} = \frac{\sum_{i=1}^n w_i \theta_i}{\sum_{i=1}^n w_i} \quad (4.3)$$

In addition a solid angle correction has to be applied when moving from the laboratory to the CM frame since obviously:

$$W_{lab} d\Omega_{lab} = W_{CM} d\Omega_{CM} \quad (4.4)$$

has to be valid. It is therefore:

$$W_{CM}(\theta_{CM}) = W_{lab}(\theta_{lab}) d\Omega_{lab} / d\Omega_{CM} \quad (4.5)$$

with

$$d\Omega_{lab} / d\Omega_{CM}(\theta_{lab}) = [1 - \beta \cos(\theta_{lab})]^2 / (1 - \beta^2) \quad (4.6)$$

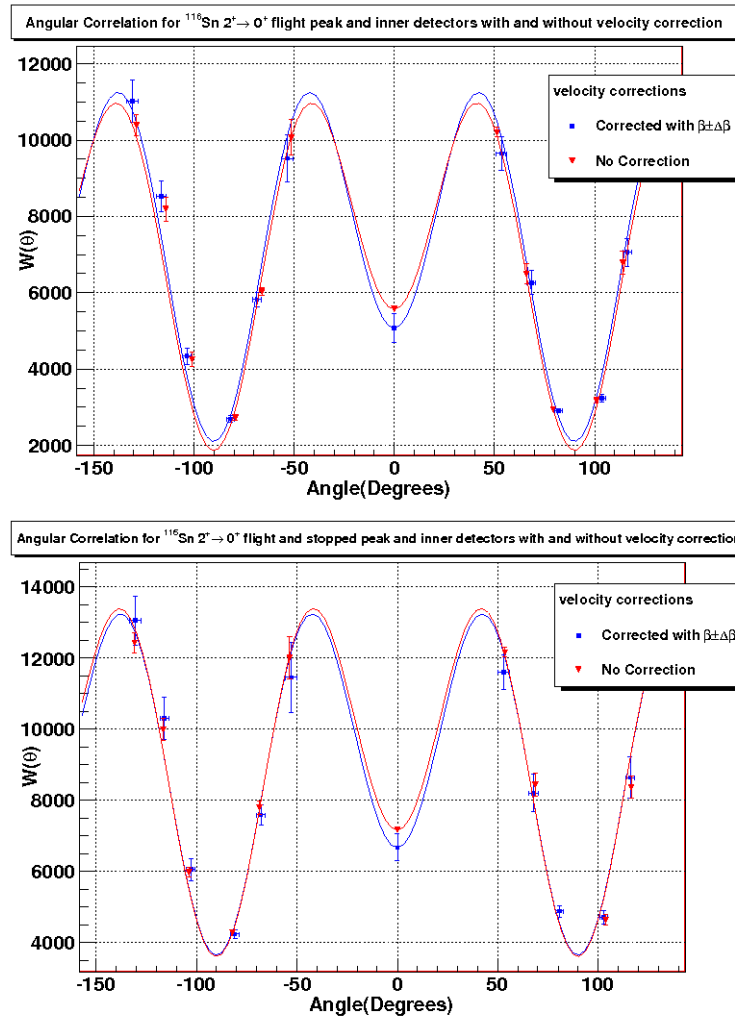


Figure 4.2: The angular correlation for the inner Si detectors for $^{116}\text{Sn } 2^+ \rightarrow 0^+$ transition, comparing the results without any correction for the Doppler shift (data points and fit curve in red) and with velocity correction (data points and fit curve in blue). Top) The angular correlation of the flight peak only Bottom) The angular correlation of the total peak.

Figure (4.2) shows the effect the corrections for the Lorentz boost make on the angular correlation. The top figure corresponds to the flight peak only, where the red is the uncorrected correlation, and the blue is corrected. One can see here that for the uncorrected there were data points which lie outside the fit, even within errors. When the correction for this Lorentz boost is applied, the correlation fits the data within the errors. The bottom figure accounts for the total peak, where there is a stopped (no correction needed) and a flight component. This was obtained

as described above, and the difference between the two are shown. The change in the angular correlation for this case between the uncorrected and correct is less prominent when compared to the flight peak only case, but this is because the stopped component is not affected by the Lorentz boost.

Determining the Lifetimes from the lineshapes

The lifetime of the state can also be obtained directly from the shape of the γ -ray lineshape, as the shape of the line is directly related to the velocity distribution of the recoils as they decay. If the slowing down process of the recoil within the target is known, then the nuclear lifetime can be obtained from the lineshape of the transition of interest as a function of Ge detector angle. The shape of the line is dependent on what velocity the recoiling ion had when it emitted the γ -ray as well as the lifetime of the state. The average velocity is given by the centroid of the peak, and the stopped component (corresponding to the energy of the transition) occurs at $v=0$.

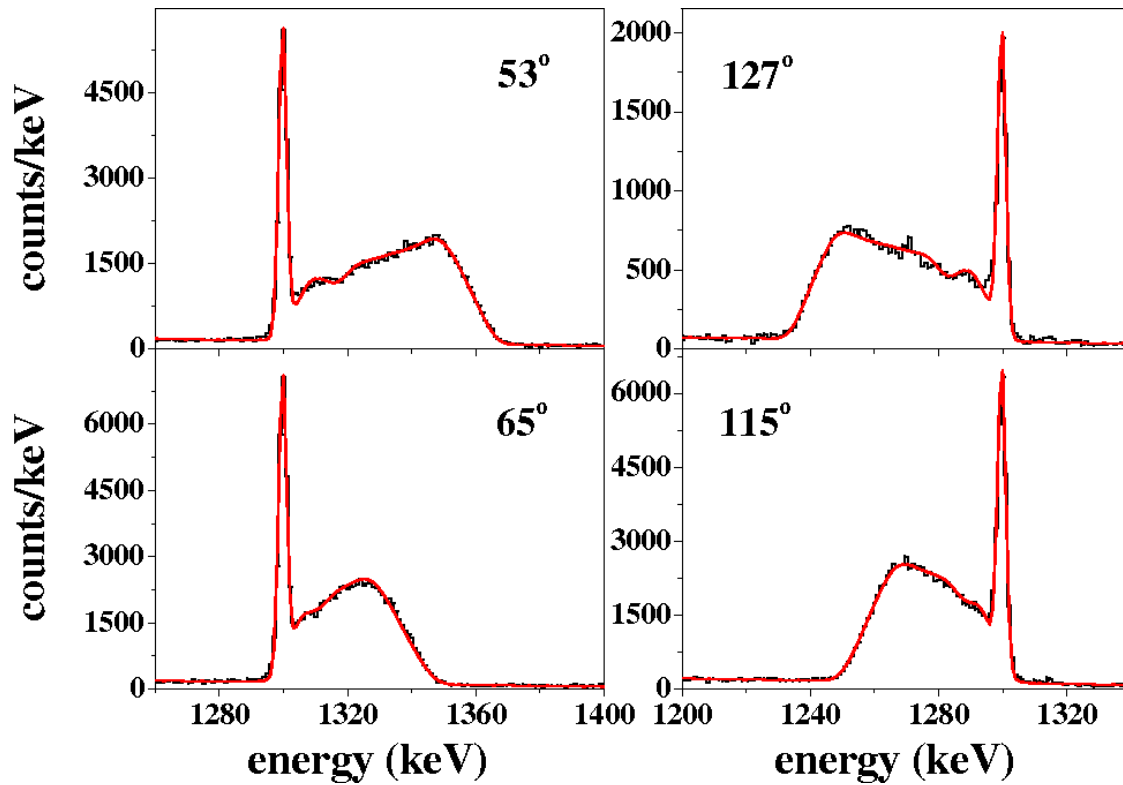


Figure 4.3: Examples of the fitted lineshapes for the observed $2^+ \rightarrow 0^+$ transitions in ^{114}Sn in the Ge crystals located at polar angles 53° , 65° , 115° and 127° with respect to the beam axis. These were detected in coincidence with the carbon ions in the inner Si detectors. [21]

In our setup, the lineshapes of the forward detectors were introduced previously, and one can see that even between forward detectors the shape of the flight peak for the $2^+ \rightarrow 0^+$ transition (and also the $3^- \rightarrow 2^+$ transition) is dependent on the angle of the Ge detector. From these Doppler broadened lineshapes the lifetimes of these states can be extracted using the LINESHAPE program package [24]. This program when modified to account for the kinematics used in the set up as well as for the geometry of the particle detector used in this experimental set up and modified to account for the multilayer target used in the experiment can be used to extract the lifetime by fitting the lineshapes. For further details please refer to [21].

Another consideration to using the DSAM method to extract the lifetime, is that one must be aware that if the $2^+ \rightarrow 0^+$ transition is contaminated with significant feeding from higher states (this is discussed in detail later in the context of the g-factors), this effect on the lineshapes also needs to be accounted for in the analysis in the program. The intensities were obtained from the gamma spectra and taking into account the effects from the angular correlation, this feeding comes to 15-30% from the 3^- and 5-15% from the 4^+ . The $4^+ \rightarrow 2^+$ has a long lifetime, so undergoes negligible Doppler shift, whereas the 3^- states are all short lived. Their lifetimes were also obtained from the observed lineshapes in this experiments.

Even though the backward and forward detectors were symmetrical in their set up, the lineshapes vary here due to the large recoil velocity of $v \approx 0.07c$, so these relativistic effects also need to be included. By fitting the lineshape, accounting for the above mentioned considerations, the lifetimes of the 3^- and the 2^+ states were obtained from this experimental set up. The actual measured lifetime will be discussed along with the measured g-factors in the discussion.

Angular Correlations

The experimentally measured angular correlations were obtained from the efficiency corrected intensities at each angle. Because of our detector set up with a wide detector range, the angular correlation could be directly measured. A fit was made to the data using equation (4.7) (where $P_2(\cos(\theta_\gamma))$ and $P_4(\cos(\theta_\gamma))$ are Legendre polynomials) to fit for a_2, a_4 , the experimentally measured results for these are given in the tables (4.1) and (4.2).

$$W(\theta_\gamma) = C[1 + a_2P_2(\cos(\theta_\gamma)) + a_4P_4(\cos(\theta_\gamma))] \quad (4.7)$$

$$P_2(\cos(\theta_\gamma)) = \frac{1}{2}(3\cos^2(\theta_\gamma) - 1) \quad (4.8)$$

$$P_4(\cos(\theta_\gamma)) = \frac{1}{8}(35\cos^4(\theta_\gamma) - 30\cos^2(\theta_\gamma) + 3) \quad (4.9)$$

Nuc.	Transition	Correlation coefficient	Inner	Outer
^{112}Sn	$2^+ \rightarrow 0^+$ all	C	3180(90)	12311(300)
		a_2	0.606(40)	0.844(40)
		a_4	-0.882(40)	-0.788(50)
^{114}Sn	$2^+ \rightarrow 0^+$ all	C	10810(240)	7493(200)
		a_2	0.541(40)	0.760(50)
		a_4	-0.822(40)	-0.685(60)
^{116}Sn	$2^+ \rightarrow 0^+$ all	C	8924(230)	5898(160)
		a_2	0.568(40)	0.755(50)
		a_4	-0.821(50)	-0.670(60)
^{122}Sn	$2^+ \rightarrow 0^+$ all	C	7822(140)	3462(70)
		a_2	0.600(30)	0.868(30)
		a_4	-0.869(30)	-0.733(40)
^{124}Sn	$2^+ \rightarrow 0^+$ all	C	2488(60)	8886(200)
		a_2	0.528(50)	0.916(40)
		a_4	-0.971(50)	-0.791(50)

Table 4.1: The angular correlation coefficients for the transition $2^+ \rightarrow 0^+$ for the total peak (stopped and flight).

Nuc.	Transition	Correlation coefficient	Inner	Outer
^{112}Sn	$3^- \rightarrow 2^+$	C	670(30)	2357(70)
		a_2	-0.611(130)	-0.234(90)
		a_4	0(0)	0(0)
^{114}Sn	$3^- \rightarrow 2^+$	C	2953(100)	1651(70)
		a_2	-0.480(100)	-0.475(100)
		a_4	0(0)	0(0)
^{116}Sn	$3^- \rightarrow 2^+$	C	2874(80)	1533(50)
		a_2	-0.400(80)	-0.475(100)
		a_4	0(0)	0(0)
^{122}Sn	$3^- \rightarrow 2^+$	C	1307(10)	231(10)
		a_2	-0.322(30)	-0.574(100)
		a_4	0(0)	0(0)
^{124}Sn	$3^- \rightarrow 2^+$	C	324(10)	459(20)
		a_2	-0.419(80)	-0.938(150)
		a_4	0(0)	0(0)
^{112}Sn	$4^+ \rightarrow 2^+$	C	379(8)	955(18)
		a_2	0.480(60)	0.365(60)
		a_4	-0.204(60)	-0.197(60)
^{114}Sn	$4^+ \rightarrow 2^+$	C	1565(15)	924(15)
		a_2	0.381(20)	0.328(40)
		a_4	-0.226(20)	-0.114(40)
^{116}Sn	$4^+ \rightarrow 2^+$	C	198(3)	92(3)
		a_2	0.357(40)	0.347(80)
		a_4	-0.176(40)	-0.120(70)
^{122}Sn	$4^+ \rightarrow 2^+$	C	1003(20)	273(20)
		a_2	0.413(50)	0.408(20)
		a_4	-0.025(50)	-0.597(20)
^{124}Sn	$4^+ \rightarrow 2^+$	C	196(10)	228(10)
		a_2	0.521(20)	-0.180(150)
		a_4	-0.092(20)	-0.497(150)

Table 4.2: The angular correlation coefficients for the $3^- \rightarrow 2^+$ and $4^- \rightarrow 2^+$ transitions.

Nuc.	Si det.	$2^+ \rightarrow 0^+$	$4^+ \rightarrow 2^+$	$3^- \rightarrow 2^+$
^{112}Sn	in.	100	18(1)	31(2)
^{112}Sn	out.	100	11(0)	26(1)
^{114}Sn	in.	100	25(1)	47(3)
^{114}Sn	out.	100	19(1)	34(2)
^{116}Sn	in.	100	3(0)	49(2)
^{116}Sn	out.	100	2(0)	36(2)
^{122}Sn	in.	100	18(0)	24(1)
^{122}Sn	out.	100	9(0)	8(0)
^{124}Sn	in.	100	10(1)	17(4)
^{124}Sn	out.	100	3(1)	6(0)

Table 4.3: The normalized intensities relative to the directly populated 2^+ state.

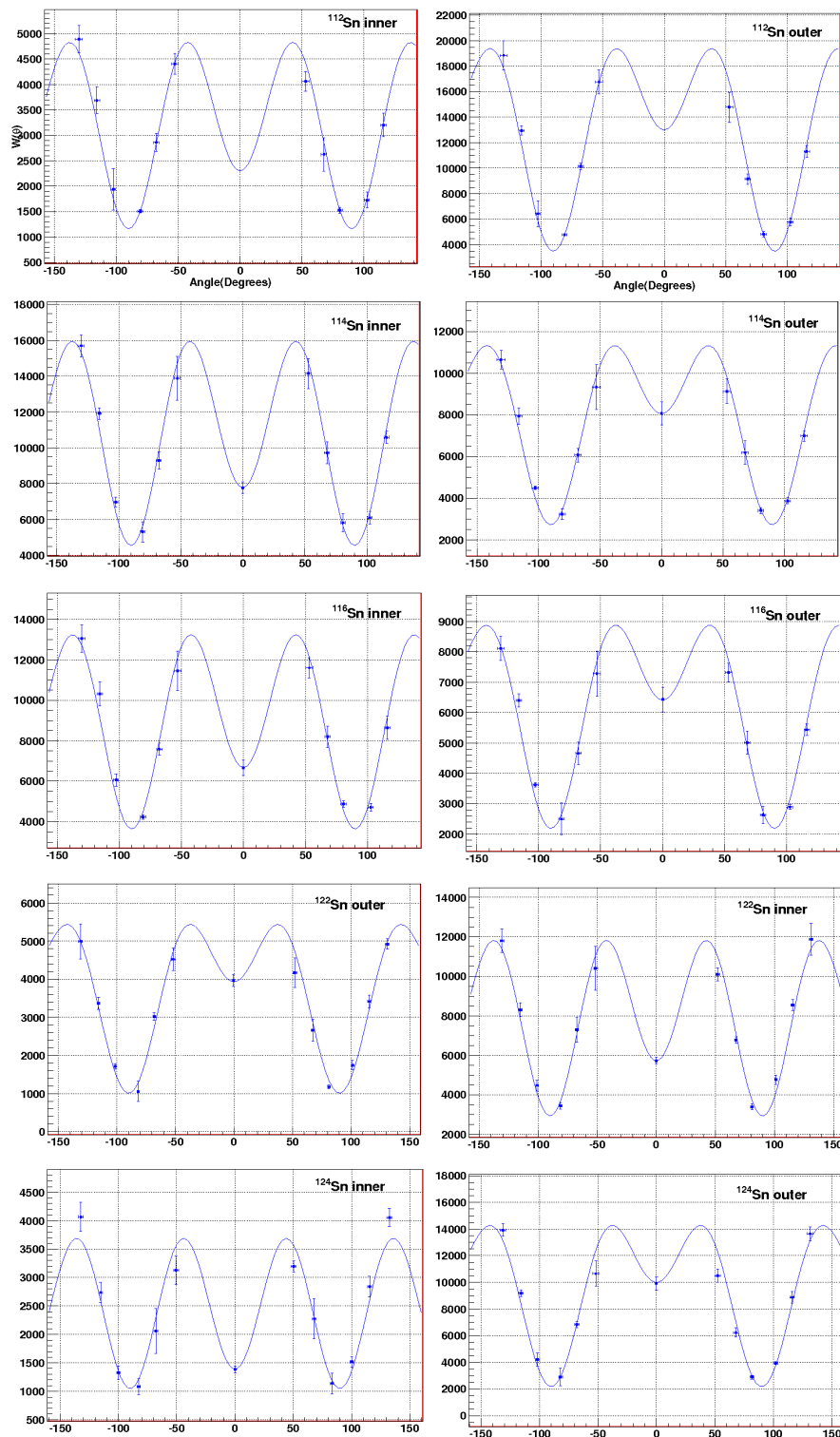


Figure 4.4: The angular correlation for the $2^+ \rightarrow 0^+$ transition as observed from data for flight and stopped peak, the left hand side denotes the inner Si detector geometry, the right hand side the outer Si detector geometry, and the angular correlations are given for each isotope measured.

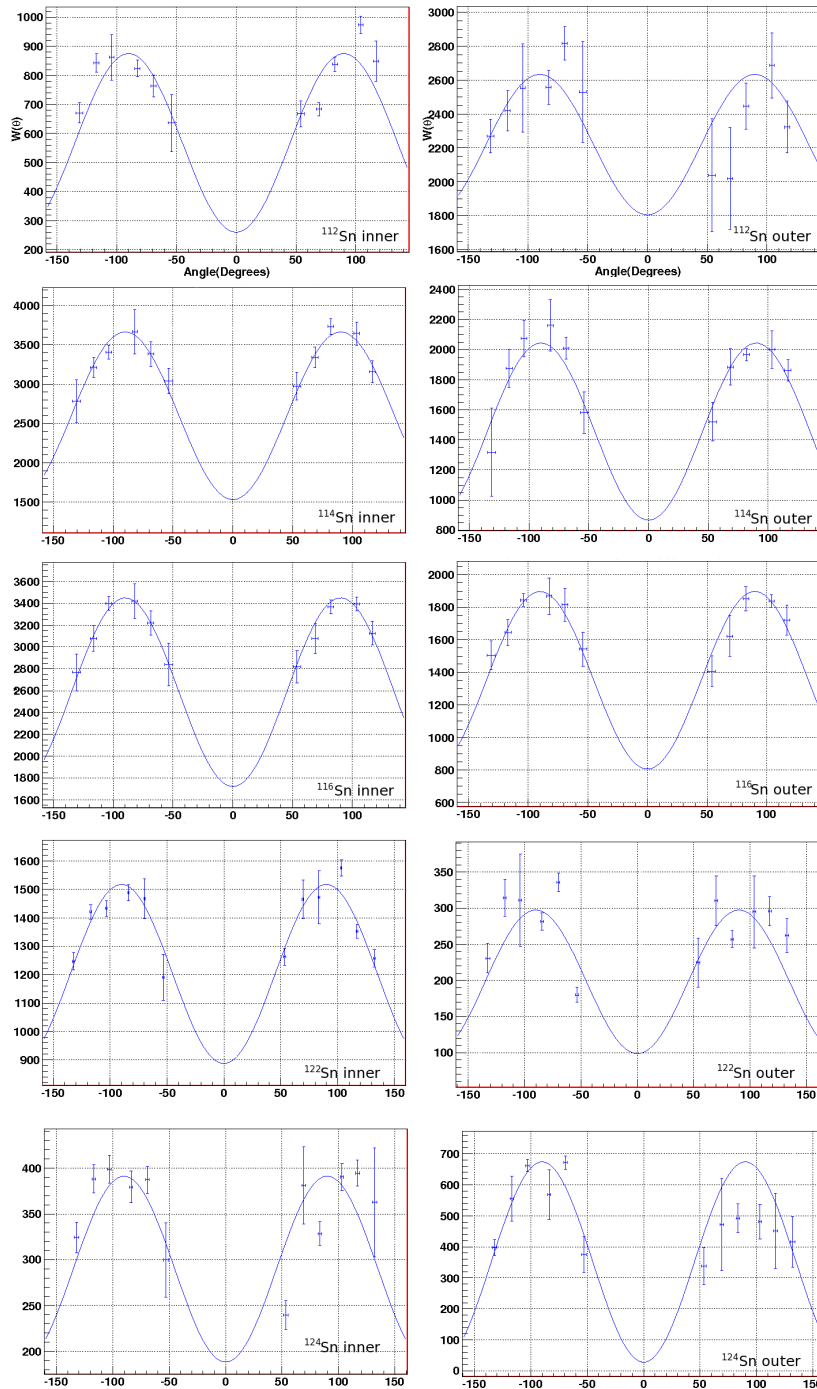


Figure 4.5: The angular correlation for the $3^- \rightarrow 2^+$ transition as observed from data, the left hand side denotes the inner Si detector geometry, the right hand side the outer Si detector geometry, and the angular correlations are given for each isotope measured.

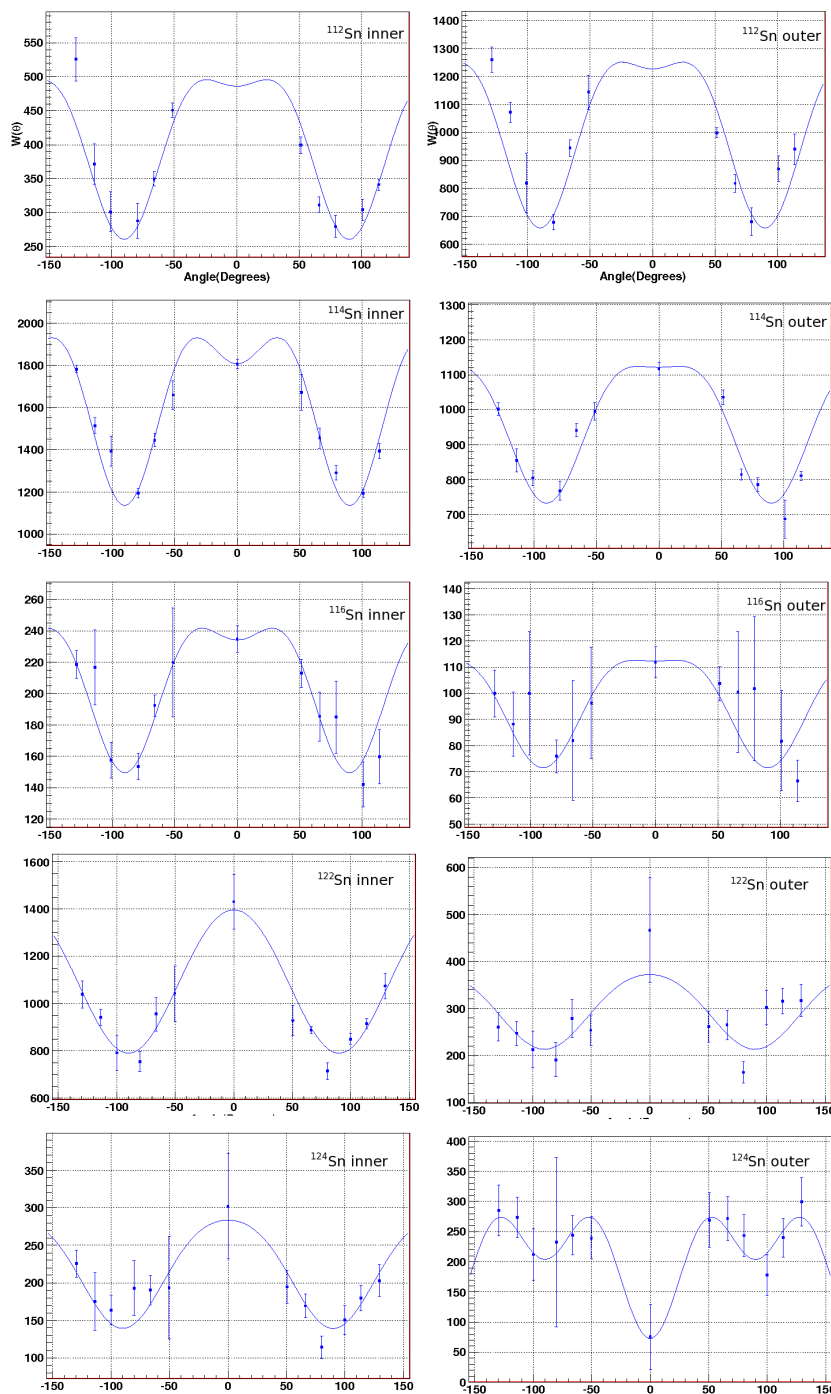


Figure 4.6: The angular correlation for the $4^+ \rightarrow 2^+$ transition as observed from data, the left hand side denotes the inner Si detector geometry, the right hand side the outer Si detector geometry, and the angular correlations are given for each isotope measured.

Combining the total number of detected events for the $3^- \rightarrow 2^+$ and $4^+ \rightarrow 2^+$ transitions in cases with large yields

For the angular correlations for transitions $3^- \rightarrow 2^+$ and $4^+ \rightarrow 2^+$, the total number of detected events is much lower than the for the observed $2^+ \rightarrow 0^+$ transition. Because the 3^- and 4^+ states were directly populated in this experiment, the angular correlation for their transition to the 2^+ state should be the same for each isotope; to compensate for the poor yield and in order to obtain a better angular correlation, the cases with the larger number of counts were used. Using the efficiency corrected counts, each isotope with sufficient statistics were normalized to $C=1$ and fitted for the coefficients for a_2 and a_4 . This results should yield an improved measurement of the angular correlations of the feeding states which are not impaired by lack of counts. The error in the angular correlations of $3^- \rightarrow 2^+$ and $4^+ \rightarrow 2^+$ are also reduced as a result of combining more reliable data points.

$3^- \rightarrow 2^+$	$4^+ \rightarrow 2^+$
^{112}Sn (outer)	^{112}Sn (outer)
^{114}Sn (inner)	^{114}Sn (inner)
^{114}Sn (outer)	^{114}Sn (outer)
^{116}Sn (inner)	-
^{116}Sn (outer)	-
^{122}Sn (inner)	^{122}Sn (inner)

Table 4.4: The experimentally measured correlations used for fitting the angular correlations of $3^- \rightarrow 2^+$ and $4^+ \rightarrow 2^+$ transitions fitted to the data with the best yield.

Transition	Correlation Parameter	
$3^- \rightarrow 2^+$	a_2	-0.365(25)
	a_4	0(0)
$4^+ \rightarrow 2^+$	a_2	0.365(10)
	a_4	-0.192(10)

Table 4.5: The angular correlation parameters for the $3^- \rightarrow 2^+$ and $4^+ \rightarrow 2^+$ transitions fitted to the data with the best yield (refer to table (4.4)).

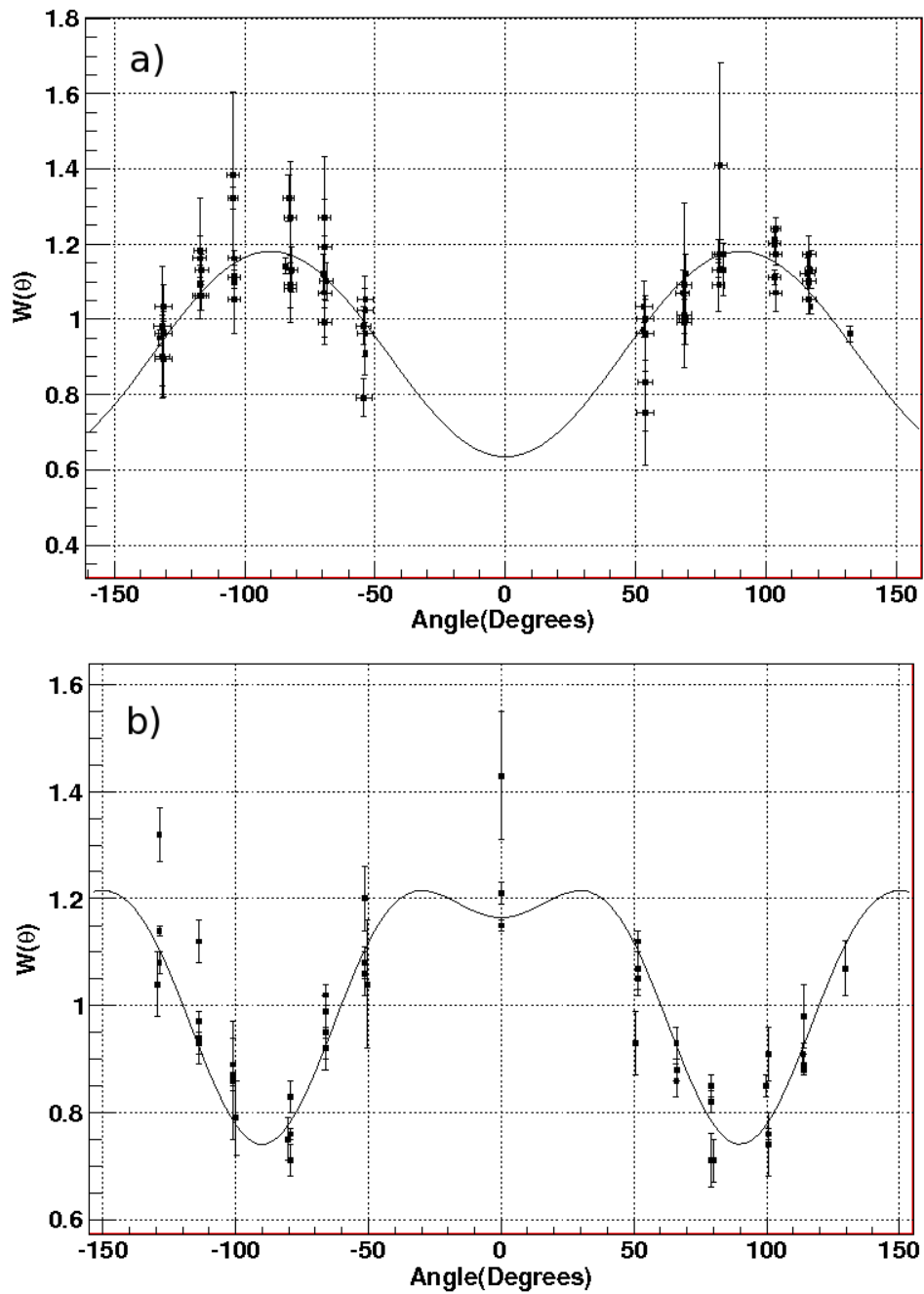


Figure 4.7: The angular correlation for the normalized counts from high statistics cases a) $3^- \rightarrow 2^+$ b) $4^+ \rightarrow 2^+$

4.1.2 Comparison between experimental and calculated angular correlations

Using MuSTanG to obtain the angular correlation for directly populated states

MuSTanG is a program based on the Coulex code [49], written by A. Stuchbery to simulate the outcome of angular correlations for specific experimental conditions such as the silicon detector set up, transition type, beam energy, etc. MuSTanG can be used to calculate the angular correlation of a transition from a directly populated state.

The input file in MuSTanG takes into account variables such as the projectile and target A and Z, the projectile energy, the level number (the number in the program assigned for each level, e.g. ground state has 1, first excited state has 2, etc.), the level spin and parity, and level energy for the ground state and excited states, as well as B(EL) transition strength values where L is the multipole order of the excited state and is also a variable input. Other input variables include the geometry of the Si detectors and the Q_2 and Q_4 factors.

These Q_2 and Q_4 values are the attenuations to the correlations due to the finite size of the Germanium detectors. These vary depending on the size and distance of these detectors from the target. For the detector set up employed in the experiment the appropriate Q_2 and Q_4 values need to be included in this calculation.

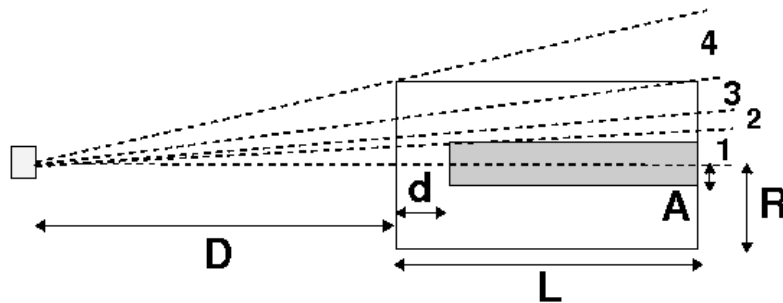


Figure 4.8: The different regions of the Ge crystal used in calculating the parameters, the grey area is the dead core.

Q_k , is obtained by equation (4.10) [43]:

$$Q_k(\gamma) = \frac{J_k(\gamma)}{J_0(\gamma)} \quad (4.10)$$

where

$$J_k(\gamma) = \int P_k(\cos\beta\{1 - \exp(-\tau(\gamma)X(\beta))\})\sin\beta d\beta \quad (4.11)$$

and $\tau(\gamma)$ is the gamma absorption coefficient, β is the angle between the path of the γ -ray and the symmetry axis of the detector and $X(\beta)$ is the path-length through the active volume of the detector [43]. Figure (4.8) shows the various regions which need to be accounted for in calculating equation (4.11), these are given by the following:

$$1: \quad 0 \leq \beta \leq \tan^{-1} \frac{A}{D+L} \rightarrow X(\beta) = \frac{d}{\cos\beta} \quad (4.12)$$

$$2: \quad \tan^{-1} \frac{A}{D+L} \leq \beta \leq \tan^{-1} \frac{A}{D+d} \rightarrow X(\beta) = \frac{D+L+d}{\cos\beta} - \frac{A}{\sin\beta} \quad (4.13)$$

$$3: \quad \tan^{-1} \frac{A}{D+d} \leq \beta \leq \tan^{-1} \frac{R}{D+L} \rightarrow X(\beta) = \frac{L}{\cos\beta} \quad (4.14)$$

$$4: \quad \tan^{-1} \frac{R}{D+L} \leq \beta \leq \tan^{-1} \frac{R}{D} \rightarrow X(\beta) = \frac{R}{\sin\beta} - \frac{A}{\cos\beta} \quad (4.15)$$

where D is the distance between the target and the detector, L is the length of the detector, R is the radius of the detector and d is the distance from the dead core to the front face of the detector. In region 2 shown in figure (4.8), an additional factor needs to be included in $J_k(\gamma)$ to account for the attenuation of the γ -ray in the inactive p-type detector: $K(\beta) = \exp(-J(\gamma)X'(\beta))$ where $X'(\beta)$ is the length through the dead core. $X'(\beta) = \frac{A}{\sin\beta} - \frac{D+d}{\cos\beta}$. Hence the $J_k(\gamma)$ for region 2 is expressed as:

$$J_k(\gamma) = \int P_k(\cos\beta)\{\{1 - \exp(-\tau(\gamma)X_1(\beta))\} + \{1 + \exp(-\tau(\gamma)X_2(\beta))\}\exp(-\tau(\gamma)X'(\beta))\}\sin\beta d\beta \quad (4.16)$$

where $X_1(\beta)$ is the path length in the closed end of the detector and $X_2(\beta)$ is the extra path length for the gammas in the inactive part of the detector.

The function $\tau(\gamma)$ is a function of the energy of the γ -ray and corresponds to:

$$\tau(\gamma) = \tau_{pe}(\gamma) + P_{pe}(\gamma_c)\tau_c(\gamma) \quad (4.17)$$

where $\tau_{pe}(\gamma)$ is the attenuation coefficient for the photoelectric interaction, $\tau_c(\gamma)$ is the attenuation coefficient for the Compton scattering, and $P_{pe}(\gamma_c)$ is the probability that a Compton scattered photon γ_c , will be photoelectrically absorbed. While Q_k experiences a dependence on the gamma energy, the distance from the detector to the target is large, this energy dependence becomes negligible, as shown in figure (4.9).

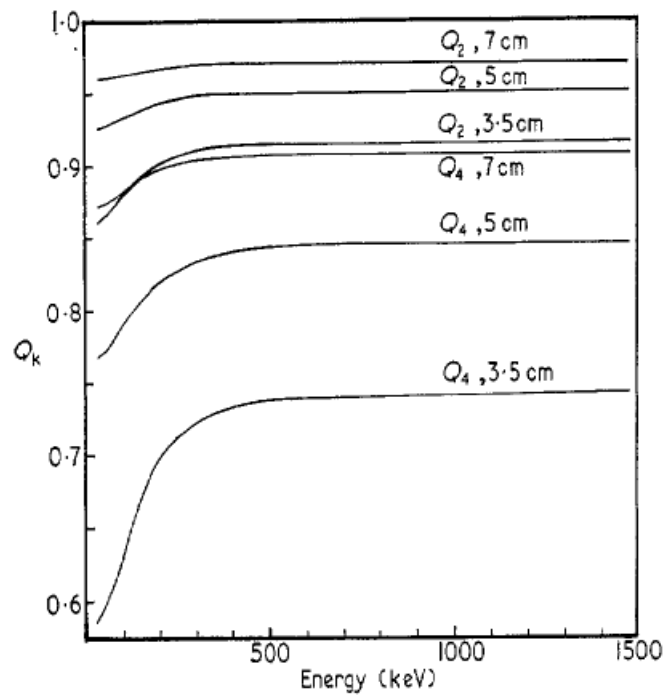


Figure 4.9: The general trend of Q_2 and Q_4 as a function of both distance and gamma energy [43].

Parameter	Value
A	0.55cm
R	2.7 cm
L	6.8cm
d	1.5 cm
D	20.5/21.9cm

Table 4.6: The input parameters to calculate Q_2 and Q_4

In the setup used in the experiment, the distance between the Germanium cluster detectors and the target was ≥ 20 cm, and the γ -energies of interest ≥ 500 keV; as can be seen in figure (4.9), for these values the Q_k values lose their dependence on the energy of the γ -ray. Using the program template given in the paper by Aung and Rice-Evans [43], and the detector parameters for the Euroball detector set up, the values of Q_k in this set up are:

$$Q_2 = 0.989 \quad (4.18)$$

$$Q_4 = 0.963 \quad (4.19)$$

Each Ge crystal, ground into shape for the cluster detectors of the former EUROBALL set up has the following dimensions: front diameter of 48.5mm, an end diameter of 58.9mm and a crystal length of 68mm [44]. The parameters used in the calculation, given in table (4.6), come from these dimensions. The diameters are averaged over the front and end values. The inner dead core dimensions are estimated to have a diameter of 11mm and a length of 66.5mm, varying this core size in the program has negligible effects on the values of Q_k returned by the program.

Comparing the results

The MuSTanG calculations for Sn isotopes yield the same results for the angular correlation for each isotope, which are shown in figure (4.10). The corresponding coefficients are given in table (4.7). Figures (4.10),(4.11) and (4.12) show how the measured angular correlations compare with the MuSTanG calculations. There is an expected discrepancy between the angular correlation given by MuSTanG and the data due to effects of feeding from higher states (this is discussed in section 5.1). Although the measured angular correlations for $4^+ \rightarrow 2^+$ and $3^- \rightarrow 2^+$ transitions for the weighted mean of the events from the isotopes measured in U234 ($^{112,114,116}\text{Sn}$), treated separately for the inner and outer Si detectors have no feeding contributions, the comparison between MuSTanG and the measured angular correlations are not in agreement.

Set Up	coefficients	$2^+ \rightarrow 0^+$	$4^+ \rightarrow 2^+$	$3^- \rightarrow 2^+$
$^{112,114,116}\text{Sn}$ inner	a_2	0.789	0.526	-0.370
	a_4	-1.360	-0.308	0
$^{122,124}\text{Sn}$ inner	a_2	0.788	0.528	-0.371
	a_4	-1.362	-0.310	0
$^{112,114,116}\text{Sn}$ outer	a_2	1.209	0.693	-0.309
	a_4	-0.842	-0.249	0
$^{122,124}\text{Sn}$ outer	a_2	1.206	0.700	-0.320
	a_4	-0.847	-0.255	0

Table 4.7: The parameters derived from MuSTanG for $^{112,114,116}\text{Sn}$ at inner detectors.

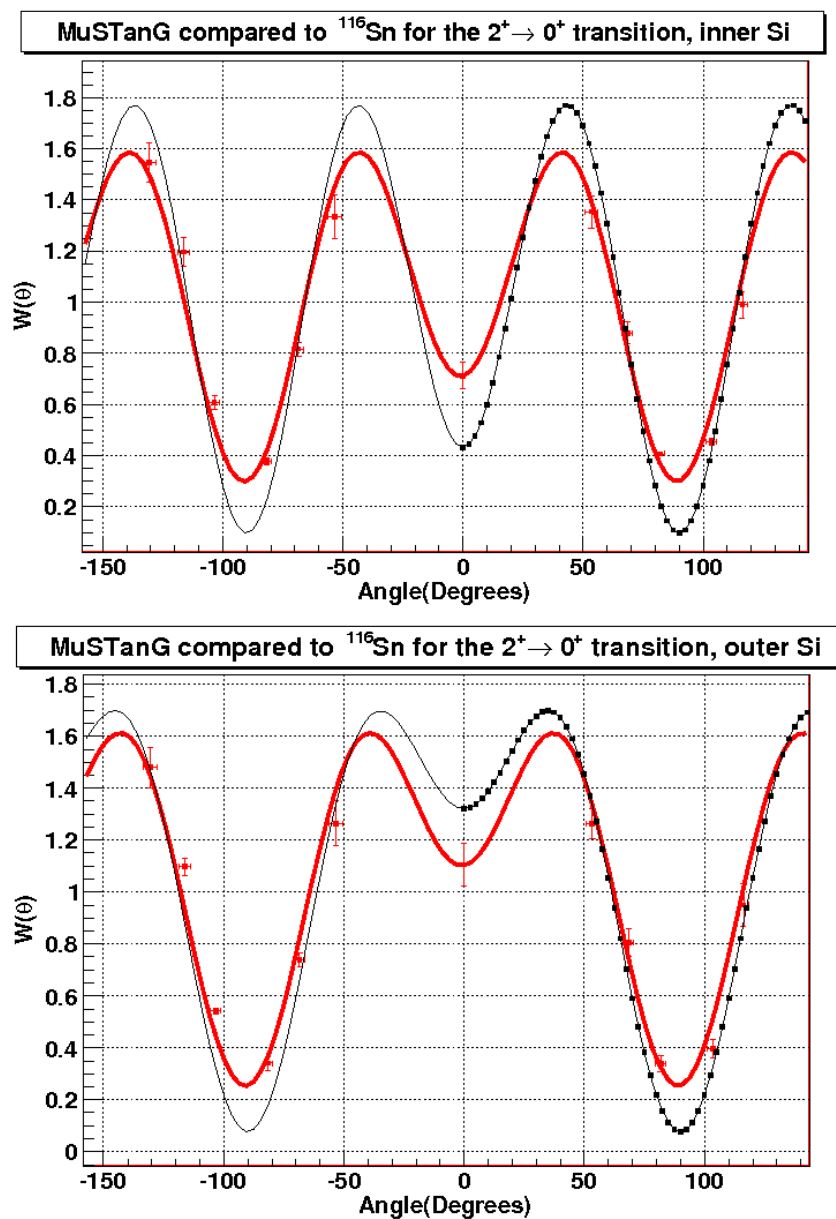


Figure 4.10: The angular correlations given in MuSTanG for the inner and outer detectors respectively, for the flight peak only in $2^+ \rightarrow 0^+$, the red data points and fit are for the experimentally measured data normalized to C, the black is from MuSTanG which gives discrete data points for $W(\theta)$ for angles from 0-180°, the black line is the corresponding fit.

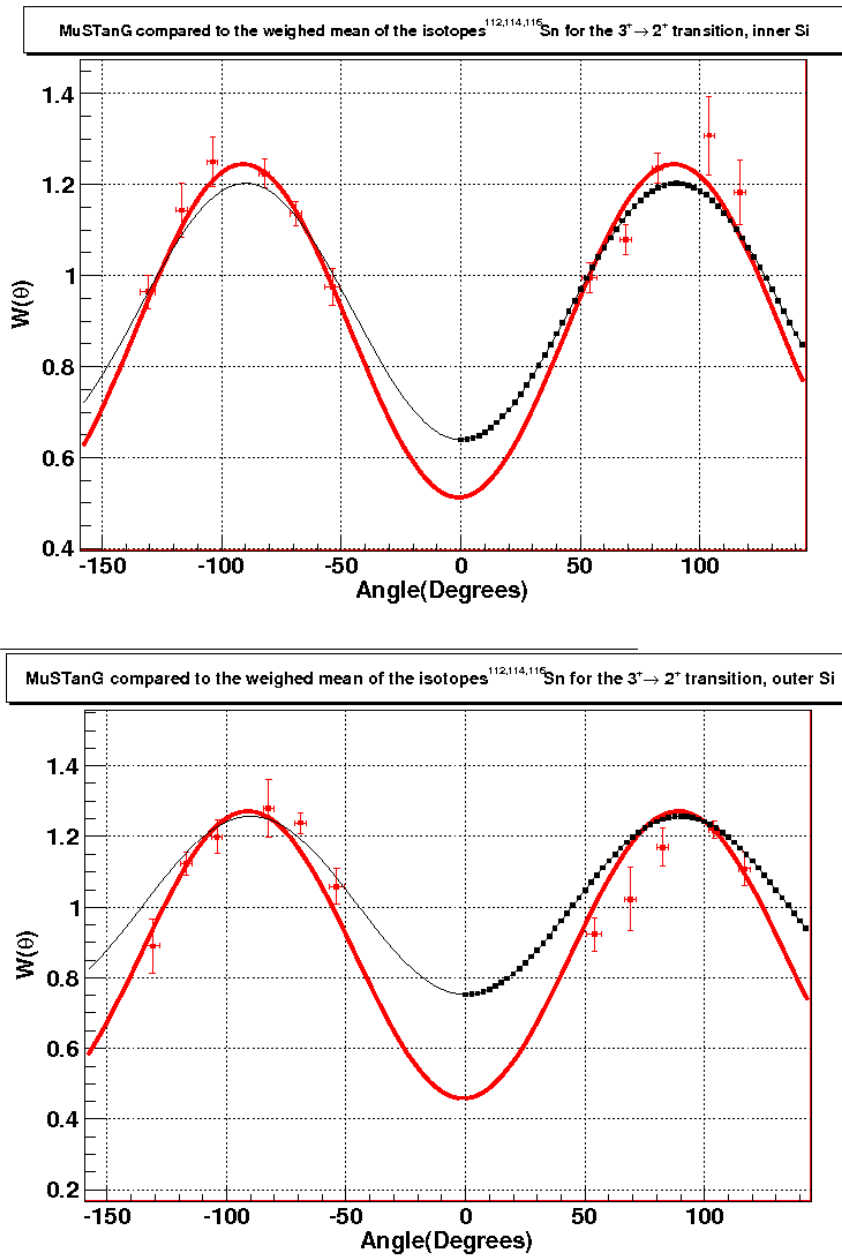


Figure 4.11: The angular correlations given in MuSTanG for the inner and outer detectors respectively for the $3^- \rightarrow 2^+$ transition compared with the summed experimental values, the red data points and fit are for the experimentally measured data normalized to C, the black is from MuSTanG which gives discrete data points for $W(\theta)$ for angles from $0-180^\circ$, the black line is the corresponding fit.

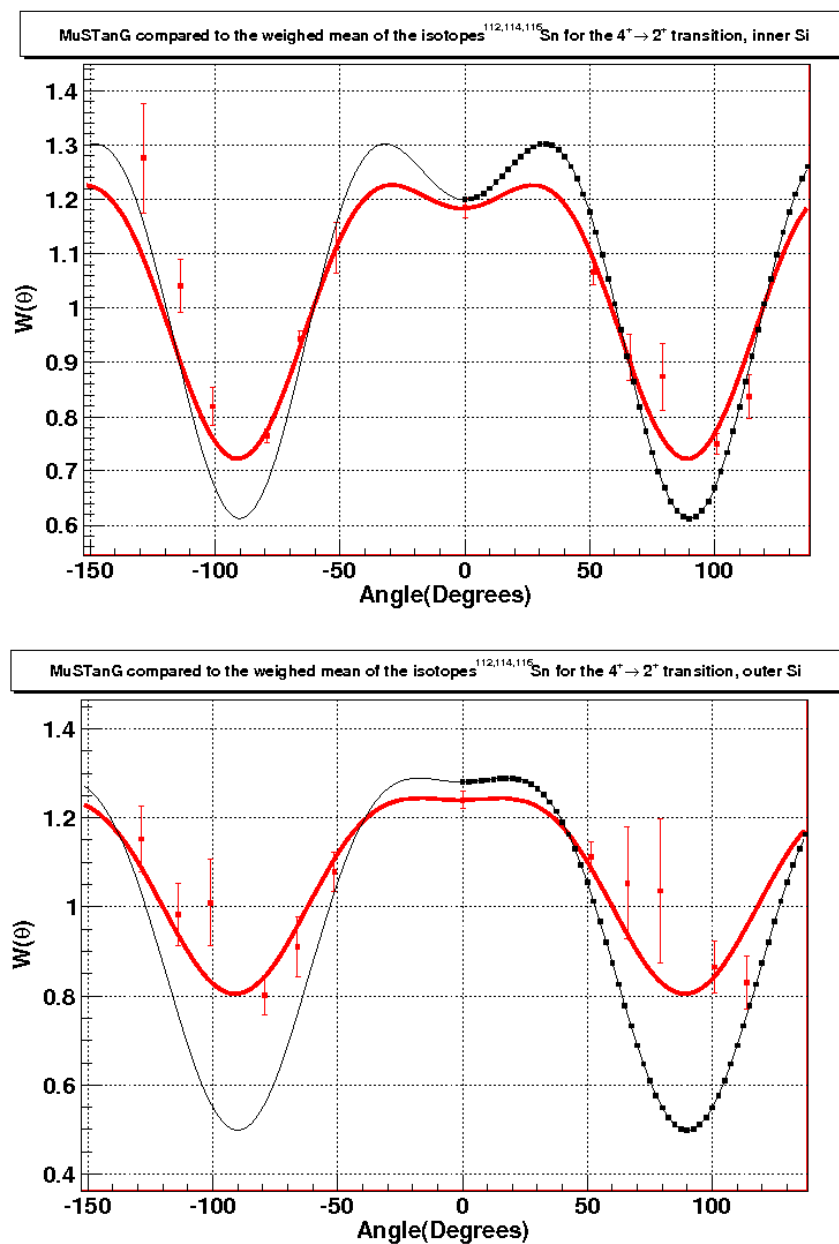


Figure 4.12: The angular correlations given in MuSTanG for the inner and outer detectors respectively for the $4^+ \rightarrow 2^+$ transition compared with the summed experimental values, the red data points and fit are for the experimentally measured data normalized to C, the black is from MuSTanG which gives discrete data points for $W(\theta)$ for angles from $0-180^\circ$, the black line is the corresponding fit.

4.1.3 The Angular Correlation of the directly populated $2^+ \rightarrow 0^+$ transition

The comparison of the MuSTanG correlations with the measured data reveals a significant deviation between them - even for the directly populated states. However for the comparison between the angular correlations for the directly populated states there is a continued disagreement, whether this discrepancy is attributed to poor yield only is something which needs to be considered before using MuSTanG to obtain the angular correlation for the directly populated $2^+ \rightarrow 0^+$ angular correlation. A possible way to determine MuSTanG's validity to reproduce the observed angular correlations of $2^+ \rightarrow 0^+$ is to take into account the feeding effects into the angular correlation using the relation:

$$W(\theta_\gamma)^{obs} = \alpha_1 W_1(\theta_\gamma) + \alpha_2 W_2(\theta_\gamma) + \dots + \alpha_n W_n(\theta_\gamma) = \sum_{i=1}^n \alpha_i W_i(\theta_\gamma) \quad (4.20)$$

$$\alpha_1 + \alpha_2 + \alpha_3 + \dots + \alpha_n = \sum_{i=1}^n \alpha_i = 1 \quad (4.21)$$

where the angular correlation parameters of the feeding states were taken from the experimentally measured parameters and α is the ratio of intensities relative to the observed $2^+ \rightarrow 0^+$ intensity, which should be a sum of all transitions from that state (the directly populated $2^+ \rightarrow 0^+$, plus its feeding components). This was done as an example in ^{122}Sn which experiences small feeding compared to its lighter neighbours, and the observed correlation was reproduced using the parameters from MuSTanG as the directly populated $2^+ \rightarrow 0^+$ angular correlation in equation (4.20).

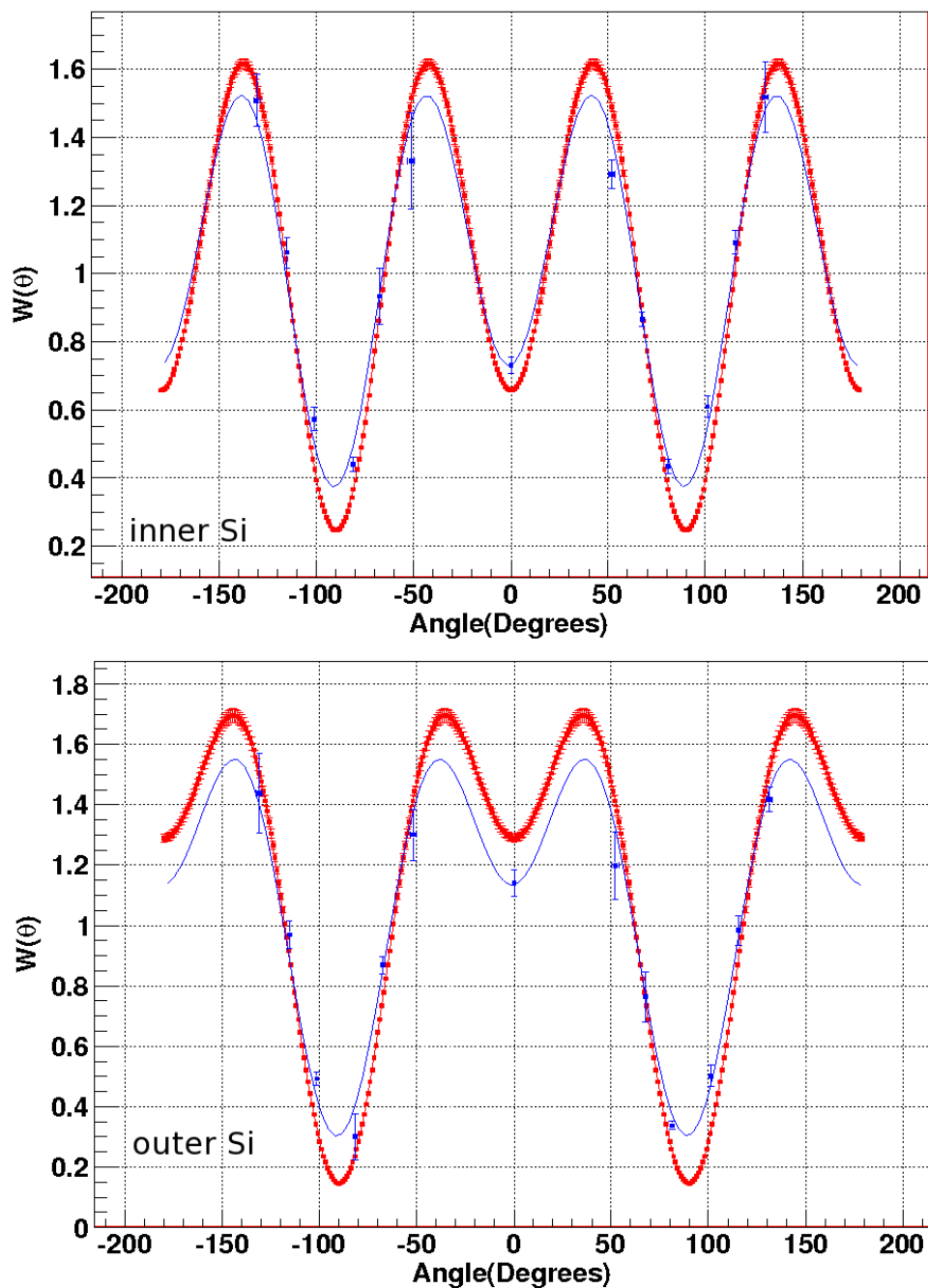


Figure 4.13: Attempt to reproduce the observed $2^+ \rightarrow 0^+$ angular correlation in ^{122}Sn using MuSTanG angular correlation coefficients for purely populated $2^+ \rightarrow 0^+$ transition, and the experimentally measured angular correlation coefficients for feeding states (based on the values given in table (4.5)) and measured intensity ratios compared with the data. The top is for the inner Si, and the bottom for the outer Si.

One can see that this is not a good fit to the observed data - there is a significant difference in the slopes of the two angular correlations, which are the essential components for measuring the precession and hence the g-factor. A method which may be preferable to obtaining these angular correlation parameters is by fitting equation (4.20) to the observed $2^+ \rightarrow 0^+$ angular correlation data for the parameters a_2, a_4 of the purely populated state.

Using the angular correlation parameters from table (4.5) for the $3^- \rightarrow 2^+$ and $4^+ \rightarrow 2^+$ transitions, and the ratios of measured intensities given from the individual angular correlations, the fits to the observed angular correlation for the directly populated state parameters are calculated to be:

Nuc.	Inner	Outer
^{112}Sn	$a_2 = 0.654(60)$ $a_4 = -1.131(70)$	0.933(50) -0.884(60)
^{114}Sn	$a_2 = 0.561(60)$ $a_4 = -1.052(70)$	0.869(70) -0.801(90)
^{116}Sn	$a_2 = 0.558(60)$ $a_4 = -0.984(70)$	0.837(70) -0.720(80)
^{122}Sn	$a_2 = 0.644(60)$ $a_4 = -1.067(40)$	0.938(40) -0.797(40)
^{124}Sn	$a_2 = 0.533(60)$ $a_4 = -1.118(60)$	0.952(40) -0.823(50)
Weighted mean	$a_2 = 0.601(25)$ $a_4 = -1.072(26)$	0.924(22) -0.812(25)

Table 4.8: The purely populated $2^+ \rightarrow 0^+$ parameters from fit.

4.1.4 Other methods to determine the slopes

In past experiments of magnetic moment measurements, a pair of γ detectors symmetric to the beam axis were used [12]. In these cases, one cannot simply measure the logarithmic slope by fitting for the coefficients of the angular correlation as done in this set-up. When there is only one pair of detectors, or even two, the angular correlation and the logarithmic slope require a different technique to measure them. The set up used in U234 and U236 has the advantage of a wide angular range in our Ge detector set up, but with various possible methods available, these were looked into for obtaining the angular correlation parameters from the experimental data. Such methods are:

1. Fit the data points with errors for the parameters a_2 and a_4 by iteration with a fit program (e.g. gnuplot or ROOT), as discussed in the last section.
2. The parameter η , relates the theoretical angular correlation coefficients, a_2^{th} and a_4^{th} to the experimental coefficients by equations [26]:

$$a_2 = a_2^{th}(1 - 6\eta) \quad (4.22)$$

$$a_4 = a_4^{th}(1 - 20\eta) \quad (4.23)$$

which allows one to fit by iteration for only one parameter to obtain a_2 and a_4 .

3. Obtain η using equation (4.24):

$$\frac{W(51)}{W(79)} = \frac{1 + a_2^{th}(1 - 6\eta)P_2(51) + a_4^{th}(1 - 20\eta)P_4(51)}{1 + a_2^{th}(1 - 6\eta)P_2(79) + a_4^{th}(1 - 20\eta)P_4(79)} \quad (4.24)$$

The intensities of the peaks at the angles of maximum anisotropy can be used to find the angular correlation parameters by solving (4.24) for η . This is particularly useful when using a set up limited to a detector geometry, as the slope can be established from the ratios of detectors set at 51° and 79° .

4. The ratios of $\frac{W(51)}{W(65)}$ and $\frac{W(65)}{W(79)}$ from the experimentally measured intensities can also be used to obtain the angular correlation parameters a_2, a_4 . Using the form given in equation (4.24) the angular correlation parameters can be found for each ratio which satisfy the condition:
-

$$\frac{W(\theta_1)}{W(\theta_2)} = \frac{1 + a_2 P_2(\theta_1) + a_4 P_4(\theta_1)}{1 + a_2 P_2(\theta_2) + a_4 P_4(\theta_2)} \quad (4.25)$$

By using a program to solve for a_2, a_4 combinations which satisfy the above condition for both ratios, the region where the a_2, a_4 values cross are the valid ones for the correlation. An example is shown for the case of ^{114}Sn inner Si detector geometry in figure (4.14). From the experimentally calculated ratio with errors, a program calculates an array of compatible a_2, a_4 values for each ratio case, whether it be $\frac{W(51)}{W(65)}, \frac{W(65)}{W(79)}$. These two ratios are super imposed, and where the two regions meet, their weighted mean gives the corresponding a_2, a_4 pairs, and the errors are also calculated from the range.

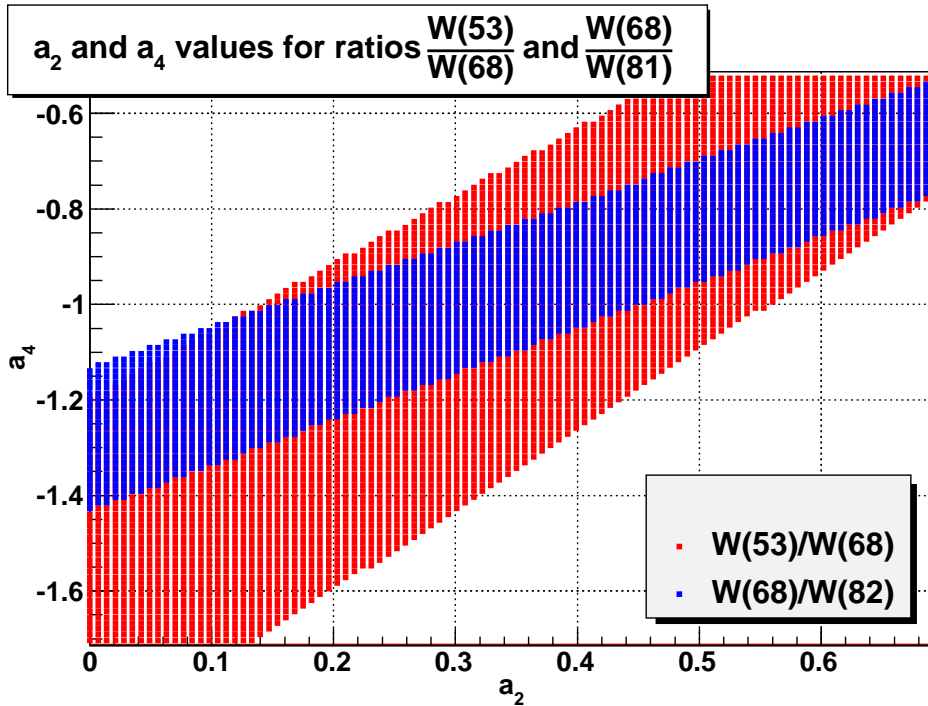


Figure 4.14: The combinations of a_2 and a_4 parameters which satisfy $\frac{W(51)}{W(65)}$ and $\frac{W(65)}{W(79)}$ for ^{114}Sn inner Si detectors $2^+ \rightarrow 0^+$

The different methods yield the angular correlation coefficients given in table (4.9).

One can see that the smallest errors come from fitting to η , and the largest come from method 4, which is more an approximation of the coefficient's range.

Method 4 is probably the most complicated method to obtain the parameters of the angular correlation, it is also very time consuming to do when compared with

parameter	1: a_2, a_4 fit	2: η fit	3: Ratio of $\frac{W(51)}{W(79)}$	4: Ratios of $\frac{W(51)}{W(65)}, \frac{W(65)}{W(79)}$
a_2	0.541(40)	0.610(4)	0.591(40)	0.339(200)
a_4	-0.822(40)	-0.785(30)	-0.728(40)	-0.975(200)
S(65°)	-1.995(80)	-2.057(40)	-1.946(90)	-1.86(390)

Table 4.9: The angular correlation parameters compared for different methods for ^{114}Sn inner Si.

the others; the errors it yields are also very large. The ratio of $\frac{W(51)}{W(65)}$ in method 3 gives values which are comparable to fitting the a_2 and a_4 to the data; the main flaw with method 3 is that for a set up with a wide angle range, it seems redundant.

These ratio methods are useful if there is only a pair of γ -detectors available in the set up, where a full angular correlation cannot be experimentally fitted. In the set up in this experiment, the cluster geometry covers a wide range of angles from $\pm 51^\circ$, $\pm 65^\circ$, $\pm 79^\circ$, $\pm 101^\circ$, $\pm 115^\circ$, $\pm 129^\circ$ and 0° , so a fit of the angular correlation to the data is the best way to obtain the coefficients of the angular correlation, so in this case methods 3 and 4 are redundant. Fitting to η yields small errors, but it forces the measured a_2 and a_4 coefficients to conform to the theoretical values, so the best representation of the experimentally measured a_2 and a_4 coefficients would come for fitting to the parameters themselves.

Another consideration in the feeding correction calculations are the differential angular correlations $\frac{dW_{2^+}}{d\theta}$, $\frac{dW_{320}}{d\theta}$ and $\frac{dW_{420}}{d\theta}$ obtained from the angular correlation coefficients a_2 and a_4 via the equation:

$$\frac{dW}{d\theta} = \sin(\theta)\cos(\theta)(-3a_2 - 17.5a_4\cos^2(\theta) + 7.5a_4). \quad (4.26)$$

The angular correlation parameters are read in by the program for the experimentally observed $2^+ \rightarrow 0^+$ transition, the directly populated $2^+ \rightarrow 0^+$ transition (see subsection 4.1.3), for the $4^+ \rightarrow 2^+ \rightarrow 0^+$, where the experimentally measured $4^+ \rightarrow 2^+$ transition can be used, as their values are identical as both $4^+ \rightarrow 2^+$ and $2^+ \rightarrow 0^+$ are E2 transitions. The angular correlation for the cascade $3^- \rightarrow 2^+ \rightarrow 0^+$, is obtained from the experimentally measured $3^+ \rightarrow 2^+$ and equation (4.27)[26]:

$$W_{320}^{exp}(\theta_\gamma) = \frac{W_{320}^{theory}(\theta_\gamma)}{W_{32}^{theory}(\theta_\gamma)} \cdot W_{32}^{exp}(\theta_\gamma) \quad (4.27)$$

where the theoretical parameters of W_{320}^{theory} are $a_2 = 0.571$ and $a_4 = -0.571$. The angular correlations used have been introduced already in table (4.1) for the observed $2^+ \rightarrow 0^+$, and table (4.5) (the angular correlation of all isotopes with good yield) for $4^+ \rightarrow 2^+$. For the cascade $3^+ \rightarrow 2^+ \rightarrow 0^+$, the values used the correlation parameters from table (4.5) in conjunction with equation (4.27).

Si det.		^{112}Sn	^{114}Sn	^{116}Sn	^{122}Sn	^{124}Sn	Mean
inner	a_2	0.406(30)	0.508(20)	0.571(20)	0.632(10)	0.435(20)	0.598(10)
	a_4	-0.613(20)	-0.582(20)	-0.571(20)	-0.556(10)	-0.606(20)	-0.564(10)
outer	a_2	0.700(20)	0.512(20)	0.512(20)	0.556(20)	0.152(30)	0.598(10)
	a_4	-0.538(20)	-0.586(20)	-0.586(20)	-0.575(20)	-0.678(30)	-0.564(10)

Table 4.10: The angular correlation coefficients for cascade $3^+ \rightarrow 2^+ \rightarrow 0^+$.

4.2 Determination of the precession angles

4.2.1 Obtaining the precession experimentally

The precessions were measured by taking the double ratio at each angle and for each magnetic polarity (see section 2.1). The field up data was used for the gate on `adc[0]`, and the field down was taken from the ADC gate `adc[1]`. Each ADC channel registers the valid event for each magnetic polarity read in by the field direction switcher. Gating on the peak and on the appropriate ADC channel gives the field up or field down events.

The precession $\Delta\Phi$ is determined from the ratio of the intensity of a specific γ -ray peak between the intensity ratios between up and down field directions for a pair of detectors placed in a plane at symmetric angles, $\pm\theta$, relative to the beam direction. The individual intensities for each of the 28 detector crystals were measured from the cleaned γ -spectra for both up and down magnetic polarity separately. The double ratios are independent of efficiency, so the raw intensities are used in this case. For the detectors located at 115° and 65° , there were 3 crystals per cluster (3 in the $-\theta$ and 3 in $+\theta$) and for the other angles: 51° , 79° , 101° , 129° , there were 2 crystals per cluster. For the cases when there are 2 crystals per cluster, the double ratio was taken as follows:

$$\rho(\theta) = \left(\frac{N_1(+\theta \uparrow)}{N_1(+\theta \downarrow)} \cdot \frac{N_2(+\theta \uparrow)}{N_2(+\theta \downarrow)} \cdot \frac{N_3(-\theta \downarrow)}{N_3(-\theta \uparrow)} \cdot \frac{N_4(-\theta \downarrow)}{N_4(-\theta \uparrow)} \right)^{1/4} \quad (4.28)$$

where 1,2 are different crystals at $+\theta$ and 3,4 for crystals at $-\theta$. For the case with 3 crystals per cluster at the same angle:

$$\rho(\theta) = \left(\frac{N_1(+\theta \uparrow)}{N_1(+\theta \downarrow)} \cdot \frac{N_2(+\theta \uparrow)}{N_2(+\theta \downarrow)} \cdot \frac{N_3(+\theta \uparrow)}{N_3(+\theta \downarrow)} \cdot \frac{N_4(-\theta \downarrow)}{N_4(-\theta \uparrow)} \cdot \frac{N_5(-\theta \downarrow)}{N_5(-\theta \uparrow)} \cdot \frac{N_6(-\theta \downarrow)}{N_6(-\theta \uparrow)} \right)^{1/6} \quad (4.29)$$

where 1,2,3 are for crystals at $+\theta$, 4,5,6 for crystals at $-\theta$ and $N(+\theta \uparrow)$ is the number of counts measured in the detector at $+\theta$ for field up. A program reads in the individual intensities for field up and down, the ρ for each angle is calculated as shown in equations (4.28,4.29). Once the double ratios are established, the effect, ϵ is then obtained by equation (4.31) for each angle, this has already been introduced in section 2.1. The logarithmic slope at each angle is calculated from the angular

correlation coefficients which have been discussed before, and the $\Delta\Phi$ at each angle is hence obtained from equation (4.31). The general precession is obtained from the weighted means of the precessions at each angle, which should agree with each other within the errors.

$$\epsilon = \frac{\rho - 1}{\rho + 1} \quad (4.30)$$

$$\Delta\Phi = \frac{\epsilon}{S(\theta_\gamma)} \quad (4.31)$$

After the precession and $\Delta\Phi$ has been measured, in the case of no feeding, the g-factor of the state can be determined from the equation [12]:

$$\Delta\Phi = -g \frac{\mu_N}{\hbar} \int_{t_{in}}^{t_{out}} B_{TF}(v_{ion}(t)) e^{-t/\tau} dt \quad (4.32)$$

4.2.2 Precession Results

The precessions from the $2^+ \rightarrow 0^+$ transition use the slopes obtained from the experimentally measured angular correlations for each isotope and inner and outer Si detector geometry individually given in table (4.1). For the precessions from $3^- \rightarrow 2^+$ and $4^+ \rightarrow 2^+$ the slopes used in the calculation come from the angular correlation coefficients from the fit of the isotopes with good yield in table (4.5). This has already been discussed in the angular correlation chapters. These tables show the values of ρ , the effect (ϵ), the logarithmic slope and precession at each angle as described in section 4.2.1. These precessions were not only obtained for the observed $2^+ \rightarrow 0^+$ transitions, but also for the transitions from the feeding states into the 2^+ state of $3^- \rightarrow 2^+$, $4^+ \rightarrow 2^+$ in order to calculate the feeding corrections to be discussed later on. The tables currently show these measured parameters from the data for $2^+ \rightarrow 0^+$ - inner followed by outer, then $3^- \rightarrow 2^+$ inner and outer, and $4^+ \rightarrow 2^+$ inner and outer. Their weighted means between the Si detector geometry are given at the end of the chapter and are used for obtaining the raw g-factors.

Table 4.11: The measured precessions for $2^+ \rightarrow 0^+$ stopped and flight peak, inner Si detector geometry.

Nuclei	θ (degs)	ρ	$\epsilon \times 1000$	$S(\theta)$	$\Delta\Phi(\text{mrad})$
^{112}Sn	53	0.978(20)	-11(10)	-0.985(40)	11(10)
^{112}Sn	68	1.021(20)	10(9)	-2.468(110)	-4(4)
^{112}Sn	81	0.994(30)	-3(15)	-2.664(220)	1(6)
^{112}Sn	102	0.996(30)	-2(14)	2.918(200)	-1(5)
^{112}Sn	116	0.948(20)	-27(8)	2.083(80)	-13(4)
^{114}Sn	53	1.003(10)	1(5)	-0.911(40)	-1(5)
^{114}Sn	68	0.993(10)	-4(4)	-2.234(100)	2(2)
^{114}Sn	81	1.003(10)	1(7)	-2.209(180)	-1(3)
^{114}Sn	102	0.982(10)	-9(6)	2.500(180)	-4(3)
^{114}Sn	116	1.008(10)	4(4)	1.909(80)	2(2)
^{116}Sn	53	1.004(10)	2(5)	-0.939(40)	-2(5)
^{116}Sn	68	0.990(10)	-5(5)	-2.284(120)	2(2)
^{116}Sn	81	1.017(10)	9(8)	-2.311(210)	-4(4)
^{116}Sn	103	0.972(10)	-14(7)	2.616(200)	-5(3)
^{116}Sn	116	1.008(10)	4(5)	1.949(90)	2(4)
^{122}Sn	52	0.981(10)	-9(5)	-0.882(30)	11(6)
^{122}Sn	67	0.994(10)	-3(5)	-2.343(70)	1(2)
^{122}Sn	81	0.977(20)	-11(10)	-2.592(160)	4(4)
^{122}Sn	101	1.032(20)	15(10)	2.794(150)	5(3)
^{122}Sn	115	1.020(10)	9(5)	2.155(60)	4(2)
^{122}Sn	131	1.012(10)	6(6)	0.601(30)	10(10)
^{124}Sn	52	1.003(20)	1(11)	-0.816(50)	-1(14)
^{124}Sn	68	0.943(20)	-29(10)	-2.473(130)	11(4)
^{124}Sn	81	0.927(40)	-38(18)	-2.733(270)	13(6)
^{124}Sn	102	1.032(40)	15(20)	2.977(250)	5(6)
^{124}Sn	116	1.004(20)	2(10)	2.068(100)	1(5)
^{124}Sn	131	1.041(20)	20(11)	0.515(50)	39(22)

Table 4.12: The measured precessions for $2^+ \rightarrow 0^+$ stopped and flight peak, outer Si detector geometry.

Nuclei	θ (degs)	ρ	$\epsilon \times 1000$	S(θ)	$\Delta\Phi$ (mrad)
^{112}Sn	53	1.008(10)	4(5)	-1.219(40)	-3(4)
^{112}Sn	68	1.030(10)	15(5)	-2.801(130)	-5(2)
^{112}Sn	81	1.050(20)	24(10)	-3.263(330)	-7(3)
^{112}Sn	103	0.969(10)	-16(7)	3.484(280)	-5(2)
^{112}Sn	116	0.966(10)	-17(4)	2.362(90)	-7(2)
^{114}Sn	53	1.016(10)	8(6)	-1.125(50)	-7(5)
^{114}Sn	68	0.971(10)	-15(5)	-2.416(160)	6(2)
^{114}Sn	81	0.987(20)	-17(9)	-2.435(300)	3(4)
^{114}Sn	103	0.985(20)	-7(8)	2.749(280)	-3(3)
^{114}Sn	116	1.033(10)	16(6)	2.088(110)	8(3)
^{116}Sn	53	0.990(10)	-4(6)	-1.119(50)	4(5)
^{116}Sn	68	1.022(10)	10(6)	-2.376(160)	-4(2)
^{116}Sn	81	1.0047(20)	2(11)	-2.359(290)	0(4)
^{116}Sn	103	0.992(20)	-3(9)	2.678(270)	-1(3)
^{116}Sn	116	0.991(10)	-4(5)	2.060(110)	-2(2)
^{122}Sn	52	1.047(20)	22(10)	-1.151(30)	-19(8)
^{122}Sn	68	1.026(20)	12(10)	-2.748(100)	-4(3)
^{122}Sn	82	0.698(20)	-177(14)	-2.938(250)	60(7)
^{122}Sn	101	1.109(40)	51(19)	3.292(240)	15(6)
^{122}Sn	116	1.014(20)	7(9)	2.335(70)	3(4)
^{122}Sn	131	1.024(20)	11(9)	0.887(30)	13(11)
^{124}Sn	52	0.936(10)	-32(5)	-1.196(40)	27(4)
^{124}Sn	68	0.975(10)	-12(6)	-2.976(140)	4(2)
^{124}Sn	82	0.928(20)	-37(11)	-3.688(400)	10(3)
^{124}Sn	102	1.002(20)	0(11)	3.854(340)	0(2)
^{124}Sn	116	1.038(10)	18(6)	2.493(90)	7(2)
^{124}Sn	131	1.041(10)	20(6)	0.916(40)	22(6)

Table 4.13: The measured precessions for $3^- \rightarrow 2^+$, inner Si detector geometry

Nuclei	θ (degs)	ρ	$\epsilon \times 1000$	$S(\theta)$	$\Delta\Phi(\text{mrad})$
^{112}Sn	54	1.124(110)	58(52)	0.525(40)	111(100)
^{112}Sn	69	1.015(50)	7(25)	0.329(20)	22(77)
^{112}Sn	83	0.965(40)	-17(21)	0.113(10)	-159(192)
^{112}Sn	104	1.027(50)	13(23)	-0.223(10)	-58(105)
^{112}Sn	117	1.007(50)	3(26)	-0.414(30)	-7(63)
^{114}Sn	53	1.000(30)	0(16)	0.535(40)	0(30)
^{114}Sn	68	1.020(20)	9(12)	0.344(20)	29(35)
^{114}Sn	82	1.035(30)	17(13)	0.129(10)	134(102)
^{114}Sn	103	1.032(30)	15(12)	-0.208(10)	-75(60)
^{114}Sn	116	1.000(20)	0(12)	-0.400(30)	0(31)
^{116}Sn	54	1.024(30)	11(15)	0.524(40)	22(30)
^{116}Sn	69	0.987(20)	-6(10)	0.329(20)	-19(32)
^{116}Sn	82	0.980(20)	-10(9)	0.129(10)	-79(75)
^{116}Sn	104	0.999(20)	0(10)	-0.223(10)	2(47)
^{116}Sn	117	0.969(20)	-15(10)	-0.414(30)	38(25)
^{122}Sn	53	0.974(40)	-13(19)	0.535(40)	-24(36)
^{122}Sn	70	0.983(30)	-8(15)	0.315(20)	-27(48)
^{122}Sn	84	1.027(40)	13(19)	0.097(10)	137(205)
^{122}Sn	103	1.012(40)	5(20)	-0.208(10)	-28(97)
^{122}Sn	117	0.987(30)	-6(16)	-0.414(30)	15(40)
^{122}Sn	132	0.996(40)	-1(22)	-0.581(40)	3(38)
^{124}Sn	53	1.291(150)	127(65)	0.535(40)	237(123)
^{124}Sn	69	0.982(60)	-9(30)	0.330(20)	-28(91)
^{124}Sn	84	0.904(60)	-50(33)	0.097(10)	-522(348)
^{124}Sn	103	1.013(80)	6(39)	-0.208(10)	-31(190)
^{124}Sn	117	1.074(70)	35(35)	-0.414(30)	-86(87)
^{124}Sn	132	0.982(90)	-8(42)	-0.581(40)	15(73)

Table 4.14: The measured precessions for $3^- \rightarrow 2^+$, outer Si detector geometry

Nuclei	θ (degs)	ρ	$\epsilon \times 1000$	$S(\theta)$	$\Delta\Phi$ (mrad)
^{112}Sn	54	1.123(60)	57(28)	0.524(40)	110(55)
^{112}Sn	69	1.014(30)	6(16)	0.329(20)	21(49)
^{112}Sn	83	1.005(30)	2(13)	0.113(10)	22(122)
^{112}Sn	104	1.017(30)	8(14)	-0.223(10)	-38(63)
^{112}Sn	117	1.026(30)	12(16)	-0.414(30)	-31(40)
^{114}Sn	54	0.978(60)	-11(28)	0.524(40)	-21(54)
^{114}Sn	69	1.051(40)	24(21)	0.329(20)	74(65)
^{114}Sn	82	0.977(30)	-11(12)	0.129(10)	-90(99)
^{114}Sn	104	1.005(40)	2(18)	-0.223(10)	-10(83)
^{114}Sn	117	0.966(40)	-17(18)	-0.414(30)	42(44)
^{116}Sn	54	1.116(60)	54(29)	0.524(40)	104(56)
^{116}Sn	69	0.974(30)	-13(15)	0.329(20)	-39(46)
^{116}Sn	82	0.996(30)	-2(14)	0.129(10)	-16(113)
^{116}Sn	104	0.954(30)	-23(14)	-0.223(10)	105(65)
^{116}Sn	117	1.014(30)	6(16)	-0.414(30)	-16(40)
^{122}Sn	54	0.923(90)	-40(46)	0.524(40)	-76(88)
^{122}Sn	70	1.007(70)	3(33)	0.315(20)	10(107)
^{122}Sn	84	0.820(60)	-98(33)	0.097(10)	-1021(351)
^{122}Sn	104	0.905(70)	-50(38)	-0.223(10)	224(173)
^{122}Sn	117	0.894(60)	-55(31)	-0.414(30)	135(76)
^{122}Sn	132	0.823(70)	-97(38)	-0.581(40)	167(67)
$^{124}\text{Sn.}$	53	0.949(90)	-26(45)	0.535(40)	-49(84)
$^{124}\text{Sn.}$	69	1.218(80)	98(37)	0.329(20)	298(115)
$^{124}\text{Sn.}$	84	1.190(90)	86(41)	0.097(60)	897(436)
$^{124}\text{Sn.}$	103	0.992(70)	-3(32)	-0.208(10)	19(157)
$^{124}\text{Sn.}$	117	0.908(50)	-47(27)	-0.414(30)	115(66)
$^{124}\text{Sn.}$	132	0.905(70)	-50(36)	-0.581(40)	86(63)

Table 4.15: The measured precessions for $4^+ \rightarrow 2^+$, inner Si detector geometry

Nuclei	θ (degs)	ρ	$\epsilon \times 1000$	$S(\theta)$	$\Delta\Phi(\text{mrad})$
^{112}Sn	51	0.988(50)	-6(25)	-0.528(10)	11(49)
^{112}Sn	66	0.956(50)	-22(25)	-0.789(20)	28(32)
^{112}Sn	79	1.084(100)	40(48)	-0.572(20)	-70(85)
^{112}Sn	101	1.115(90)	54(41)	0.572(20)	95(72)
^{112}Sn	115	0.943(40)	-29(19)	0.784(20)	-37(25)
^{114}Sn	51	0.988(10)	-5(2)	-0.528(10)	11(4)
^{114}Sn	66	0.938(10)	-31(2)	-0.789(20)	40(2)
^{114}Sn	79	1.066(10)	32(5)	-0.572(20)	-56(9)
^{114}Sn	101	0.957(10)	-21(3)	0.572(20)	-38(7)
^{114}Sn	115	1.073(10)	35(2)	0.784(20)	44(3)
^{116}Sn	51	1.165(140)	76(65)	-0.528(10)	-144(124)
^{116}Sn	66	1.179(120)	81(55)	-0.789(20)	-103(70)
^{116}Sn	79	1.305(210)	132(88)	-0.572(20)	-231(155)
^{116}Sn	101	0.705(60)	-172(36)	0.572(20)	-302(65)
^{116}Sn	115	1.072(100)	34(50)	0.784(20)	44(63)
^{122}Sn	51	0.943(10)	-29(5)	-0.529(10)	55(10)
^{122}Sn	66	0.972(10)	-14(6)	-0.789(20)	18(7)
^{122}Sn	80	0.939(20)	-31(9)	-0.532(20)	59(17)
^{122}Sn	100	1.010(20)	4(10)	0.532(20)	9(18)
^{122}Sn	114	1.090(10)	4(6)	0.789(20)	5(7)
^{122}Sn	129	0.967(10)	-16(6)	0.528(10)	-31(11)
^{124}Sn	51	1.104(230)	49(108)	-0.528(10)	-93(205)
^{124}Sn	66	1.199(240)	90(110)	-0.789(20)	-114(140)
^{124}Sn	80	0.877(280)	-65(151)	-0.532(20)	123(284)
^{124}Sn	100	0.905(210)	-50(109)	0.532(20)	-94(205)
^{124}Sn	114	0.986(210)	-7(103)	0.789(20)	-9(131)
^{124}Sn	129	0.724(90)	-160(51)	0.528(10)	-303(97)

Table 4.16: The measured precessions for $4^+ \rightarrow 2^+$, outer Si detector geometry

Nuclei	θ (degs)	ρ	$\epsilon \times 1000$	$S(\theta)$	$\Delta\Phi(\text{mrad})$
^{112}Sn	51	1.026(10)	12(6)	-0.528(10)	-24(11)
^{112}Sn	66	1.108(20)	51(7)	-0.789(20)	-64(9)
^{112}Sn	79	1.156(40)	72(17)	-0.572(20)	-126(30)
^{112}Sn	101	1.010(20)	4(9)	0.572(20)	8(16)
^{112}Sn	115	1.076(10)	36(5)	0.784(10)	46(7)
^{114}Sn	51	0.997(20)	-1(8)	-0.528(10)	2(16)
^{114}Sn	66	1.049(20)	24(9)	-0.789(20)	-30(12)
^{114}Sn	80	0.984(30)	-8(15)	-0.532(20)	15(29)
^{114}Sn	100	0.952(30)	-24(14)	0.532(20)	-45(26)
^{114}Sn	114	0.992(20)	-4(8)	0.789(20)	-5(11)
^{116}Sn	51	0.631(70)	-226(43)	-0.528(10)	428(82)
^{116}Sn	66	0.921(140)	-40(71)	-0.789(20)	51(90)
^{116}Sn	79	0.875(130)	-66(69)	-0.572(20)	116(122)
^{116}Sn	101	1.027(170)	13(85)	0.572(20)	23(150)
^{116}Sn	115	1.508(350)	202(143)	0.784(20)	258(183)
^{122}Sn	51	0.991(140)	-4(70)	-0.528(10)	8(132)
^{122}Sn	66	0.865(80)	-72(45)	-0.789(20)	92(57)
^{122}Sn	80	0.804(150)	-108(84)	-0.532(20)	204(159)
^{122}Sn	100	1.171(250)	78(114)	0.532(20)	147(214)
^{122}Sn	114	1.068(120)	32(60)	0.789(20)	41(76)
^{122}Sn	129	1.476(310)	192(131)	0.528(20)	364(248)
^{124}Sn	51	1.596(500)	229(198)	-0.528(10)	-434(375)
^{124}Sn	66	0.970(190)	-15(94)	-0.789(20)	19(119)
^{124}Sn	80	0.953(350)	-24(178)	-0.532(20)	45(335)
^{124}Sn	100	0.587(250)	-259(160)	0.532(20)	-489(302)
^{124}Sn	114	1.015(170)	7(82)	0.789(20)	9(105)
^{124}Sn	129	1.197(250)	89(112)	0.528(10)	170(213)

Table 4.17: The weighed mean of the precessions.

Nuclei	Si	$2^+ \rightarrow 0^+$ (mrad)	$3^- \rightarrow 2^+$ (mrad)	$4^+ \rightarrow 2^+$ (mrad)
^{112}Sn	Inner	$-5(2/3)$	$5(40/30)$	$-5(17/20)$
^{114}Sn		$0(1/1)$	$5(18/17)$	$26(2/14)$
^{116}Sn		$0(1/2)$	$12(15/15)$	$-127(36/69)$
^{122}Sn		$4(1/1)$	$-7(20/11)$	$16(4/12)$
^{124}Sn		$8(3/3)$	$-3(43/57)$	$-151(60/59)$
^{112}Sn	Outer	$-6(1/1)$	$11(24/27)$	$-4(5/25)$
^{114}Sn		$4(1/2)$	$16(27/23)$	$-14(7/8)$
^{116}Sn		$-2(2/1)$	$16(24/31)$	$209(49/86)$
^{122}Sn		$7(2/9)$	$78(39/79)$	$87(41/29)$
^{114}Sn		$7(1/3)$	$94(37/58)$	$-10(69/67)$

Chapter 5

The feeding corrections

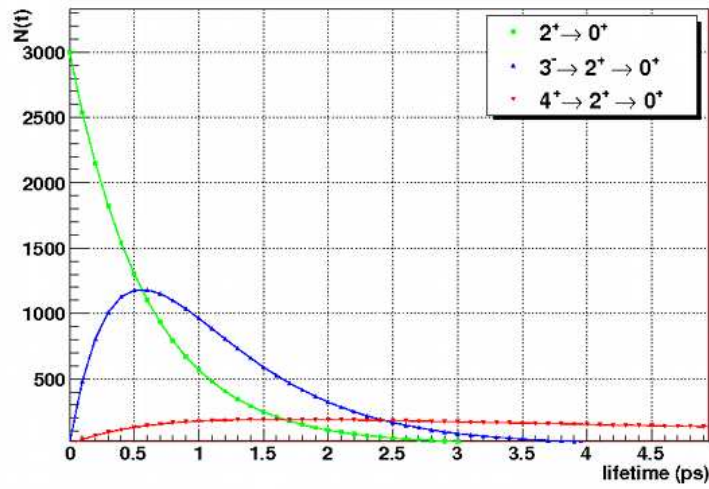
5.1 Introduction

For the nuclei $^{112,114,116,122,124}\text{Sn}$, there is significant feeding (as evidenced by the intensities reported in table (4.3)) which occurs from the higher states ($3^-, 4^+$) into the 2^+ state. Figure (5.1b) shows the level scheme of ^{114}Sn and one can see that the 4^+ and 3^- states contribute to the final observed $2^+ \rightarrow 0^+$ transition. These feeding contributions will affect the measured precession of the $2^+ \rightarrow 0^+$ transition, as the precession, $\Delta\Phi$, given in equation (5.1) is a function of the lifetime of the state, and since the feeding states have a different lifetimes to the lifetime of the 2^+ state, the precessions observed where feeding occurs will be altered from the precession of a purely populated $2^+ \rightarrow 0^+$ transition.

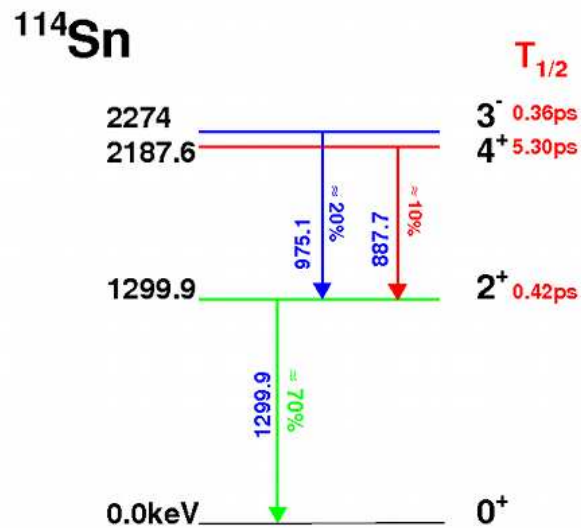
$$\Delta\Phi = g\phi(\tau_i) = -g\frac{\mu_N}{\hbar} \int_{t_{in}}^{t_{out}} B_{TF}(v_{ion}(t))e^{-t/\tau} dt \quad (5.1)$$

Figure (5.1a) shows $N(t)$ i.e. the number of nuclei for each possible decay route for the $2^+ \rightarrow 0^+$ transition from states with different lifetimes (either by direct population of the 2^+ state or from feeding of higher states). To obtain the g-factor of the 2^+ state, a correction is implemented to account for these feeding contributions.

The method used here to correct for the feeding into the 2^+ state is given in equation (5.2) [32]. This takes into account factors such as the lifetime, the branching ratios and the angular correlations of each state. This is a rather comprehensive method to calculate the feeding correction for the precession in question. However, in the case of the measured stable Sn isotopes there are only two relevant feeding



a)



b)

Figure 5.1: a) $N(t)$ over the time in ps for each possible decay b) Level scheme including feeding percentages.

contributions into the 2^+ state, this specific case is given in (5.3) and is the feeding correction applied to this data:

$$\Delta\Phi_{obs}^i = \frac{\frac{dW_i}{d\theta} |_{\theta_\gamma} \Delta\Phi_i + \sum_{j,p} \eta_{j,i} \left[\prod_p b(I_m \rightarrow I_{m-1}) \right] \frac{dW_{ji}^p}{d\theta} |_{\theta_\gamma} \langle \Delta\Phi_{ji}^p \rangle}{\frac{dW_{obs}}{d\theta} |_{\theta_\gamma} \{1 + \sum_{j,p} \eta_{j,i} \left[\prod_p b(I_m \rightarrow I_{m-1}) \right]\}} \quad (5.2)$$

$$\Delta\Phi_{obs}^{2+} = \frac{\frac{dW_{2+}}{d\theta} |_{\theta_\gamma} \Delta\Phi_{2+} + \eta_{3,2} \frac{dW_{320}}{d\theta} |_{\theta_\gamma} \langle \Delta\Phi_{32} \rangle + \eta_{4,2} \frac{dW_{420}}{d\theta} |_{\theta_\gamma} \langle \Delta\Phi_{42} \rangle}{\frac{dW_{obs}}{d\theta} |_{\theta_\gamma} \{1 + \eta_{3,2} + \eta_{4,2}\}} \quad (5.3)$$

where $\frac{dW(\theta)}{d\theta}$ denotes the differential angular correlation for each transition at an angle θ_γ . $W_i(\theta)$ is the angular correlation of the directly populated state. W_{obs} is the angular correlation of the measured transition, and contains both the directly populated component and the feeding contribution. $W_{ji}^p(\theta)$ is for the angular correlation of the total cascade of the feeding to the state of interest and then the ground state, with cascades $4^+ \rightarrow 2^+ \rightarrow 0^+$ and $3^- \rightarrow 2^+ \rightarrow 0^+$ are taken from experimentally measured angular correlations. η_{ji} is the ratio of the directly populated state at level I_j to that of the level I_i . This ratio is proportional to the Coulomb excitation cross-section (for safe coulex) or can be experimentally measured from the gamma intensities. $n_{jm}^p(t)$ is obtained from the Bateman equations. The function $\left[\prod_p b(I_m \rightarrow I_{m-1}) \right]$ represents the product of the branching ratios along the cascade pathway p, but for $4^+ \rightarrow 2^+ \rightarrow 0^+$ and $3^- \rightarrow 2^+ \rightarrow 0^+$ the branching ratio for the Sn nuclei for these transitions is 1.

When there is feeding from the transition of a directly populated higher state into the state of interest (in this case the 2^+ state), the precession affected by the feeding component of higher states can be expressed by:

$$\langle \Delta\Phi_{ji}^p \rangle = \int_{t_{in}}^{t_{out}} \sum_{m=j}^i n_{jm}^p(t) d\phi_m(t), \quad (5.4)$$

where:

$$d\phi_m(t) = -g_m \frac{\mu_N}{\hbar} B_{tr}(t) dt \quad (5.5)$$

There are different possible ways to obtain the precession of the feeding component: one by using the experimentally measured precessions of the higher feeding states as:

$$\langle \Delta\Phi_{320} \rangle = -g(3^-) \frac{\mu_N}{\hbar} \int_{t_{in}}^{t_{out}} B_{tf}(t) e^{-t/\tau_3} dt - g(2^+) \frac{\mu_N}{\hbar} \int_{t_{in}}^{t_{out}} \frac{\lambda_3}{\lambda_2 - \lambda_3} (e^{-t/\tau_3} - e^{-t/\tau_2}) B_{tf}(t) dt \quad (5.6)$$

$$= \Delta\Phi(3^-) - g(2^+) \frac{\mu_N}{\hbar} \int_{t_{in}}^{t_{out}} \frac{\lambda_3}{\lambda_2 - \lambda_3} (e^{-t/\tau_3} - e^{-t/\tau_2}) B_{tf}(t) dt \quad (5.7)$$

$$\langle \Delta\Phi_{420} \rangle = -g(4^+) \frac{\mu_N}{\hbar} \int_{t_{in}}^{t_{out}} B_{tf}(t) e^{-t/\tau_4} dt = \Delta\Phi(4^+) \quad (5.8)$$

The 2^+ component from the 4^+ feeding is neglected, as its contribution is negligible. $\Delta\Phi(3^-)$ and $\Delta\Phi(4^+)$ can be used from experimentally measured precessions, or one can calculate the precession $\phi(\tau)$ for each case when $g=1$ (explained later in section 5.6) and assume values for $g(3^-)$ and $g(4^+)$. The values of η_{ij} can either be obtained by using the measurement of experimental intensities or from the Coulomb excitation cross-section. The methods explored in handling this feeding correction are explained in the results section.

5.2 The structure of the computer program

The program consisted of different sections which deal with calculating:

1. the stopping power
2. the kinematics - energies and angles after coulex
3. the coulex cross-section
4. the precession $\phi(\tau)$
5. the slope of $W(\theta)$ and $\frac{dW_{ij}}{d\theta}$

From the above sections, information such as the velocity in and out of the targets and the time inside the ferromagnet and were obtained in order to calculate for $\phi(\tau)$. Using this $\phi(\tau)$, and all the above information, the experimentally measured precessions and intensities, the feeding correction formula given later in equation(5.9) can be solved to give the g-factor of the purely populated 2^+ state.

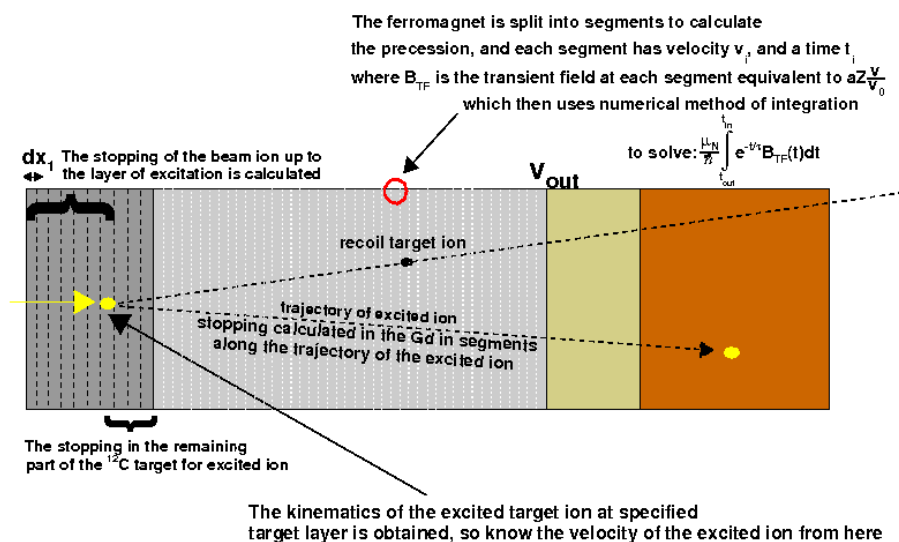


Figure 5.2: A graphical description of the calculations made in the program.

The program assumed a segmented target with 10 sublayers in the carbon, and would calculate the stopping power in each segment in the excitation target. The assumption made was that the Sn beam interacts with the excitation layer at

various depths in the carbon target, the program assumes this will occur in either of the 10 layers; at each layer the excitation kinematics are calculated as a function of the detected recoil target ion angle (which are also split into 10 detected angles), and the energy of the excited Sn ion, and its trajectory angle is established. Using the energy of the excited Sn ion, and by calculating the slowing down portion in the remaining part of the C target, the velocity into the ferromagnet is established. The slowing in the Gd layer is also calculated to extract the velocity out of the target, but accounts for various trajectories which are affected by the angle of the excited Sn ion. The flight path through the remaining C sublayers and then the Gd targets are established as a function of the angle, θ . The information for v_{in} , v_{out} , t_{in} and t_{out} are calculated, and hence one can also obtain the precession $\phi(\tau)$ from the program (via numerical integration). This is explained later in section 5.5 equations (5.44,5.45).

Either the Coulomb excitation cross-section or the measured intensities can be used for the η_{ij} ratio. With η_{ij} (from intensities or cross-sections) and $\phi(\tau)$ (from the program) established, the $g(2^+)$ with feeding correction can be obtained by rearranging equation (5.3) as:

$$g(2^+) = \frac{\frac{dW_{obs}}{d\theta}(1 + \eta_{32} + \eta_{42})\Delta\Phi_{2^+}^{obs} - \eta_{32}\frac{dW_{320}}{d\theta}\Delta\Phi_{32} - \eta_{42}\frac{dW_{420}}{d\theta}\Delta\Phi_{42}}{\frac{dW_{20}^{pure}}{d\theta}\phi_{20}^{pure} + \eta_{32}\frac{dW_{320}}{d\theta}\phi_{20}^{feeding\ from\ 3^-}}, \quad (5.9)$$

where the following equations are calculated by the program:

$$\phi_{20}^{pure} = -\frac{\mu_N}{\hbar} \int_{t_{in}}^{t_{out}} B_{tf}(t)e^{-t/\tau_2} dt, \quad (5.10)$$

$$\phi_{20}^{feeding\ from\ 3^-} = -\frac{\mu_N}{\hbar} \int_{t_{in}}^{t_{out}} \frac{\lambda_3}{\lambda_2 - \lambda_3} (e^{-t/\tau_3} - e^{-t/\tau_2}) B_{tf}(t) dt. \quad (5.11)$$

One can also obtain the feeding corrected g-factor by taking approximations for the g-factors of the 3^- and 4^+ states and the calculated values of $\phi(\tau)$ in the program.

5.3 Stopping power

The total stopping power, S_t in a material is given by equation (5.12), which is a function of the electronic stopping, S_e , and the nuclear stopping, S_n :

$$S_t = S_e + S_n \quad (5.12)$$

The nuclear stopping component is given by [45]:

$$S_n(E) = \frac{8.462 \cdot Z_1 \cdot Z_2 \cdot S_n(\epsilon)}{(M_1 + M_2)(Z_1^{0.23} + Z_2^{0.23})} \quad (5.13)$$

$$\epsilon = \frac{32.53 \cdot M_1 \cdot M_2(E/M_1)}{Z_1 \cdot Z_2(M_1 + M_2)(Z_1^{0.23} + Z_2^{0.23})} \quad (5.14)$$

where Z is the proton number, M is the mass number of the particle, and E is the energy of the particle. If $\epsilon \leq 30keV$ then:

$$S_n(\epsilon) = \frac{\ln(1 + 1.1383\epsilon)}{2(\epsilon + 0.01321\epsilon^{0.21226} + 0.19593\epsilon^{0.5})} \quad (5.15)$$

If $\epsilon \geq 30keV$ then:

$$S_n(\epsilon) = \frac{\ln(\epsilon)}{2\epsilon} \quad (5.16)$$

Electronic stopping is more complex as different cases are treated differently. Firstly the case of a nucleus with one proton, i.e. 1H is examined. [45]

$$\frac{1}{S_e} = \frac{1}{S_{low}} + \frac{1}{S_{high}} \quad (5.17)$$

$$S_{low} = A_1 E^{A_2} + A_3 E^{A_4} \quad (5.18)$$

$$S_{high} = \frac{A_5 \ln(\frac{A_7}{E} + A_8 E)}{E^{A_6}} \quad (5.19)$$

For the case of 2He (not necessary for this particular case but included for completeness):

$$\begin{aligned}
S_e &= \frac{S_e^{ref}(\gamma Z_1)^2}{(Z_1^{ref})^2} \\
\gamma^2 &= 1 - \exp(-0.2865 - 0.1266B + 0.001429B^2 - \\
&\quad 0.02402B^3 + 0.01135B^4 - 0.001475B^5)C^2 \\
B &= \ln\left(\frac{E}{M_1}\right) \\
C &= 1 + (0.007 + 0.00005Z_2)\exp(-(7.6 - \ln(\frac{E}{M_1}))^2)
\end{aligned}$$

For the cases of $Z > 2$: Same as in the case for ${}^2\text{He}$ except:

$$\gamma = q + 0.5(1 - q)\left(\frac{v_0}{v_f}\right)^2 \ln\left(1 + \left(\frac{4\Lambda v_f}{1.919}\right)^2\right)C \quad (5.20)$$

$$q = 1 - \exp(0.803y_r^{0.3} - 1.3167y_r^{0.6} - 0.38157y_r - 0.008983y_r^2) \quad (5.21)$$

$$C = 1 + \frac{1}{Z^2}(0.18 + 0.0015Z_2)\exp(-(7.6 - \ln(\frac{E}{M_1}))^2) \quad (5.22)$$

$$\Lambda = \frac{a_0(1 - q)^{1/3}}{Z_1^{1/3}(1 - (1 - q)/7)} \quad (5.23)$$

$$(5.24)$$

where v_f is the Fermi velocity, v_0 is the Bohr velocity and q is the degree of ionization. Λ is the ion screening length.

The effective ion velocity y_r is given in terms of the ion velocity $v_r = \sqrt{(2E/M_1)}$.

For $v_1 > v_f$

$$y_r = \frac{v_1}{v_0 Z_1^{2/3}} \left(1 + \frac{v_f^2}{5v_1^2}\right) \quad (5.25)$$

For $v_1 < v_f$

$$y_r = \frac{0.75v_f}{v_0 Z_1^{2/3}} \left(1 + \frac{2v_1^2}{3v_f^2} - \frac{1}{15}\left(\frac{v_1}{v_f}\right)^4\right) \quad (5.26)$$

For the case of a Sn nucleus Λ is given as: $\Lambda = \frac{0.43}{Z_1^{1/3}}$.

Using the simulation program, SRIM [46] - which calculates the stopping powers - the results from the stopping header file written for the program calculating the feeding corrections can be compared, and verified. SRIM gives the results for the stopping power for ${}^{116}\text{Sn}$ on ${}^{157}\text{Gd}$ from the program written by J.P. Biersack and

J.F. Ziegler, and stopping.h denotes the stopping component of the feeding program. The table (5.1) shows the results for the electronic stopping power ($\frac{dE}{dX_e}$), the nuclear stopping power ($\frac{dE}{dX_n}$) and the total stopping power ($\frac{dE}{dX_t}$), these are expressed in the units of MeV/ μm .

Energy (MeV)	SRIM: $\frac{dE}{dX_e}$	$\frac{dE}{dX_n}$	$\frac{dE}{dX_t}$	stopping.h: $\frac{dE}{dX_e}$	$\frac{dE}{dX_n}$	$\frac{dE}{dX_t}$
150	18.74	0.104	18.84	20.10	0.102	20.20
200	20.78	0.082	20.86	22.10	0.081	22.18
225	21.52	0.074	21.59	22.78	0.073	22.85
250	22.34	0.068	22.41	23.32	0.067	23.34
275	23.06	0.063	23.06	23.74	0.054	23.76
300	24.49	0.059	23.55	24.08	0.058	24.09
325	23.89	0.055	23.95	24.33	0.062	24.35
350	24.21	0.052	24.26	24.53	0.067	24.55

Table 5.1: The stopping powers at different energies for ^{116}Sn on ^{157}Gd , when compared to the stopping tables calculated in SRIM in units of MeV/ μm .

If the energy going into a Gd target of 10.8 mg/cm² is 250 MeV, stopping.h used in the feeding program gives the average energy out of the ferromagnetic layer to be approximately 27 MeV, whereas SRIM gives the average energy out to be 28 MeV. The energy into the ferromagnetic layer was chosen as 250 MeV in this example as this is the average energy of the excited projectile in the carbon layer after excitation. With these values, there is a fairly good agreement between SRIM and the stopping.h file.

5.4 Kinematics

When a Coulomb excitation reaction occurs, the target recoil and the excited projectile are scattered at certain angles. The target recoil is detected in the Silicon particle detector array, which due to its geometry, accepts recoil target ions at a certain angular range. From this lab recoil angle the scattered angle of the excited projectile in both the lab and centre of mass frames can also be extracted.

One can think of each Si detector as consisting of 10x10 pixels as shown in figure (5.3), symmetrical about the x axis. Each pixel has an angle of $d\theta[i, j]$ and a solid

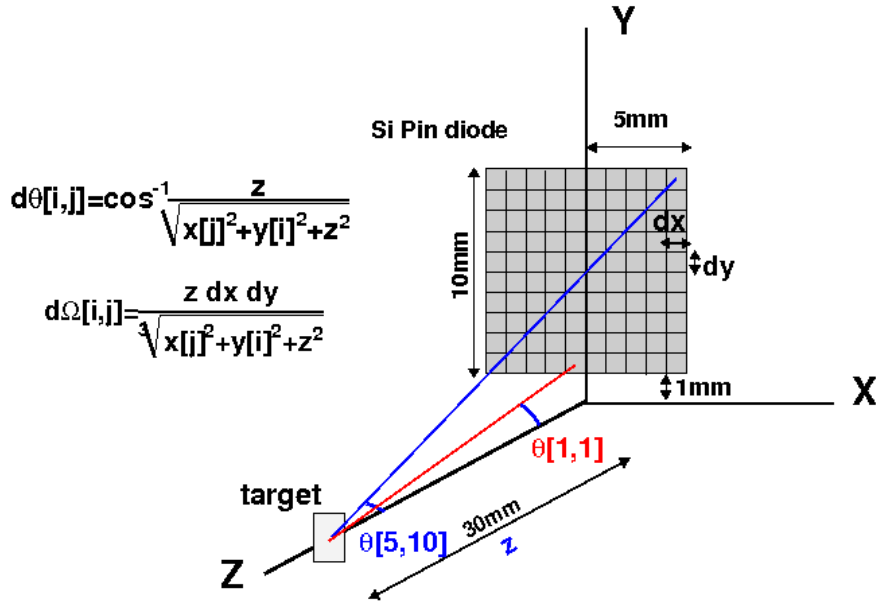


Figure 5.3: Obtaining the angle of the recoil target particle detected in the Si detector.

angle of $d\Omega[i, j]$, these are given by:

$$d\theta[i, j] = \cos^{-1} \frac{z}{\sqrt{x[i]^2 + y[j]^2 + z^2}} \quad (5.27)$$

$$d\Omega[i, j] = \frac{z dx dy}{\sqrt{x[i]^2 + y[j]^2 + z^2}} \quad (5.28)$$

where i and j are the array numbers for each pixel on the x and y axis, $y[j]$ represents the height of the Si detector for each pixel in the y -direction and $x[i]$ the width of the detector for each pixel in the x -direction, both with respect to the beamline, and the distance z is from the target to the detector. To obtain the angle for each horizontal strip the angles are normalized to the solid angles, the array i runs up to 5 instead of 10 because of the symmetry about the x axis and yields the same result:

$$\theta[j] = \frac{\sum_{i=1}^5 d\theta[i, j] \cdot d\Omega[i, j]}{\sum_{i=1}^5 d\Omega[i, j]} \quad (5.29)$$

Calculating the angles given from the geometry of the particle detector gives the lab frame angle of the detected recoil particle, this then needs to be converted into the centre of mass frame before obtaining the angles of the scattered excited projectile:

$$\theta_{rec}^{cm}[i] = \theta_{rec}^{lab}[i] + \sin^{-1}(\tau \cdot \sin(\theta_{rec}^{lab}[i])) \quad (5.30)$$

$$\theta_{proj}^{cm}[i] = \pi - \theta_{rec}^{cm}[i] \quad (5.31)$$

$$\theta_{proj}^{lab}[i] = \tan^{-1}\left(\frac{\sin(\theta_{proj}^{cm}[i])}{\cos(\theta_{proj}^{cm}[i]) + \gamma}\right) \quad (5.32)$$

where *rec* represents the recoil target ion, *proj* represents the excited projectile and *cm,lab* are the frame of reference. Also:

$$\tau = \sqrt{\left(\frac{E_{beam}}{E_i}\right)} \quad (5.33)$$

$$E_i = E_{beam} - Q\left(\frac{M_{proj} + M_{rec}}{M_{proj}}\right) \quad (5.34)$$

$$\gamma = \frac{M_{proj}}{M_{rec}} \quad (5.35)$$

$$(5.36)$$

E_{beam} is the beam energy at the point of interaction in the excitation target layer and Q is the energy of excitation.

The energy of the excited projectile and recoil target ion can be given as follows [41]:

$$T_{rec}^{1/2} = \frac{(M_{proj}M_{rec})^{1/2}\cos(\theta_{rec}^{lab}(i)) + \{M_{proj}M_{rec}E_{beam}\cos^2(\theta_{rec}^{lab}(i)) + (M_{proj} + M_{rec})[M_{rec}Q + (M_{rec} - M_{proj})E_{beam}]\}^{1/2}}{M_{rec} + M_{proj}}$$

$$T_{proj} = -Q - T_{rec} + E_{beam}$$

By calculating the stopping in each sublayer of the carbon target before excitation occurs, and by using the kinematics equations one can determine the energy of the excited particle after Coulomb excitation. With these energies the velocity inside the ferromagnet can be obtained from calculating the stopping of the excited ion in the remaining C layer. The velocity out of the ferromagnet can be obtained from the energy out of the ferromagnet obtained from shopping in the Gd.

To run the program, the angular range as defined by the Si detector geometry is split up into 10 angles for calculation. Using equation (5.30) to calculate the angle

of the recoil target ion for a rectangular detector (the inner and outer Si detectors are treated separately), the angles of the excited projectile, as well as the energy of the projectile and recoil after excitation, can be obtained.

When comparing the feeding program with the Coulex code [49], the angles and energies are in good agreement with each other. The Coulex code used the lab angle of the projectile as the input angle for its calculations which is why in both programs this value is identical. The energy of the recoil target ion and the excited projectile are given in units of MeV and the angles are in degrees.

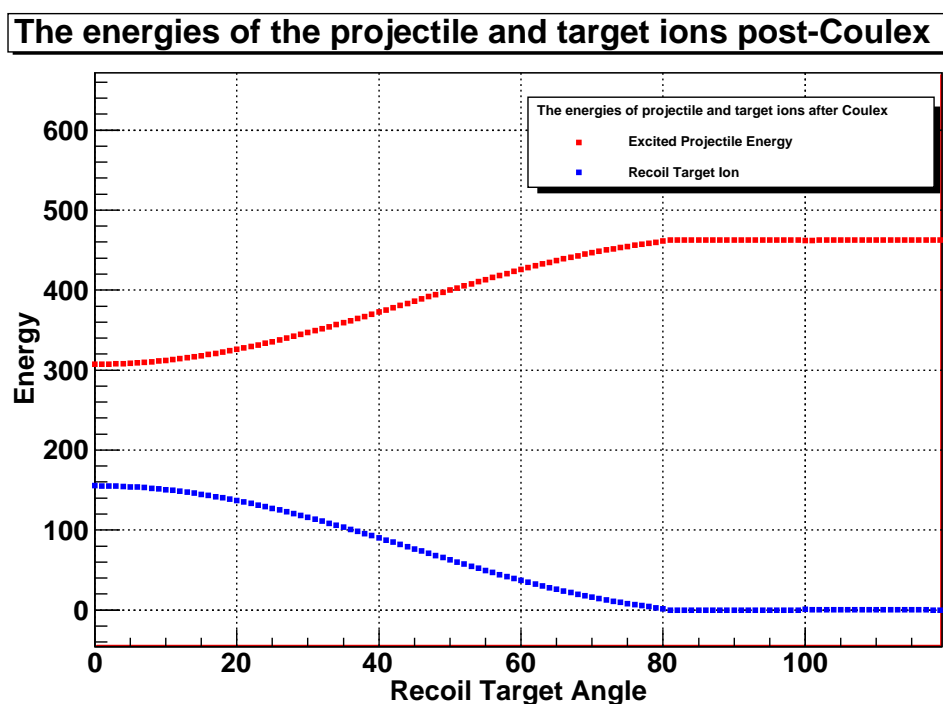


Figure 5.4: The energies of the recoiling target ion and the excited projectile after Coulex as a function of the recoil lab angle.

5.5 Coulomb excitation cross sections

The differential Coulomb excitation cross section in the lab frame is given by equation (5.37), where one can see that the differential cross-section is a function of the particle velocity v , Z , the $B(E2;0^+ \rightarrow 2^+)$, and the centre of mass angle θ . From the information obtained from kinematics and previously known values such as the $B(E2;0^+ \rightarrow 2^+)$ values; the cross-section of Coulomb excitation can be calculated. If factors such as slowing down in the target via stopping, and the kinematics at different recoil angles, and the solid angle of the particle detector are taken into account, then the cross-section can be obtained. Currently this can be calculated from programs such as TRANSI, MuSTanG and the Coulex code, but it gives the feeding correction program more control if it is incorporated directly into the code. Also, one should note that equation (5.37) is written for a case in inverse kinematics, for standard kinematics Z_2 should be replaced by Z_1 [30].

$$d\sigma_{E\lambda} = \left(\frac{Z_2 e}{\hbar v}\right)^2 a^{-\lambda+2} B(E\lambda) df_{E\lambda}(\theta, \xi) \quad (5.37)$$

where $a = \frac{Z_1 Z_2 e^2}{m_0 v^2}$.

$$df_{E\lambda}(\theta, \xi) = \frac{4\pi^2}{(2\lambda + 1)^3} \sum_{\mu} |Y_{\lambda\mu}(\frac{\pi}{2}, 0)|^2 |I_{\lambda\mu}(\theta, \xi)|^2 \sin^{-4} \frac{\theta}{2} d\Omega \quad (5.38)$$

where:

$$Y_{\lambda\mu}(\frac{\pi}{2}, 0) = \left(\frac{2\lambda + 1}{4\pi}\right)^{1/2} \frac{[(\lambda - \mu)!(\lambda + \mu)!]^{1/2}}{(\lambda - \mu)!(\lambda + \mu)!} (-1)^{\frac{\lambda+\mu}{2}} \text{ if } (\lambda + \mu) = \text{even} \quad (5.39)$$

$$= 0 \text{ if } (\lambda + \mu) = \text{odd} \quad (5.40)$$

The orbital integrals are given by:

$$I_{\lambda\mu}(\theta, \xi) = \int_{-inf}^{+inf} e^{i\xi(\epsilon \sinh(\omega) + \omega)} \frac{[\cosh(\omega) + \epsilon + i(\epsilon^2 - 1)^{1/2} \sinh(\omega)]^{\mu} d\omega}{[\epsilon \cosh(\omega) + 1]^{\lambda + \mu}} \quad (5.41)$$

where θ is the deflection angle and:

$$\xi = \frac{Z_1 Z_2 e^2}{\hbar v} \frac{\Delta E}{2E} \quad (5.42)$$

$$\epsilon = \frac{1}{\sin(\frac{\theta}{2})} \quad (5.43)$$

The integral of equation (5.41), was solved or estimated by a numerical method of integration. In this case the orbital integrals were solved using the trapezium method, shown in equations (5.44) and (5.45).

$$\int_{x_0}^{x_1} f(x)dx \approx \frac{\Delta x}{2} \sum_{i=0}^{n-1} (f(x_0 + i\Delta x) + f(x_0 + (i+1)\Delta x)) \quad (5.44)$$

$$\begin{aligned} &= \frac{\Delta x}{2} [f(x_0) + 2f(x_0 + \Delta x) + 2f(x_0 + 2\Delta x) + \\ &\dots + 2f(x_0 + (n-1)\Delta x) + f(x_1)] \quad (5.45) \end{aligned}$$

However, for the population of the 4^+ state this occurs via a second order excitation from $0^+ \rightarrow 2^+$ and then $2^+ \rightarrow 4^+$. In order to obtain the Coulex cross-section for this, the double excitation needs to be treated differently [30]. Again, like with the first order Coulomb excitation cross-section, equation (5.46) is for inverse kinematics in this case [47].

$$d\sigma_{E2,E2} = \left(\frac{Z_2}{\hbar v}\right)^4 a^{-6} B(E2 : 0^+ \rightarrow 2^+) B(E2 : 2^+ \rightarrow 4^+) df_{E\lambda}(\xi_1, \xi_2 J\theta) \quad (5.46)$$

$$df_{E\lambda}(\xi_1, \xi_2 J\theta) = \frac{16\pi^4}{5^4} \sum_{\kappa} \{ \alpha_{J\kappa}^2(22\xi_1, \xi_2\theta) + \beta_{J\kappa}^2(22\xi_1, \xi_2\theta) \} \sin^{-4} \frac{1}{2} \theta d\Omega \quad (5.47)$$

where

$$\begin{aligned} \alpha_{J\kappa}(22\xi_1, \xi_2\theta) &= \sum_{\mu_1 \mu_2} \begin{pmatrix} 2 & 2 & J \\ \mu_1 & \mu_2 & \kappa \end{pmatrix} Y_{2\mu_1} \left(\frac{1}{2}\pi, 0 \right) Y_{2\mu_2} \left(\frac{1}{2}\pi, 0 \right) I_{2\mu_1}(\theta\xi_1) I_{2\mu_2}(\theta\xi_2) \\ \beta_{J\kappa}(22\xi_1, \xi_2\theta) &= \sum_{\mu_1 \mu_2} \begin{pmatrix} 2 & 2 & J \\ \mu_1 & \mu_2 & \kappa \end{pmatrix} Y_{2\mu_1} \left(\frac{1}{2}\pi, 0 \right) Y_{2\mu_2} \left(\frac{1}{2}\pi, 0 \right) \times \dots \\ &\dots \frac{1}{\pi} \mathcal{P} \int_{-\infty}^{\infty} \frac{d\xi'}{\xi'} I_{2\mu_1}(\theta\xi_1 + \xi') I_{2\mu_2}(\theta\xi_2 - \xi') \end{aligned}$$

where \mathcal{P} is the Cauchy Principal value of the integral, which can be expressed as [48]:

$$I = \mathcal{P} \int_{-\infty}^{\infty} \frac{f(x)}{x} dx = i\pi f(0) \quad (5.48)$$

To make the transformation to the lab frame the conversion is as follows:

$$\sigma(\theta_{cm}) = \sigma(\theta_{lab}) \frac{d\Omega_{lab}}{d\Omega_{cm}} \quad (5.49)$$

$$\frac{d\Omega_{lab}}{d\Omega_{cm}} = \left(\frac{\sin(\theta_{cm})}{\sin(\theta_{lab})} \right)^2 / \text{abs}(\cos(\theta_{cm} - \theta_{lab})) \quad (5.50)$$

For Coulomb excitation in standard kinematics, one should use the centre of mass and lab angles of the target recoil, but in the case of inverse kinematics, it is the scattered projectile which should be used which is what the program uses.

To obtain the total excitation cross-section one needs to obtain the solid angle of the Silicon particle detectors.

$$\sigma = d\Omega \cdot \frac{d\sigma_{lab}}{d\Omega} \quad (5.51)$$

For a square Silicon pin diode the solid angle is obtained by splitting the detector segments and summing them. So the solid angle for each segment is given as:

$$d\Omega = \frac{z dx dy}{\sqrt{(x^2 + y^2 + z^2)}} \quad (5.52)$$

The most complex part of calculating the Coulomb excitation cross-section are the calculations of the orbital integrals given in equation (5.41). To test the program's ability in calculating these values via a numerical method of integration, the results were compared to the tables of orbital integrals given in the review paper by Bohr and Adler [30]. The comparison between the results from the program and the published tables are shown in table (5.2) and are shown to agree.

To check the cross-section, the Coulex code [49] was used to check the results of both the centre of mass and the lab frame differential cross-sections. The assumption here is that a projectile with an energy of 464 MeV impinges on carbon, with set centre of mass angles were used in the comparison with the differential cross-section results in the feeding program with the Coulex code.

$\lambda \cdot \mu$	$I_{\lambda\mu}$ program	$I_{\lambda\mu}$ table
2,2	0.335	0.335
2,0	0.387	0.387
2,-2	0.437	0.437
3,3	0.159	0.159
3,1	0.177	0.177
3,-1	0.195	0.195
3,-3	0.212	0.212

Table 5.2: The comparison between the orbital integrals given by the program and from the table of orbital integrals [30] for the case of $\theta=160^\circ$ and $\xi=0.4$ for an E2 transition.

θ_{part}^{cm}	Prog.: $d\sigma_{cm}^{2+}$	Coulex: $d\sigma_{cm}^{2+}$	Prog.: $d\sigma_{cm}^{3-}$	Coulex: $d\sigma_{cm}^{3-}$	Prog.: $d\sigma_{cm}^{4+}$	Coulex: $d\sigma_{cm}^{4+}$
20	6.58	6.72	0.06	0.05	0.000	5.2×10^{-6}
40	9.73	10.15	0.44	0.42	9.0×10^{-4}	3.1×10^{-4}
60	8.29	8.59	0.69	0.67	3.9×10^{-3}	1.2×10^{-3}
80	6.75	6.90	0.77	0.75	7.0×10^{-3}	2.5×10^{-3}
100	5.60	5.63	0.75	0.72	9.0×10^{-3}	3.8×10^{-3}
120	4.81	4.75	0.70	0.66	9.3×10^{-3}	4.9×10^{-3}
140	4.29	4.17	0.63	0.60	8.6×10^{-3}	5.9×10^{-3}
160	3.99	3.85	0.59	0.55	7.8×10^{-3}	6.6×10^{-3}
180	3.90	3.75	0.57	0.53	7.5×10^{-3}	6.7×10^{-3}

Table 5.3: The comparison in the centre of mass differential cross-section values between the feeding program and the Coulex Code. The units of the differential cross-section are mb/str and θ_{cm} is in degrees

θ_{part}^{cm}	Prog.: $d\sigma_{lab}^{2+}$	Coulex: $d\sigma_{lab}^{2+}$	Prog.: $d\sigma_{lab}^{3-}$	Coulex: $d\sigma_{lab}^{3-}$	θ_{part}^{cm}	Prog.: $d\sigma_{lab}^{4+}$	Coulex: $d\sigma_{lab}^{4+}$
100	3293	3263	665	513	113	2.72	1.42
110	2074	2113	404	389	125	1.55	0.93
120	1085	1099	171	165	133	1.17	0.78
130	672	676	102	99	140	0.96	0.69
140	487	486	73	70	146	0.83	0.64
150	386	383	58	55	152	0.74	0.61
160	331	327	49	46	157	0.68	0.58
170	302	297	44	42	162	0.63	0.57
180	293	288	43	41	166	0.60	0.55
-	-	-	-	-	171	0.58	0.55
-	-	-	-	-	176	0.57	0.54
-	-	-	-	-	180	0.56	0.54

Table 5.4: The comparison in the lab frame differential cross-section values between the feeding program and the Coulex Code. The units of the differential cross-section in mb/str.

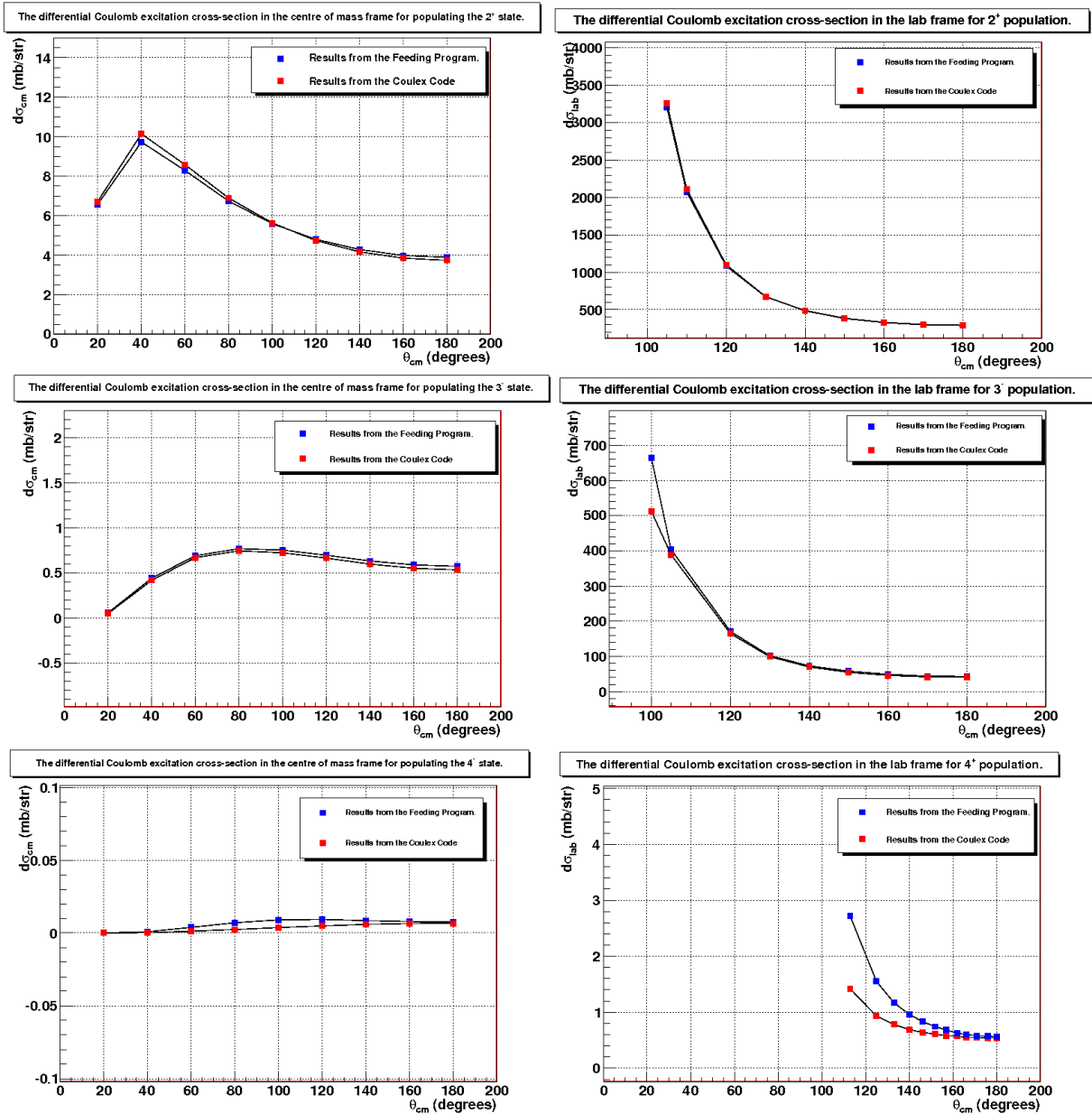


Figure 5.5: The differential cross-section in the centre of mass frame and the lab frame as calculated from this program and from the Coulex code.

There is a general agreement between the two programs. However, the Coulex code can only give the cross-section for one energy and one angle case, it is useful to test out for a specific case, but for an entire experimental set up one needs to take into account the stopping in the target and the possibility for excitation in different parts of the target. The examples shown here for the comparison between the Coulex code and the feeding program used the excitation ^{116}Sn at 464MeV on a carbon target.

For calculation purposes, the carbon target is segmented into 10 layers, the incident projectile is assumed to undergo Coulomb excitation in any of these layers; in addition to this there are also 10 detected recoil angles in the Si detector. This yields the differential cross-section for each layer and angle, this is then summed and averaged over 100. The total cross-section is then obtained when this averaged differential cross-section (lab frame) includes the solid angle.

5.6 Calculated Precessions

The component of $\phi(\tau_i)$ is the value $\Delta\Phi$ would have when $g=1$. It is presented as the equation:

$$\phi(\tau_i) = -\frac{\mu_N}{\hbar} \int_{t_{in}}^{t_{out}} e^{-t/\tau_i} B_{tr}(t) dt \quad (5.53)$$

where $B_{tf}(v_{ion}(t))$ is the time dependent magnitude of the transient field that varies with the velocity of the ion as it traverses the target. This function, equation (5.53), also depends on the lifetime of the excited state, as well as the time required to traverse the ferromagnetic layer. In order to calculate $\phi(\tau_i)$, the velocity into the ferromagnetic layer is obtained from the stopping of the excited projectile as it traverses the carbon layer. The velocity out of the ferromagnetic target is obtained from the stopping inside the ferromagnetic layer, there is no excitation to consider so only the energy loss is calculated. The header file calculates v_{in} and v_{out} as well as t_{in} and t_{out} . t_{in} is the time the projectile takes to traverse the carbon layer until its exit into the Gd and also the time on exiting the carbon target marks t_{in} as it enters the ferromagnet; this is taken for each sub-layer in the carbon, and also for each recoil angle. t_{out} takes the time of t_{in} into account, plus the time it takes for the excited ion to traverse the ferromagnetic layer. Each velocity and time component is calculated individually as a function of the carbon sub-layer where excitation occurs and the detected recoil particle angle. The mean of these values is returned to the main program for use in calculating $\phi(\tau_i)$, which is obtained via numerical integration. The transient field $B_{tf}(v_{ion}(t))$ is also a function of time, as the velocity will change as the excited projectile slows down in the target. At each velocity, the transient field can be expressed as equation (5.54) which assumes the linear parametrization [12]:

$$B^{LIN} = a \cdot Z \cdot \frac{v}{v_0} \quad (5.54)$$

where a is the field parameter, which in the case of a gadolinium target is 17 T. Z is the charge of the projectile and v is the velocity in units of the Bohr velocity. Equation (5.54) gives the transient field at each velocity, and a function of time in the integration. The numerical methods of integration are employed as given in equations (5.44) and (5.45). The transient field attenuation, G_{beam} also should be included when obtaining $\phi(\tau)$ as:

$$B_{TF} = B^{LIN} \cdot G_{beam} \quad (5.55)$$

G_{beam} is a function of the energy loss $\frac{dE}{dx}$ of a beam of ions in a ferromagnetic layer. Figure (5.6) shows the attenuation G against the stopping power for a Gd host. In order to obtain the parameter G_{beam} , the average stopping inside the Gd layer needs to be known. By calculating the approximate average energy inside the Gd host, which is approximately 135MeV, and yields a stopping power of 19 MeV/ μm . Also, to calculate G_{beam} from figure (5.6) $\frac{v}{Zv_0}$ needs to be known too, and for an average velocity of approximately 7 v_0 and hence yields $\frac{v}{Zv_0}$ 0.14. Using the figure (5.6) this gives $G_{beam}=0.55(5)$.

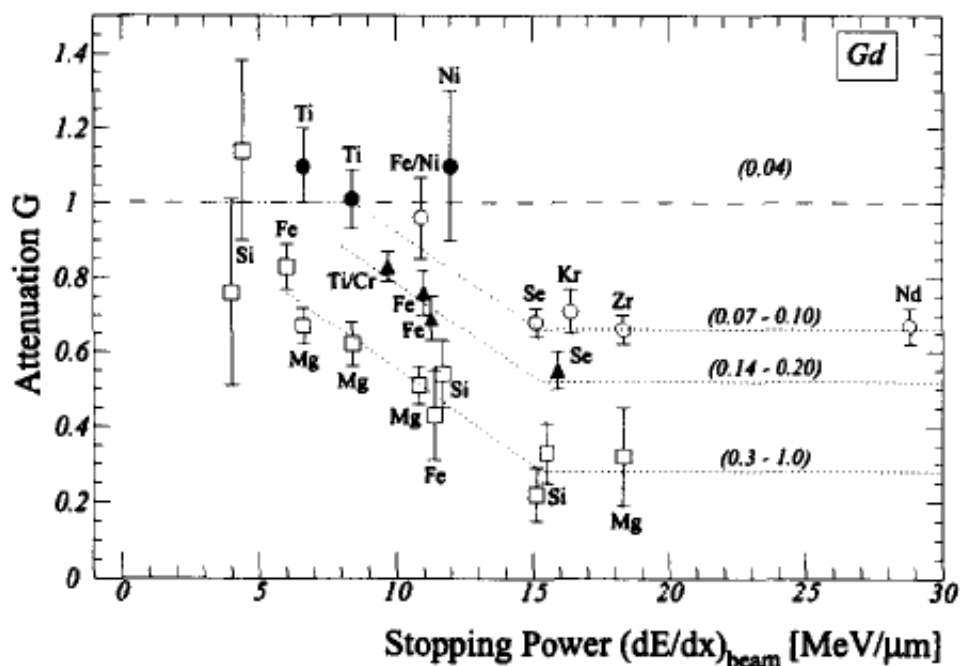


Figure 5.6: Transient field attenuations of various probe ions in Gd hosts vs. the stopping power of the beam ions, the different regions are characterized by $\frac{v}{Zv_0}$ [12].

The values of $\phi(\tau_i)$ for each nucleus directly populated 2^+ were compared using the TRANSI program for $g=1$. The results in the table assume that $G_{beam}=1$, for comparison purposes with TRANSI, which does not include G_{beam} in the program.

Nucleus	Transition	Si detector	Feeding Program: $\phi(\tau)$	TRANSI: $\phi(\tau)$
^{112}Sn	$2^+ \rightarrow 0^+$	inner	-129.4mrad	-128.5mrad
^{112}Sn	$2^+ \rightarrow 0^+$	outer	-133.5mrad	-135.3mrad
^{114}Sn	$2^+ \rightarrow 0^+$	inner	-124.3mrad	-123.3mrad
^{114}Sn	$2^+ \rightarrow 0^+$	outer	-128.3mrad	-129.9mrad
^{116}Sn	$2^+ \rightarrow 0^+$	inner	-132.7mrad	-132.6mrad
^{116}Sn	$2^+ \rightarrow 0^+$	outer	-136.7mrad	-139.0mrad
^{122}Sn	$2^+ \rightarrow 0^+$	inner	-174.9mrad	-178.7mrad
^{122}Sn	$2^+ \rightarrow 0^+$	outer	-178.1mrad	-183.8mrad
^{124}Sn	$2^+ \rightarrow 0^+$	inner	-172.9mrad	-178.2mrad
^{124}Sn	$2^+ \rightarrow 0^+$	outer	-175.6mrad	-182.1mrad
^{112}Sn	$3^- \rightarrow 2^+$	inner	-76.6mrad	-72.3mrad
^{112}Sn	$3^- \rightarrow 2^+$	outer	-80.2mrad	-78.1mrad
^{114}Sn	$3^- \rightarrow 2^+$	inner	-114.3mrad	-111.6mrad
^{114}Sn	$3^- \rightarrow 2^+$	outer	-118.5mrad	-118.3mrad
^{116}Sn	$3^- \rightarrow 2^+$	inner	-109.0mrad	-106.3mrad
^{116}Sn	$3^- \rightarrow 2^+$	outer	-113.0mrad	-112.7mrad
^{122}Sn	$3^- \rightarrow 2^+$	inner	-29.6mrad	-26.7mrad
^{122}Sn	$3^- \rightarrow 2^+$	outer	-31.1mrad	-29.2mrad
^{124}Sn	$3^- \rightarrow 2^+$	inner	-20.2mrad	-18.1mrad
^{124}Sn	$3^- \rightarrow 2^+$	outer	-21.3mrad	-19.9mrad
^{112}Sn	$4^+ \rightarrow 2^+$	inner	-219.9mrad	-229.2mrad
^{112}Sn	$4^+ \rightarrow 2^+$	outer	-221.8mrad	-232.0mrad
^{114}Sn	$4^+ \rightarrow 2^+$	inner	-228.0mrad	-238.6mrad
^{114}Sn	$4^+ \rightarrow 2^+$	outer	-229.6mrad	-240.7mrad
^{116}Sn	$4^+ \rightarrow 2^+$	inner	* -95.6mrad	-92.3mrad
^{116}Sn	$4^+ \rightarrow 2^+$	outer	* -99.5mrad	-98.4mrad
^{122}Sn	$4^+ \rightarrow 2^+$	inner	-201.4mrad	-207.26mrad
^{122}Sn	$4^+ \rightarrow 2^+$	outer	-204.0mrad	-211.1mrad
^{124}Sn	$4^+ \rightarrow 2^+$	inner	-203.5mrad	-211.2mrad
^{124}Sn	$4^+ \rightarrow 2^+$	outer	-205.3mrad	-213.6mrad

Table 5.5: The precessions for $g=1$ for all Sn nuclei in the feeding program and in TRANSI, for direct population. (* The lifetime for the state of 4^+ in ^{116}Sn used here is the NNDC value of 0.4ps)

Chapter 6

g-factor results including feeding corrections

There are various methods to calculate the feeding correction in the 2^+ g-factors using the equation (5.9), these are:

1. Using the calculated cross-sections for each populated state for the η_{ij} component in equation (5.9) along with the experimentally measured $\Delta\Phi(3^-), \Delta\Phi(4^+)$
2. Using the measured intensities for η_{ij} with experimentally measured $\Delta\Phi(3^-), \Delta\Phi(4^+)$
3. Using measured intensities for η_{ij} , with $\phi(\tau_{3^-})$ and $\phi(\tau_{4^+})$ from calculated values in the code, and $g(3^-), g(4^+)$ are taken as a range, based on the weighted means of the measured g-factors for cases with high statistics.

For method 1, the values η_{ij} use the Coulex cross-section, and method 2 reads in the intensities into the program, and then obtains η_{ij} from these. The comparison between the two ratios are given in table (6.1). One can see that there is a significant difference between the Coulex cross-section ratios and the intensity ratios; the intensity ratios show a higher proportion of the higher states being populated than given by the calculations, the intensities and the cross sections should be proportional however one needs to consider is this experiment did not operate in safe coulex.

Nucleus	Si	I ₂₊	I ₃₋	I ₄₊	$\frac{I_{3-}}{I_{2+}^{pure}}$	$\frac{I_{4+}}{I_{2+}^{pure}}$	σ_{2+} (mb)	σ_{3-} (mb)	σ_{4+} (mb)	$\frac{\sigma_{3-}}{\sigma_{2+}}$ (mb)	$\frac{\sigma_{4+}}{\sigma_{2+}}$ (mb)
¹¹² Sn	in	3180(90)	670(30)	379(10)	0.31(2)	0.18(1)	57.9	8.6	0.04	0.15	0.0007
¹¹² Sn	out	12311(300)	2357(70)	955(20)	0.26(1)	0.11(0)	153.4	23.7	0.09	0.15	0.0006
¹¹⁴ Sn	in	10810(240)	2953(100)	1565(15)	0.47(3)	0.25(1)	53.6	7.6	0.04	0.14	0.0007
¹¹⁴ Sn	out	7493(200)	1651(70)	924(20)	0.34(2)	0.19(1)	141.0	20.2	0.10	0.14	0.0007
¹¹⁶ Sn	in	8924(230)	2874(80)	198(3)	0.49(2)	0.03(0)	51.3	8.9	0.07	0.17	0.0014
¹¹⁶ Sn	out	5898(160)	1533(50)	92(3)	0.36(2)	0.02(0)	134.3	23.5	0.17	0.17	0.0013
¹²² Sn	in	7822(140)	1307(10)	1003(20)	0.24(1)	0.18(0)	58	2	0.07	0.03	0.0012
¹²² Sn	out	3462(70)	231(10)	273(20)	0.08(0)	0.09(0)	146	6	0.15	0.04	0.0010
¹²⁴ Sn	in	2488(60)	324(10)	196(10)	0.17(4)	0.10(1)	55	5	0.03	0.09	0.0005
¹²⁴ Sn	out	8886(200)	459(20)	228(10)	0.06(0)	0.03(1)	138	14	0.08	0.1	0.0006

Table 6.1: The comparison between the intensities and the total cross-sections for each transition. Where $I_{2+}^{pure} = I_{2+} - I_{3-} - I_{4+}$.

Nucleus	E_{CB}	E_{beam}	ΔE
^{112}Sn	431 MeV	448MeV	17MeV
^{114}Sn	436 MeV	456MeV	20MeV
^{116}Sn	442 MeV	464MeV	22MeV
^{122}Sn	456 MeV	464MeV	8MeV
^{124}Sn	464 MeV	471MeV	7MeV

Table 6.2: The Coulomb barrier heights for $^{112,114,116,122,124}\text{Sn}$ beams on a ^{12}C target compared to the beam energies used in the experiment.

Table (6.2) shows the beam energies and Coulomb barrier energies, so one can see that the energies of the beams used in this set up were above the Coulomb barrier, so the Sn nuclei were excited via unsafe Coulex, so it is likely other excitations may have occurred in this reaction, hence the ratio of the experimental intensities are larger than the ratio of the calculated Coulex cross-section, and therefore method 1 is an unrealistic assumption to use in the calculations. The g-factor results from this method using the cross-section are included in Appendix B, but really serve just as a curiosity.

The precessions, $\phi(\tau)$ are calculated by the program and are given in table (6.3). These are used for the directly populated $2^+ \rightarrow 0^+$ precessions, and the precessions of the $2^+ \rightarrow 0^+$ affected by higher feeding states. Also for the final feeding correction method, where $g(3^-)$ and $g(4^+)$ are approximated, these values in table (6.3) are used in the g-factor correction. The input values of the programs are given by tables (B.1,B.2).

Nuc.	Si det.	ϕ_{20}^{pure} (mrad)	ϕ_{32} (mrad)	ϕ_{42} (mrad)	$\phi_{20}^{feed. 3^-}$ (mrad)	$\phi_{20}^{feed. 4^+}$ (mrad)
^{112}Sn	in.	-71.2(6.5)	-42.1(3.8)	-120.9(11.0)	-55.8(5.1)	-7.8(0.7)
^{112}Sn	out.	-73.4(6.7)	-44.1(4.0)	-122.0(11.1)	-56.4(5.1)	-7.6(0.7)
^{114}Sn	in.	-68.4(6.2)	-62.9(5.7)	-125.4(11.4)	-41.2(3.9)	-4.6(0.4)
^{114}Sn	out.	-70.5(6.4)	-65.2(5.9)	-126.3(11.5)	-41.3(3.9)	-4.5(0.4)
^{116}Sn	in.	-73.0(6.6)	-59.9(5.4)	*-119.2(10.8)	-46.7(4.2)	-9.2(0.8)
^{116}Sn	out.	-75.2(6.8)	-62.2(5.6)	*-120.4(10.9)	-46.8(4.3)	-9.0(0.8)
^{122}Sn	in.	-96.2(8.7)	-16.3(1.5)	-110.7(10.1)	-88.9(8.1)	-18.9(1.7)
^{122}Sn	out.	-98.0(8.9)	-17.1(1.6)	-112.2(10.2)	-90.0(8.2)	-18.4(1.7)
^{124}Sn	in.	-95.1(8.6)	-11.1(1.0)	-111.9(11.2)	-89.9(8.2)	-10.9(1.0)
^{124}Sn	out.	-96.6(8.8)	-11.7(1.1)	-112.9(10.3)	-90.9(8.3)	-10.5(1.0)

Table 6.3: The ϕ values where $G_{beam}=0.55(5)$. (* The lifetime of the 4^+ state of ^{116}Sn is taken to be 4ps here)

Nucleus	Si detector	$g(3^-)$	$g(4^+)$
^{112}Sn	in.	-0.119(560)	0.041(165)
^{112}Sn	out.	-0.249(610)	0.033(205)
^{114}Sn	in.	-0.079(286)	-0.207(114)
^{114}Sn	out.	-0.245(415)	0.111(63)
^{116}Sn	in.	-0.200(251)	1.065(587)
^{116}Sn	out.	-0.257(499)	-1.736(731)
^{122}Sn	in.	0.429(1227)	-0.145(108)
^{122}Sn	out.	4.56(4620)*	-0.775(365)
^{124}Sn	in.	0.270(5135)	1.349(536)
^{124}Sn	out.	-8.034(4957)*	-0.089(611)

Table 6.4: The measured g-factors of the 3^- and 4^+ states respectively. In the cases marked by the asterisk, these values are unreasonable and most likely due to bad statistics, for the g-factor feeding correction the inner Si values were used.

Method 2 takes equation (5.9) with the experimental intensities, and the experimentally measured weighted means of the precessions of the feeding states. The angular correlations of the feeding states are obtained, as discussed in the

angular correlation chapter, from the normalized $W(\theta)$ for the angular correlations with the best yields, these results are used in the feeding program, as opposed to MuSTanG, since this is more realistic for our data. Table (6.6) shows what parameters were used in obtaining the feeding correction. For the cases such as the $^{122,124}\text{Sn}$ outer Si detectors, the measured $g(3^-)$ were unrealistic in their values due to their small statistics so the measured precession from the inner Si detector cases were used instead.

Parameter	Inputs Used						
$dW_{obs}(\theta)$	Measured correlation (see Angular Correlation chapter)						
$dW_{2^+ \rightarrow 0^+ \text{ pure}}(\theta)$	<table style="width: 100%; border: none;"> <tr> <td style="width: 50%;">Inner</td> <td style="width: 50%;">Outer</td> </tr> <tr> <td>$a_2 = 0.601(25)$</td> <td>$0.924(22)$</td> </tr> <tr> <td>$a_4 = -1.072(26)$</td> <td>$-0.812(25)$</td> </tr> </table>	Inner	Outer	$a_2 = 0.601(25)$	$0.924(22)$	$a_4 = -1.072(26)$	$-0.812(25)$
Inner	Outer						
$a_2 = 0.601(25)$	$0.924(22)$						
$a_4 = -1.072(26)$	$-0.812(25)$						
$dW_{3^- \rightarrow 2^+ \rightarrow 0^+}(\theta)$	<table style="width: 100%; border: none;"> <tr> <td>$a_2 = 0.598(10)$</td> </tr> <tr> <td>$a_4 = -0.564(10)$</td> </tr> </table>	$a_2 = 0.598(10)$	$a_4 = -0.564(10)$				
$a_2 = 0.598(10)$							
$a_4 = -0.564(10)$							
$dW_{4^+ \rightarrow 2^+ \rightarrow 0^+}(\theta)$	<table style="width: 100%; border: none;"> <tr> <td>$a_2 = 0.365(10)$</td> </tr> <tr> <td>$a_4 = -0.192(10)$</td> </tr> </table>	$a_2 = 0.365(10)$	$a_4 = -0.192(10)$				
$a_2 = 0.365(10)$							
$a_4 = -0.192(10)$							
η_{ij}	Ratio of Measured intensities						
$\Delta\Phi_{32}, \Delta\Phi_{42}$	Experimentally measured precessions (see precession chapter)						
$\phi_{20}^{pure}, \phi_{20}^{feeding \text{ from } 3^-}$	Calculated in program (table (6.3))						

Table 6.5: Input details for feeding correction.

For the third method, the values $\phi(\tau)$ for the feeding states used the calculated values given in table (6.3), where the g-factors of the feeding states are given a range based on the measured g-factors for results with good yields. Some of the nuclei and Si detector configurations yield poor statistics for their $3^- \rightarrow 2^+$, $4^+ \rightarrow 2^+$ states and hence also have either extreme precessions and/or large statistical errors. The cases taken were for those with good number events, and the values and range determined from the weighed mean and the errors. Using these ranges for the feeding g-factors, another way of obtaining the feeding could be obtained.

Nucleus	Si detector	$g(3^-)$	$g(4^+)$
^{112}Sn	inner	-0.119(950)	-
^{112}Sn	outer	-0.249(611)	0.033(205)
^{114}Sn	inner	-0.079(286)	-0.207(112)
^{114}Sn	outer	-0.245(414)	0.111(63)
^{116}Sn	inner	-0.200(250)	-
^{116}Sn	outer	-0.257(498)	-
^{122}Sn	inner	0.429(1227)	-0.145(117)
Weighted mean	all	-0.168(153)	0.004(79)

Table 6.6: Input details for method three - g-factors with sufficient statistics.

Because the weighted means of the g-factors are estimates in this method, the approximation of $g(3^-)$ was rounded up to -0.170(200) and $g(4^+) \approx 0.005(100)$, these were then inputted into the program with their errors to calculate the feeding correction for the g-factors.

6.1 Results

The results presented here are for methods 2 and 3, while for method 1 are referred to in appendix B. The results for the inner and outer detectors were initially treated as separate, table (6.7) show the independent results for inner and outer for a) the raw g-factor without feeding correction, b) Method 2 using the experimentally measured precessions (the final weighted mean) of the feeding states, c) Method 3 with calculated $\phi(\tau)$, $g(3^-) = -0.200(200)$ and $g(4^+) = 0.005(100)$.

Nuc.	Si det.	$g(2^+)$		
		raw	method 2	method 3
^{112}Sn	Inner	0.070(40)	0.057(60)	0.083(50)
^{112}Sn	Outer	0.082(10)	0.110(30)	0.105(20)
^{112}Sn	Mean		0.099(30)	0.102(20)
^{114}Sn	Inner	0.000(20)	0.044(40)	0.040(30)
^{114}Sn	Outer	-0.060(30)	0.000(40)	-0.013(40)
^{114}Sn	Mean		0.022(30)	0.021(30)
^{116}Sn	Inner	0.000(30)	0.044(30)	0.049(30)
^{116}Sn	Outer	0.027(30)	0.079(50)	0.054(30)
^{116}Sn	Mean		0.053(30)	0.051(20)
^{122}Sn	Inner	-0.042(10)	-0.052(20)	-0.042(20)
^{122}Sn	Outer	-0.071(90)	-0.032(80)	-0.026(70)
^{122}Sn	Mean		-0.051(20)	-0.041(20)
^{124}Sn	Inner	-0.084(30)	-0.135(30)	-0.082(30)
^{124}Sn	Outer	-0.072(30)	-0.085(30)	-0.072(30)
^{124}Sn	Mean		-0.110(30)	-0.077(20)

Table 6.7: The g-factors with and without feeding corrections for methods 2 and 3 - for inner and outer detectors and their weighted means.

One can see in figure (6.1) that there is a general upward shift in the g-factors relative to the raw g-factors which do not take feeding into account. For all the feeding results, from methods 2 and 3, there is an agreement within the errors in general. There is also consistent agreement within the errors of the inner and outer detectors, so the weighted mean of the g-factors were taken, this is shown in table (6.7) and figure (6.2).

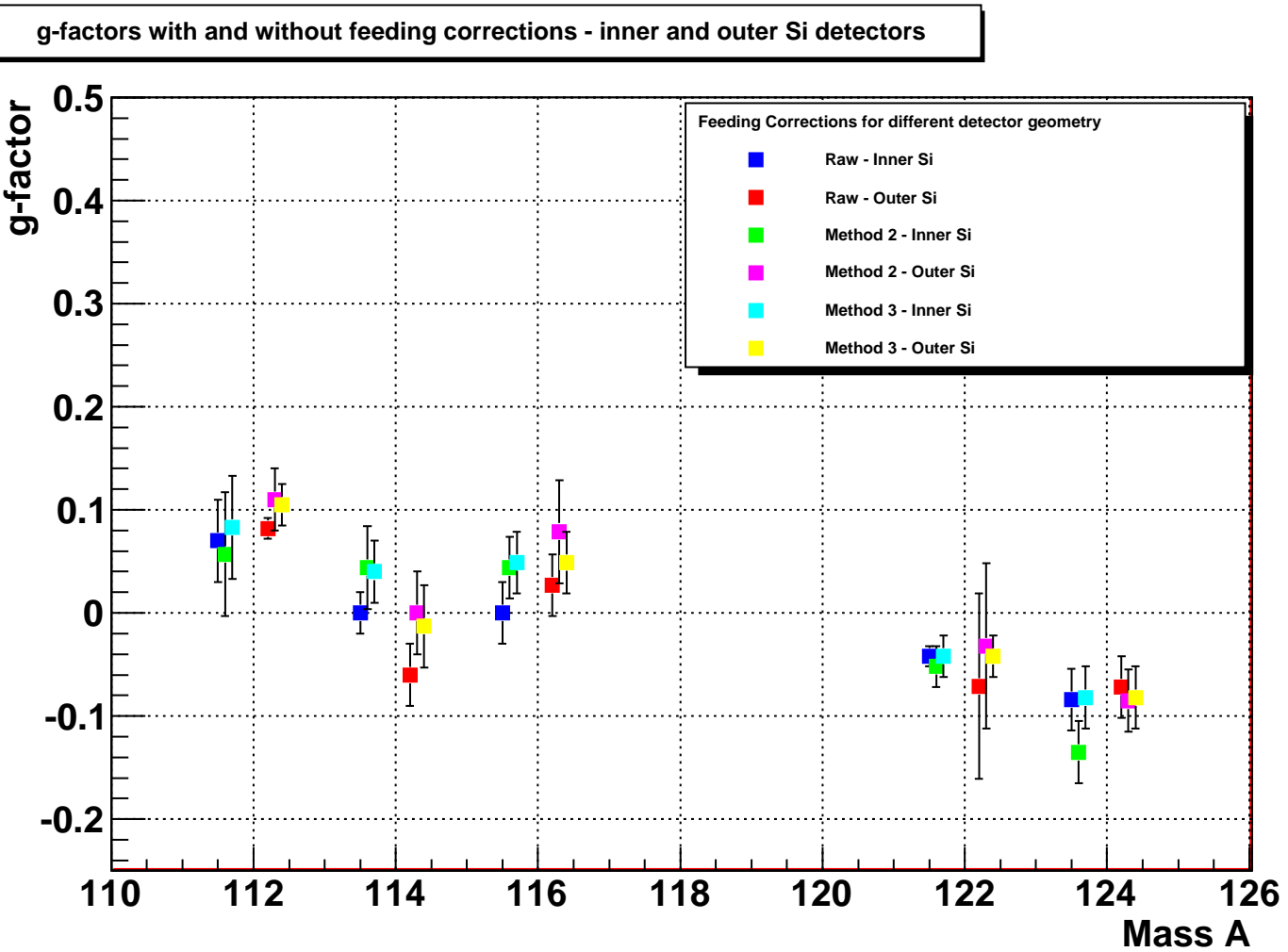


Figure 6.1: The g-factors for both the raw, un-corrected values and corrected by for feeding effects. The data are split in terms of inner and outer Si detector geometry respectively, with inner on the left hand side of the mass number, and outer to the right.

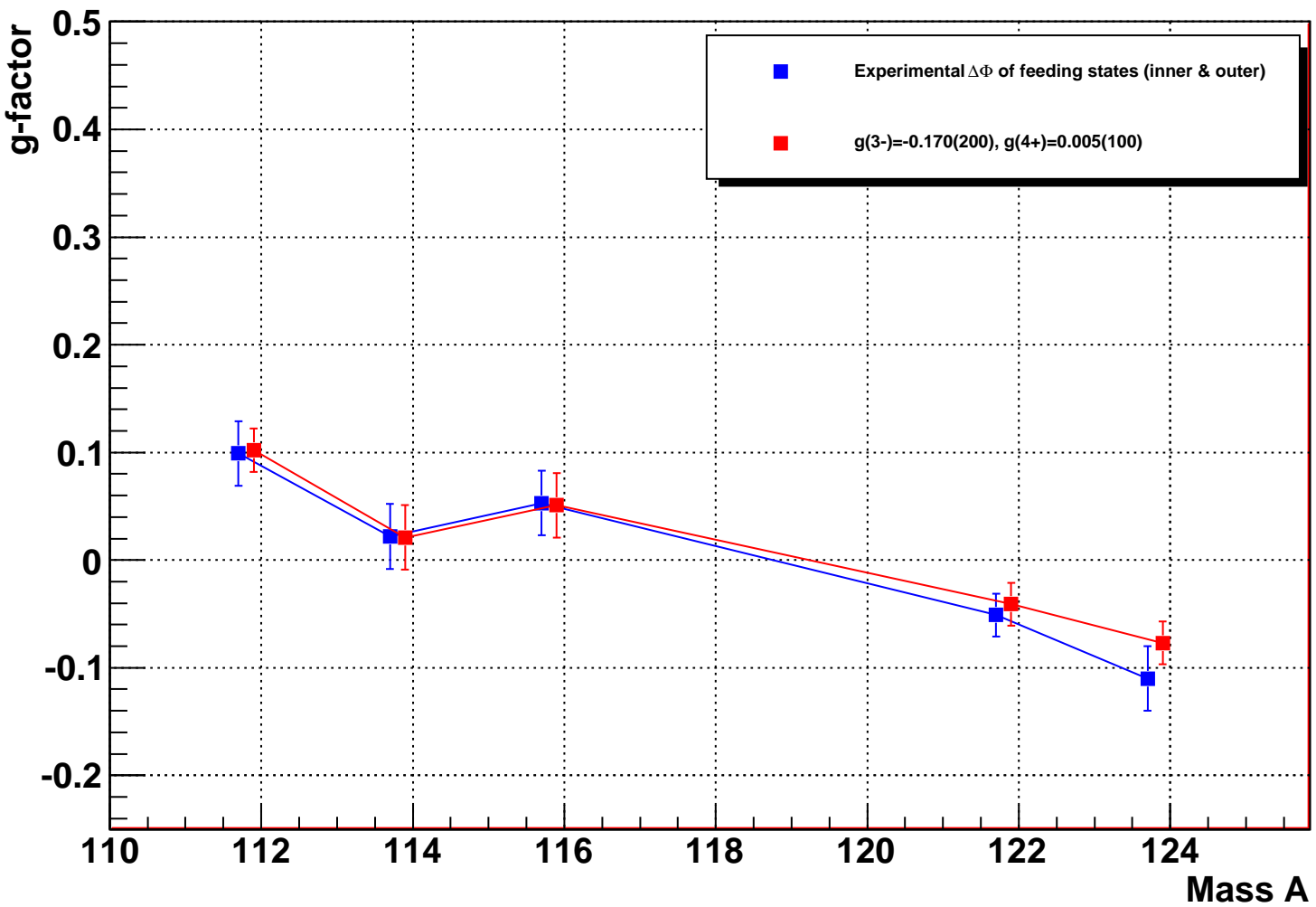


Figure 6.2: The g-factors for the weighted means over the inner and outer Si detectors for the feeding correction methods 2 and 3.

In figure (6.2) one can see that both method 2 and 3 agree within the errors. Because method 2 utilizes the actual precessions for each case, this is a better representation of the experimentally measured g-factors, these g-factors from method 2 are the results which will be discussed from now on.

The g-factors of the Sn isotopes has been studied before in previous experiments, the most notable one was conducted in 1980 by M. Hass et al at the Weizmann Institute of Science in Israel [19], which measured the g-factors of the Sn chain from A=112-124. There was a follow up measurement by M.C. East and A. Stuchbery et al. in 2008 at ANU[20], which looked at isotopes with A=116-120. The values from these experiments, as well as the current measurements from GSI are listed in table (6.8) and are also given in figure (6.3). One can see that for the heavier isotopes there is consistent agreement between the previously measured g-factors in WIS by Hass et al, and also between the ANU results with the WIS results. In the case of ^{116}Sn , the results from ANU are in agreement with both the previously measured results from WIS and the current results from GSI, however the error bars are very large for both previous experiments. The GSI results are not in agreement with the measured g-factor for ^{116}Sn , however with improvements to the experimental techniques since 1980, such as inverse kinematics and improved detector set up, the GSI results show a reduced error in this re-measurement. The g-factors from all 3 experiments took the weighted mean to obtain new adopted values for the g-factors for the Sn chain, which are shown in red in figure (6.3). In the discussion, these adopted values for the g-factors which are considered.

Nucleus	GSI	WIS	ANU	adopted
^{112}Sn	0.099(30)	0.370(130)	-	0.113(60)
^{114}Sn	0.022(30)	-	-	0.022(30)
^{116}Sn	0.053(30)	-0.160(100)	-0.150(260)	0.033(40)
^{118}Sn	-	0.020(100)	0.170(100)	0.100(70)
^{120}Sn	-	-0.140(70)	-0.090(70)	-0.120(50)
^{122}Sn	-0.051(20)	-0.070(110)	-	-0.052(20)
^{124}Sn	-0.110(30)	-0.150(100)	-	-0.113(30)

Table 6.8: The old and remeasured g-factors for the Sn isotopes from this experiment, ref [19] and ref[20]

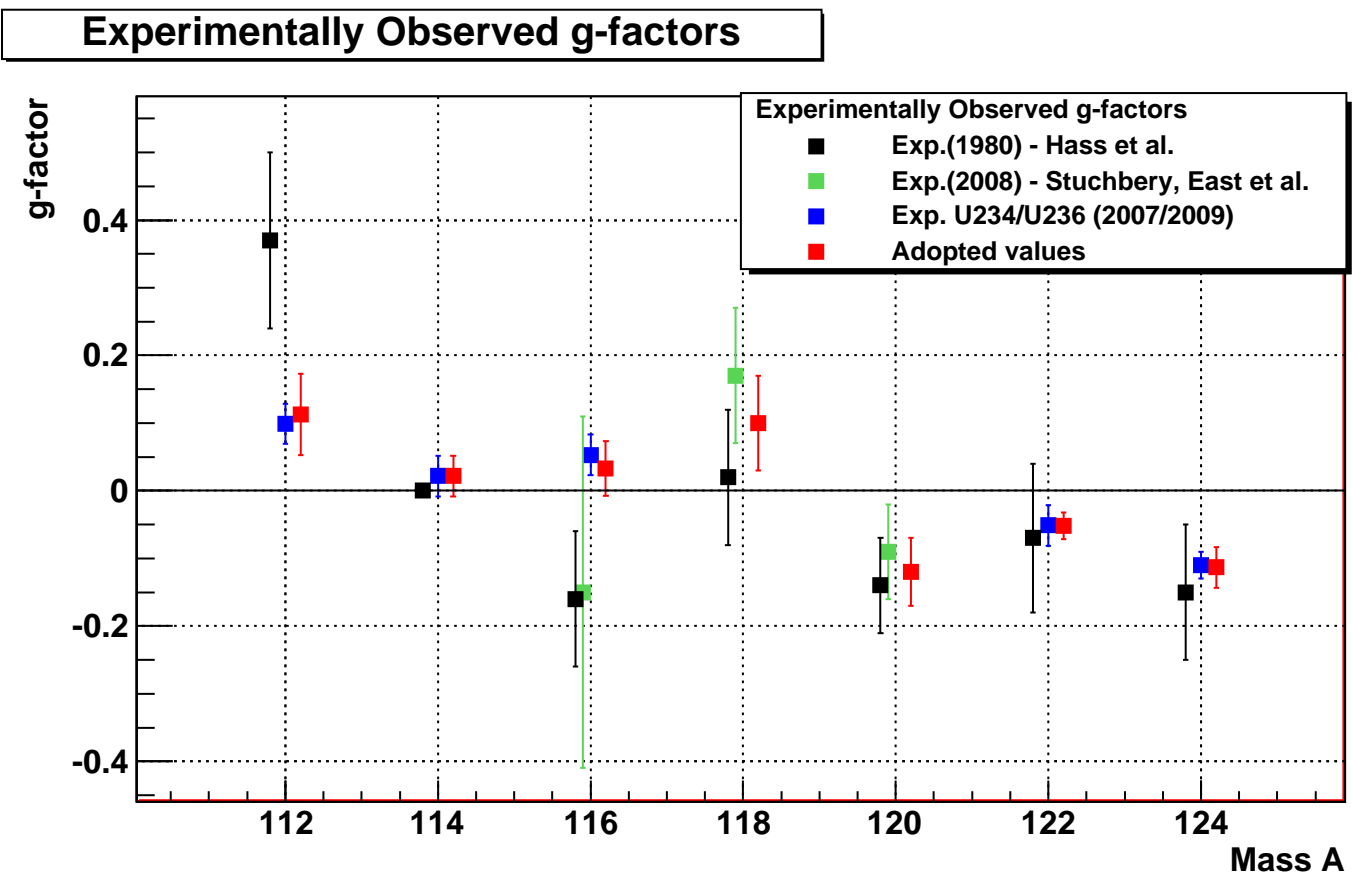


Figure 6.3: The g-factors for the current and previously measured g-factor results.

Chapter 7

Discussion

The final adopted g-factor measurements are shown in figure (7.1) where one can see that for the lighter isotopes, the g-factors yield positive values and decrease with increasing neutron number. Before discussing these observed g-factors, I'd like to draw attention back to the $B(E2; 0_{g.s}^+ \rightarrow 2_1^+)$ transition strengths referred to in the introduction, as well as to discuss the remeasured $B(E2; 0_{g.s}^+ \rightarrow 2_1^+)$ values for these isotopes with our experimental setup [21].

In ref [21], the lifetimes of the stable Sn isotopes were measured in our experiments U234 and U236, by extracting the lifetime via the Doppler Shift Attenuation method which was introduced in section 4.1. These remeasured lifetimes and transition strengths are given in table (7.1). In 2008, another experiment was conducted in the Australian National University [20] which studied the g-factors of $^{116-120}\text{Sn}$ isotopes. Using the data from the lineshapes in the spectra from this experiment, the lifetimes were also remeasured, and published in ref [21]. These lifetimes are also given in table (7.1).

Figure (7.2) shows both new and old experimental results and their comparison with shell model calculations made with ^{100}Sn and ^{90}Zr closed shell cores, as well as the calculations following the RQRPA model [15][16] and the QRPA model [18]. In the case of the previously measured $B(E2; 0_{g.s}^+ \rightarrow 2_1^+)$ results, the general trend was one which followed the parabolic shell model case by smoothly increasing from ^{124}Sn until the neutron mid-shell of ^{116}Sn , however for the lighter isotopes there was an unusual enhancement in the observed $B(E2; 0_{g.s}^+ \rightarrow 2_1^+)$ transition strengths. In the case of the remeasured results from GSI and ANU, one can see that they begin to deviate from the shell model calculations before the neutron mid-shell is

Nucleus	$\tau(2^+)$:GSI	ANU	previous	B(E2):GSI	ANU	previous
^{112}Sn	0.65(4)	-	0.544(32)	0.200(12)	-	0.240(14)
^{114}Sn	0.60(4)	-	0.474(16)	0.183(12)	-	0.232(8)
^{116}Sn	0.66(4)	0.68(4)	0.539(15)	0.170(10)	0.165(10)	0.209(6)
^{118}Sn	-	0.79(4)	0.695(27)	-	0.183(9)	0.209(8)
^{120}Sn	-	0.97(5)	0.916(19)	-	0.191(10)	0.202(4)
^{122}Sn	1.29(8)	-	1.1011(23)	0.164(10)	-	0.192(4)
^{124}Sn	-	1.48(15)	1.324(32)	-	0.148(15)	0.166(4)

Table 7.1: The old and remeasured lifetimes and $B(E2; 0_{g.s}^+ \rightarrow 2_1^+)$ transition strengths in $^{112-124}\text{Sn}$ [21][20].

reached, with a maximum around $^{118-120}\text{Sn}$ and decreases until ^{116}Sn , after which there is a smooth increase in the $B(E2; 0_{g.s}^+ \rightarrow 2_1^+)$ transition strengths in ^{112}Sn . For isotopes lighter than ^{120}Sn , the transition strengths cease to follow the parabolic behavior expected from the seniority scheme and the shell model calculations with ^{100}Sn core (calculations from ref [6]). Looking into the non-shell model calculations depicted in figure (7.2), such as the RQRPA model, one can see that the maximum occurs around $^{106-108}\text{Sn}$ before steadily decreasing until it plateaus out at the neutron mid-shell at $N=66$ until ^{124}Sn before it decreasing again. This nicely describes the data of the light isotopes but as one can see, beyond ^{116}Sn this ceases to agree. The QRPA model is shown in pink. Unfortunately the calculations for this model have only been performed for the upper half of the shell for the heavier Sn isotopes beyond $N=66$, but this is a close reproduction of the recent experimental results of the $B(E2; 0_{g.s}^+ \rightarrow 2_1^+)$ values for the heavier isotopes. Looking into these $B(E2; 0_{g.s}^+ \rightarrow 2_1^+)$ transition strengths, there is no single calculation of the various theoretical models which can replicate the data of the chain of Sn isotopes currently present. Because of this ongoing question about the $B(E2)$ values, the g-factor measurements will hopefully give some insight into understanding the nature of the $B(E2; 0_{g.s}^+ \rightarrow 2_1^+)$ transition strengths.

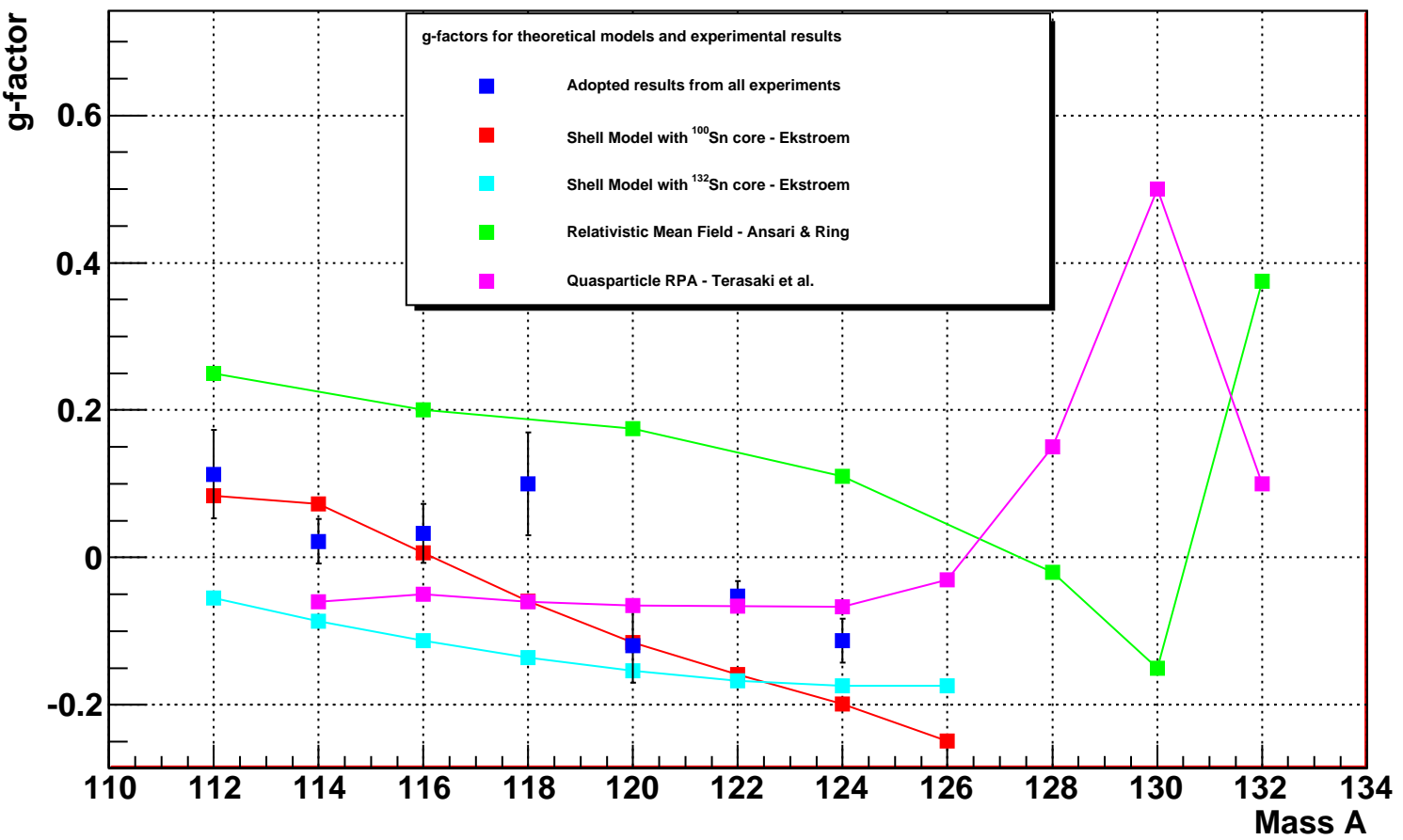


Figure 7.1: The g-factors for experimental adopted results (the weighted mean of this measurement with the previously measured g-factors) and theoretical results.

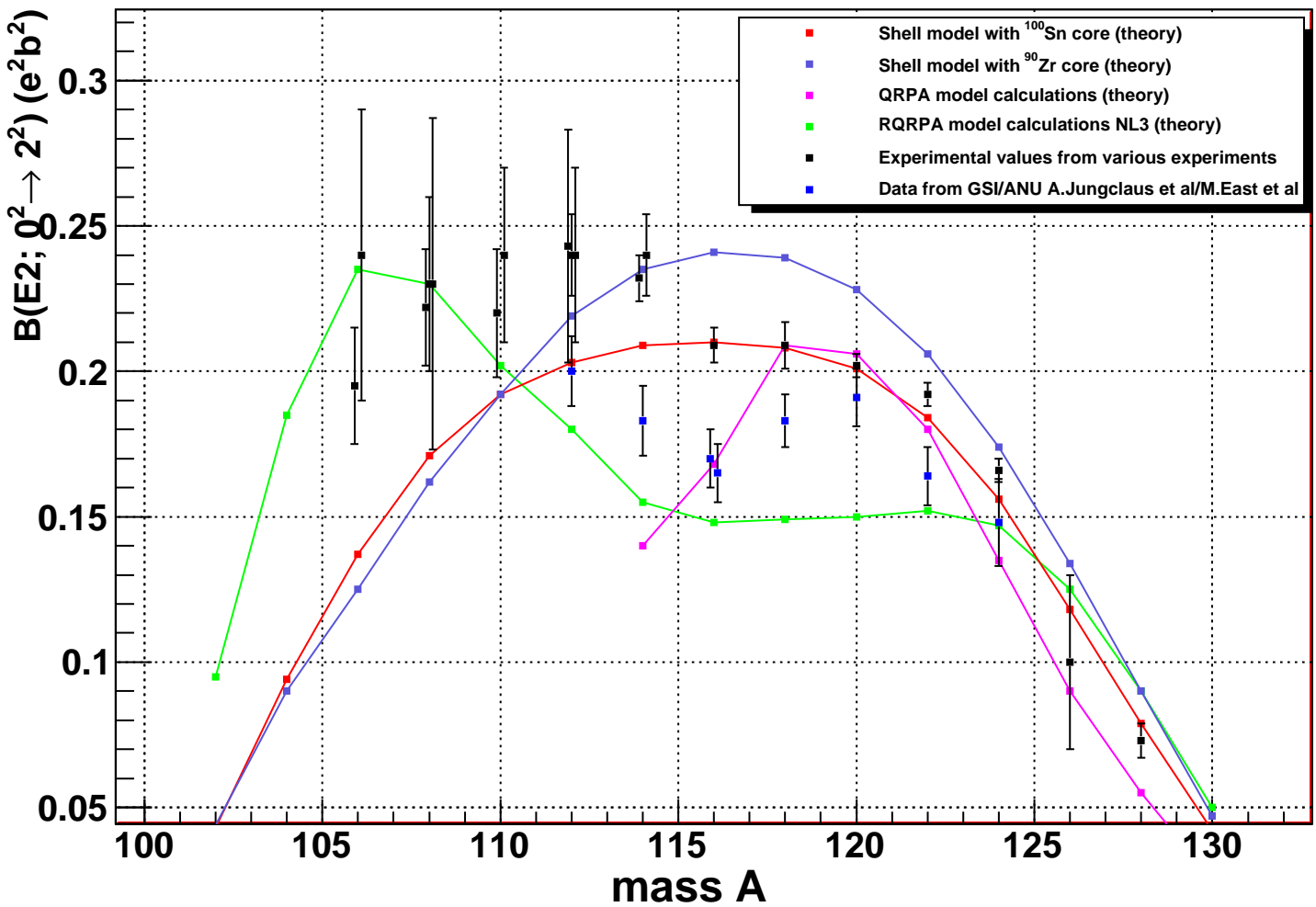


Figure 7.2: The remeasured $B(E2)$ s from GSI/ANU compared to the calculations and previous data.

Figure (7.1) shows the remeasured adopted g-factor results compared to the shell model calculations with closed shell cores of ^{100}Sn and ^{132}Sn , the QRPA model [18] and the relativistic mean field theory/RQRPA model [15][16]. The shell model calculations given in this work were performed by A. Ekström[50], using the software CENS [51]. The first calculation assumed a ^{100}Sn closed shell core considering the neutron orbitals outside the core as particle valence space. This calculation used the N3LO nucleon-nucleon interaction which included Coulomb interaction, breaking of charge symmetry, and charge independence between nucleons. This shell model calculation is shown in red in figure (7.1). The second shell model calculation used a closed shell core of ^{132}Sn , where the same orbitals were considered as neutron holes with respect to the ^{132}Sn core; a CD-Bonn potential was used in the calculation in conjunction with the experimental single hole energies from ^{131}Sn , the results for this shell model calculation are shown in figure (7.1) in cyan.

The initial observation in the measured g-factors is that the lighter Sn isotopes show a tendency to having positive g-factors, which generally decrease and tend towards negative g-factors as the neutron number increases. This general trend is seen in the case of the shell model calculation with a closed ^{100}Sn shell core. For the lightest isotope being investigated, ^{112}Sn , this is a positive g-factor of $g(2^+) = +0.11(6)$; for $N=62$ the orbital closest to the Fermi level is $g_{7/2}$ which has an effective g-factor of $+0.18$. The possible neutron configurations for the 2^+ state are $g_{7/2}^2$ and $d_{5/2}g_{7/2}$ ($g_{eff}=+0.23$), and both have g-factors $\approx +0.2$, in agreement with the positive experimental g-factor given here. For ^{114}Sn , the g-factor is small and positive; at $N=64$ there is a subshell closure where excitations have to cross the Fermi surface, the configurations for such excitations in this case are $g_{7/2}^{-1}d_{3/2}$ ($g_{eff}=+0.04$) and $d_{3/2}^{-1}s_{1/2}$ ($g_{eff}=-0.20$), the observed g-factor suggests a configuration of $g_{7/2}^{-1}d_{3/2}$, since the extracted value agrees within the errors. For $N=66$, the Fermi level moves to the $s_{1/2}$ orbital, and the configuration of $d_{3/2}s_{1/2}$ with an effective g-factor of -0.11 would decrease the $g(2^+)$ value of ^{116}Sn . This decrease is mirrored by the shell model calculation when compared to its lighter neighbors, which agrees within the uncertainties with the measured value of $g(2^+) \approx +0.03(4)$. For the lighter Sn isotopes between $^{112}-^{116}\text{Sn}$, the measured g-factors agree within the errors with the shell model calculation given in red. Around ^{118}Sn however, there is a sudden increase in the g-factor back up to a large and positive value. The reasons for this positive g-factor has already been suggested in the paper by M.C East et al [20]; in this case the $s_{1/2}$ orbital is fully occupied, so the $(d_{3/2}^2)$ configuration with $g_{eff}=+0.46$ may be

the most prominent, which supports the large and positive observed g-factor. There is however also the expectation for competition between the $d_{3/2}s_{1/2}$ configuration with $g_{eff}=-0.11$, which is also a likely candidate for describing the wavefunction, but this g-factor was unfortunately not remeasured in this experiment, and both the measured g-factors for ^{118}Sn have large uncertainties. This may be an isotope worth remeasuring with the techniques used in U234/U236, to confirm whether this g-factor has the observed configuration of $(d_{3/2}^2)$, or the expected $d_{3/2}s_{1/2}$. There is an observed drop in the g-factors for $^{120-124}\text{Sn}$, which could be explained by the significant role that the $h_{11/2}$ orbital plays in the configurations for neutron numbers from $N=70$ and above, with its large negative effective g-factor of -0.25 . It is expected that as the neutrons begin to populate the $h_{11/2}$ orbital, this exerts dominance with increasing importance against the $d_{3/2}^2$ and $d_{3/2}s_{1/2}$ configurations. As neutron number increases, one would expect an enhancement of negative g-factors since there is no alternative but to populate the $h_{11/2}$ orbital which has a large negative g-factor. However the experimentally measured g-factors for $^{122,124}\text{Sn}$, while these are consistent in the sense they have negative g-factors, they show reduced g-factor values which one would not expect as the $h_{11/2}$ orbital is filled. But this current explanation holds for cases when one doesn't take into account the effect which pairing would have on the effective g-factor. For $^{122,124}\text{Sn}$, the $h_{11/2}$ shell becomes increasingly occupied. Breaking the neutron pairs in the $h_{11/2}$ orbital to excite to the 2^+ state would cost a lot more energy than to excite its lighter neighbor orbits. However if one considers breaking of a neutron pair from one of the other orbitals for which it would be more cost effective, such as the $d_{3/2}$, an estimated contribution of 25-30% in the wavefunction configuration would suffice to account for the experimentally observed g-factors in $^{122,124}\text{Sn}$.

These observed g-factors indicate that there is a general tendency to follow the shell model of a closed shell core of ^{100}Sn , but only the neutrons configurations have been discussed so far. What about the key question asked in the motivation, does one observe core proton excitations across the $Z=50$ shell gap? Looking again at the recent measurements of the $B(E2; 0_{g.s}^+ \rightarrow 2_1^+)$ transition strengths, there is a dip in the results between $A=112$ to $A=116$ before the transition strengths increase after $A=116$ to $A=120$, this current trend lies in contradiction to the previously observed $B(E2; 0_{g.s}^+ \rightarrow 2_1^+)$ transition strengths, which prompted the motivation to investigate whether proton core excitations occur in the light Sn isotopes. The re-measured $B(E2; 0_{g.s}^+ \rightarrow 2_1^+)$ show that proton excitation is unlikely, however examining the

measured g-factors even though they are positive in sign for $^{112-116}\text{Sn}$, do not satisfy the expected proton configurations which have very large and positive g-factors ($g_{9/2d_{5/2}} g_{eff}=+1.09$, $g_{9/2d_{7/2}} g_{eff}=+1.34$), so proton core excitations can be ruled out for the light stable Sn isotopes. It would be important in the future to remeasure the g-factors of the lighter Sn isotopes to explain the observed enhancements of the $B(E2; 0_{g.s}^+ \rightarrow 2_1^+)$ transition strengths observed.

There still remains the question of whether the shell model reproduces satisfactorily the measured data. Looking at the $B(E2; 0_{g.s}^+ \rightarrow 2_1^+)$ transition strengths, there is a clear disagreement between the light isotopes up to ^{120}Sn when compared to the shell model calculations with a closed shell core of ^{100}Sn , but there is a tendency for the heavy isotopes to follow the QRPA model [18], where unfortunately the calculations have only been made until ^{114}Sn . The lighter isotopes instead appear to be better described by the mean field theory, but does not agree with the heavier isotopes and in spite of that, one can clearly see in figure (7.1) that the relativistic mean field theory can be ruled out from the measured g-factors. There is however a trend for the QRPA model describing the g-factors for the isotopes of $^{120-124}\text{Sn}$, but ceases to reproduce the g-factors for the lighter isotopes with positive values. The shell model with the ^{100}Sn closed shell core best describes the measured g-factors, however it may be worth investigating into further theoretical calculations for the g-factors and the $B(E2; 0_{g.s}^+ \rightarrow 2_1^+)$ transitions strengths in order to obtain a theoretical picture capable to describe the data in all cases.

Chapter 8

Resumen en Castellano

8.1 Motivación

La cadena de los isótopos de estaño es un interesante tema de investigación debido a los núcleos que existen cerca de la línea de $N=Z$, sobre los que es posible estudiar temas de física de la estructura nuclear como polarización del core, apareamiento protón-neutrón y simetría de isospin. El estaño es especialmente interesante porque tiene dos isótopos que tienen números mágicos en protones y neutrones; el ^{100}Sn es el núcleo doblemente mágico de mayor número de protones con $N=Z$ que es ligado. Los estaños son la cadena más larga de isótopos semi-mágicos accesibles para estudios experimentales de física nuclear, y son muy útiles para la investigación de modelos en estructura nuclear. Se presta una especial atención a las excitaciones del core de $Z=50$ y al espacio de valencia de los neutrones en una capa completa. La región próxima a la cadena de estaño es un buen campo de estudio para comprender la estructura nuclear de los núcleos situados lejos del valle de estabilidad. Medidas como la energía de excitación y los valores de $B(E2)$ nos ayudan a comprender conceptos fundamentales como el esquema de senioridad. Un buen método para la investigación sobre excitaciones del core, con una buena sensibilidad para el estudio de la estructura de estos núcleos, son los valores de $B(E2)$.

Debido a la capa cerrada de protones con el número mágico $Z=50$, el aumento de colectividad se produce por la ocupación de los neutrones de los orbitales de $d_{5/2}$, $g_{7/2}$, $d_{3/2}$, $s_{1/2}$ y $h_{11/2}$. En el modelo de capas, con truncación de senioridad, se espera que tengan los valores de $B(E2)$ en una forma parabólica, con una forma simétrica y que crezca hasta el centro de la capa de neutrones, entre los núcleos doblemente

mágicos de ^{100}Sn y ^{132}Sn . Han sido realizados muchos experimentos que han medido los valores de $B(E2)$ para la cadena de los isótopos de estaño entre $A=106-126$. Los resultados de estos experimentos presentan la peculiaridad de que los estaños ligeros tienen los valores de $B(E2)$ que crecen desde el centro de la capa de los neutrones en ^{116}Sn hasta los isótopos mas ligeros. Estos resultados no se corresponden con los cálculos de los valores de $B(E2)$ en el modelo de capas.

Una forma de explicar los datos es que existe la posibilidad de que haya excitaciones de protones que crucen el espacio de capas $Z=50$. Los cálculos del modelo de capas que tienen en cuenta estas excitaciones de los protones observan un cierto aumento en los valores de $B(E2)$, aunque siguen sin corresponderse con los resultados medidos.

Un método para investigar la estructura del núcleo es la medida de los momentos magnéticos. Un momento magnético es el producto vectorial de una corriente eléctrica y el área que encierra la trayectoria que sigue esta corriente, donde:

$$\vec{\mu} = g\mu_N\vec{I}. \quad (8.1)$$

Los momentos magnéticos proporcionan información muy sensible a la configuración de los nucleones de los iones de la corriente y los orbitales de partícula independiente que ellos ocupan. Hay una gran diferencia entre los factores g de los neutrones y protones en magnitud y signo, $g_s^\pi=+5.587$, $g_l^\pi=1$, y $g_s^\nu = -3.826$, $g_l^\nu=0$. Dado que los factores g de los nucleones presentan esta diferencia, esta es la razón de que los momentos magnéticos sean tan sensibles al estructura del estado pudiendo proporcionar información sobre la estructura de partícula independiente. Si hay excitaciones de los protones a través del espacio entre capas $Z=50$ y la siguiente, esperamos que haya un aumento en el valor del factor g , ya que todos los orbitales de protones tienen valores positivos y grandes. Asimismo, en la figura (1.4b) se puede ver que los factores g también presentan sensibilidad a los modelos nucleares como el la teoría del campo medio relativista y el la aproximación de partícula de fase aleatoria . Hay diferencias entre los factores g de los modelos; esta información nos permite entender mejor qué modelo siguen los estaños, y nos lleva por tanto a una mejor comprensión de los valores de $B(E2)$.

Los momentos magnéticos de los estaños fueron medidos en dos experimentos: uno en Israel en 1980 [19] y otro en Australia en 2008 [20]. Estos resultados aparecen representados en la figura (??), donde se puede observar unas barras de

8.2 La técnica de los campos magnéticos transitorios en combinación con la excitación coulombiana en cinemática inversa

error relativamente grandes. Si dispusiéramos de una medida con mejor precisión, podríamos entender mejor el motivo por el cual los valores de $B(E2)$ de los estaños ligeros crecen desde la mitad de la capa de los neutrones. Por esta razón, hemos vuelto a medir los factores g de $^{112,114,116,122,124}\text{Sn}$ otra vez en GSI con métodos mejorados, como la excitación coulombiana en cinemática inversa en combinación con campos magnéticos transitorios. También podemos medir la vida media del estado a partir de la forma del pico gracias al efecto Doppler, y por último hemos vuelto a medir los valores de $B(E2)$ con el método por atenuación por efecto Doppler.

8.2 La técnica de los campos magnéticos transitorios en combinación con la excitación coulombiana en cinemática inversa

8.2.1 Correlaciones Angulares perturbadas

Cuando un núcleo con un momento magnético está en un campo magnético externo, un par de torsión induce este núcleo a precesar. Para un estado que tiene un tiempo de vida τ , el par de torsión de la precesión provoca que la correlación angular de los rayos gamma emitidos en decaimiento rote con un ángulo ϕ . Si conocemos el tiempo de vida, podemos calcular el factor g mediante la medida de ese ángulo de precesión con un campo magnético en direcciones arriba y abajo y si medimos también su correlación angular. La magnitud de esta diferencia de precesión es proporcional a la fuerza del campo magnético y al tiempo de vida. Si tenemos un tiempo de vida corto, necesitamos un campo magnético más fuerte para observar una precesión significativa. En nuestro caso, cuando medimos estados con tiempos de vida en el rango de picosegundos, necesitamos campos magnéticos del orden de kT para medir una precesión del rango de mrad. Estas fuerzas no se pueden crear en campos magnéticos externos, sino en campos magnéticos hiperfinos estáticos. Trataremos este tipo de campos magnéticos en la siguiente sección.

Para vidas cortas se pueden medir las precesiones con correlaciones angulares perturbadas. Para rayos gamma detectados en coincidencia con los iones de retroceso del blanco, la forma de las correlaciones angulares para el decaimiento de una transición de tipo E2 es de tipo:

$$W(\theta_\gamma) = C[1 + A_2^{exp} P_2(\cos(\theta_\gamma)) + A_4^{exp} P_4(\cos(\theta_\gamma))] \quad (8.2)$$

A partir de aquí obtenemos la pendiente logarítmica, mediante la ecuación:

$$S(\theta_\gamma) = \frac{1}{W(\theta_\gamma)} \frac{dW(\theta_\gamma)}{d\theta_\gamma} \quad (8.3)$$

La precesión está medida por a razón doble, ρ , por las intensidades de los gamma en ángulos simétricos respecto a la dirección del haz y por el campo magnético en direcciones arriba y abajo.

$$\rho = \sqrt{\frac{N(+\theta \uparrow)N(-\theta \downarrow)}{N(+\theta \downarrow)N(-\theta \uparrow)}} \quad (8.4)$$

Partiendo de esto, podemos obtener la precesión del núcleo en el estado excitado a partir de las ecuaciones (8.7), así como el factor g.

$$\epsilon = \frac{\rho - 1}{\rho + 1} \quad (8.5)$$

$$\Phi = \frac{\epsilon}{S(\theta_\gamma)} \quad (8.6)$$

$$\Phi = -g \frac{\mu_N}{\hbar} \int_{t_{in}}^{t_{out}} B_{TF}(v_{ion}(t)) e^{-t/\tau} dt \quad (8.7)$$

8.2.2 Campos Magnéticos Transitorios

Para medir la precesión de un estado que tiene una vida corta, precisamos de un campo magnético muy fuerte. Cuando un ión atraviesa un material ferromagnético con una velocidad v , aparece un campo magnético transitorio que tiene magnitudes de kT al MT; se trata de un campo magnético hiperfino interno cuya magnitud depende de la carga del ion, Z , y su velocidad. Cuando un ion cargado entra en un blanco ferromagnético con una velocidad v , hay un intercambio del espín entre los electrones magnetizados del ferromagnético, lo que produce una polarización de espín en los electrones del ión no emparejados, y que la orientación del campo magnético transitorio se alinee con el campo magnético externo. Los campos magnéticos transitorios tienen parametrizaciones de la forma:

$$B^{LIN} = a \cdot Z \cdot \frac{v}{v_0} \quad (8.8)$$

$$B^{RUT} = a' \cdot Z^{1.1} \cdot \frac{v^{0.45}}{v_0} \cdot M \quad (8.9)$$

$$B^{CR} = a'' \cdot Z \frac{v}{v_0} \cdot e^{-\beta v/v_0} \quad (8.10)$$

y lo usamos el parametrización de B^{LIN} en nuestro experimento.

8.2.3 Excitación Coloumbiana en cinemática inversa

Se induce la excitación en los estados de bajo espín mediante un campo eléctrico cuadrupolar con una interacción electromagnética entre un proyectil y un núcleo del blanco. Si la energía del haz se encuentra por debajo de la barrera coulombiana, pueden darse excitaciones nucleares debidas a interacciones electromagnéticas de largo alcance entre un proyectil y un blanco.

La ventaja de la excitación coulombiana es que tiene grandes secciones eficaces que contribuyen a maximizar la estadística obtenida en las medidas. Asimismo, poblar un estado mediante la excitación coulombiana introduce una gran alineación del espín, lo que significa que se observa una anisotropía grande en las correlaciones angulares medidas, lo que conduce a pendientes logarítmicas grandes con gran sensibilidad en la observación de las precesiones.

La excitación coulombiana en cinemática inversa tiene lugar cuando un proyectil pesado experimenta excitación tras la interacción con un blanco ligero. La ventaja es que las partículas de retroceso del blanco se ven proyectadas hacia adelante en la dirección del haz, lo que facilita su detección, y se observan más partículas en coincidencia con los rayos gamma, de modo que este método proporciona mayor estadística. Para usar la cinemática inversa también es necesario crear campos magnéticos transitorios más fuertes, dado que el proyectil tiene una velocidad más alta que en las excitaciones de cinemática estándar. En la cinemática inversa, al ocurrir la excitación en el proyectil, no es necesario cambiar el blanco para medir isótopos distintos, sino que sólo debemos cambiar el haz durante el experimento, lo cual constituye un método mucho más eficiente.

8.3 Montaje Experimental

La medida de los factores-g del estado 2+ para los isótopos de $^{112,114,116,122,124}\text{Sn}$ fue realizada con la técnica de campos magnéticos transitorios con excitación coulombiana en cinemática inversa. En el primer experimento en 2007 (U234), haces puros de $^{112,114,116}\text{Sn}$ con 4 MeV/u fueron provistos por el acelerador de UNILAC en GSI, Darmstadt, los cuales entraron en contacto con un blanco de multicapas.

La excitación coulombiana ocurre en la primer capa de $0.68\text{mg}/\text{cm}^2$ de ^{nat}C . A continuación, los iones excitados atraviesan la capa ferromagnética, que consiste en $10.8\text{ mg}/\text{cm}^2$ de Gd, y en esta capa los iones excitados experimentan el campo magnético transitorio. Dado que el Gd solo presenta ferromagnetismo cuando es enfriado por debajo de su temperatura de Curie, el blanco fue enfriado mediante un dewar con nitrógeno líquido. Los iones atraviesan la capa ferromagnética y experimentan precesión, y después se detienen en una capa de Cu de $4.86\text{ mg}/\text{cm}^2$, donde se desexcitan en un medio libre de efectos hiperfinos.

En el siguiente experimento (U236), realizado también en GSI en 2009 se utilizaron el mismo montaje que el U234 para medir los isótopos $^{122,124}\text{Sn}$. Las diferencias entre los dos fueron los haces de ^{122}Sn y ^{124}Sn con una energía de 3.8 MeV/u y el blanco, que ha cambiado en este montaje. Para medir el ^{124}Sn se tuvieron $0.647\text{ mg}/\text{cm}^2$ de ^{nat}C , $10.1\text{ mg}/\text{cm}^2$ Gd, $1.0\text{ mg}/\text{cm}^2$ Ta, y $7.24\text{ mg}/\text{cm}^2$, así como 5 micras de Ta como tapón de haz. No obstante, durante la medición, una parte de la capa de carbono se despegó de la capa de Gd. Por esta razón observamos formas de línea modificadas.

Es muy probable que las formas de línea modificadas se deban a que de los núcleos fueron excitados en la parte de la capa despegada que pasaron al vacío y decayeron antes de llegar al Gd.

Para la medida del ^{122}Sn se sustituyó el blanco roto por uno nuevo, consistente en $0.66\text{mg}/\text{cm}^2$ de ^{nat}C , $10.9\text{ mg}/\text{cm}^2$ de Gd, $1.0\text{ mg}/\text{cm}^2$ de Ta y $5.23\text{ mg}/\text{cm}^2$ Cu y un tapón de haz de $20\text{ }\mu\text{m}$ de Ta.

A 3cm por detrás del blanco se colocó una matriz de detectores de diodos de pin de Si para la detección de partículas de C desde el blanco para hacer una coincidencia con los gammas.

Los rayos gammas de desexcitación de iones de Sn fueron detectados cuatro

detectores en “cluster” de Euroball, situados a $\pm 65^\circ$ y $\pm 115^\circ$ respecto del eje del haz. La distancia de los detectores Ge hasta el blanco fue de 22(1)cm. El montaje también tuvo un detector Ge a 0° .

8.3.1 Preparación de los datos

Para limpiar los espectros gamma se implementaron condiciones en el análisis de los datos. La primera condición fue la sustracción evento a evento de los TDCs: sustraemos el TDC de Si del TDC de Ge, porque hay una diferencia entre las partículas del blanco que tienen tiempos de vuelo distintos dependiendo en qué detector de Si se detectan. Entonces, una ventana temporal es iniciada cuando recibimos una señal de detector de rayos gamma y concluida cuando recibimos una señal del detector de Si exterior o interior siendo diferentes para ambos detectores de Si. Con este espectro de tiempo con las sustracciones realizadas entre los dos tiempos es nuestra ventana de tiempo de un evento válido. Dicha ventana está localizada en el pico, pero también se toma una otra ventana de igual ancho en la parte del valle. Con la primera condición, el espectro gamma se incrementa si esta condición es válida, y se decrementa si está de acuerdo con la segunda. Con estas condiciones obtenemos un espectro limpio de los gammas que se han producido en el blanco. Para limpiar más el espectro se implementa una condición de partículas y así también se pone una condición en la parte de carbono que fue detectado en el Si. Con estas condiciones obtenemos espectros limpios de estaño y de telurio (si se pone una condición en el alfa), y una vez limpios se pone la condición de polaridad del campo magnético por los ratios dobles.

8.4 Análisis de los datos

Para determinar las pendientes logarítmicas, las correlaciones angulares fueron medidas experimentalmente. Dado que había detectores gamma en un gran rango de ángulos, hemos medido las correlaciones angulares directamente de las intensidades, corrigiendo por eficiencias. Los parámetros a_2 , a_4 y la intensidad, C , los he obtenido mediante un ajuste a estos parámetros.

Para las intensidades que vienen desde los picos que tienen una parte en vuelo, es necesario hacer algunas correcciones por el efecto Doppler:

$$E'_\gamma(\theta, t) = E_\gamma^0 \frac{\sqrt{1 - \beta^2(t)}}{1 - \beta(t)\cos(\theta)} \quad (8.11)$$

para obtener la velocidad desde el pico. Y para obtener el ángulo en centro de masas:

$$\cos(\theta)_{CM} = \frac{\cos(\theta)_{lab} - \beta}{1 - \beta\cos(\theta)_{lab}} \quad (8.12)$$

Para los ángulos sólidos:

$$W_{lab}d\Omega_{lab} = W_{CM}d\Omega_{CM} \quad (8.13)$$

tiene que ser valido, entonces:

$$W_{CM}(\theta_{CM}) = W_{lab}(\theta_{lab})d\Omega_{lab}/d\Omega_{CM} \quad (8.14)$$

con

$$d\Omega_{lab}/d\Omega_{CM}(\theta_{lab}) = [1 - \beta\cos(\theta_{lab})]^2/(1 - \beta^2). \quad (8.15)$$

Para obtener las precesiones, (el método está explicado en el parte de Correlaciones Angulares Perturbadas), obtenemos los ratios dobles a partir las intensidades, y luego la pendiente logarítmica para obtener la precesión. Las precesiones medidas se encuentran en las tablas (4.11) al (4.16) y los promedios de las precesiones en tabla (4.17).

8.5 Correcciones por poblaciones desde estados de alto espín

Para los núcleos $^{112,114,116}\text{Sn}$ existen poblaciones desde estados de espín alto ($4^+, 3^-$) que tienen efectos significativos en el estado 2^+ observado. Estas contribuciones desde los estados 4^+ y 3^- van a afectar a la precesión observada en el caso de la transición de 2^+ a 0^+ . La precesión es una función del tiempo de vida del estado, como refleja la ecuación:

$$\Delta\Phi = g\phi(\tau_i) = -g\frac{\mu_N}{\hbar} \int_{t_{in}}^{t_{out}} B_{TF}(v_{ion}(t))e^{-t/\tau} dt \quad (8.16)$$

8.5 Correcciones por poblaciones desde estados de alto espín 167

El método empleado para obtener estas correcciones debidas a las contaminaciones desde los otros estados viene dado por la ecuación:

$$\Delta\Phi_{obs}^{2+} = \frac{\frac{dW_{2+}}{d\theta} |_{\theta_\gamma} \Delta\Phi_{2+} + \eta_{3,2} \frac{dW_{320}}{d\theta} |_{\theta_\gamma} \langle \Delta\Phi_{32} \rangle + \eta_{4,2} \frac{dW_{420}}{d\theta} |_{\theta_\gamma} \langle \Delta\Phi_{42} \rangle}{\frac{dW_{obs}}{d\theta} |_{\theta_\gamma} \{1 + \eta_{3,2} + \eta_{4,2}\}} \quad (8.17)$$

Se tiene en cuenta el tiempo de vida y las correlaciones angulares de todos los estados. Donde por ecuación (8.17):

$$\langle \Delta\Phi_{320} \rangle = -g(3^-) \frac{\mu_N}{\hbar} \int_{t_{in}}^{t_{out}} B_{tf}(t) e^{-t/\tau_3} dt - g(2^+) \frac{\mu_N}{\hbar} \int_{t_{in}}^{t_{out}} \frac{\lambda_3}{\lambda_2 - \lambda_3} (e^{-t/\tau_3} - e^{-t/\tau_2}) B_{tf}(t) dt \quad (8.18)$$

$$= \Delta\Phi(3^-) - g(2^+) \frac{\mu_N}{\hbar} \int_{t_{in}}^{t_{out}} \frac{\lambda_3}{\lambda_2 - \lambda_3} (e^{-t/\tau_3} - e^{-t/\tau_2}) B_{tf}(t) dt \quad (8.19)$$

$$\langle \Delta\Phi_{420} \rangle = -g(4^+) \frac{\mu_N}{\hbar} \int_{t_{in}}^{t_{out}} B_{tf}(t) e^{-t/\tau_4} dt = \Delta\Phi(4^+) \quad (8.20)$$

Las ecuaciones (8.18,8.20) son empleadas para obtener la componente de las precesiones por los estados de alto espín, donde la parte de población pura está tomada de los valores medidos, y la parte que contribuye al estado 2+ está calculada.

La estructura del programa incluye distintas partes para calcular:

1. El poder de frenado. Está hecho para obtener cuánta energía ha perdido el núcleo dentro de los blancos. En el carbono es importante saber qué energía tiene el núcleo cuando ocurre la excitación y que nos permitiría saber con qué energía entra y sale el ión en la capa ferromagnética.
2. Cinemática. Cuando hay una excitación coulombiana, una partícula del blanco retrocede y el proyectil es excitado siendo ambas partículas dispersadas con ángulos distintos. A partir de las ecuaciones de cinemática se puede obtener no sólo los ángulos de las partículas dispersadas sino también la energía de los iones. Con esta información es posible saber qué energía tiene el ion que ha sido excitado en alguna parte del blanco. Esta información, en combinación con el poder de frenado, permite saber las energías y velocidades en el blanco.
3. Sección eficaz. En la ecuación (8.17), la componente η_{ij} se obtiene a través del cociente entre las secciones eficaces en los casos donde hay excitación coulombiana y cuando no hay excitaciones por interacciones nucleares. Pero también se puede obtener η_{ij} a partir de las intensidades medidas.

4. Obtener $\phi(\tau)$. Viene expresado por

$$\phi(\tau_i) = -\frac{\mu_N}{\hbar} \int_{t_{in}}^{t_{out}} e^{-t/\tau_i} B_{tr}(t) dt \quad (8.21)$$

donde $B(v_{ion}(t))$ es la magnitud del campo magnético transitorio que es dependiente de la velocidad del ión cuando se atraviesa la capa ferromagnética. Se conoce la velocidad con que entra y sale de la capa, y también el tiempo que el ión está dentro de la capa. Con esta información, puede resolverse la ecuación (8.21) mediante el método de integración numérica.

8.6 Los resultados

Hay tres posibles métodos para obtener las correcciones por la alimentación desde estados de alto espín con ecuación (8.17), estos son:

1. Usar las secciones eficaces calculadas para la razón de η_{ij} en combinación con las precesiones medidas de $3^- \rightarrow 2^+$ y $4^+ \rightarrow 2^+$.
2. Usar las intensidades medidas para la razón de η_{ij} en combinación con las precesiones medidas de $3^- \rightarrow 2^+$ y $4^+ \rightarrow 2^+$.
3. Utilizando las intensidades medidas para la razón de η_{ij} en combinación con $\phi(\tau)$ calculados para $3^- \rightarrow 2^+$ y $4^+ \rightarrow 2^+$ y los factores g de $3^- \rightarrow 2^+$ y $4^+ \rightarrow 2^+$ de los resultados que tienen mejor estadística.

El método 1 no es bueno porque este experimento no es de excitación coulombiana segura, la energía de los haces es mayor que la barrera coulombiana. Puede verse en la tabla (6.1) que las proporciones de las intensidades y de las secciones eficaces son significativamente diferentes. Los resultados de la tabla (6.7) son para los factores g sin corregir por alimentación, para el método 2 y 3 con los detectores de Si dentro, fuera y también el promedio. Puede verse en la figura (6.1) que los dos métodos están en acuerdo y también entre los detectores de Si.

Puede verse que los resultados anteriores tienen errores muy grandes en comparación con estos nuevos datos. Los factores g obtenidos en estos 3 experimentos están en tabla (8.1) y también se incluye el promedio de los tres. Los promedios son los factores g adoptados.

Nuc.	GSI	WIS	ANU	adoptados
^{112}Sn	0.099(30)	0.370(130)	-	0.113(60)
^{114}Sn	0.022(30)	-	-	0.022(30)
^{116}Sn	0.053(30)	-0.160(100)	-0.150(260)	0.033(40)
^{118}Sn	-	0.020(100)	0.170(100)	0.100(70)
^{120}Sn	-	-0.140(70)	-0.090(70)	-0.120(50)
^{122}Sn	-0.051(20)	-0.070(110)	-	-0.052(20)
^{124}Sn	-0.110(30)	-0.150(100)	-	-0.113(30)

Table 8.1: Los datos por los factores g en los isotopos de Sn medidas de este experimento (U234/U236), y de referencia [19] y de [20]

8.7 Resumen y conclusiones

Los factores g del estado 2+ fueron medidos con buen precisión para los isótopos de $^{112,114,116,122,124}\text{Sn}$ mediante la técnica de campos magnéticos transitorios en combinación con excitación coulombiana en cinemática inversa, con EUROBALL, que son detectores de radiación gamma de alta eficiencia.

Los valores obtenidos para los factores g pueden ser explicados con el modelo de capas y con los orbitales de partícula independiente (tabla (1)). También se aprecia que los factores g están en acuerdo con el modelo de capas con un core de ^{100}Sn (figura (7.1)). No observamos factores g con valores de gran magnitud y signo positivo en los estaños ligeros para que sean excitaciones de protones a través del core de $Z=50$. Los factores g no se reproducen tan bien con los otros modelos RQRPA y QRPA como con el modelo de capas.

Appendix A

Summary of literature information concerning level schemes, lifetimes, moments and transition strengths for $^{112,114,116,122,124}\text{Sn}$

The values for the lifetimes and γ energies were obtained from [42]. The $B(E\lambda)$ s were either obtained from [42] or calculated using the equation(A.2) [13].

$$B(E\lambda : J_i \rightarrow J_f) = T_{fi}(E\lambda) \left(\frac{E_\gamma}{\hbar c}\right)^{-(2L+1)} \frac{\hbar L((2L+1)!!)^2}{8\pi(L+1)} \quad (\text{A.1})$$

$$B(E\lambda : J_f \rightarrow J_i) = \frac{2J_f + 1}{2J_i + 1} \quad (\text{A.2})$$

where $T_{fi}(E\lambda) = \frac{I(E\lambda)}{I_{total}} \frac{1}{\tau}$ with I being the intensity of the transition and τ the lifetime.

**Summary of literature information concerning level schemes,
lifetimes, moments and transition strengths for ^{112,114,116,122,124}Sn**

Nucleus	State	τ (ps)	E_γ (keV)	$B(E\lambda:J_f \rightarrow J_i)$ (e^2b^2)
¹¹² Sn	2 ⁺	0.65(4)[21]	1256.7(5)	$B(E2;0^+ \rightarrow 2^+)=0.200(12)[21]$
	4 ⁺	4.76(90)	990.7(1)	$B(E2;0^+ \rightarrow 2^+)=0.032(6)[42]$
	3 ⁻	0.31(2)[21]	1097.7(3)	$B(E3)=0.087(12)[42]$
¹¹⁴ Sn	2 ⁺	0.60(4)[21]	1299.92(7)	$B(E2;0^+ \rightarrow 2^+)=0.183(12) [21]$
	0 ₂ ⁺	9.4(31)	653.36(2)	$B(E2;0^+ \rightarrow 2^+)=0.07(3)[42]$
	4 ⁺	7.65(60)	887.690(8)	$B(E2;0^+ \rightarrow 2^+)=0.035(3)$
	3 ⁻	0.52(3)[21]	975.076(8)	$B(E1)=3.88 \times 10^{-6}$
¹¹⁶ Sn	2 ⁺	0.66(4)[21]	1293.558(15)	$B(E2;0^+ \rightarrow 2^+)=0.170(10)[21]$
	2 ₂ ⁺	2.60(+10-4)	818.718(21)	$B(E2;0^+ \rightarrow 2^+)=0.013(5)[42]$
	3 ⁻	0.48(3)[21]	972.564(19)	$B(E1)=1.95 \times 10(40)^{-8}$
	3 ⁻	0.48(3)[21]	2266.1(10)	$B(E3)=0.127(17) [42]$
	4 ⁺	0.40(8)	1097.326(22)	$B(E2;0^+ \rightarrow 2^+)=0.076(14) [42]$
¹²² Sn	2 ⁺	1.29(8)[21]	1140.52(4)	$B(E2;0^+ \rightarrow 2^+)=0.164(12)[21]$
	4 ⁺	2.25(30)	1001.54(2)	$B(E2;0^+ \rightarrow 2^+)=0.065(9)[42]$
	3 ⁻	0.13(2)[21]	1352.17(3)	$B(E3)=0.066(10)[42]$
¹²⁴ Sn	2 ⁺	1.48(15)[21]	1131.69(2)	$B(E2;0^+ \rightarrow 2^+)=0.148(15)[21] \pm 0.10$
	4 ⁺	5.33(68)	969.97(2)	$B(E2;0^+ \rightarrow 2^+)=0.032(4)[42]$
	3 ⁻	0.098(9)[21]	1470.71(2)	$B(E3)=0.155(20)[42]$

Table A.1: The lifetimes, γ -ray energies and transition strengths for the Sn isotopes.

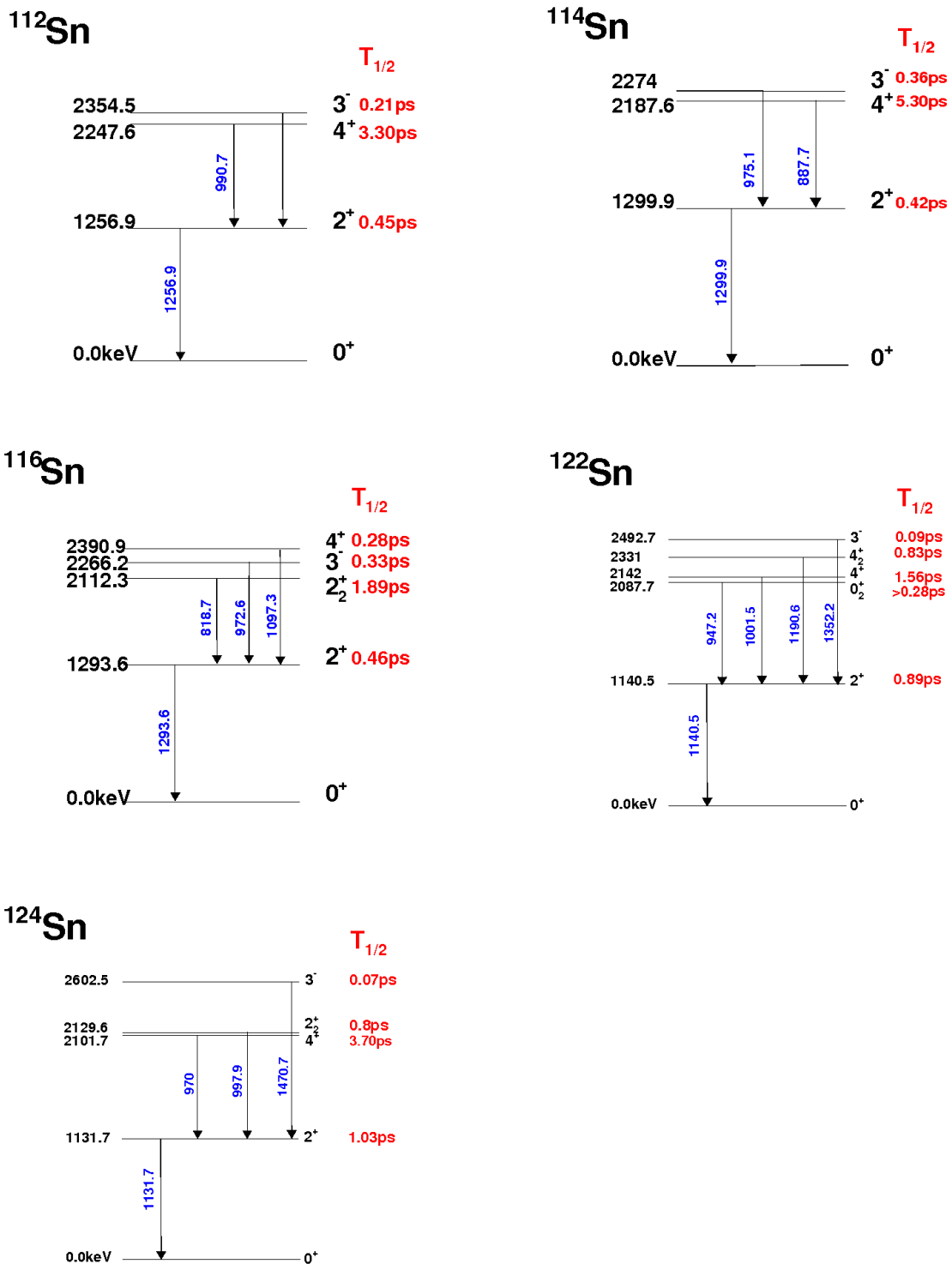


Figure A.1: Partial level schemes of the Sn isotopes as observed in the present work.

**Summary of literature information concerning level schemes,
lifetimes, moments and transition strengths for $^{112,114,116,122,124}\text{Sn}$**

Appendix B

Result Details

The input parameters into the program for the results are given in tables (B.1,B.2). These parameters were used to calculate the stopping in the target, the kinematics in Coulomb excitation and the cross-section, and later on the $\phi(\tau)$ or each populated state. These details have been discussed previously, and here the actual parameters for each case is given. These parameters are read into the program prior to calculations and one can obtain the velocity into and out of the targets, the time, the field strength and hence the precession.

Nuc.	Beam: Z1	A1	Energy
¹¹² Sn	50	112	448
¹¹⁴ Sn	50	114	456
¹¹⁶ Sn	50	116	464
Nuc.	Target1 : Z2	A2	thickness1
all	6	12	0.68
Nuc.	Target2 : Z3	A3	thickness3
all	64	157	10.8
Nuc.	L	Excitation Energy	B(EL)
¹¹² Sn	2	1.257	0.200
¹¹² Sn	3	2.355	0.195
¹¹² Sn	2	2.248	0.032
¹¹⁴ Sn	2	1.300	0.184
¹¹⁴ Sn	3	2.274	0.149
¹¹⁴ Sn	2	2.188	0.035
¹¹⁶ Sn	2	1.294	0.168
¹¹⁶ Sn	3	2.266	0.165
¹¹⁶ Sn	2	2.391	0.023
Nuc.	Detector: Distance		
all	30		
Nuc.	Detector: Height	Width	Vertical Distance
all	10	10	1/13
Nuc.	No. X	Y strips	
all	10	10	
Nuc.	Field parameters:	a	G
all		17	0.55
Nuc.	lifetime: 2 ⁺	3 ⁻	4 ⁺
¹¹² Sn	0.65	0.31	4.76
¹¹⁴ Sn	0.60	0.52	7.65
¹¹⁶ Sn	0.67	0.48	4.00

Table B.1: Variables read in for U234 run.

Nuc.	Beam: Z1	A1	Energy
^{122}Sn	50	122	464
^{124}Sn	50	124	471
Nuc.	Target1 : Z2	A2	thickness1
^{122}Sn	6	12	0.66
^{124}Sn	6	12	0.647
Nuc.	Target2 : Z3	A3	thickness3
^{122}Sn	64	157	10.9
^{124}Sn	64	157	10.1
Nuc.	L	Excitation Energy	B(EL)
^{122}Sn	2	1.141	0.164
^{122}Sn	3	2.493	0.066
^{122}Sn	2	2.142	0.065
^{124}Sn	2	1.132	0.148
^{124}Sn	3	2.603	0.155
^{124}Sn	2	2.103	0.032
Nuc.	Detector: Distance		
all	30		
Nuc.	Detector: Height	Width	Vertical Distance
^{122}Sn	10	10	1/13
^{124}Sn	10	10	1/13
Nuc.	No. X	Y strips	
^{122}Sn	10	10	
^{124}Sn	10	10	
Nuc.	Field parameters:	a	G
all		17	0.55
Nuc.	lifetime: 2^+	3^-	4^+
^{122}Sn	1.29	0.13	2.25
^{124}Sn	1.48	0.098	3.7

Table B.2: Variables read in for the U236 run.

Nuc.	Si det.	g-factor
^{112}Sn	inner	0.099(80)
^{112}Sn	outer	0.170(40)
^{112}Sn	all	0.156(40)
^{114}Sn	inner	0.010(30)
^{114}Sn	outer	-0.026(60)
^{114}Sn	all	0.003(30)
^{116}Sn	inner	0.044(40)
^{116}Sn	outer	0.080(50)
^{116}Sn	all	0.058(30)
^{122}Sn	inner	-0.070(20)
^{122}Sn	outer	-0.081(130)
^{122}Sn	all	-0.070(20)
^{124}Sn	inner	-0.146(60)
^{124}Sn	outer	-0.173(70)
^{124}Sn	all	-0.157(50)

Table B.3: The feeding corrected g-factor using cross-section ratios for η_{ij} and experimentally measured $\Delta\Phi$ s for feeding states.

One of the feeding corrections obtained η_{ij} from the ratio of the calculated Coulex cross-sections, however, when comparing these ratios to the ratios of the measured intensities, there was a significant difference between the two, and because the experiment ran at energies above the Coulomb barrier and with unsafe Coulex, the cross-sections were not an accurate representation of the population of said states. However, for curiosity's sake, these feeding corrections were also done, and included here in table (B.3).

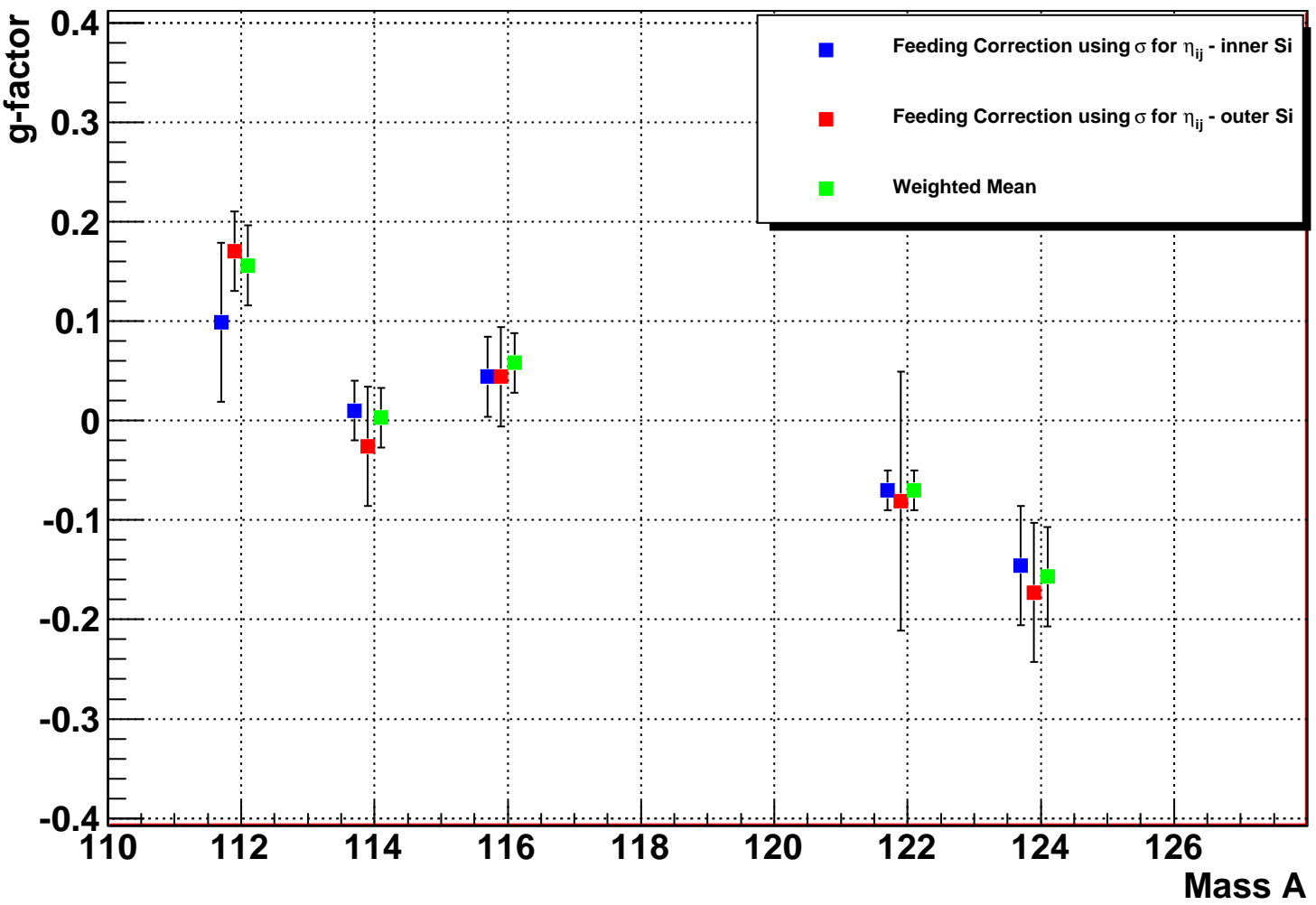


Figure B.1: The g-factors for the weighted means over the inner and outer detectors, plus individual Si detectors for the feeding method 1 with σ ratios.

Appendix C

Error Propagation

C.1 Error Treatment of Data

There are two methods for obtaining the error in the data. The first looks at the internal error or the standard deviation of the data. The second looks at the external error, the actual scattering of the data relative to the mean. At each angle there is more than one crystal which is taking the data, up to about 2-3 crystals per angle. As there is more than one detector being accounted for, the scattering of counts between them should also be considered. The internal error is expressed in the equation (C.2) and the external in equation (C.3). The weighted mean, $\overline{\overline{G}}$, is given in (C.1)[52].

$$\overline{\overline{G}} = \frac{\sum_{i=1}^k g_i \overline{G}_i}{\sum_{i=1}^k g_i} \quad (\text{C.1})$$

Where \overline{G}_i is the number of counts and g_i are the weights with k being the number of detectors. $g_i = \frac{1}{m_i^2}$ where m_i^2 is the variance of the data. Equation (C.2) calculates the standard deviation of the error over the combination of the detectors otherwise known as the internal error.

$$S_{int} = \left(\sum_{i=1}^k \frac{1}{m_i^2} \right)^{-\frac{1}{2}} \quad (\text{C.2})$$

So equation (C.2) calculates the standard deviation of the error over the combination of the detectors.

Apart from the standard error of the data, one also needs to consider that the number of counts in each detector will vary between each other and is sometimes outside the error range of the standard deviation. So this scattering of data points needs to be considered when thinking about the error in the data. Equation (C.3) gives the external error.

$$S_{ext} = \left(\frac{\sum_{i=1}^k g_i (\overline{G}_i - \overline{\overline{G}})^2}{(k-1) \sum_{i=1}^k g_i} \right)^{\frac{1}{2}} \quad (\text{C.3})$$

For all of the data sorting both methods were used for the error analysis and the largest uncertainty was selected to be used as the error for that data point.

The handling of the propagation of errors when dealing with functions is also of interest where either one or more parameters have their own error. In most of the cases like the calculation of the error for $S(\theta)$ where there is a complex function with two parameters with errors standard error propagation is not used. What is required is that a partial differential is taken for each parameter and then account for the errors, d_a and d_b are the errors of the parameters and d_{ab}^2 is the estimated covariance between a,b measurements. If the terms a,b are independent then the covariance can be assumed to be zero.

$$df(a, b) = \sqrt{\left(\left(\frac{\delta f}{\delta a} \right)^2 d_a^2 + \left(\frac{\delta f}{\delta b} \right)^2 d_b^2 + \left(\frac{\delta f}{\delta a} \right) \left(\frac{\delta f}{\delta b} \right) d_{ab}^2 \right)} \quad (\text{C.4})$$

C.2 Error propagation in the Centre of Mass velocity transformations

C.2.1 Error in β

The relationship between the observed γ -energy and the velocity of the ion can be obtained from:

$$E'_\gamma(\theta, t) = E_\gamma^0 \frac{\sqrt{1 - \beta^2(t)}}{1 - \beta(t) \cos(\theta)} \quad (\text{C.5})$$

In order to obtain β from the measured $E'_\gamma(\theta, t)$, equation (C.5) needs to be rearranged into a quadratic equation to give β :

$$\underbrace{\left[1 + \left(\frac{E'_\gamma(\theta, t)}{E_\gamma^0}\right)^2 \cos^2(\theta)\right]}_a \beta^2 + \underbrace{\left[-2 \left(\frac{E'_\gamma(\theta, t)}{E_\gamma^0}\right)^2 \cos(\theta)\right]}_b \beta + \underbrace{\left[\left(\frac{E'_\gamma(\theta, t)}{E_\gamma^0}\right)^2 - 1\right]}_c = 0 \quad (C.6)$$

The quadratic in equation (C.6) can be solved by equation(C.7):

$$\beta = \frac{-b \pm \sqrt{b^2 - 4ac}}{2a} \quad (C.7)$$

Where a,b,c are defined in the underbraces in equation(C.6). The contribution to the error comes from σ measured from the FWHM and corresponds to the error range of $E'_\gamma(\theta, t)$, hence the error given in $\left(\frac{E'_\gamma(\theta, t)}{E_\gamma^0}\right)^2$ is given as:

$$\Delta \left(\frac{E'_\gamma(\theta, t)}{E_\gamma^0}\right)^2 = 2 \frac{\sigma}{E'_\gamma(\theta, t)} \left(\frac{E'_\gamma(\theta, t)}{E_\gamma^0}\right)^2 \quad (C.8)$$

since for $f = aA^b$ where a and b are constants and A is the variable the error of the function is: $\sigma_f = b \frac{\sigma_A}{A} f$. To obtain the errors in a,b and c using: $f = aA \rightarrow \sigma_f = a\sigma_A$ and are given as:

$$\Delta a = \Delta \left(\frac{E'_\gamma(\theta, t)}{E_\gamma^0}\right)^2 \cdot \cos^2(\theta) \quad (C.9)$$

$$\Delta b = \Delta \left(\frac{E'_\gamma(\theta, t)}{E_\gamma^0}\right)^2 \cdot 2\cos(\theta) \quad (C.10)$$

$$\Delta c = \Delta \left(\frac{E'_\gamma(\theta, t)}{E_\gamma^0}\right)^2 \quad (C.11)$$

$$(C.12)$$

The solution of β given in equation (C.7), the error in β can therefore be obtained from equation (C.13):

$$\Delta f(a, b, c) = \sqrt{\left(\frac{\delta f}{\delta a} \Delta a\right)^2 + \left(\frac{\delta f}{\delta b} \Delta b\right)^2 + \left(\frac{\delta f}{\delta c} \Delta c\right)^2} \quad (C.13)$$

Using equation (C.7) as $f(a, b, c)$, the error can be calculated from (C.13).

C.2.2 Error in θ

The centre of mass angle θ_{CM} is given by:

$$\cos(\theta)_{CM} = \frac{\overbrace{\cos(\theta)_{lab} - \beta}^{\text{top}}}{\underbrace{1 - \beta \cos(\theta)_{lab}}_{\text{bot}}} \quad (\text{C.14})$$

Where

$$\Delta_{top} = \Delta\beta \quad (\text{C.15})$$

$$\Delta_{bot} = \Delta\beta \cdot \cos(\theta)_{lab} \quad (\text{C.16})$$

$$\Delta \cos(\theta)_{CM} = \sqrt{\left(\frac{\Delta_{top}}{top}\right)^2 + \left(\frac{\Delta_{bot}}{bot}\right)^2} \cdot \cos(\theta)_{CM} \quad (\text{C.17})$$

To obtain $(\theta)_{CM}$ the error for the function $\cos(\theta)_{CM}$ needs solving. For $F = f(A) \rightarrow \delta F = \Delta A \frac{\delta f}{\delta A}$ hence:

$$\Delta(\theta)_{CM} = \Delta \cos(\theta)_{CM} \cdot \frac{-1}{\sqrt{1 - (\cos(\theta)_{CM})^2}} \quad (\text{C.18})$$

C.2.3 Error in $W_{cm}(\theta)$

For the centre of mass transformation for the angular correlations $W(\theta)$ are obtained by equation (C.19)

$$W_{CM}(\theta_{CM}) = W_{lab}(\theta_{lab}) d\Omega_{lab} / d\Omega_{CM} \quad (\text{C.19})$$

with

$$d\Omega_{lab} / d\Omega_{CM}(\theta_{lab}) = \frac{\overbrace{[1 - \beta \cos(\theta_{lab})]^2}^{\text{top}}}{\underbrace{(1 - \beta^2)}_{\text{bot}}} \quad (\text{C.20})$$

Where:

$$\Delta_{top} = \frac{\Delta\beta\cos(\theta_{lab})}{1 - \beta\cos(\theta_{lab})} \cdot 2 \cdot top \quad (C.21)$$

$$\Delta_{bot} = \frac{\Delta\beta}{\beta} \cdot 2 \cdot \beta^2 \quad (C.22)$$

$$\Delta \frac{d\Omega_{lab}}{d\Omega_{CM}(\theta_{lab})} = \sqrt{\left(\frac{\Delta_{top}}{top}\right)^2 + \left(\frac{\Delta_{bot}}{bot}\right)^2} \cdot \frac{d\Omega_{lab}}{d\Omega_{CM}(\theta_{lab})} \quad (C.23)$$

There is an error $\Delta W_{lab}(\theta_{lab})$ which is also included accounted for in the error propagation, this is just used in conjunction with $\Delta \frac{d\Omega_{lab}}{d\Omega_{CM}(\theta_{lab})}$ in standard error propagation.

Appendix D

$\beta \pm \Delta\beta$ obtained for all isotopes

Nuclei	Si det.	E_0 (keV)	θ	E_s (keV)	FWHM (keV)	σ (keV)	β
^{112}Sn	Inner	1257	51°	1286.5	53	22.6	0.038(30)
^{112}Sn	Inner	1257	65°	1277	34	14.5	0.040(31)
^{112}Sn	Inner	1257	79°	1267.5	17	7.2	0.049(41)
^{112}Sn	Outer	1257	51°	1288.5	55	23.4	0.040(32)
^{112}Sn	Outer	1257	65°	1278.5	37	15.7	0.044(34)
^{112}Sn	Outer	1257	79°	1268	16	6.8	0.053(39)
^{114}Sn	Inner	1300	51°	1331.5	55	23.4	0.039(31)
^{114}Sn	Inner	1300	65°	1321.5	37	13.7	0.042(29)
^{114}Sn	Inner	1300	79°	1310.5	15	6.4	0.048(34)
^{114}Sn	Outer	1300	51°	1334.5	61	26.0	0.042(34)
^{114}Sn	Outer	1300	65°	1322.5	39	16.6	0.044(35)
^{114}Sn	Outer	1300	79°	1312.5	17	7.2	0.059(42)
^{116}Sn	Inner	1294	51°	1327	60	25.5	0.041(33)
^{116}Sn	Inner	1294	65°	1316	38	16.2	0.043(34)
^{116}Sn	Inner	1294	79°	1306	17	7.2	0.056(40)
^{116}Sn	Outer	1294	51°	1327	60	25.5	0.041(33)
^{116}Sn	Outer	1294	65°	1316	38	16.2	0.043(34)
^{116}Sn	Outer	1294	79°	1305	16	6.8	0.051(38)

Table D.1: The measured $\beta \pm \Delta\beta$ for the forward angles in all isotopes/Si detector configuration for the flight peak of the $2^+ \rightarrow 0^+$ transition γ peak.

Nuclei	Si det.	E_0 (keV)	θ	E_s (keV)	FWHM (keV)	σ (keV)	β
^{112}Sn	Inner	1098	51°	1137	32	13.6	0.057(22)
^{112}Sn	Inner	1098	65°	1124	24	10.2	0.061(27)
^{112}Sn	Inner	1098	79°	1109	20	8.5	0.062(60)
^{112}Sn	Outer	1098	51°	1137	32	13.6	0.057(22)
^{112}Sn	Outer	1098	65°	1124	24	10.2	0.061(27)
^{112}Sn	Outer	1098	79°	1109	20	8.5	0.062(60)
^{114}Sn	Inner	975	51°	1002	42	17.9	0.039(31)
^{114}Sn	Inner	975	65°	993.5	33	14	0.042(29)
^{114}Sn	Inner	975	79°	983	18	7.7	0.048(34)
^{114}Sn	Outer	975	51°	1003.5	43	18.3	0.047(32)
^{114}Sn	Outer	975	65°	994.5	31	13.2	0.051(38)
^{114}Sn	Outer	975	79°	984.5	15	6.4	0.060(50)
^{116}Sn	Inner	973	51°	1002	36	15.3	0.048(27)
^{116}Sn	Inner	973	65°	992.5	27	11.5	0.052(33)
^{116}Sn	Inner	973	79°	982	16	6.8	0.056(52)
^{116}Sn	Outer	973	51°	1005.5	35	14.9	0.054(27)
^{116}Sn	Outer	973	65°	995	24	10.2	0.058(30)
^{116}Sn	Outer	973	79°	983.5	15	6.4	0.068(53)

Table D.2: The measured $\beta \pm \Delta\beta$ for the forward angles in all isotopes/Si detector configuration for the flight peak of the $3^- \rightarrow 2^+$ transition γ peak.

Nuclei	Si det.	E_0 (keV)	θ	E_s (keV)	FWHM (keV)	σ (keV)	β
^{122}Sn	Inner	1140.5	51°	1168.5	47	20.0	0.039(30)
^{122}Sn	Inner	1140.5	65°	1159	30	12.8	0.040(30)
^{122}Sn	Inner	1140.5	79°	1149.5	11	4.7	0.047(30)
^{122}Sn	Outer	1140.5	51°	1171	52	22.1	0.043(30)
^{122}Sn	Outer	1140.5	65°	1161	32	13.6	0.044(40)
^{122}Sn	Outer	1140.5	79°	1151.5	15	6.4	0.059(40)
^{124}Sn	Inner	1131.7	51°	1167.5	37	15.7	0.051(20)
^{124}Sn	Inner	1131.7	65°	1156.0	24	10.2	0.053(20)
^{124}Sn	Inner	1131.7	79°	1141	10	4.3	0.050(30)
^{124}Sn	Outer	1131.7	51°	1167	37	15.7	0.051(20)
^{124}Sn	Outer	1131.7	65°	1156	24	10.2	0.053(20)
^{124}Sn	Outer	1131.7	79°	1141	10	4.3	0.050(30)

Table D.3: The measured $\beta \pm \Delta\beta$ for the forward angles in all isotopes/Si detector configuration for the flight peak of the $2^+ \rightarrow 0^+$ transition γ peak.

Nuclei	Si det.	E_0 (keV)	θ	E_s (keV)	FWHM	σ	β
^{112}Sn	Inner	1098	51°	1137	32	13.6	0.057(22)
^{112}Sn	Inner	1098	65°	1124	24	10.2	0.061(27)
^{112}Sn	Inner	1098	79°	1109	20	8.5	0.062(60)
^{112}Sn	Outer	1098	51°	1137	32	13.6	0.057(22)
^{112}Sn	Outer	1098	65°	1124	24	10.2	0.061(27)
^{112}Sn	Outer	1098	79°	1109	20	8.5	0.062(60)
^{114}Sn	Inner	975	51°	1002	42	17.9	0.039(31)
^{114}Sn	Inner	975	65°	993.5	33	14	0.042(29)
^{114}Sn	Inner	975	79°	983	18	7.7	0.048(34)
^{114}Sn	Outer	975	51°	1003.5	43	18.3	0.047(32)
^{114}Sn	Outer	975	65°	994.5	31	13.2	0.051(38)
^{114}Sn	Outer	975	79°	984.5	15	6.4	0.060(50)
^{116}Sn	Inner	973	51°	1002	36	15.3	0.048(27)
^{116}Sn	Inner	973	65°	992.5	27	11.5	0.052(33)
^{116}Sn	Inner	973	79°	982	16	6.8	0.056(52)
^{116}Sn	Outer	973	51°	1005.5	35	14.9	0.054(27)
^{116}Sn	Outer	973	65°	995	24	10.2	0.058(30)
^{116}Sn	Outer	973	79°	983.5	15	6.4	0.068(53)

Table D.4: The measured $\beta \pm \Delta\beta$ for the forward angles in all isotopes/Si detector configuration for the flight peak of the $3^- \rightarrow 2^+$ transition γ peak.

Nuclei	Si det.	E_0 (keV)	θ	E_s (keV)	FWHM (keV)	σ (keV)	β
^{122}Sn	Inner	1352.2	51°	1405.5	25	10.6	0.063(10)
^{122}Sn	Inner	1352.2	65°	1386.5	25	10.6	0.063(20)
^{122}Sn	Inner	1352.2	79°	1367.5	21	8.9	0.072(60)
^{122}Sn	Outer	1352.2	51°	1408.5	31	13.2	0.067(20)
^{122}Sn	Outer	1352.2	65°	1387.5	35	14.9	0.065(30)
^{122}Sn	Outer	1352.2	79°	1369	28	11.9	0.082(80)
^{124}Sn	Inner	1470.7	51°	1531.5	33	14.0	0.066(20)
^{124}Sn	Inner	1470.7	65°	1509.5	33	14.0	0.066(30)
^{124}Sn	Inner	1470.7	79°	1480	14	6.0	0.036(30)
^{124}Sn	Outer	1470.7	51°	1531.5	33	14.0	0.066(20)
^{124}Sn	Outer	1470.7	65°	1509.5	33	14.0	0.066(30)
^{124}Sn	Outer	1470.7	79°	1480	14	6.0	0.036(30)

Table D.5: The measured $\beta \pm \Delta\beta$ for the forward angles in all isotopes/Si detector configuration for the flight peak of the $3^- \rightarrow 2^+$ transition γ peak.

Nuclei	Si det.	$2^+ \rightarrow 0^+$	$3^- \rightarrow 2^+$
^{112}Sn	Inner	0.041(35)	0.059(35)
^{112}Sn	Outer	0.045(35)	0.059(35)
^{114}Sn	Inner	0.043(30)	0.046(40)
^{114}Sn	Outer	0.047(40)	0.051(40)
^{116}Sn	Inner	0.046(35)	0.050(40)
^{116}Sn	Outer	0.044(35)	0.057(40)
^{122}Sn	Inner	0.042(20)	0.063(10)
^{122}Sn	Outer	0.048(30)	0.071(20)
^{124}Sn	Inner	0.052(30)	0.059(20)
^{124}Sn	Outer	0.052(30)	0.059(20)

Table D.6: The measured $\beta \pm \Delta\beta$ for all isotopes/Si detector configuration for the flight peak of the $2^+ \rightarrow 0^+$ and $3^- \rightarrow 2^+$ transition γ peak.

Appendix E

Acknowledgements

I would like to acknowledge that this thesis is based on four years of research funded by an FPU fellowship from the Universidad Autónoma de Madrid. The project was supported by the Spanish Ministerio de Ciencia e Innovación under the contracts FPA-2007-66069 and FPA2009-1337-C02-02, the Spanish Consolidar-Ingenio 2010 Program CPAN (CSD2007-00042) and the German BMBF under grant No. 06DA214I.

It is a pleasure to thank those who made this thesis possible. First and foremost I would like to thank my PhD supervisor Andrea Jungclaus for her help and support in this work. I would also like to thank José Luis Egido for his help with the university administration.

I would also like to thank my colleagues for their work and contribution to the setting up and the running of the experiments U234 and U236, most notably I would like to thank Karl-Heinz Speidel and Jörg Leske for their help during the PhD with my numerous questions and their useful advice. I would also like to thank the rest of our collaboration: A. Ekström, P. Boutachkov, J. Cederkäll, P. Doornenbal, J. Gerl, R. Gernhäuser, N. Goel, M. Górska, I. Kojoujarov, P. Maier-Komor, V. Modamio, N. Pietralla, S. Pietri, W. Prokopowicz, H. Schaffner, R. Schwengner, H.-J. Wollersheim and GSI accelerator team for their effort to provide high quality beams.

I would also like to thank my friends and colleagues at CSIC, Madrid for both their moral and knowledgeable support and help, especially to Riccardo Orlandi for his help with my thesis, and to José Antonio Briz and José Sánchez del Río for helping me with my Spanish.

And finally, I would like to thank the people who are outside my academic circle, firstly my parents for financial and moral support, Peter and Zsuzsanna Walker, a special thanks to Joseph Maussen for his psychological and professional support which enabled me to overcome some of the greatest hurdles of the PhD, to all my friends who encouraged me and supported me, most notably Kathleen Berger and Alex Hennessey who were always there for me, and to María Barrios and Rubén García for their help with the Spanish summary.

Bibliography

- [1] I.Talmi, *Nucl. Phys.*, A172, 1 (1972)
 - [2] I. Talmi, ”*Simple Models of Complex Nuclei*”, Harwood Academic Publishers, (1993)
 - [3] J.Cederkäll et al, *Phys. Rev. Lett.* 98 172501 (2007)
 - [4] A.Ekström et al, *Phys. Rev. Lett.* 101 012502 (2008)
 - [5] C.Vaman et al, *Phys. Rev. C*99 162501 (2007)
 - [6] A.Banu et al, *Phys. Rev. C* 72 061305 (2005)
 - [7] P.Doornenbal et al, *Phys. Rev. C* 78 031303 (2008)
 - [8] R. Kumar et al, *Phys. Rev. C* 81 024306 (2010)
 - [9] D.C. Radford et al. *Nuc. Phys. A* 747 (2004) 83c
 - [10] S.Raman et al, *Atomic data and Nuclear data tables* 36 1-96 (1987)
 - [11] J.N.Orce et al, *Phys. Rev. C* 76 021302 (2007); *Phys. Rev. C* 77 029902 (2008)
 - [12] K.-H.Speidel, O.Kenn, F.Nowack, *Prog. Part. Nucl. Phys.* 49 91, (2002)
 - [13] P.Regan, *Post Graduate Nuclear Physics Experimental Techniques Course Notes*,University of Surrey, UK, (2003)
 - [14] A.Ansari,P.Ring, *Phys. Letts. B* 649 (2007)
 - [15] A.Ansari, *Phys. Letts. B* 623 (2005)
 - [16] A.Ansari, P.Ring, *Phys. Rev. C* 74 (2006)
 - [17] J.Terasaki et al, *Phys. Rev. C* 66 (2002)
-

-
- [18] J.Terasaki et al, *Nucl. Phys. A* 746 (2004) 583c
- [19] M.Hass,C.Broude,Y.Niv and A.Zemel *Phys. Rev. C* 22 97 (1980)
- [20] M.C. East , A.E. Stuchbery et al, *Phys. Letts. B* 655 (2008)
- [21] A. Jungclaus et al, *Phys.Lett. B* 695, 110 (2011)
- [22] J.Leske, PhD Thesis, University of Bonn, Germany, (2006)
- [23] K.Siegbahn, *Alpha,Beta and Gamma-ray Spectroscopy*, North-Holland Publication Co. (1966)
- [24] J.C. Wells, N.R. Johnson. *Computer Code LINESHAPE*, ORNL, (1994)
- [25] N.A.Matt,*Phys. Rev. C* 59 665, (1999)
- [26] K.-H.Speidel, Private Communication
- [27] J.L. Eberhardt et al, *Hyp. Int.* 3, (1977) 195
- [28] N.K.B. Shu et al, *Phys. Rev. C* 21 (1980), 1828
- [29] H.R.Andrews et al,*Nucl. Phys. A* 383 (1982) 509
- [30] K.Alder, A.Bohr, T. Huus, B. Mottelson and A.Winther *Study of Nuclear Structure by Electromagnetic Excitation with Accelerated Ions*, Reviews of Modern Physics, Vol. 28 4 (1956)
- [31] A.Osman and S.A. Saleh, *Acta. Physica Polonica* B16 865,(1985)
- [32] M.P.Robinson et al, *Nucl. Phys. A* 647 (1999), 175-196
- [33] N.W. Ashcroft and D.N. Mermin, *Solid State Physics*, W.B. Saunders Company 1976
- [34] G. de Angelis, A. Bracco and D. Curien, *Europhysics News* Vol. 34 No. 5 (2003)
- [35] A.E. Stuchbery et al, *Phys. Rev. C* 74 (2006) 054307
- [36] G.F.Knoll, *Radiation Detection and Measurement* 3rd Edition, John Wiley and Sons (2000)
-

-
- [37] <http://radware.phy.ornl.gov/gf3/gf3.html>
- [38] http://www.caen.it/nuclear/Printable/data_sheet.php?mod=V785&fam=vme&fun=pkadc
- [39] http://www.caen.it/nuclear/Printable/data_sheet.php?mod=V775&fam=vme&fun=tdc
- [40] <http://www.xia.com/DGF-4C.html>
- [41] K.S.Krane, *Introductory Nuclear Physics* 3rd Edition, John Wiley and Sons (1988)
- [42] <http://www.nndc.bnl.gov/ensdf/>
- [43] Z. Aung & P. Rice-Evans, *J. Phys. E. Sci. Instrum.* 7 145, (1974)
- [44] J.Eberth et al, *Prog. Part. Nucl. Phys.* 28 495, (1992)
- [45] R.B. Firestone, V.S. Shirley et al, *Table of Isotopes - CD ROM Edition*, version 1.0, (1996)
- [46] J.F. Ziegler, *SRIM: The Stopping and Range of Ions in Matter*, www.srim.org (2009)
- [47] A. C. Douglas, *insert reference here* (1962)
- [48] http://www.damtp.cam.ac.uk/user/stcs/courses/fcm/handouts/cauchy_principal_value.pdf (2007)
- [49] J. De Boer, *Multiple Coulomb Excitation Program COULEX*, (1978)
- [50] A. Ekström, Private Communication (2011)
- [51] T. Engeland et al, *The CENS software, a Computational Environment for Nuclear Structure*, <http://www.fys.uio.no/compphys/cp/software.html> (2011)
- [52] W.Walcher, *Praktikum der Physik*, B.G. Teubner Studienbücher (1994)
-

List of Figures

1.1	The location of the Sn chain in the chart of nuclides.	2
1.2	The experimentally measured $B(E2;0^+ \rightarrow 2^+)$ transition strengths for the chain of Sn isotopes compared to a shell model calculation.	4
1.3	The effective g-factors in ^{114}Sn at various excitations across the neutron and proton shell gaps, where a) is the configuration of $\nu g_{7/2}^{-1}d_{3/2}$ b) has the configuration $\nu d_{5/2}^{-1}s_{1/2}$ c) $\pi g_{9/2}d_{5/2}$ d) $\pi g_{9/2}d_{7/2}$	7
1.4	a) The $B(E2;0^+ \rightarrow 2^+)$ values from calculations of different nuclear models compared to the experimental data. b) The g-factors from calculations of different nuclear models when compared to previous data.	9
1.5	The measured g-factors from the experiment conducted by M.Hass et al. (For ^{114}Sn , due to the low-purity target (30%), the experimental $\Delta\phi$ implies only $g(^{114}\text{Sn}, 2_1^+) \gtrsim 0$ and hence an upper limit is shown here, for more information see reference) [19] and M.C. East and A.E. Stuchbery[20].	11
2.1	The shift 2ϕ for angular correlations measured with two field directions up and down. The points marked in red and blue denote the intensity shift between the up and down field directions for angles $\pm 65^\circ$	14
2.2	The spin exchange between the ferromagnet and the unpaired electrons of the s-shell of the ion, inducing the transient field.	17
2.3	Transient field attenuations for different probe ions in Gd hosts vs. the stopping power of the beam ions, where the different regions are divided into sections based on a function of $Z\frac{v}{v_0}$ [12].	20

2.4	Trajectory of the projectile in orbit in the Coulomb field of the target nucleus in the classical picture.	22
2.5	A schematic of the standard kinematics in Coulomb excitation where the heavy target ion is excited and the light beam ion is backscattered [22].	23
2.6	A schematic of the inverse kinematics in Coulomb excitation where the heavy beam ion is excited and the light target ion is scattered in the forward direction [22].	24
3.1	The difference seen in the peak between runs.	28
3.2	A possible explanation as to why the line shape shows a separate flight peak.	28
3.3	Sketch of the multilayer target used in the experiment U234.	29
3.4	Top) Photo of our target chamber. Bottom) A schematic diagram of the particle detector positioned behind the target.	31
3.5	Top) Photo of our target chamber. Bottom) The schematic diagram of the Ge detectors with respect to the target and the beam axis.	32
3.6	Detail of the cluster detectors and the crystals for U234.	33
3.7	Obtaining the relative ϕ between the crystals	34
3.8	Obtaining the relative angle θ between the crystals	34
3.9	The coordinate system showing the detector angles and the polar angles relative to the beam axis [35]	35
3.10	The schematic diagram of the electronics set up.	38
3.11	An uncalibrated raw gamma spectrum of ^{152}Eu for one crystal.	39
3.12	The energy of known γ transitions in ^{152}Eu in keV vs the channel number for one Ge crystal.	40
3.13	The efficiency calibration for one of the Ge crystals.	41
3.14	The gamma spectrum of ID 1 (Cluster 1 Crystal A) with calibrated energy.	45
3.15	The time spectrum of the Ge detector ID 1 (Cluster 1 Crystal A).	45
3.16	The time spectra of the four Si detectors.	46

3.17 a) The time spectra from the Ge detectors when gated on the four different Si TDC's separately. b) The time spectra when the Ge time is subtracted from the time of the triggering Si. (The time is inverted in this spectra as Si TDC - Ge TDC is applied)	47
3.18 Example of the gates applied to the time spectra.	48
3.19 Gamma spectrum with the TDC prompt gate implemented and background subtraction for the inner Si detectors for all Ge crystals. . . .	49
3.20 Gamma spectrum with the TDC prompt gate implemented and background subtraction for the outer Si detectors for all Ge crystals. . . .	50
3.21 The particle energy spectrum for one of the outer silicon detectors a) raw spectrum for ADC2 and b) spectrum gated on the prompt peaks in both Ge and Si TDC's. The particle energy spectrum for one of the inner silicon detectors c) raw spectrum for ADC3 and b) spectrum gated on the prompt peaks in both Ge and Si TDC's.	51
3.22 The Sn beam interacts with the target to produce the excited Sn ion and an ejected target ion, both scattered in angles ζ and θ , respectively.	52
3.23 The energy of the recoiling target ion vs the recoil angle shown for both inner and outer Si detectors.	53
3.24 The total reaction cross-section vs the recoil angle of the target ions shown for both inner and outer Si detectors.	55
3.25 Particle energy gates applied in the cases of the outer (left) and inner (right) Si detectors.	55
3.26 Spectrum and applied gate for ADC channel 1 - external magnetic field direction up, the spectra for magnet field down is identical. . . .	56
3.27 ^{114}Sn spectrum obtained with a particle gate in the inner Si detectors.	58
3.28 ^{118}Te spectrum obtained with a particle gate in the inner Si detectors.	59
3.29 ^{114}Sn spectrum obtained with a particle gate in the outer Si detectors.	60
3.30 ^{118}Te spectrum obtained with a particle gate in the outer Si detectors.	61
3.31 The Ge TDC subtracted by Si TDC (+3000 ch). The top set of figures show the subtraction from of the Ge TDCs by the Si TDCs of the inner Si detectors, and the bottom is the same for the outer Si TDCs. The colors red, blue, green and black correspond to the Si TDCs for each Si detector individually.	62

3.32	The gates used to clean the ^{122}Sn spectra for the inner Si detectors, the red arrows denote the gates used to increment the spectra, and the blue to decrement (background subtraction).	65
3.33	The gates used to clean the ^{122}Sn spectra for the outer Si detectors, the red arrows denote the gates used to increment the spectra, and the blue to decrement (background subtraction).	66
3.34	The two dimensional matrix between the γ -ray energy detected in the Ge detectors and the energy of the charged particle detected in one of the outer Si detectors for ^{122}Sn	67
3.35	The gates used to clean the ^{126}Te spectra for the inner Si detectors, the red arrows denote the gates used to increment the spectra, and the blue to decrement (background subtraction).	68
3.36	The gates used to clean the ^{126}Te spectra for the inner Si detectors, the red arrows denote the gates used to increment the spectra, and the blue to decrement (background subtraction).	69
3.37	^{122}Sn spectrum obtained with a particle gate in the inner Si detectors.	70
3.38	^{126}Te spectrum obtained with a particle gate in the inner Si detectors.	71
3.39	^{122}Sn spectrum obtained with a particle gate in the outer Si detectors.	72
3.40	^{126}Te spectrum obtained with a particle gate in the outer Si detectors.	73
4.1	The lineshape of the $2^+ \rightarrow 0^+$ transition in ^{116}Sn observed in the inner angles, with the FWHM and σ for the flight peak.	76
4.2	The angular correlation for the inner Si detectors for ^{116}Sn $2^+ \rightarrow 0^+$ transition, comparing the results without any correction for the Doppler shift (data points and fit curve in red) and with velocity correction (data points and fit curve in blue). Top) The angular correlation of the flight peak only Bottom) The angular correlation of the total peak.	78
4.3	Examples of the fitted lineshapes for the observed $2^+ \rightarrow 0^+$ transitions in ^{114}Sn in the Ge crystals located at polar angles $53^\circ, 65^\circ, 115^\circ$ and 127° with respect to the beam axis. These were detected in coincidence with the carbon ions in the inner Si detectors. [21]	80

-
- 4.4 The angular correlation for the $2^+ \rightarrow 0^+$ transition as observed from data for flight and stopped peak, the left hand side denotes the inner Si detector geometry, the right hand side the outer Si detector geometry, and the angular correlations are given for each isotope measured. 85
- 4.5 The angular correlation for the $3^- \rightarrow 2^+$ transition as observed from data, the left hand side denotes the inner Si detector geometry, the right hand side the outer Si detector geometry, and the angular correlations are given for each isotope measured. 86
- 4.6 The angular correlation for the $4^+ \rightarrow 2^+$ transition as observed from data, the left hand side denotes the inner Si detector geometry, the right hand side the outer Si detector geometry, and the angular correlations are given for each isotope measured. 87
- 4.7 The angular correlation for the normalized counts from high statistics cases a) $3^- \rightarrow 2^+$ b) $4^+ \rightarrow 2^+$ 89
- 4.8 The different regions of the Ge crystal used in calculating the parameters, the grey area is the dead core. 90
- 4.9 The general trend of Q_2 and Q_4 as a function of both distance and gamma energy [43]. 92
- 4.10 The angular correlations given in MuSTanG for the inner and outer detectors respectively, for the flight peak only in $2^+ \rightarrow 0^+$, the red data points and fit are for the experimentally measured data normalized to C, the black is from MuSTanG which gives discrete data points for $W(\theta)$ for angles from 0-180°, the black line is the corresponding fit. 95
- 4.11 The angular correlations given in MuSTanG for the inner and outer detectors respectively for the $3^- \rightarrow 2^+$ transition compared with the summed experimental values, the red data points and fit are for the experimentally measured data normalized to C, the black is from MuSTanG which gives discrete data points for $W(\theta)$ for angles from 0-180°, the black line is the corresponding fit. 96
-

4.12	The angular correlations given in MuSTanG for the inner and outer detectors respectively for the $4^+ \rightarrow 2^+$ transition compared with the summed experimental values, the red data points and fit are for the experimentally measured data normalized to C, the black is from MuSTanG which gives discrete data points for $W(\theta)$ for angles from 0-180°, the black line is the corresponding fit.	97
4.13	Attempt to reproduce the observed $2^+ \rightarrow 0^+$ angular correlation in ^{122}Sn using MuSTanG angular correlation coefficients for purely populated $2^+ \rightarrow 0^+$ transition, and the experimentally measured angular correlation coefficients for feeding states (based on the values given in table (4.5)) and measured intensity ratios compared with the data. The top is for the inner Si, and the bottom for the outer Si.	99
4.14	The combinations of a_2 and a_4 parameters which satisfy $\frac{W(51)}{W(65)}$ and $\frac{W(65)}{W(79)}$ for ^{114}Sn inner Si detectors $2^+ \rightarrow 0^+$	102
5.1	a) $N(t)$ over the time in ps for each possible decay b) Level scheme including feeding percentages.	116
5.2	A graphical description of the calculations made in the program. . .	119
5.3	Obtaining the angle of the recoil target particle detected in the Si detector.	124
5.4	The energies of the recoiling target ion and the excited projectile after Coulex as a function of the recoil lab angle.	126
5.5	The differential cross-section in the centre of mass frame and the lab frame as calculated from this program and from the Coulex code. . .	132
5.6	Transient field attenuations of various probe ions in Gd hosts vs. the stopping power of the beam ions, the different regions are characterized by $\frac{v}{Zv_0}$ [12].	135
6.1	The g-factors for both the raw, un-corrected values and corrected by for feeding effects. The data are split in terms of inner and outer Si detector geometry respectively, with inner on the left hand side of the mass number, and outer to the right.	146
6.2	The g-factors for the weighted means over the inner and outer Si detectors for the feeding correction methods 2 and 3.	147

6.3	The g-factors for the current and previously measured g-factor results.	149
7.1	The g-factors for experimental adopted results (the weighted mean of this measurement with the previously measured g-factors) and theoretical results.	153
7.2	The remeasured B(E2)s from GSI/ANU compared to the calculations and previous data.	154
A.1	Partial level schemes of the Sn isotopes as observed in the present work.	173
B.1	The g-factors for the weighted means over the inner and outer detectors, plus individual Si detectors for the feeding method 1 with σ ratios.	179

List of Tables

1.1	The effective g-factors for the single particle and 2^+ configurations.	6
1.2	The g-factors of the previously conducted experiments. *Result obtained from a low purity target.	12
2.1	Theoretical parameters A_k for different relevant transitions.	15
2.2	The Coulomb radii R_C and Coulomb barrier heights for $^{112,114,116,122,124}\text{Sn}$ beams on a ^{12}C target.	21
3.1	The crystals and their angles and polar angles: θ', ϕ' are the angles of the detectors, θ, ϕ are the polar angles and d is the distance from the crystal to the target for runs U234.	36
3.2	The crystals and their angles and polar angles: θ', ϕ' are the angles of the detectors, θ, ϕ are the polar angles and d is the distance from the crystal to the target for runs U236.	37
3.3	The relative intensities of the γ -transitions in the calibration source, ^{152}Eu [36].	40
3.4	The raw data information and the corresponding electronic modules.	43
3.5	The DGF module configuration for experiment U234.	44
3.6	The DGF module configuration for experiment U236, the DGFs for Cluster 2 G and F are in reverse order to the set up in U234.	64
4.1	The angular correlation coefficients for the transition $2^+ \rightarrow 0^+$ for the total peak (stopped and flight).	82
4.2	The angular correlation coefficients for the $3^- \rightarrow 2^+$ and $4^- \rightarrow 2^+$ transitions.	83
4.3	The normalized intensities relative to the directly populated 2^+ state.	84

4.4	The experimentally measured correlations used for fitting the angular correlations of $3^- \rightarrow 2^+$ and $4^+ \rightarrow 2^+$ transitions fitted to the data with the best yield.	88
4.5	The angular correlation parameters for the $3^- \rightarrow 2^+$ and $4^+ \rightarrow 2^+$ transitions fitted to the data with the best yield (refer to table (4.4)).	88
4.6	The input parameters to calculate Q_2 and Q_4	93
4.7	The parameters derived from MuSTanG for $^{112,114,116}\text{Sn}$ at inner detectors.	94
4.8	The purely populated $2^+ \rightarrow 0^+$ parameters from fit.	100
4.9	The angular correlation parameters compared for different methods for ^{114}Sn inner Si.	103
4.10	The angular correlation coefficients for cascade $3^+ \rightarrow 2^+ \rightarrow 0^+$	104
4.11	The measured precessions for $2^+ \rightarrow 0^+$ stopped and flight peak, inner Si detector geometry.	107
4.12	The measured precessions for $2^+ \rightarrow 0^+$ stopped and flight peak, outer Si detector geometry.	108
4.13	The measured precessions for $3^- \rightarrow 2^+$, inner Si detector geometry . .	109
4.14	The measured precessions for $3^- \rightarrow 2^+$, outer Si detector geometry . .	110
4.15	The measured precessions for $4^+ \rightarrow 2^+$, inner Si detector geometry . .	111
4.16	The measured precessions for $4^+ \rightarrow 2^+$, outer Si detector geometry . .	112
4.17	The weighed mean of the precessions.	113
5.1	The stopping powers at different energies for ^{116}Sn on ^{157}Gd , when compared to the stopping tables calculated in SRIM in units of $\text{MeV}/\mu\text{m}$	123
5.2	The comparison between the orbital integrals given by the program and from the table of orbital integrals [30] for the case of $\theta=160^\circ$ and $\xi=0.4$ for an E2 transition.	130
5.3	The comparison in the centre of mass differential cross-section values between the feeding program and the Coulex Code. The units of the differential cross-section are mb/str and θ_{cm} is in degrees	130

5.4	The comparison in the lab frame differential cross-section values between the feeding program and the Coulex Code. The units of the differential cross-section in mb/str.	131
5.5	The precessions for $g=1$ for all Sn nuclei in the feeding program and in TRANSI, for direct population. (* The lifetime for the state of 4^+ in ^{116}Sn used here is the NNDC value of 0.4ps)	137
6.1	The comparison between the intensities and the total cross-sections for each transition. Where $I_{2^+}^{pure}=I_{2^+}-I_{3^-}-I_{4^+}$	140
6.2	The Coulomb barrier heights for $^{112,114,116,122,124}\text{Sn}$ beams on a ^{12}C target compared to the beam energies used in the experiment.	141
6.3	The ϕ values where $G_{beam}=0.55(5)$. (* The lifetime of the 4^+ state of ^{116}Sn is taken to be 4ps here)	142
6.4	The measured g-factors of the 3^- and 4^+ states respectively. In the cases marked by the asterisk, these values are unreasonable and most likely due to bad statistics, for the g-factor feeding correction the inner Si values were used.	142
6.5	Input details for feeding correction.	143
6.6	Input details for method three - g-factors with sufficient statistics.	144
6.7	The g-factors with and without feeding corrections for methods 2 and 3 - for inner and outer detectors and their weighted means.	145
6.8	The old and remeasured g-factors for the Sn isotopes from this experiment, ref [19] and ref[20]	148
7.1	The old and remeasured lifetimes and $B(E2; 0_{g.s}^+ \rightarrow 2_1^+)$ transition strengths in $^{112-124}\text{Sn}$ [21][20].	152
8.1	Los datos por los factores g en los isotopos de Sn medidas de este experimento (U234/U236), y de referencia [19] y de [20]	169
A.1	The lifetimes, γ -ray energies and transition strengths for the Sn isotopes.	172
B.1	Variables read in for U234 run.	176
B.2	Variables read in for the U236 run.	177

B.3	The feeding corrected g-factor using cross-section ratios for η_{ij} and experimentally measured $\Delta\Phi$ s for feeding states.	178
D.1	The measured $\beta \pm \Delta\beta$ for the forward angles in all isotopes/Si detector configuration for the flight peak of the $2^+ \rightarrow 0^+$ transition γ peak. . .	187
D.2	The measured $\beta \pm \Delta\beta$ for the forward angles in all isotopes/Si detector configuration for the flight peak of the $3^- \rightarrow 2^+$ transition γ peak. . .	188
D.3	The measured $\beta \pm \Delta\beta$ for the forward angles in all isotopes/Si detector configuration for the flight peak of the $2^+ \rightarrow 0^+$ transition γ peak. . .	189
D.4	The measured $\beta \pm \Delta\beta$ for the forward angles in all isotopes/Si detector configuration for the flight peak of the $3^- \rightarrow 2^+$ transition γ peak. . .	190
D.5	The measured $\beta \pm \Delta\beta$ for the forward angles in all isotopes/Si detector configuration for the flight peak of the $3^- \rightarrow 2^+$ transition γ peak. . .	191
D.6	The measured $\beta \pm \Delta\beta$ for all isotopes/Si detector configuration for the flight peak of the $2^+ \rightarrow 0^+$ and $3^- \rightarrow 2^+$ transition γ peak. . . .	191
